

**Site Response Analysis and Microzonation of Anchorage, Alaska, USA,  
Using Strong-Motion Data from Recent Earthquakes**

John David Thornley

Thesis submitted to the Department of Civil and Environmental Engineering, University of  
Strathclyde, Glasgow, in fulfilment of the requirements for the degree of:

Doctor of Philosophy

In


Civil and Environmental Engineering

## Declaration of authenticity and author's right

This thesis is the result of the author's original research. It has been composed by the author and has not been previously submitted for examination, which has led to the award of a degree.

The copyright of this thesis belongs to the author under the terms of the United Kingdom Copyright Acts as qualified by University of Strathclyde Regulation 3.50. Due acknowledgement must always be made of the use of any material contained in, or derived from, this thesis.

Signed:

A handwritten signature in blue ink, consisting of several fluid, connected strokes that are difficult to decipher as specific letters.

Date: October 25, 2021

## **Acknowledgements**

First and foremost, my gratitude goes out to my wife, Terri, and our children who have been encouraging and supportive throughout the years of late nights and long weekends, and the occasional trip to Scotland. Their encouragement has made this path even more enjoyable. It can be hard to live with someone who enjoys the earth shaking the house on occasion, but Terri's continued patience needs one more mention, so, thank you Terri. I also want to thank my advisor, John Douglas, who took a chance on me working on this research remotely and offered me clear guidance and thoughtful criticism (who saw that we would all be working remotely in 2020-2021?). I have benefitted and grown significantly as a researcher under John's steady hand. It has truly been a pleasure to study under John and I look forward to future opportunities to collaborate. Utpal Dutta, who has been a constant colleague and supporter for the last decade has provided considerable guidance and direction both before and during this research adventure. Our discussions have been lively and very enjoyable. Joey Yang has also been a strong supporter, both before and during this research, and I have appreciated his critical eye and consistent presence throughout the work. I would be remiss not to thank Andy Garrigus for providing regular support in my learning enough GIS to produce half-way acceptable figures. His eye for presenting geospatial data is second to none.

This research would not have been as successful without the people who dedicate their days to the collection of the strong-motion data utilized in this research. This includes the maintenance and commitment to grow the network. The Alaska Earthquake Center was critical to this research. They provided much of the data utilized in this study. Key individuals have been acknowledged in the several journal articles that have resulted from this work, and they include Natalia Rupert, Mike West, and Mitch Robinson.

Jamie Steidl and the team at University of California Santa Barbara need a special callout as well. The Delaney Park Downhole Array is an amazing research tool and their tireless focus to keep the system operational and to provide data to the public is amazing. While Jamie may not think it, I have enjoyed each opportunity to help troubleshoot the system for him when there is an issue and have enjoyed being able to give back, in a small way, to the work that he and his team continue to provide. The teams at the USGS and Alaska Volcano Observatory who have offered continued support of the instruments in Anchorage are also very much appreciated.

While there are numerous others, including friends and family, who deserve the special thanks, I would be amiss if I did not thank the more local support. This includes the Municipality of Anchorage Geotechnical Advisory Commission, and especially Dave Cole, Buzz Scher, and John Aho. Their constant focus on earthquake risk mitigation gave real purpose to my work. I also would like to acknowledge Golder Associates who have been supportive of this effort. Their support has made it substantially easier to work the long hours after my day job to perform this research and attempt to contribute to the science of earthquakes and risk mitigation.

I would also like to thank the second member of my program committee. Stella Pytharouli was my second advisor and provided regular support throughout the program, attending yearly progress meetings, and supporting my needs as a student. I would also like to thank Stephen Suryasentana, who acted as internal reviewer, and Benedikt Halldorsson of the University of Iceland, who acted as external reviewer of my Viva. It was a pleasure discussing my research with them and I believe I grew even more through that experience.

## Abstract

Anchorage, Alaska, is located in one of the most active tectonic settings in the world. The city and region were significantly impacted by the  $M_w$ 9.2 Great Alaska Earthquake in 1964, and they were recently shaken by a  $M_w$ 7.1 event in 2018. The city was developed in an area underlain by complex soil deposits of varied geological origins and stiffnesses, with the deposits' thicknesses increasing east to west. Situated at the edge of the North American Plate, with the actively subducting Pacific Plate below, Anchorage is susceptible to both intraslab and interface earthquakes, along with crustal earthquakes. Strong-motion stations were installed across the city in an attempt to capture the variability in site response. Strong-motion recordings from 35 stations over the years of 2004 to 2019 were collected, processed, and prepared for analysis of that variability. The Generalized Inversion Technique (GIT) was used to calculate the Fourier spectral amplification at each strong-motion station and the variability of amplification at 1 Hz and 5 Hz were mapped for Anchorage. The 2018  $M_w$ 7.1 strong-motion recordings were compared to the lower-magnitude events in the database to evaluate the differences at strong-motion stations related to linear and nonlinear site response. The horizontal to vertical spectral ratio (HVSr) was calculated for each strong-motion station and regional relationships between  $f_{\text{peak}}$  and the time-averaged shear wave velocity in the upper 30m ( $V_{s30}$ ) were developed. A contour map estimating seismic site class across Anchorage was developed using 70  $V_{s30}$  estimates and measurements at other locations. A methodology is also developed using Fourier spectral amplification and Random Vibration Theory (RVT) to estimate engineering site response spectra at strong-motion stations. An approach to address nonlinear site response is applied to the methodology because the database is predominantly composed of linear site response recordings.

## Publications

### Journal Articles:

1. Thornley, J., U. Dutta, P. Fahringer, Z. Yang, 2019, In Situ Shear-Wave Velocity Measurements at the Delaney Park Downhole Array, Anchorage, Alaska. *Seismological Research Letters*, Volume 90, Number 1, January/February 2019 (p 395-400) doi: 10/1785/0220180178.
2. Thornley, J., J. Douglas, U. Dutta, Z. Yang, 2021, Site Response Analysis of Anchorage, Alaska Using Generalized Inversions of Strong-Motion Data (2014-2019), *Geophysical Journal International* (In Review after revisions).
3. Thornley, J., U. Dutta, J. Douglas, Z. Yang, 2021, Nonlinear Site Effects from the 30 November 2018 Anchorage, Alaska Earthquake, *Bulletin of the Seismological Society of America*, Accepted February 2021, doi: 10.1785/0120200347.
4. Thornley, J., U. Dutta, J. Douglas, Z. Yang, 2021, Evaluation of Horizontal to Vertical Spectral Ratio and Spectral Amplitude Methods for Estimating Shear Wave Velocity in Anchorage, *Soil Dynamics and Earthquake Engineering* (In Review after revisions).
5. Thornley, J., J. Douglas, U. Dutta, Z. Yang, 2021, Engineering Site Response Analysis of Anchorage, Alaska Using Site Amplifications and Random Vibration Theory, *Earthquake Spectra*, (In Review).

### Other Relevant Paper (Included in Appendix B):

1. Thornley, J., U. Dutta, Z. Yang, J. Douglas, 2020, Nonlinear Site Response Analysis at the Delaney Park Downhole Array in Anchorage, Alaska, *17<sup>th</sup> World Conference on Earthquake Engineering, 17WCEE*, Paper No. C004020.

Other Relevant Articles and Reports as Coauthor (Introduction/Abstracts in Appendix C):

1. Hassan, W., J. Thornley, J. Rodgers, C. Motter, 2021, EERI Earthquake Reconnaissance Report: M7.1 Anchorage Earthquake on Nov 30, 2018, Earthquake Engineering Research Institute Learning from Earthquakes Program, 2021 (In Publication).
2. West, M. E., A. Bender, M. Gardine, L. Gardine, K. Gately, P. Haeussler, W. Hassan, F. Meyer, C. Richards, N.A. Ruppert, C. Tape, J. Thornley, and R.C. Witter, 2020, The 30 November 2018 Mw 7.1 Anchorage Earthquake. *Seismological Research Letters*, 91(1), 66–84. doi: 10.1785/0220190176
3. Rodgers, J., W. Hassan, C. Motter, J. Thornley, 2021, Impacts of the 2018 M7.1 Anchorage Earthquake on Schools, *Earthquake Spectra*, March 2021, doi: 10.1177/8755293020988022.
4. Hassan, W., J. Rodgers, C. Motter, J. Thornley, 2021, Structural Performance of Buildings during the November30, 2018 M7.1 Anchorage, Alaska Earthquake, *Earthquake Spectra* (In Review).

## Table of Contents

Acknowledgements .....	ii
Abstract.....	iv
Publications.....	v
List of Tables .....	xiii
List of Figures .....	xiv
1.0 Introduction .....	1
2.0 A Brief History of Earthquake Recording Stations and Microzonation Studies in Anchorage .....	6
2.1 Seismic Monitoring Station History in Anchorage.....	6
2.2 Growth and Upgrades to the Network .....	12
2.3 Summary of Recent Anchorage Strong-Motion Network Microzonation Studies .....	14
3.0 Strong-Motion Selection and Time History Processing .....	17
3.1 Ground Motion Selection .....	17
Database Procurement.....	21
3.2 Magnitude Conversion.....	21
Effects on the Database .....	25
3.3 Time History Processing.....	26
Header Data .....	27
Multipliers.....	28
Compression and Shear Wave Arrival Picking .....	28



Time History Filtering.....	28
Processing Summary.....	29
3.4 Generalized Inversion Technique .....	38
4.0 In-Situ Shear Wave Velocity Measurements at the Delaney Park Downhole Array, Anchorage, Alaska.....	41
4.1 Abstract.....	41
4.2 Introduction .....	42
4.3 Background .....	42
4.4 Field Study.....	45
4.5 Vertical Seismic Profiling of the Casing.....	45
4.6 Summary of Results .....	46
4.7 Transfer Function Evaluation.....	48
4.8 Comparison of Results to those for Nearby Sites .....	51
4.9 Relevant Engineering Properties .....	53
4.10 Conclusions .....	53
5.0 Site Response Analysis of Anchorage, Alaska Using Generalized Inversions of Strong- Motion Data (2004-2019).....	55
5.1 Abstract.....	55
5.2 Introduction .....	56
5.3 Tectonic Setting and Seismicity of the Southcentral Alaska.....	58
5.4 Geology.....	60

5.5 Anchorage Strong Motion Network.....	62
5.6 Strong Motion Data Used in the Current Study.....	63
Seismic Sensor and Data Collection.....	64
5.7 Site Response Evaluation.....	66
GIT Background Information.....	66
5.8 Sensitivity of Model.....	72
5.9 Site Response.....	76
5.10 Spectral Amplification Variability Across Anchorage.....	79
5.11 Geological impacts on Spectral Amplification.....	83
5.12 Conclusions.....	85
6.0 Nonlinear Site Effects from the 30 November 2018 Anchorage, Alaska, Earthquake ....	87
6.1 Abstract.....	87
6.2 Introduction.....	88
6.3 Seismotectonic Setting and Geology of Southcentral Alaska.....	89
6.4 Strong-Motion Network and Data.....	92
6.5 Methodology.....	93
6.6 Site Response and Nonlinear Effects.....	96
6.7 Conclusions.....	101
7.0 Evaluation of Horizontal to Vertical Spectral Ratio and Standard Spectral Ratio Methods for Mapping Shear Wave Velocity Across Anchorage, Alaska.....	102
7.1 Abstract.....	102

7.2 Introduction .....	103
7.3 Geology .....	107
7.4 Strong-Motion Stations and Dataset .....	109
7.5 HVSr Analysis.....	110
7.6 Evaluation of $V_{S30}$ by HVSr (an evaluation of several methods).....	112
7.7 Relationship Between $V_{S30}$ and HVSr .....	117
7.8 Comparison of $f_{peak}$ and $A_{peak} V_{S30}$ relationships to global models.....	118
7.9 $V_{S30}$ Map of Anchorage .....	121
7.10 Concluding Remarks .....	124
8.0 Engineering Site Response Analysis of Anchorage, Alaska Using Site Amplifications and Random Vibration Theory.....	126
8.1 Abstract.....	126
8.2 Introduction .....	127
8.3 Tectonic Setting and Seismicity .....	128
8.4 Geology.....	129
8.5 Strong-motion Stations and Dataset .....	131
8.6 Site Spectral Amplification Evaluation.....	131
8.7 Engineering Site Response Using Random Vibration Theory .....	133
Proposed Methodology .....	134
Generalized Approach .....	135
Application of the Proposed Methodology .....	137

8.8 Nonlinear Site Effects.....	139
8.9 Comparison to EQL Site Response Modeling.....	140
8.10 Ground Motion Model Comparison .....	142
8.11 Discussion and Application .....	148
8.12 Conclusions .....	149
9.0 Conclusions and Future Research.....	150
9.1 Key Take-Aways .....	151
9.2 Further Research Opportunities .....	154
10.0 References .....	157
Appendix A.....	172
Appendix A-1: List of Stations and $V_{S30}$ Estimates and the $f_{peak}$ and $A_{peak}$ results from the HVSR analysis.....	173
Appendix A-2: List of Events .....	174
Appendix A-3: Strong-motion Station Spectral Amplification .....	177
Appendix A-4: Horizontal to Vertical Spectral Ratios .....	180
Appendix A-5: $V_{S30}$ Data (Dutta et al. 2000).....	183
Appendix A-6: Spectral Amplifications – Nonlinear Site Response .....	184
Appendix B: NONLINEAR SITE RESPONSE ANALYSIS AT THE DELANEY PARK DOWNHOLE ARRAY IN ANCHORAGE, ALASKA.....	186
Appendix C: Relevant Coauthored Papers and Reports .....	202
Appendix C-1: Hassan et al. 2021 (In Publication) .....	203

INTRODUCTION.....	204
<b>Overview of the November 30, 2018, Anchorage Earthquake.....</b>	<b>204</b>
<b>EERI Reconnaissance Team Members .....</b>	<b>204</b>
<b>EERI Reconnaissance Team Activities .....</b>	<b>204</b>
<b>Coordination with Other Reconnaissance Teams .....</b>	<b>205</b>
<b>EERI Clearinghouse Coordination .....</b>	<b>205</b>
<b>EERI and LFE Program.....</b>	<b>206</b>
<b>EERI and LFE Program.....</b>	<b>206</b>
Appendix C-2: West et al. 2020 .....	207
Appendix C-3: Rodgers et al. 2021.....	208
Appendix C-4: Hassan et al. (In Review) .....	209

## List of Tables

Table 2.1 Earthquakes greater than M4.0 within 300km of Anchorage (1974-1993).

Table 4.1. Earthquake Event Details.

Table 6-1. Stations with November 2018  $M_w$ 7.1 event estimated shear strain proxy ( $PGV/V_{s30}$ ) divided by site class using the corresponding  $V_{s30}$  ranges (ranges based on BSSC 2019). Estimates of  $V_{s30}$  are presented in Thornley et al. (2021b). PGA and PGV values are found in Center for Engineering Strong Motion Data (2020).

Table 7.1. Seismic Site Classification (modified from BSSC 2019)

Table 8.1. Ground motions utilized for DPDA calibrated model comparison with the RVT-based technique. Time histories and station data from PEER (2021). Maximum shear strain and surface PGA are calculated in the Strata DPDA model.

Table 8.2.  $V_{s30}$  ranges by site class proposed by BSSC (2020) and Anchorage strong-motion station estimates used in this study.

## List of Figures

Figure 2.1. Alaska Accelerograph Station Locations (reproduced from Porcella 1979)

Figure 2.2. Accelerograph Stations in Anchorage from 1974 through 1993. Fire Stations are denoted by FS and by number.

Figure 2.3. Earthquake epicenters recorded in Anchorage between 1974 and 1993. Magnitude scales are indicated, and ML is for local magnitude, Mw is for moment magnitude, and Mb is for body magnitude. Inset figure presents the location of the figure with respect to Alaska and is not to scale.

Figure 2.4. Strong-motion stations utilized in the microzonation analysis of Anchorage, Alaska for this study.

Figure 3.2. Epicentral distance versus local magnitude – Entire DPDA dataset.

Figure 3.3. Epicentral distance versus local magnitude.

Figure 3.3. Epicentral distance versus local magnitude –  $M_L4.5$  with a maximum distance of 300km.

Figure 3.4. Instrument K212 HNE Record for the July 8, 2010  $M_w4.8$  Event. The unfiltered acceleration time history is in the upper frame and the signal and noise spectra are plotted in the lower frame for the unfiltered time history.

Figure 3.5. Instrument K212 HNE Record for the July 8, 2010  $M_w4.8$  Event. Acceleration, Velocity, and Displacement Time Histories for a Butterworth Bandpass Filter with Cutoff Frequencies of 0.1 and 30 Hz.

Figure 3.6. Instrument K212 HNE Record for the July 8, 2010  $M_w4.8$  Event. Signal to Noise Ratio of the time history with a Butterworth Bandpass Filter with Cutoff Frequencies of 0.1 and 30 Hz. (Compare to Figure 3.4)

Figure 3.7. Instrument 8011 HNE Record for the July 29, 2015  $M_w6.3$  Event. The acceleration time history and the signal and noise spectra of the unfiltered event are shown in the top and bottom frames, respectively.

Figure 3.8. Instrument 8011 HNE Record for the July 29, 2015  $M_w6.3$  Event. Acceleration, Velocity, and Displacement Time Histories for a Butterworth Bandpass Filter with Cutoff Frequencies of 0.1 and 30 Hz.

Figure 3.9. Instrument 8011 HNE Record for the July 29, 2015  $M_w6.3$  Event. The signal and noise spectra of the time history with a Butterworth Bandpass Filter with Cutoff Frequencies of 0.1 and 30 Hz. (Compare to Figure 3.7)

Figure 3.10. Example time history plot (a.) where the pre-event noise window is indicated in red and the S-wave window is in grey and (b.) the Fourier amplitude spectrum of the filtered signal (in black) and the noise (in red).

Figure 3.11. HVSR of the strong-motion stations used in this study. K216, the selected reference station, is the black line and 8040 is the blue line.

Figure 4.1. Delaney Park Borehole Array sensor layout and generalized geology with the previously assumed shear wave velocity profile.

Figure 4.2. Location of the Delaney Park Downhole Array. Inset Figure (Upper Left) shows the location of the array site adjacent to Delaney Park in downtown Anchorage. Inset Figure (Lower Right) shows the relative locations of the two earthquake events used in this study.

Figure 4.3. Measured Five-Point Moving Average Shear Wave Velocity Profile.

Figure 4.4. Measured Five-point Moving Average Compression Wave Velocity Profile.

Figure 4.5. Comparison of theoretical transfer functions of the assumed and measured shear wave velocity profiles using two recent earthquakes.

Figure 4.6. Comparison of Measured Shear Wave Velocity and Estimated Shear Wave Velocity through CPT and SPT.

Figure 5.1. Southcentral Alaska tectonics and earthquake epicenters used in this study. Subduction zone depth contours in black using Slab 2.0 (Hayes 2018) and active crustal faults in red (Koehler 2013). The inset map indicates the location of the study in Alaska. The large red dot in the southwest corner of the figure presents the epicentral location of the January 24, 2016  $M_w$ 7.1 Iniskin Earthquake. The red dot located near the center of the figure presents the location of the November 30, 2018  $M_w$ 7.1 Anchorage Earthquake.

Figure 5.2. Strong motion station locations in Anchorage, Alaska. The generalized surficial geology is provided in the background to show variability, along with cross-section locations (dashed black lines) with figure references described in subsequent sections.

Figure 5.4. Epicentral distance versus magnitude with crustal, intraslab, and interface events identified.

Figure 5.5. Summary of Database Event Parameters. (a) Magnitude Distribution, (b) Epicentral Distance to Anchorage, (c) Event Depth, (d) Azimuthal Direction from Anchorage. The mean value for each bin is presented on the x-axis.

Figure 5.6. Number of earthquake recordings per station from 2004 to 2019 used in this study.

Figure 5.7. Sensitivity of  $Q_0$  and  $\eta$  on spectral amplification for Station 8040. (a.) Range of  $Q_0$  from 100 to 250 holding  $\eta$  at 1.00. (b.) Range of  $\eta$  from 0.5 to 1.2 holding  $Q_0$  at 150.

Figure 5.8. Sensitivity of  $Q_0$  and  $\eta$  on source spectra for the  $M_w$ 7.1 Anchorage Earthquake. (a.) Range of  $Q_0$  from 100 to 250 holding  $\eta$  at 1.00. (b.) Range of  $\eta$  from 0.5 to 1.2 holding  $Q_0$  at 150.

Figure 5.9. Source spectra calculated for this study. (a.) Source spectra for the 95 events with the  $M_w$ 7.1 earthquake source spectrum in black and the others in grey. The dashed black line shows the general slope of Brune's omega square model. (b.) The  $M_w$ 7.1 source Spectrum with  $Q_0$  of 150 and a range of  $n$  values between 0.5 and 1.0 in black. The omega square model for the event (Brune 1970) for two stress drops in grey. Note, the y-axis scales in a. and b. are different.

Figure 5.10. Residual plot of magnitudes less than and greater than  $M_w$ 5.0. The black line indicates the average and the red lines  $\pm 1$  standard deviation.

Figure 5.11. Azimuthal residual results for the azimuth range between 330 and 360 degrees. The black line indicates the average, and the red lines are  $\pm 1$  standard deviation.



Figure 5.12. Spectral amplification results for Stations K203 (Site Class C), K213 (Site Class CD), and 8037 (Site Class D). On the left-hand side, the spectral amplifications for all events excluding the  $M_w7.1$  event are in black with the grey shading presenting the standard error and the red line presenting the spectral amplification from the  $M_w7.1$  event. On the right-hand side the spectral amplifications of the database with and without the  $M_w7.1$  event included (red line with and black line without), and the dashed line the ratio of the two (i.e., database without/database with).

Figure 5.13. Spectral amplifications of two sites (a) DPDA station (8040) in north-central Anchorage and (b) Station K209 in east Anchorage. The average spectral amplification is indicated by the red line and the standard error is indicated by the shaded area above and below the average. Amplifications are relative to the reference station.

Figure 5.14. Spectral amplification at the K220 Station – the western-most station used in this study. The vertical left shaded band is the range of the 1 Hz band average and the vertical right shaded band is the range of the 5 Hz band average.

Figure 5.15. 1 Hz band-averaged spectral amplification contour map. Contours are in 0.5 spectral amplification units. The stations are indicated along with their band average spectral amplification for 1 Hz frequency.

Figure 5.16. 5 Hz band-averaged spectral amplification contour map. Contours are in 0.5 spectral amplification units. The stations are indicated along with their band average spectral amplification for 5 Hz frequency.

Figure 5.17. North-South Geologic Cross Section (South is on the left side of the figure). Geologic Cross Section from Combellick (1999) C Street section. Vertical and horizontal spectral amplification plot axes are the same on all plots.

Figure 5.18. East-West Geologic Cross Section (West is on the left side of the figure). Geologic Cross Section from Combellick (1999) Tudor section.

Figure 5.19. Northwest-Southeast Geologic Cross Section (northwest is on the left side of the figure). Geologic Cross Section from Combellick (1999) NW/SE section.

Figure 6.1. The tectonic setting of Southcentral Alaska along with the contours of the interface between the subducting Pacific plate and the North American plate using Slab 2.0 (Hayes 2018) and crustal faults as identified by Koehler (2013). The earthquake epicentral locations used in this study are shown as circles and have been further divided into intraslab, interface, and crustal events. For reference the epicenter of the  $M_w9.2$  Great Alaska Earthquake is identified, although the rupture area of this event was very large and hence its epicenter is a relatively poor representation of its location.

Figure 6.2. A simplified geologic map of Anchorage with strong-motion station locations. Hatching identifies the site class based on estimated  $V_{s30}$ . A 10-m isopach line is added from Combellick (1999) to show the geologic break in BCF thickness, where the BCF becomes thinner to the east of the line.

Figure 6.3. An example of site response results for two stations. The solid black line with grey shading provides the average site response and standard error for the database of 94 events. The dotted line is the spectral amplification result from the 2018  $M_w7.1$  event. All sites utilized in this study have been included in the electronic supplement.

Figure 6.4. Logarithmic spectral amplification based on site class for the full dataset in grey and the  $M_w7.1$  event in red. The shading shows the range of  $\pm 1$  standard deviation for each dataset. There is more variability in the standard deviations for the  $M_w7.1$  event because it

is based on the range of site class amplification from one event, whereas the full dataset is much more constrained.

Figure 6.5. The site database (in grey) and the aftershock events (in red) with  $\pm 1$  standard deviation for site class D and DE.

Figure 6.6. Strain proxy estimates at four stations representative of each site class versus PGA. The highest PGA values and strain proxies correspond to the  $M_w 7.1$  event.

Figure 7.1. Southcentral Alaska's tectonic setting. The contours indicate the depth of the interface between the subducting Pacific plate and the North American plate and regional crustal faults (Koehler et al. 2021). The earthquake epicentral locations used in this study are shown as circles and have been further divided into intraslab, interface, and crustal events. The inset figure indicates the location in Alaska considered for this study.

Figure 7.2. Strong-motion station locations in Anchorage, Alaska. (a) The generalized surficial geology is provided in the background along with a cross-section location (dashed black line). Notably, the Bootlegger Cove Formation (BCF) is in green. (b) A simplified geologic cross-section depicting the variability of subsurface conditions across Anchorage (modified from Combellick (1999)). Note the vertical exaggeration.

Figure 7.3. Epicentral distances of the 95 events used in this study to central Anchorage versus magnitude with crustal, intraslab, and interface events identified. Distances are calculated from Station 8040 (Figure 7.1) located in downtown Anchorage (location presented in Appendix A).

Figure 7.4. HVSr data presenting three conditions where the selected peak may vary. (a) shows a single peak where the peak frequency is approximately 3 Hz. (b) shows multiple peaks where the second peak is the highest peak. (c) shows double peaks where there are two peaks, and the amplitude of the highest peak is not much different from the amplitude of the second peak. Arrows indicate selected peaks.

Figure 7.5.  $V_{S30}$  data for several strong-motion stations in Anchorage and the HVSr  $f_{\text{peaks}}$  for those sites plotted with models from four different studies. The black diamonds represent measured  $V_{S30}$  data and the red triangles ("1 Hz Estimate") represent the results from an SSR estimate of  $V_{S30}$  (introduced subsequently). NGA-West2 and Japan models are only applicable from 1 to 10 Hz.

Figure 7.6. Plot of the relationship between 1 Hz logarithmic band-averaged spectral amplification and measured  $V_{S30}$  profiles. The SSR values plotted for this study are from the results presented in Thornley et al. (2021a). The dashed black lines present  $\pm 1$  standard deviation for the data used in this study.

Figure 7.7. HVSr (black line and grey shaded area is standard error range) and SSR (red line) plots of a station in (a) central Anchorage (K213) and (b) a site in eastern Anchorage (K215).

Figure 7.8. Comparison between band-averaged SSR and band-averaged HVSr data at 1 and 5 Hz using a Bland-Altman difference plot for Anchorage data for the 35 stations in this study. The median and  $\pm$  one standard deviation range of the dataset are shown as solid and dashed lines, respectively.

Figure 7.9. Comparison of  $V_{S30}$  results for the 1 Hz band-averaged SSR and four HVSr-based models. (a) CEUS model, (b) Iran model, (c) Japan model, and (d) NGA-West2 model.

Figure 7.10. Estimated  $V_{S30}$  relationship with HVSr  $f_{\text{peak}}$  and  $A_{\text{peak}}$  results, black circles. The regression line (solid black line with  $\pm$  one standard deviation in black dashed lines) shows

that the results generally fit within the median  $\pm$  one standard deviation (blue solid and dashed lines, respectively) for the NGA-West2 dataset, as presented in Figure 7-8 of Ghofrani and Atkinson (2014).

Figure 7.11. Contour map of BSSC (2019) Seismic Site Class, based on  $V_{S30}$  estimates at strong-motion stations and measurements at other locations across Anchorage.

Figure 8.1. The tectonic setting of Southcentral Alaska, including contours of the interface between the North American and the subducting Pacific plates (using Slab 2.0; Hayes 2018) and crustal faults as identified by Koehler (2013). The colored circles indicate the epicenters of the earthquakes used in this study, which have been divided into intraslab, interface, and crustal events.

Figure 8.2. A simplified geologic map of Anchorage with strong-motion station locations. Hatching identifies the site class based on estimated  $V_{S30}$  (Thornley et al. 2021b). A 10-m isopach line is added from Combellick (1999) to show the geologic break in BCF thickness, where the BCF becomes thinner to the east of the line.

Figure 8.3. Spectral amplification for a station located on a shallow soil deposit over dense glacial till (a) and a station with more than 40m of variable soil, including soft silts and clays, over dense glacial till (b).

Figure 8.4. Process for using RVT and IRVT to utilize spectral amplifications to estimate site-specific response spectra given the response spectrum for a reference site. Step 1 begins in the lower right-hand corner. Step 3 is similar to the process used in standard EQL analysis (dashed arrows).

Figure 8.5. a. Station K212 (site class C), b. Station K213 (site class CD). c. Station 8040 (site class D), d. Station K208 (site class DE), where the measured response spectrum at each site is presented as the solid line and RVT-based response spectrum calculated from the K216 reference site is presented as the dashed line. For reference, the grey line indicates the K216 (reference site) geometric-mean response spectrum.

Figure 8.6. Response spectra at Station K208. The measured response spectrum is shown in black, and the EAF-based response spectrum is in red.

Figure 8.7. The results of the comparison between the DPDA EQL model and the RVT-based approach using the 1999 Chi-Chi record (a.), 1999 Duzce, Turkey record (b.), 1999 Hector Mine record (c.), and the 1999 Kocaeli, Turkey record as input motions (grey line). The DPDA EQL model is shown in black. The linear and nonlinear results from the RVT approach are shown in blue and red, respectively. Note the change in vertical scale in c) and (d.).

Figure 8.8. a. Station K212 (site class C), b. Station K213 (site class CD). c. Station 8040 (site class D), d. Station K208 (site class DE) where the black line with dotted lines indicates the median and  $\pm 1$  standard deviation response spectra for the NGA-Sub GMMs for the Mw9.2 event. The blue line is the RVT-based median response spectrum without the correction for nonlinearity and the solid red line corrects for nonlinearity using the factors recommended by Parker et al. (2020) and the dashed red lines using the factors of Seyhan and Stewart (2014).

Figure 8.9. Response spectra for strong-motion stations in Anchorage by site class (frames a. through d. presents site class C, CD, D, and DE, respectively). The median is the black line and the  $\pm 1$  standard is shaded.

Figure 8.10. Response spectra for the combination of strong-motion stations in Anchorage by site class (frames a. through d. present site class C, CD, D, and DE, respectively). The black

line with dotted lines indicates the median and  $\pm 1$  standard deviation response spectra for the NGA-Sub GMMs for the M9.2 event. The blue line is the RVT-based median response spectrum without the correction for nonlinearity, and the solid red line corrects for nonlinearity using the factors recommended by Parker et al. (2020) and the dashed red lines for Seyhan and Stewart (2014).

Figure 8.11. Response Spectra for the combination of Anchorage site classes (frames a. through d. present site class C, CD, D, and DE, respectively). The black line with dotted lines indicates the median and  $\pm 1$  standard deviation response spectra for the NGA-West2 GMMs for the  $M_w 7.5$  event. The blue line is the RVT-based median response spectrum without the correction for nonlinearity, and the red line corrects for nonlinearity.

## 1.0 Introduction

Anchorage, Alaska, USA is home to approximately half of the State's population, with roughly 300,000 residents. More than 75% of the goods delivered to Alaska travel through the Port of Alaska, located in Anchorage. The international airport is the 4<sup>th</sup> busiest cargo hub in the world, linking Asia and North America. In addition, a large military installation is located at the north end of the city. Anchorage is also home to sources of significant earthquake hazards. The  $M_w$ 9.2 Great Alaska Earthquake, the second largest earthquake in recorded history, struck southcentral Alaska in 1964, and caused significant destruction to Anchorage and surrounding communities (Hansen 1965).

With both active subduction and crustal earthquake sources in the region, Anchorage offers an urban earthquake laboratory that allows for relatively easy study of earthquakes, due to their high frequency of occurrence. The Aleutian Megathrust subduction zone, responsible for the 1964 Great Alaska Earthquake, produces earthquakes greater than  $M$ 7 on average once every 11 years (West et al. 2020). The recent  $M_w$ 7.1 Anchorage Earthquake in 2018 resulted in widespread damage across southcentral Alaska, especially in Anchorage.

Over the past several decades strong-motion stations have been installed in Anchorage to record earthquakes and understand the varying site response across the city. Through the analysis of earthquake ground motions recorded at these strong-motion stations, the generalized site response can be estimated. However, one of the main challenges has been the lack of high-intensity ground motions that can cause nonlinear site response within the soil. Development of a novel technique that bridges seismology and earthquake engineering together, using lower-intensity ground motions would not only benefit the population of Anchorage, but could be used at strong motion networks in other parts of the world. To that end, there are several key objectives that this research aims to achieve.

- **Update the spectral amplification mapping of Anchorage:** Previous studies have developed maps of spectral amplification variability across Anchorage (e.g., Dutta et al. 2003). However, the previous studies used fewer strong-motion stations, a smaller earthquake dataset, and lower-intensity ground motions. Updating the spectral amplification mapping of Anchorage provides more granularity related to the variable geologic conditions and provides a baseline for evaluating site response, focusing on 1 Hz and 5 Hz spectral amplifications.
- **Evaluation of nonlinear site response across Anchorage:** Utilizing the  $M_w 7.1$  Anchorage Earthquake, comparisons can be made between low-intensity spectral amplifications related to the bulk of the earthquake database available and higher-intensity ground motions. The results support the need to account for nonlinear soil behavior when using lower-intensity ground motions to estimate site response.
- **Update the  $V_{S30}$  (time-averaged shear wave velocity in the upper 30m) mapping of Anchorage:**  $V_{S30}$  is the primary parameter for estimating seismic site classification in the building code (ASCE 2017). Updating the  $V_{S30}$  map of Anchorage is updated using the spectral amplification results from strong-motion stations and additional surface and downhole  $V_{S30}$  measurements at other sites. Regional relationships are also developed to support future expansion of the strong-motion network or other temporary installations.
- **Develop a method to use lower-intensity ground motions to estimate site response:** One of the challenging aspects of previous regional site amplification studies has been the inability to directly use Fourier spectral amplification results to calculate engineering response spectra, and the applicability of the results to estimate site response due to earthquakes that result in nonlinear soil behavior. A main objective of this study is to help bridge that gap and develop a method to utilize

lower-intensity ground motions to estimate site response for a future high-intensity earthquake.

The research presented here provides the basis for planners and designers to consider earthquake hazards at a local level, with more detail than the current building code allows, thus providing a framework for estimated site response that can be used to plan future developments. The following chapters provide insight into the history of earthquake records and the strong-motion stations in Anchorage; the development of a database of recent high-quality earthquake records; and their use in analyses to better understand the variability of ground shaking across the city because of the complex geologic conditions.

### Thesis Outline

This thesis is divided into several chapters which are summarized below. Several of the chapters presented here are also journal articles that have been submitted and are in various states of review and acceptance.

#### **Chapter 2 – A Brief History of Earthquake Recording Stations and Microzonation Studies in**

**Anchorage:** This chapter provides a background of the strong-motion station development in Anchorage, Alaska, USA. A summary of the history of past microzonation studies using local strong-motion station recordings gives the reader some understanding as to the decisions made in selecting the range of earthquake ground motions used for this study.

#### **Chapter 3 – Strong Motion Selection and Time History Processing:**

This chapter provides background regarding the selection of the earthquakes utilized in the study. The methodology and examples of the processing of acceleration time histories for the study is presented. In addition, some initial background regarding the analyses and the reference site selection are presented.

**Chapter 4 – In-Situ Shear Wave Velocity Measurements at the Delaney Park Downhole Array, Anchorage, Alaska:** This chapter presents a journal article (reproduced from *Seismological Research Letters*) that summarizes the shear wave velocity measurements collected at the Delaney Park Downhole Array (DPDA). A one-dimensional equivalent linear site response model is developed from the subsurface geotechnical data, including the shear wave velocity data.

**Chapter 5 – Site Response Analysis of Anchorage, Alaska Using Generalized Inversions of Strong-Motion Data (2004-2019):** This chapter presents a journal article (reproduced from *Geophysical Journal International*) on the use of 95 earthquakes recorded at 35 strong-motion stations to evaluate the variation in earthquake site response across Anchorage, Alaska, USA. The Generalized Inversion Technique (GIT) is used to calculate the spectral amplifications at each station with respect to a reference station and two contour maps present the variation in spectral amplification across the city at 1Hz and 5Hz.

**Chapter 6 – Nonlinear Site Effects from the 30 November 2018 Anchorage, Alaska, Earthquake:** This chapter presents a journal article (reproduced from the *Bulletin of the Seismological Society of America*) on the nonlinear site response observed at several strong-motion stations in Anchorage.

**Chapter 7 – Evaluation of Horizontal to Vertical Spectral Ratio and Spectral Amplitude Methods for Estimating Shear Wave Velocity in Anchorage, Alaska:** This chapter presents a journal article (reproduced from *Soil Dynamics and Earthquake Engineering*) on the use of the strong-motions recorded at Anchorage stations to calculate the horizontal to vertical spectral ratio (HVSr) and the development of time-averaged shear wave velocity estimates of the upper 30m ( $V_{s30}$ ) from peak HVSr values. Additionally,  $V_{s30}$  estimates are also



developed from the spectral amplifications of the stations. The result is a  $V_{S30}$  contour map of Anchorage that can be used for planning purposes for future developments across the city.

#### **Chapter 8 – Engineering Site Response Analysis of Anchorage, Alaska Using Site**

**Amplifications and Random Vibration Theory:** This chapter presents a journal article (reproduced from *Earthquake Spectra*) developing a method that utilizes random vibration theory and the calculated Fourier spectral amplification results at strong-motion stations to estimate engineering site response spectra. Evaluation of the method using individual earthquakes, a calibrated equivalent linear ground response model, and ground motion models (GMMs) provide support for the method, and potential future applications are presented.

#### **Chapter 9 – Conclusions and Recommendations for Future Research.**

**Appendices:** The information presented in the appendices is subdivided into four parts. Appendix A contains information supporting several chapters described above. This information includes locations of the strong-motion stations and earthquakes used in the study, spectral amplification and HVSR results for the strong-motion stations, and other results from the studies. Appendix B contains a copy of a recent conference paper that presents some analyses related to the DPDA and takes the information presented in Chapter 4 from an equivalent linear site response model to a nonlinear site response model. Appendix C presents the excerpts from a report and abstracts from several journal articles whose contents are relevant to the study presented here although it is not a direct result of the PhD.

## **2.0 A Brief History of Earthquake Recording Stations and Microzonation Studies in Anchorage**

Anchorage's setting, within a natural earthquake laboratory, make is an ideal location for a network of strong-motion stations. The following chapter presents the history of strong-motion stations in Anchorage and previous microzonation studies.

### [2.1 Seismic Monitoring Station History in Anchorage.](#)

At the time of the Great Alaska Earthquake, March 27, 1964, there were only two seismograph stations located within Alaska. These included one station in Sitka and one in Fairbanks (Hansen 1965). The Sitka station was established in 1904 and is identified as the Sitka Observatory. In Fairbanks, the University of Alaska College Observatory was established in 1935. Both stations, at the time were seismograph stations, with Fairbanks being the closer of the two stations to Anchorage at over 400 kilometers to the north. As a result, no local strong-motion records of the Great Alaska Earthquake exist (Hansen 1965). In the years following this monumental earthquake numerous seismograph stations were installed and operated by the U.S. Geological Survey, U.S. Army Corps of Engineers, and others. By 1976 there were at least 45 stations across Alaska, including 5 stations in Anchorage (Porcella 1976 and Rojahn 1974). In 1970, the Seismic Engineering Branch of the U.S. Geological Survey began adding sites and upgrading strong-motion instrumentation from Teledyne AR-240 instruments to newer Kinometrics SMA-1 instruments (Porcella 1976). The historic station locations across Alaska, as of October 1, 1979, are presented in Figure 2.1, as reproduced from Porcella (1979).

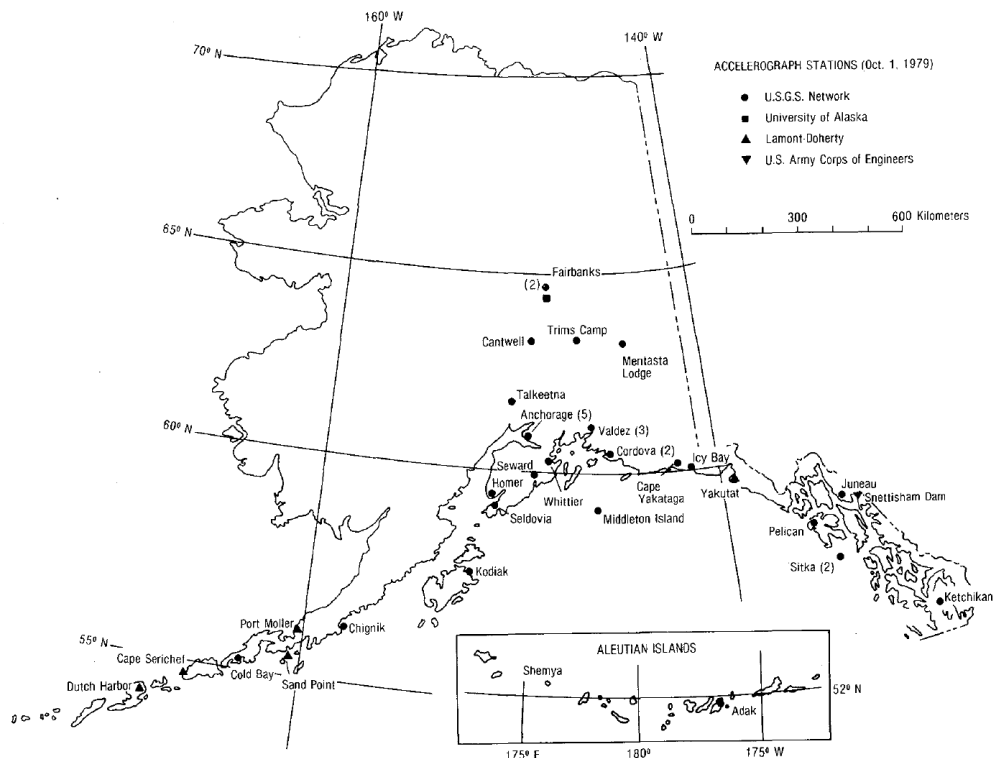


FIGURE 1. - ACCELEROGRAPH STATIONS IN ALASKA, NUMBERS IN PARENTHESIS ARE THE TOTAL ACCELEROGRAPH STATIONS AT THE INDICATED LOCALITY.

Figure 2.4. Alaska Accelerograph Station Locations (reproduced from Porcella 1979)

In the summer of 1972, the Anchorage Westward Hotel (now the Hilton Hotel) completed a new tower, where Kinemetrics SMA-1 instruments were subsequently installed in the basement and on the 20<sup>th</sup> floor (Porcella 1976). The first observations that could be found for the Anchorage Westward Hotel were from a December 29, 1974 earthquake, identified in Table 1 (Seekins et al. 1992). Three days later, on January 1, 1975, an earthquake was recorded at three stations in Anchorage, including the Anchorage Westward Hotel, Alaska Methodist University (now Alaska Pacific University), and the Anchorage Native Medical Center. This event is the first earthquake recorded by the latter two stations (Seekins et al. 1992, Beavan and Jacob 1984, and Silverstein 1986). Over the next several years, five additional earthquakes were recorded at the Anchorage Westward Hotel. In 1981 additional stations were recording earthquake ground motions in Anchorage. Around 1985 several Anchorage fire stations were instrumented, recording events in 1985, 1987, 1988, and 1993.

Through 1993 the Anchorage stations recorded 17 earthquakes within 150 kilometers of Anchorage.

Table 2.1 presents the earthquakes recorded by these stations from 1974 through 1993. The historic station locations for Anchorage are presented in Figure 2.2 and the epicenters of the earthquakes from 1974 through 1993 recorded at these stations are presented in Figure 2.3. It is important to note that the instruments installed at these stations operated in a triggered mode and the instrument sensitivity to earthquake shaking is low when compared to modern digital accelerometers. With these limitations, only larger earthquake events close to Anchorage were recorded and there are far less data available, when compared to the modern network. Some of the events presented in Table 2.1 were digitized by Ronald Porcella (personal communication with Dr. Utpal Dutta) but the time-histories are not readily accessible and only intensity measures such as the PGA are typically available. Due to the lack of availability, these data were not considered further for this study. Future studies may want to consider the digitization of the time-histories to compare to the results presented in this study. Additional detail on possibilities for comparison is provided in Chapter 9.

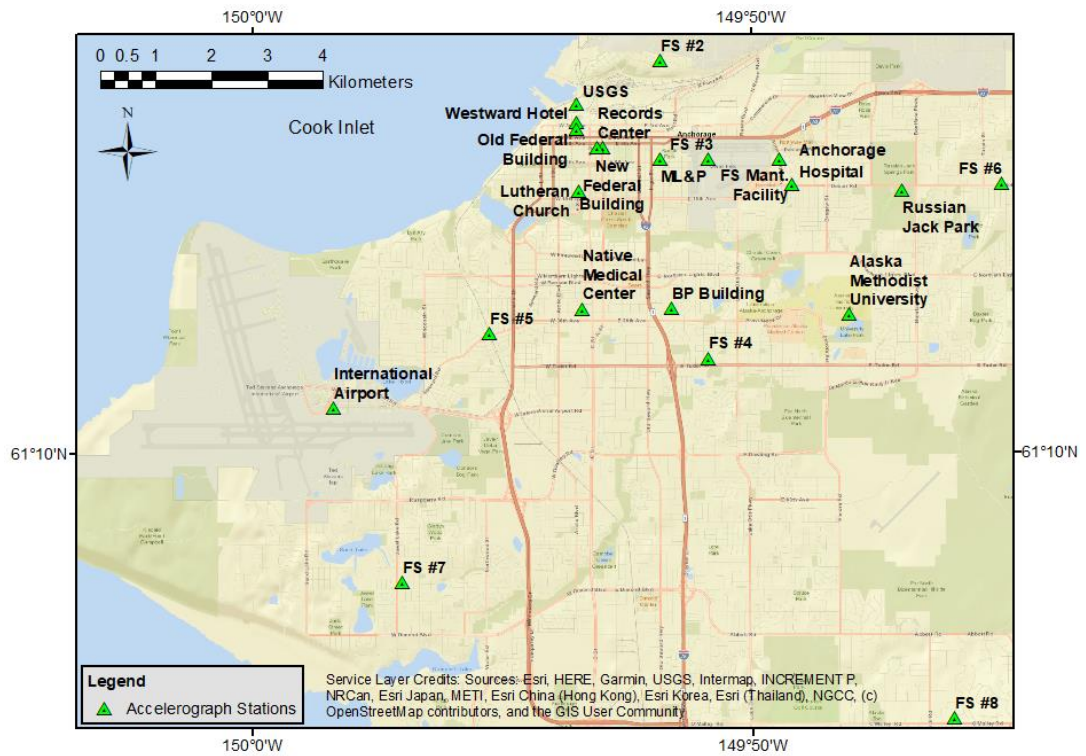


Figure 2.2. Accelerograph Stations in Anchorage from 1974 through 1993. Fire Stations are denoted by FS and by number.

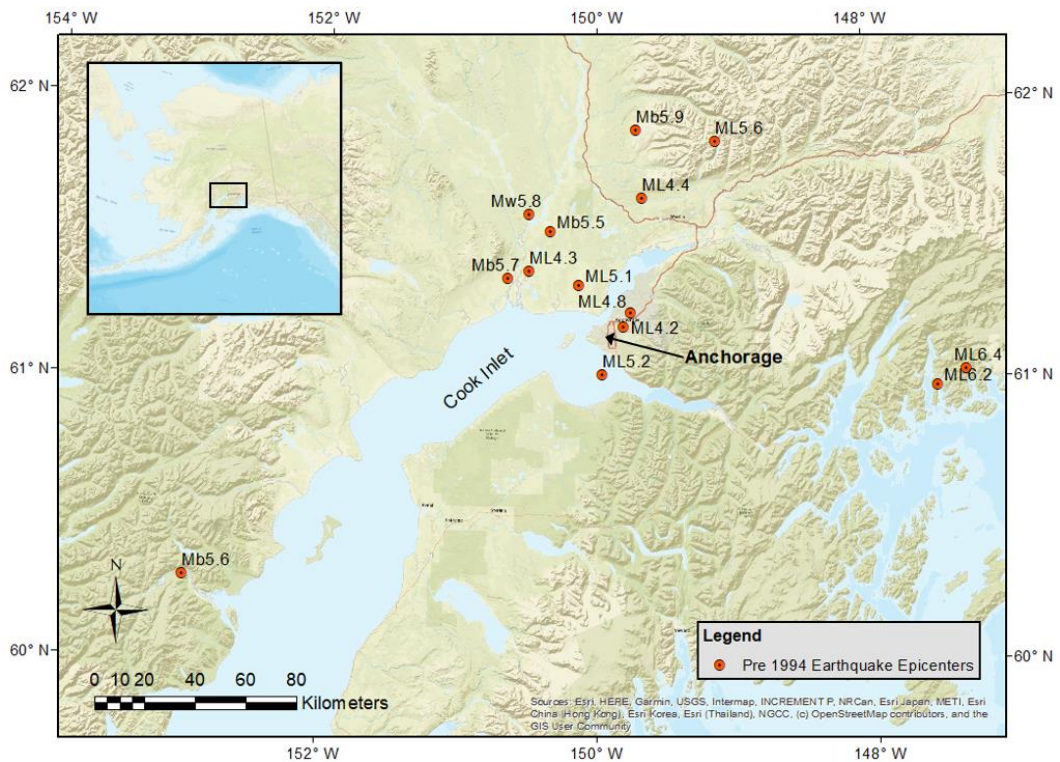


Figure 2.3. Earthquake epicenters recorded in Anchorage between 1974 and 1993. Magnitude scales are indicated, and ML is for local magnitude, Mw is for moment magnitude, and Mb is for body magnitude. Inset figure presents the location of the figure with respect to Alaska and is not to scale.

INSERT TABLE 2.1 HERE

Table 2.1 Continued (for page count)

## 2.2 Growth and Upgrades to the Network

In 1993, an effort to understand Anchorage's seismic hazard better began through a multi-agency seismic microzonation study. Sixteen free-field stations were established across the Anchorage metropolitan area and Kinometrics Altus K2 digital instruments were installed (Biswas et al. 1997). Discussion of some of the early findings is presented in Section 2.3.

The Advanced National Seismic System (ANSS) began cataloging earthquakes in Alaska in 1995. From 1995 through 2018 over 230 earthquakes with magnitudes greater than  $M_L4.5$  occurred within 300 km of Anchorage. To put this in context, over the same period San Francisco and Los Angeles, California recorded 51 earthquakes and 115 earthquakes greater than  $M_L4.5$ , respectively.

In the Anchorage Strong-Motion Network report developed by Dutta and Lemersal (2010) the network at that time was described. The following is a brief summary of the stations installed and active at that time:

- 37 strong-motion surface stations (Kinometrics Altus K2 digital instruments)
- Shallow rock site station (K216 with Kinometrics HypoSensor at 10m depth and Altus K2 at the surface)
- Delaney Park Downhole Array (DPDA) with 7 instruments installed from the surface to 60m depth (Kinometrics HypoSensors below the ground surface and a Kinometrics EpiSensor at the surface) – see Chapter 4 for array instrumentation layout
- 4 structural arrays, including three buildings and one bridge

While some sites have been taken offline in recent years most of these stations are still active and are regularly maintained by the USGS. By 2019, more than 40 sites have installed strong-



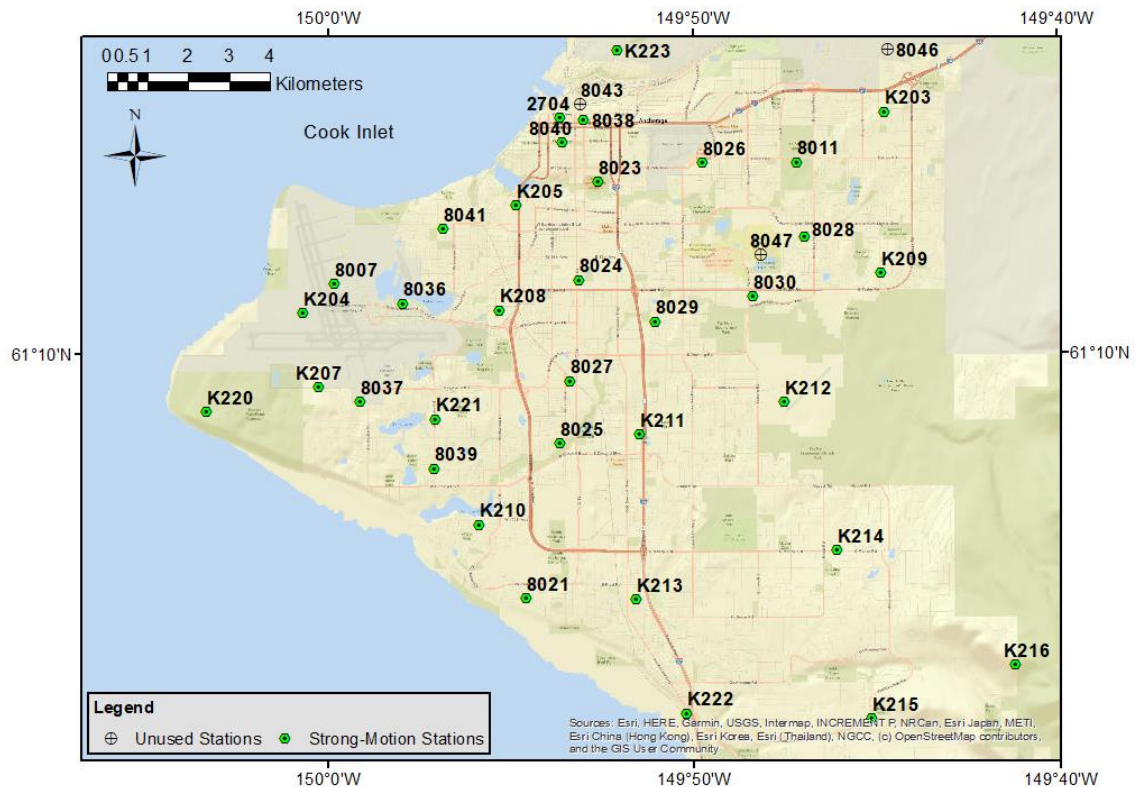
motion instrumentation. These sites include locations with structural arrays and surface stations.

The data available from these strong-motion stations is collected by several groups, including the USGS at their Menlo Park, California office; the Alaska Earthquake Center (AEC) in Fairbanks, Alaska; and University of California Santa Barbara (UCSB). However, the AEC started collecting the data for a majority of the strong-motion surface stations in 2003. Prior to that the USGS collected data and shared it with interested agencies, including the University of Alaska Fairbanks Geophysical Institute and the University of Alaska Anchorage. The USGS still collects the majority of structural array data and UCSB collects and maintains the DPDA.

Starting in 2004 the data network was improved, and the instruments were upgraded from an event- trigger mode to a constant data feed state. The AEC provides direct monitoring of many stations and can regularly perform visual health of the system evaluations. This has allowed for focused and more regular maintenance provided by the USGS, Alaska Volcano Observatory, and AEC.

At the outset of this study, it was decided to develop a database of strong motions recorded at available stations starting in 2004, the year the DPDA was installed. This start date was supported by the upgrades to the network mentioned above. Data was requested from the USGS for strong-motion station data collected at additional surface stations, and some related to existing structural arrays, but the data were regrettably not provided. This means that the density of used stations is slightly less than the density of installed stations. The collection of AEC and UCSB data provided a total of 180 earthquakes greater than M4.5 within 300km of Anchorage at 35 strong-motion stations, recorded between 2004 through January 2019, the end date of the data collection period for this study. Figure 2.4 presents

the names and locations of the strong-motion stations used in in this study. Appendix A-1 presents the strong-motion station locations. The following chapter describes the earthquake record dataset selection and its processing.



### 2.3 Summary of Recent Anchorage Strong-Motion Network Microzonation Studies

While the following summary does not attempt to capture all of the different outcomes resulting from the strong-motion network in Anchorage, it does provide some background to key studies that have been performed by others. In most cases, the data utilized in the following studies was from prior to 2004. The research presented in subsequent chapters utilizes new earthquake recordings from a larger set of strong-motion stations than has been used by others.

The early microzonation studies performed in the 1990s presented in several reports and papers is summarized in the work by Biswas et al. (1997). Sixteen strong-motion stations and recordings from 15 earthquakes with magnitudes ranging from M<sub>L</sub>3.6 to M<sub>L</sub>6.0 were analyzed. Additional studies by Nath et al. (1997), Dutta et al. (2000), and Martirosyan et al. (2002) provide additional improvements on these early microzonation studies. Dutta et al. (2003) utilized 25 stations and 60 earthquakes ranging from M<sub>L</sub>3.0 to M<sub>L</sub>6.3, with epicentral distances of up to 300km to further improve the microzonation of Anchorage. That study utilized the Generalized Inversion Technique (GIT) to calculate the average spectral amplifications measured at each site for the dataset. The GIT methodology is presented in detail in Chapter 4, as it is a key method used throughout the current study.

There have also been several research efforts related to site response and ground motion behavior measured by the Anchorage strong-motion network for individual events of note. Boore (2004) performed an analysis of ground motions measured in Anchorage as a result of the 2002 M<sub>w</sub>7.9 Denali Earthquake. While this earthquake was over 270 km from Anchorage, the results obtained by Boore (2004) agreed with the findings of previous studies. In 2016 the M<sub>w</sub>7.1 Iniskin Earthquake (260km southeast of Anchorage) shook Anchorage and southcentral Alaska at approximately 1:30am local time). The earthquake caused some minor damage throughout the region, mostly nonstructural. Several studies and presentations resulted from this earthquake, including a special session on the event at the 2016 annual meeting of the Seismological Society of America.

The results of earthquakes recorded at the DPDA have been utilized to study the response of soil layers, subjected to strong shaking, and to develop models of the downhole array. Chapter 4 presents the results of modeling of the DPDA with newly acquired shear wave

velocity measurements and Appendix B presents a recent paper describing the development of a nonlinear model used to evaluate ground response due to large earthquakes.

On November 30, 2018, Anchorage and southcentral Alaska was shaken by a  $M_w7.1$  earthquake, located approximately 10km north of Anchorage at a depth of approximately 40km. The damage related to this earthquake included widespread, but localized, ground failure, structural damage, and significant nonstructural damage. Thankfully, no loss of life and few injuries resulted from the earthquake. A general summary of the earthquake is provided by West et al. (2020) and is presented in Appendix C because the author of this thesis contributed to that paper. The depth of the earthquake and the response of the population, especially students in schools, quickly dropping and covering, contributed to the low number of injuries. A summary of the earthquake and observed damages is presented in reports such as the Geotechnical Extreme Events Reconnaissance (GEER) report (Franke et al. 2020) and the Earthquake Engineering Research Institute (EERI) Learning from Earthquakes (LFE) Report (Hassan et al. 2021). Because the author of this thesis was one of the co-authors of the LFE report on the Anchorage Earthquake, the introduction of that report is included in Appendix C-1. Numerous studies have resulted from this event thanks to the high quality and dense strong-motion recordings available. It was observed that findings from additional strong-motion stations would benefit the growing population in southcentral Alaska and additional instrumentation has been installed at new sites, as a result.

### 3.0 Strong-Motion Selection and Time History Processing

The cultivation of a strong-motion dataset is an important initial step. The selection, processing, and initial considerations of the strong-motion data are described in the sections below.

#### 3.1 Ground Motion Selection

The following section presents a discussion regarding the selection of strong motions for this study, starting first with the available records and the selection of magnitude and distance ranges considered for this study. As a starting point, the database with earthquake recordings from the Delany Park Downhole Array (DPDA) were queried to understand the time, magnitude, and distance ranges of the available data. Based on a review of the strong-motion records at the DPDA, compiled by University of California Santa Barbara (UCSB 2021), a total of 6,680 ground motions have been recorded since the start of data collection at DPDA in 2004 (as of 31 January 2019). These ground motions range from magnitude (database typically utilizes Richter Local Magnitude –  $M_L$ ) of  $M_L$  1.0 to a maximum of  $M_L$  7.1. The greatest epicentral distance from the DPDA is 655km, from an  $M_L$  6.2 earthquake on 2 April 2016 (this event's depth of 11.2km results in a nearly equivalent hypocentral distance). Based on the UCSB database the largest event,  $M_L$  7.9, was recorded on 23 January 2018 at an epicentral distance of 577km. The average of the 6,680 events is  $M_L$  1.9 with a mean epicentral distance of 26.0km. The following figures provide additional details regarding the characteristics of the initial dataset collected at the DPDA. Figure 3.1 provides a summary of the epicentral distance versus local magnitude for the entire dataset.

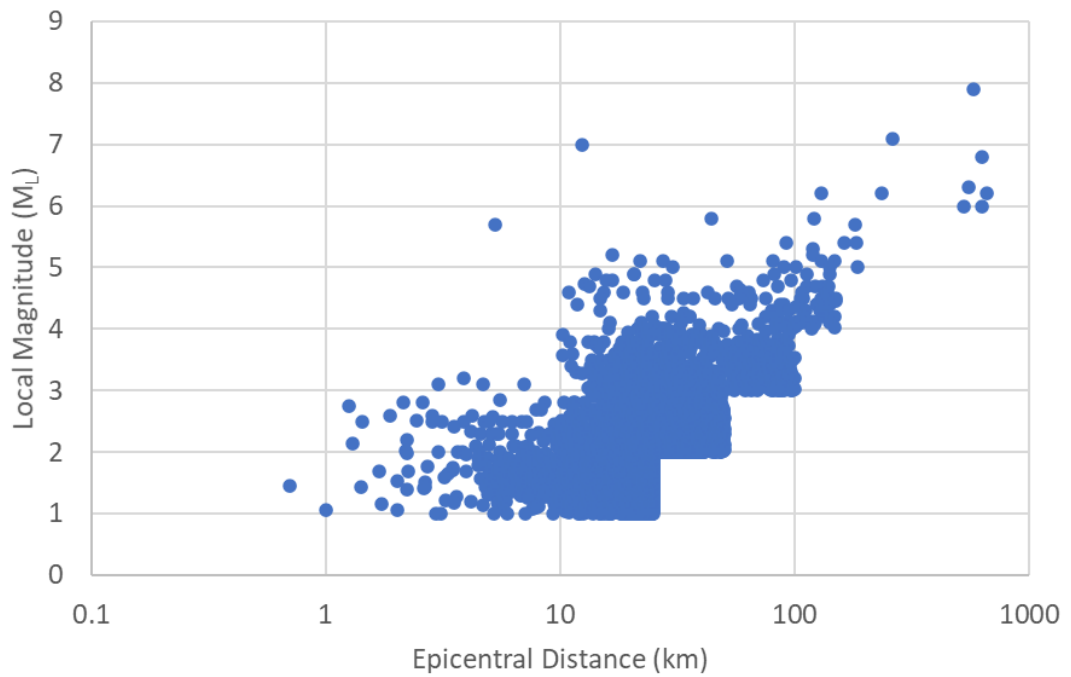


Figure 3.5. Epicentral distance versus local magnitude – Entire DPDA dataset.

One observation from Figure 3.1 is the stair stepping of the data along the right-hand side of the dataset. Based on further evaluation it appears the DPDA dataset has been truncated at a distance of 25km for  $M_L$  1.0 to  $M_L$  2.0, 50km for  $M_L$  2.0 to  $M_L$  3.0, and 100km for  $M_L$  3.0 to  $M_L$  4.0. It also appears that the dataset has been truncated at 150km for  $M_L$  4.0 to  $M_L$  5.0 and 200km for  $M_L$  5.0 to  $M_L$  6.0.

To identify a more manageable and meaningful dataset (from an engineering perspective) a cutoff for the lower magnitudes is considered. With a lower cutoff of  $M_L$  4.0 a total of 148 strong-motion records remain (Figure 3.2).

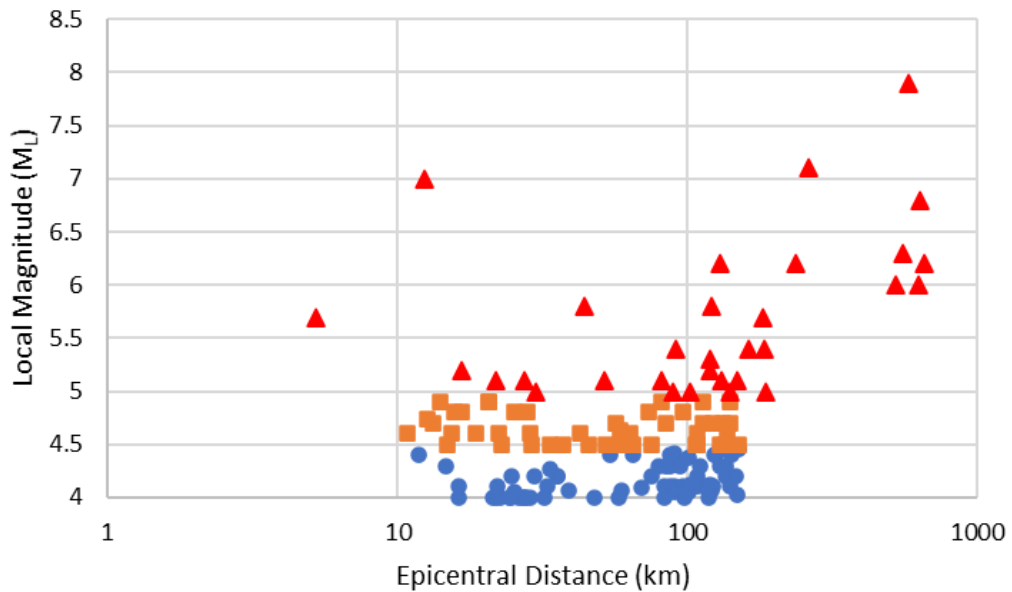


Figure 3.6. Epicentral distance versus local magnitude.

Applying a lower cutoff of  $M_L$  4.5 results in a total of 77 records remaining (Figure 3-2 orange squares and red triangles). With a cutoff of  $M_L$  5.0 there are a total of 31 strong ground motion records (Figure 3.2 red triangles). It should be noted that there were additional earthquakes recorded in Anchorage during this time frame, but there were not recorded at DPDA.

An evaluation of the spatial distribution of epicenters was considered to further evaluate the local magnitude cutoff that should be applied. It was observed that with an  $M_L$  5.0 cutoff there are no epicenters located to the east of the DPDA. When the lower cutoff is reduced to  $M_L$  4.5 several epicenters remain to the east of the DPDA. Including these in the initial evaluation of the data allowed for the consideration of possible directionality in the ground motions without adding a substantial burden on the analysis.

As is shown in Figure 3.2, there are several records with epicentral distances greater than 100km and magnitudes of  $M_L$  4.5 and greater from the DPDA. Typically, short-period ground motions (e.g., peak ground accelerations) attenuate significantly at a distance of 100km and this effect is greater for both crustal and subduction zone earthquakes (Kramer 1996). The

24 January 2016 event, which was an intermediate depth earthquake located within the subducting slab at an epicentral distance of 261km, was felt by many throughout Anchorage and the vicinity. Peak ground accelerations ranged from 0.02g (Station K220 at Kincaid Park) to 0.21g (Station 8039 Downtown Anchorage Fire Station) (CESMD 2021). Therefore, an epicentral distance cutoff of 300km was applied in order to retain this important event. Figure 3.3 presents the dataset of 71 events comprising of cutoff magnitudes and epicentral distances of  $M_L$  4.5 and 300km, respectively. It should be noted that the M7.0 event just over 10km from the DPDA is the M7.1 Anchorage Earthquake that occurred on November 30, 2018. The event shows up as a M7.0 event in the DPDA database because the event was initially characterized as a M7.0 and then was upgraded to a M7.1 event after additional analysis by the USGS and AEC. It should be noted that the AEC catalogue was used for all events used in the study, allowing for a consistent consideration of magnitude, among other data used in the study.

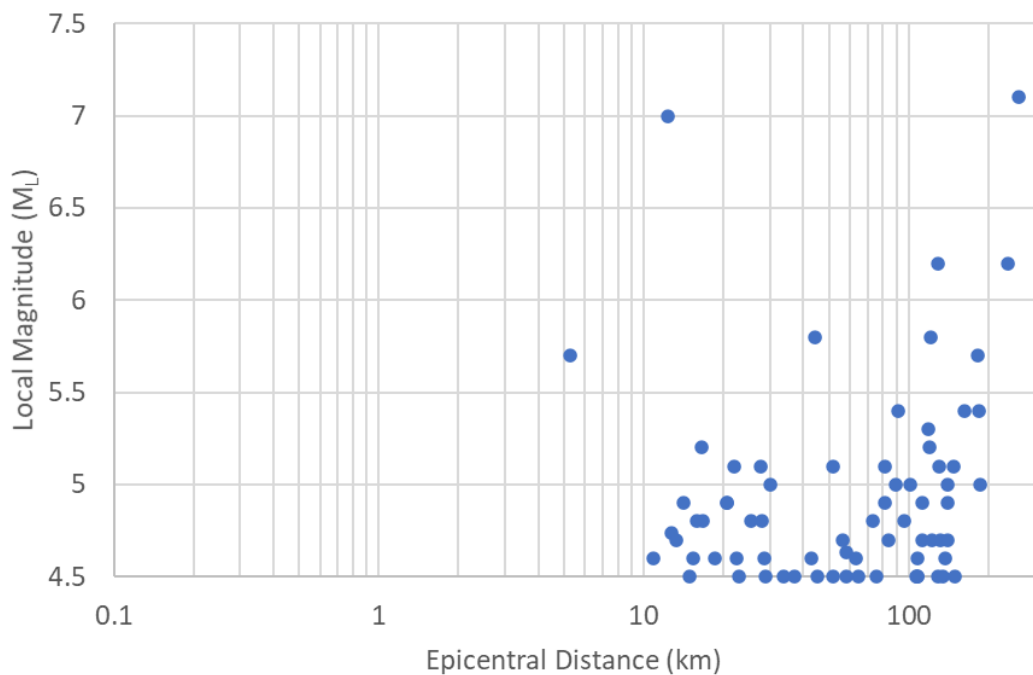


Figure 3.3. Epicentral distance versus local magnitude –  $M_L$ 4.5 with a maximum distance of 300km.



## Database Procurement

With preliminary data selection, based on available data at the DPDA, agencies storing strong-motion data were contacted. The AEC was able to provide strong-motion data from Anchorage stations with a start date of 9 December 2003. The magnitude and epicentral distance constraints described above were provided to AEC and 118 events were found over a range of dates from 9 December 2003 to 23 January 2019. As noted in Chapter 2, there are several agencies responsible for strong-motion stations in Anchorage. Strong-motion data was requested from the USGS, but data were not provided. This resulted in the omittance of several existing strong-motion stations in Anchorage from the study. In all, 2,430 three-component acceleration time histories were collected for 37 strong-motion stations, including two stations not in Anchorage (K217 in Chugiak, Alaska and K218 in Palmer, Alaska). In 2019, several agencies, including AEC and the USGS began more regular sharing of data with the Incorporated Research Institutions for Seismology (IRIS). This allows for more availability in downloading recent earthquake data from the strong-motion stations in Anchorage. The IRIS data portal was used to download the  $M_w7.1$  Anchorage Earthquake from 30 November 2018 because the IRIS dataset consisted of more stations than were originally provided in the data package from AEC for this study. The following sections present the processing of the acceleration time histories. Further details about the final dataset utilized in this study are included in Chapter 5.

### 3.2 Magnitude Conversion

Evaluation of the ground motions measured by the Anchorage strong-motion network is an important part of the process of developing a greater understanding of local site response to regional earthquakes. As part of this effort, several catalogues and data repositories of ground motions have been reviewed. The catalogues included:

- Advanced National Seismic System (ANSS)
- Alaska Earthquake Center (AEC)
- University of California Santa Barbara for the DPDA

As part of the evaluation, it is recognized that these catalogues and data repositories have identified the same earthquake but may have used different characteristics. Of specific focus is the magnitude of the event. For a majority of the earthquake ground motions, an accompanying local magnitude is given, often known as Richter magnitude, and is based on an empirical relationship with respect to the Wood-Anderson seismometer (Kramer 1996). Often, this magnitude scale is denoted by either ML, MI, or ml. Throughout this text  $M_L$  will be used as it is of the opinion of the author that “ $M_L$ ” is more readable.

As part of this engineering study, it is important for consistency to use one type of magnitude for the entire catalogue of earthquake ground motions. The Moment Magnitude ( $M_w$ ) scale has been selected as the magnitude scale of choice, as it provides a common framework for both small and large-scale magnitude events without the potential for saturation (Kanamori 1983). Also, it is most commonly used for earthquake hazard studies in engineering practice. The magnitudes used in this study have been converted to  $M_w$  if they were not already in this magnitude scale. While it is acknowledged that conversions from one magnitude scale to another may result in under or overestimation of the actual magnitude, an attempt was made to reduce the potential of this occurring in this study.

Historically, studies have utilized more generalized methods (e.g., Utsu 2002) for conversion from one magnitude scale to another. Utsu (2002) developed a series of empirical relationships between several magnitude scales. The nonlinear scale developed for the conversion of  $M_L$  to  $M_w$  suggests that at about  $M_w$  6.4 both scales are approximately the

same. At  $M_W$  less than 6.4 the  $M_L$  scale over predicts  $M_W$ , with a difference of up to 0.2. However, at magnitudes greater than  $M_W$  6.4 the  $M_L$  scale under predicts the  $M_W$  values. At magnitudes greater than approximately 6.5,  $M_L$  becomes saturated (Kramer 1996) and  $M_W$  becomes the more preferred magnitude scale because it is directly based on the seismic moment (an estimate of the energy released by an earthquake), rather than empirical relationships between instrument responses and ground motions.

In current practice researchers develop conversions of magnitude scales at a regional level. Bormann et al. (2013) caution against using a magnitude conversion scale developed from one seismotectonic region to another due the significant variability of the slopes and constants used to develop regional relationships. While evaluating methods for converting  $M_L$  to  $M_W$  the author discussed the issue with the State of Alaska Seismologist, Dr. Michael West (personal communication) and Dr. Chris Stephens, manager at the USGS National Strong Motion Project Data Center (personal communication) and found that, besides the local relationship developed by Dutta et al. (2003) and the regional relationship presented by Rupert and Hansen (2010), no other regionally-specific relationships have been developed specifically for southcentral Alaska. From a broader regional perspective, there is also a magnitude scaling relationship for western Canada that was developed by Ristau et al. (2005). The following is a summary of each of the relationships followed by a comparison of the results.

#### Dutta et al. (2003)

Part of the information presented in Dutta et al. (2003) is a magnitude scaling conversion between  $M_W$  and  $M_L$ . The relationship developed is based on nine events recorded over the time period of interest and comparisons between two catalogues for magnitudes between

$M_w$ 4.8 and  $M_w$ 6.2. The following magnitude scaling relationship shows that  $M_w$  is lower than  $M_L$  over the magnitude range considered for this database:

- $M_w = (0.855 \pm 0.04)M_L + (0.58 \pm 0.17)$

As an example, a  $M_L$ 4.5 earthquake becomes a  $M_w$ 4.4 event and a  $M_L$ 6.0 event becomes a  $M_w$ 5.7 event, using average values within the range of uncertainty.

#### Rupert and Hansen (2010)

A regional magnitude scaling conversion relationship was developed by Rupert and Hansen (2010) from Alaska earthquake data from 1970 to 2008. The conversion formulas were divided into three time periods 1977 to 1989, 1990 to 30 June 1999, and 1 July 1999 to 2008. The time periods relate to the changes in methods used to process strong motions. Because the data utilized in this study are newer than 1 July 1999, the scaling conversions for 1 July 1999 to 2008 have been considered. Rupert and Hansen found that:

- Earthquakes with depth < 40km:  $M_w = M_L$
- Earthquakes with depth  $\geq$  40km:  $M_w = M_L + 0.003$

This suggests that no real modification needs to be applied to the  $M_L$  values in the current database to convert to  $M_w$  because the magnitudes of earthquakes in the study are only evaluated to one decimal place.

#### Ristau et al. (2005)

The findings presented by Ristau et al. (2005) were developed utilizing earthquake data from several events in western Canada, an active tectonic region adjacent to Alaska. The study found that there is a notable difference in the relationship between the two magnitude scales when comparing subduction slab events and crustal events. The study suggests that the

reason for this is likely related to a complex source-to-receiver travel paths, having a significant effect on the  $M_L$  value. The two models derived from the study, with the uncertainties in parentheses, are as follows:

- Crustal Events:  $M_W = M_L - 0.06 (\pm 0.18)$  for  $M_L \geq 3.6$  and greater
- Slab Events:  $M_W = M_L + 0.58 (\pm 0.33)$  for  $M_L \geq 3.6$  and greater

It should be noted that the largest events used in the crustal and the subduction slab databases of Ristau et al. (2005) were  $M_W 5.1$  and  $M_W 6.8$  respectively. The largest earthquake in the current project database is  $M_L 5.3$  for crustal events and  $M_W 7.1$  for subduction slab events. The magnitudes of the two  $M_W 7.1$  events were determined by the USGS and others in the moment magnitude scale and hence no conversion is required for these events. The use of the crustal model from Ristau et al. (2005) will not require extrapolation for most of the current data set.

#### Effects on the Database

Of the 51 events evaluated in the 2004 through 2016 portion of the project dataset, there are 44 subduction in- or near-slab events and seven crustal events. The events were divided into these two categories based on the depth of the event and the estimated depth to the slab surface. The USGS has developed a three-dimensional model of several subduction zones around the world (Hayes et al. 2018). The model was imported into GoogleEarth™ and each of the events in the data set was evaluated with regards to the estimated depth of the event and depth of the slab. It was observed that a majority of the motions were within a few kilometers of the contours of the subduction slab, as developed by Hayes et al. (2018). Of the seven crustal events, two were at a depth of approximately 30km, about 10km above the subduction slab contours. Four of the remaining five crustal events have depths of less

than 20km. The remaining event is at a depth of 30km, but in an area where the subducting slab is approximately 50km deep.

The Dutta et al. (2003) magnitude conversion relationship was selected for the current analysis when only  $M_L$  values were reported. It was selected to utilize a regional model to estimate the magnitude of the events. The second preferred option would have been the Rupert and Hansen (2010) relationship. Because the number of events considered by those authors was more than 200, this model was considered to be a viable option as well. However, the choice of either method for converting magnitude scales is considered to have little impact on the dataset and its use for this study (generally differences of less than 0.2 magnitude units).

### 3.3 Time History Processing

Once the ranges of magnitudes and distances of interest were selected for this study ( $>M4.5$  within 300km of DPDA) data requests were sent to the data managers at the US Geological Survey (USGS) in Menlo Park, California, USA. Ultimately, in November 2017 recorded earthquake data were provided by the Alaska Earthquake Center (AEC). Through the assistance of Dr. Natalia Rupert and Mitch Robinson, with the support of Dr. Mike West (Alaska State Seismologist), over 1,300 three-component records were provided from 39 stations for 79 events. The data were provided in a SEED file format in counts and very little information was included in the headers of each acceleration time history. Each record was approximately 200 seconds long with pre-event noise ranging from 20 to 80 seconds.

To utilize the data for this study all records provided from AEC required updates to the header information and conversion from count data to acceleration units for each of the three components. The Seismic Analysis Code (SAC) computer program was selected for initial processing of the acceleration time history data. SAC Version 101.6a, downloaded from

IRIS.edu was utilized for the data processing. The general processing included updating header information, applying multipliers to count data to convert to acceleration data, compression (P) and shear (S) wave arrival picking, and filtering. Each of these processing steps are described in the following sections.

### Header Data

Scripts were developed to better automate the writing of header data to the header file of each time history. In all, more than 4,000 acceleration time history records recorded in Anchorage from 2004 to 2019 were updated with the related data. The data included the following:

- Station Information
  - Station Latitude
  - Station Longitude
  - Station Elevation
  
- Event Location Information
  - Event Latitude
  - Event Longitude
  - Event Depth

The station and event location data were provided by several different agencies. These included the report on the Anchorage Strong Motion Network (Dutta and Lemersal 2010) and the Center for Engineering Strong Motion Data (CESMD – [strongmotioncenter.org](http://strongmotioncenter.org)). A summary of the station locations is provided in Appendix A-1 and a summary of event locations is provided in Appendix A-2.

## Multipliers

The AEC data needed to be converted from count data to acceleration data. The multipliers applied for instruments tended to change over time because of equipment upgrades and modifications. Typically, the National Strong Motion Program (NSMP) stations had more multiplier changes over time. The multipliers for each instrument were carefully evaluated and several conversations with NSMP and AEC staff helped capture the correct multipliers to apply to each record. The multiplier operation was performed within the same script that was utilized for the Header Data update.

## Compression and Shear Wave Arrival Picking

An attempt was made to pick the first arrival time of P and S waves in the same script that was used to update the header information and the application of multipliers to the acceleration time histories. The use of the three-component stacking methodology in SAC was used to pick arrival times. For more than 80% of the event records the compression and shear wave arrival times were picked by visual methods prior to filtering.

Approximately 18% of the 1,400 three-component records were too noisy prior to filtering to pick reliable P and S wave arrivals. In many cases, applying a fourth-order Butterworth bandpass filter allowed picking to be completed. However, as noted in the following sections the records remained generally too noisy to utilize in the study.

## Time History Filtering

As noted in the previous section, more than 80% of the acceleration records were able to have headers updated, multipliers applied, and wave arrival times selected without further processing. Using the events that made it through this process, filtering evaluations were then performed. The objectives of the filtering effort were two-fold. The first objective was



to identify high and low-frequency filters that were effective for select ranges of magnitudes. The second was to apply the filters to the noisy records to retain as many records as possible. In all cases the acceleration data was processed by removing the mean and the trend using a least-squares fit. SAC also has a function that removes glitches or irregularities in the records caused during data acquisition. A fourth-order Butterworth bandpass filter was applied to the acceleration time histories and numerous high and low-frequency limits were evaluated. Methods presented by Akkar and Bommer (2006) were utilized to verify the low-frequency (long-period) filter cut-off selection. Considerations for high-frequency (short-period) cutoff filters utilized methods described by Douglas and Boore (2011).

#### Processing Summary

One consideration for this study was the effect of cutoff frequency selection at different magnitudes. To process the records efficiently several bins of magnitudes were created, and several events were selected within those bins. Ranges of cutoff frequencies were applied to evaluate their effects on the Fourier Amplitude Spectrum (FAS). In general, most records had signal to noise ratios (SNR) greater than 3 from 0.1 Hz to approximately 25 Hz, regardless of magnitude (Figure 3.4). For this study, a high-frequency cutoff of 30 Hz was selected as it is reasonable for most engineering studies.

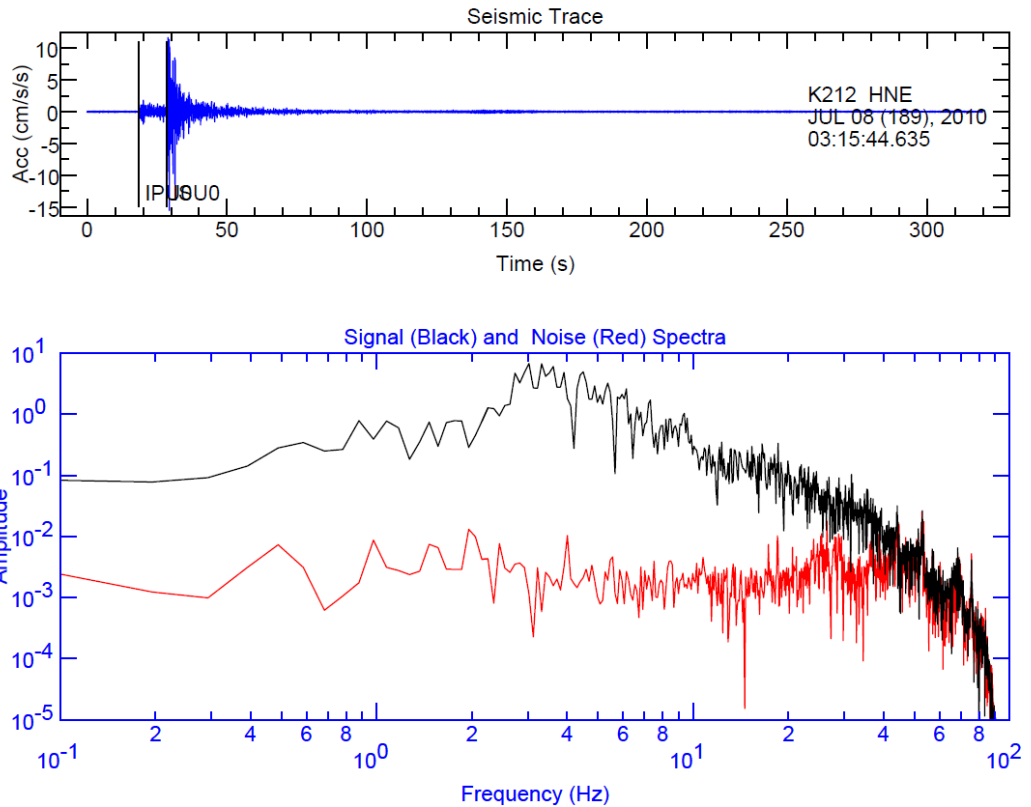


Figure 3.4. Instrument K212 HNE Record for the July 8, 2010  $M_w$ 4.8 Event. The unfiltered acceleration time history is in the upper frame and the signal and noise spectra are plotted in the lower frame for the unfiltered time history.

Single and double integration was performed to evaluate the effects of the cutoff filters on velocity and displacement time histories. This was completed in a process like that described by Massa et al. (2010). A low-frequency cutoff of 0.1 Hz was selected because displacement time histories for a variety of magnitudes appeared to trend to zero displacement (see Figure 3.5). For most of the records an automated filtering process was applied using the Butterworth bandpass filter with 0.1 and 30 Hz cutoff frequencies. The SNR was then evaluated again to observe the effects of the filtering (see Figure 3.6).

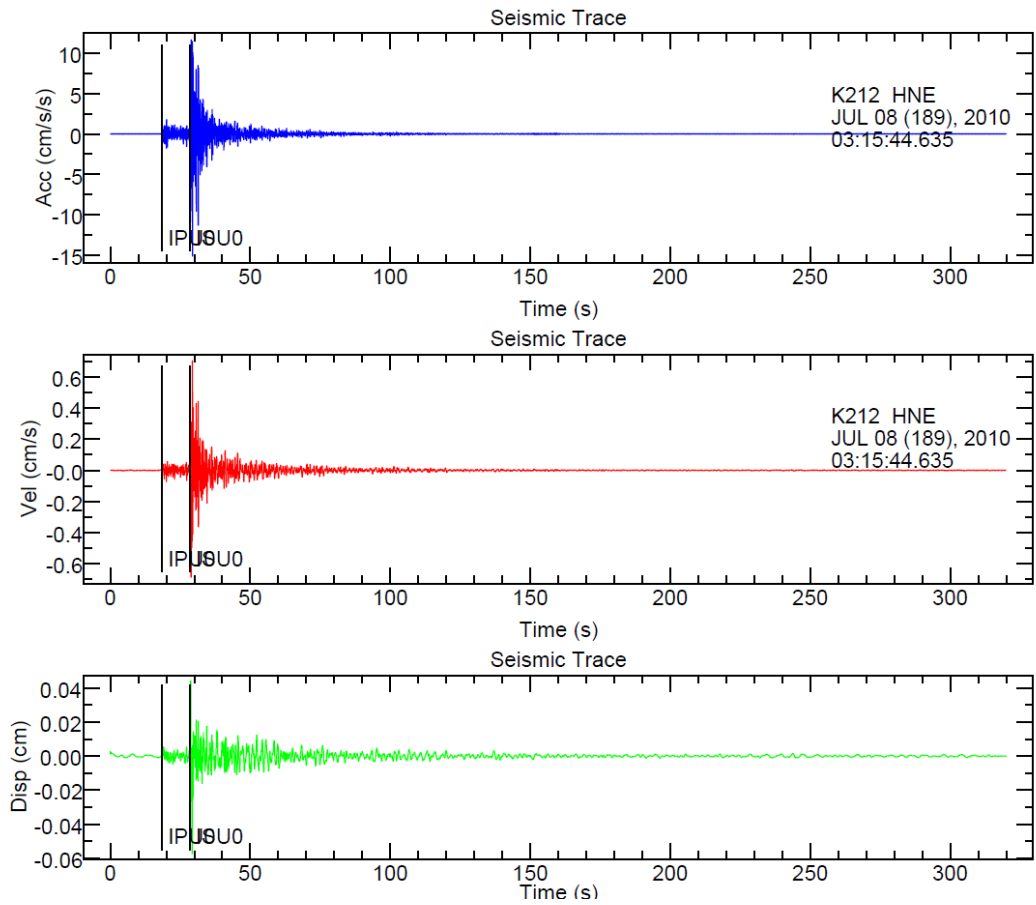


Figure 3.5. Instrument K212 HNE Record for the July 8, 2010  $M_w$ 4.8 Event. Acceleration, Velocity, and Displacement Time Histories for a Butterworth Bandpass Filter with Cutoff Frequencies of 0.1 and 30 Hz.

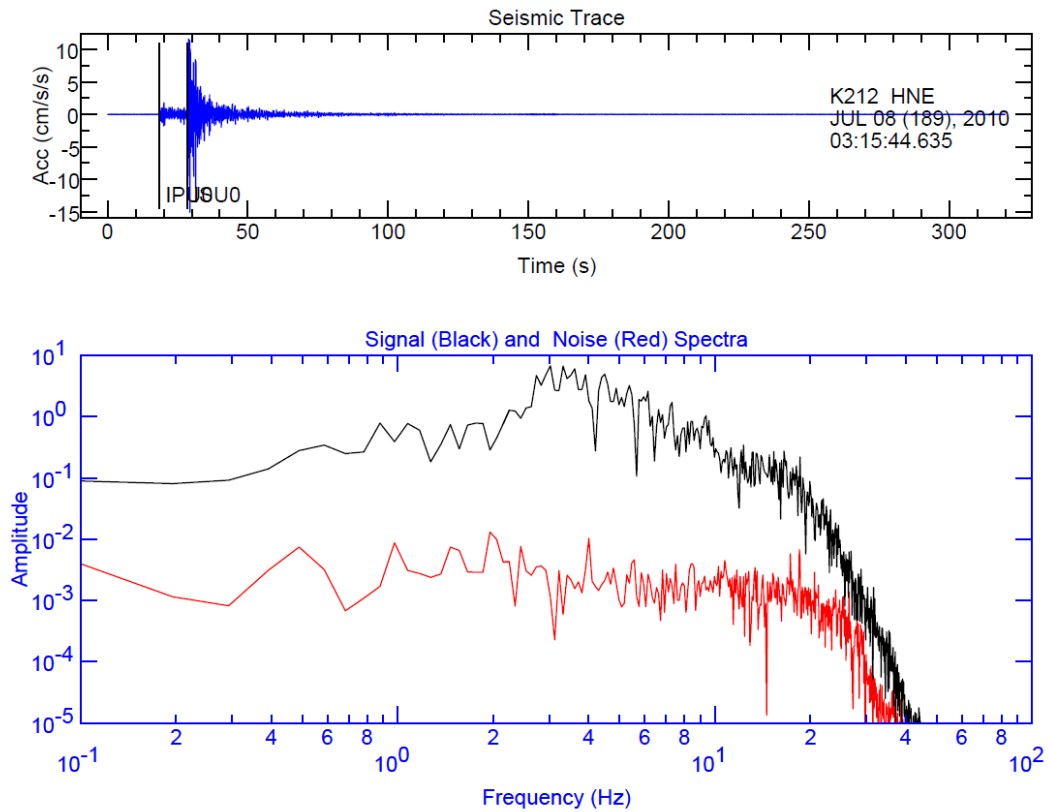


Figure 3.6. Instrument K212 HNE Record for the July 8, 2010  $M_w$ 4.8 Event. Signal to Noise Ratio of the time history with a Butterworth Bandpass Filter with Cutoff Frequencies of 0.1 and 30 Hz. (Compare to Figure 3.4)

An example of the pre and post processing results of a noisier record is presented in Figures 3.7 through 3.9. The analyses presented in subsequent chapters utilize the spectra between 0.25 and 10 Hz. This range of frequencies is well-within the passband of the selected filters, so cutoff selection has little effect on the current analyses. However, the cutoff frequencies were extended so that the ground motions of this database could be used for further analysis beyond this current research.

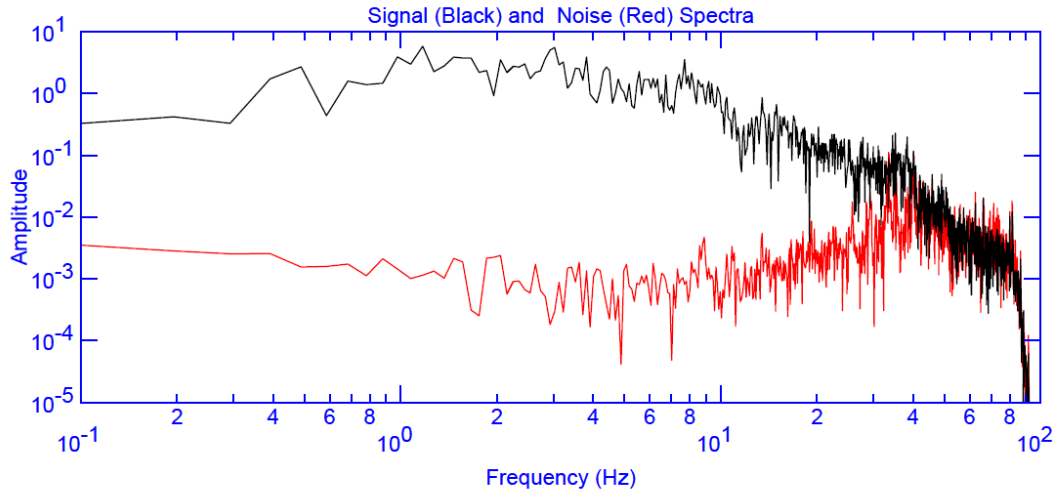
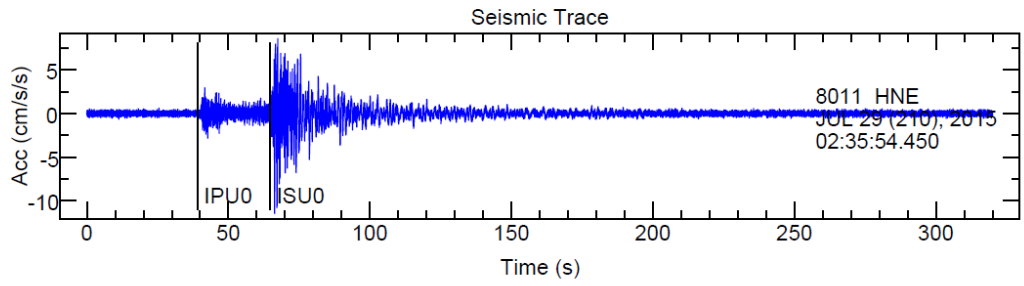


Figure 3.7. Instrument 8011 HNE Record for the July 29, 2015  $M_w$ 6.3 Event. The acceleration time history and the signal and noise spectra of the unfiltered event are shown in the top and bottom frames, respectively.

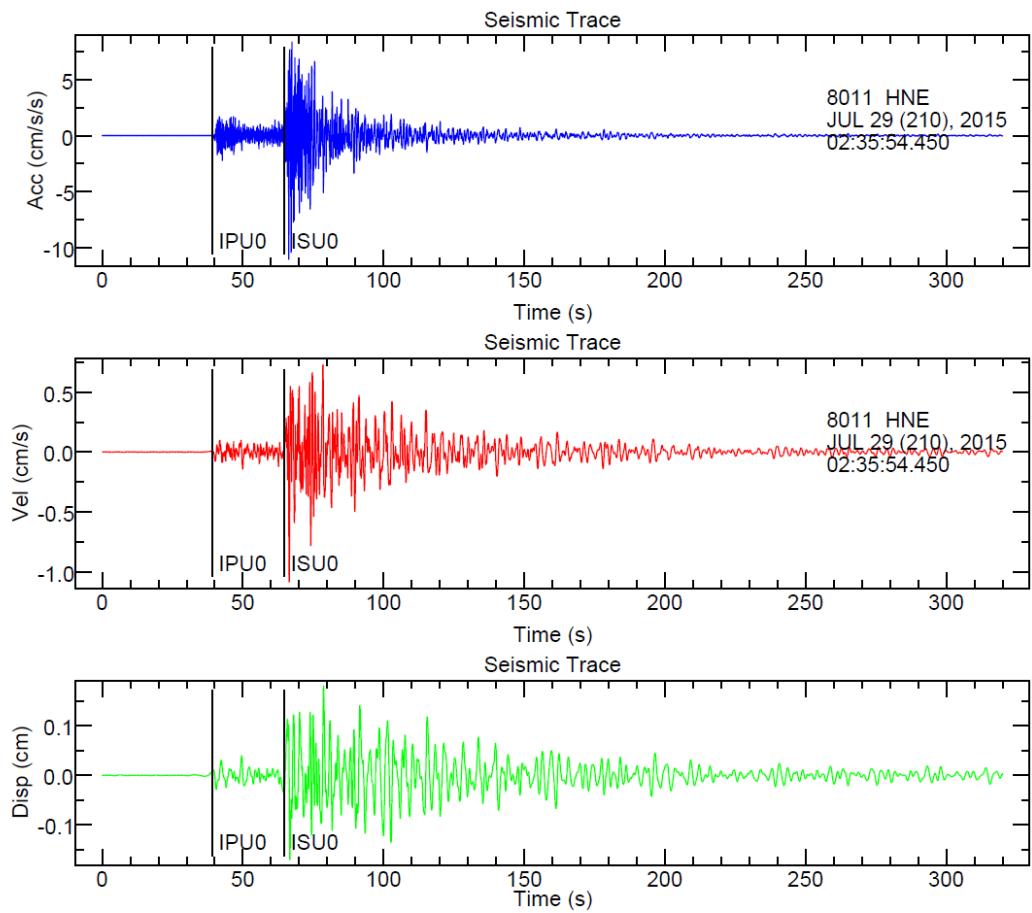


Figure 3.8. Instrument 8011 HNE Record for the July 29, 2015  $M_w$ 6.3 Event. Acceleration, Velocity, and Displacement Time Histories for a Butterworth Bandpass Filter with Cutoff Frequencies of 0.1 and 30 Hz.

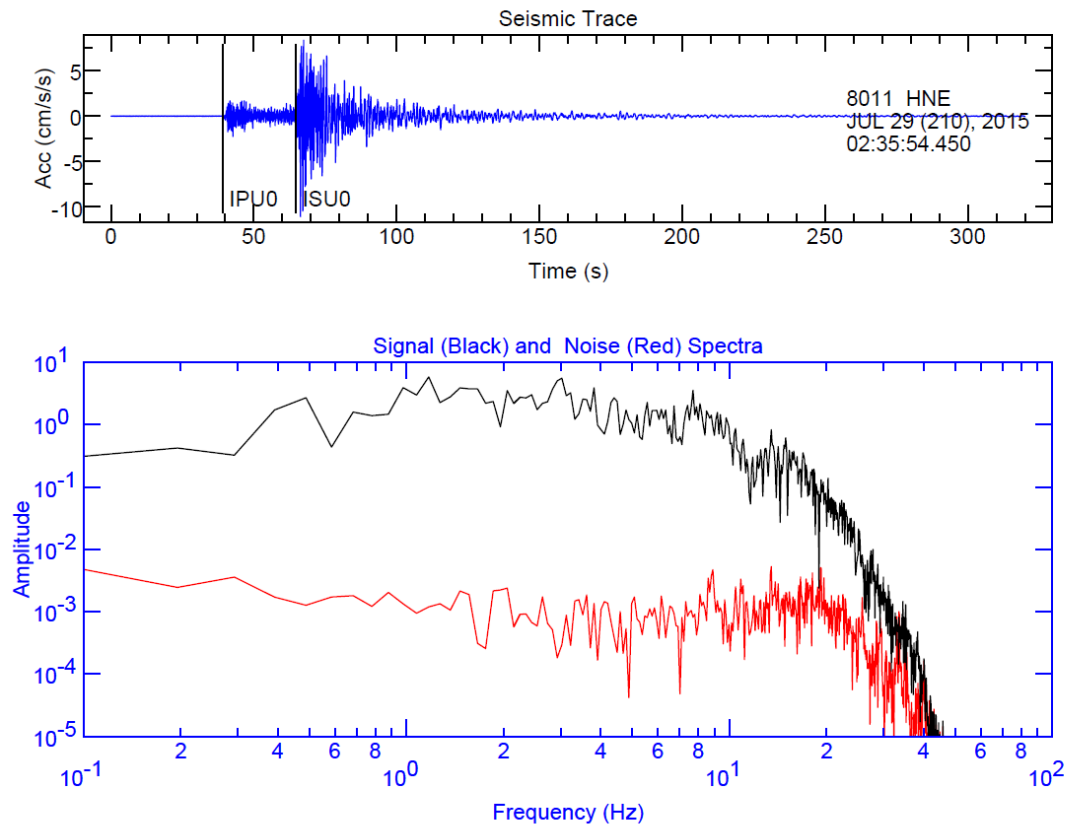
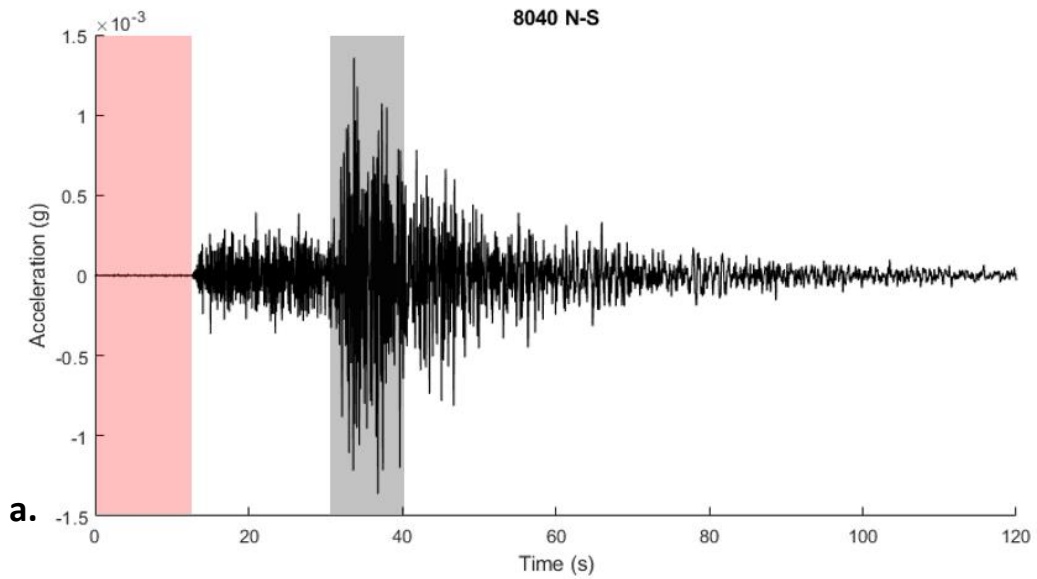


Figure 3.9. Instrument 8011 HNE Record for the July 29, 2015  $M_w$ 6.3 Event. The signal and noise spectra of the time history with a Butterworth Bandpass Filter with Cutoff Frequencies of 0.1 and 30 Hz. (Compare to Figure 3.7)

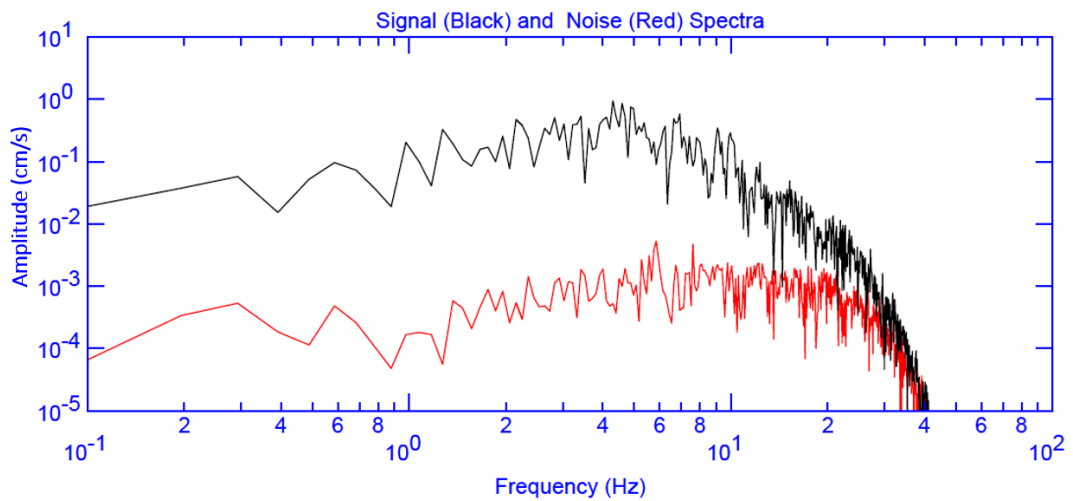
In all cases, the acceleration data was processed by removing the mean and trend using a least-squares fit (Goldstein and Snoke 2005). SAC also has a function that removes glitches or irregularities in the records caused during data acquisition, where glitches refer to artificial spikes caused by samples that are orders of magnitude higher than the surrounding data (Goldstein et al. 2003 and Helffrich et al. 2013). A fourth-order Butterworth bandpass filter was applied to the acceleration time histories, and various high and low-frequency limits were evaluated. Methods presented by Akkar and Bommer (2006) were utilized to verify the low-frequency (long-period) filter cut-off selection. Considerations for high-frequency (short-period) cutoff filters used the methods described by Douglas and Boore (2011).

The frequency range of interest for this engineering study is between 0.25 to 10 Hz, which matches the range of fundamental frequencies of structures within the city. Visual screening of records was performed to evaluate a reasonable bandwidth filter that could be applied to most records and maintain the frequency range of interest for this study. The quality of the recordings was evaluated using the signal-to-noise ratio (SNR), where the Fourier amplitude spectrum of the recorded signal and the pre-event noise were calculated. An example time history and its signal and noise Fourier amplitude spectra are shown in Figure 3.10. Records with a SNR of less than 3 after filtering between 0.1 to 30 Hz were excluded from this study. This practice reduced the number of available three-component records to 1,727 from 95 events, which is 70% of the original dataset. The records that were not used generally were from small deep (>40km) subduction earthquakes and were typically more than 100 km from Anchorage, which resulted in a SNR less than 3 within the frequency range of interest.





**a.**



**b.**

Figure 3.10. Example time history plot (a.) where the pre-event noise window is indicated in red and the S-wave window is in grey and (b.) the Fourier amplitude spectrum of the filtered signal (in black) and the noise (in red).

Surface waves can impact the results of site amplification studies like this one (Bonilla et al. 1997, Oth et al. 2009). To reduce the impact of surface waves on the results, a window of 10 seconds was used starting at the S-wave arrival. The 10-second S-wave window was selected based on a visual evaluation of the records to capture the high-amplitude portion of the records. With the selection of a general window, there is a possibility of including some of the surface waves of some records, especially for distant lower magnitude events. Varying

the window length between 5 and 15 seconds did not, however, have an observable effect on site amplification when only the lower magnitude events were included. The noise window was selected as the portion of the record before the P-wave arrival and was generally longer than 10 seconds, depending on the record. The P- and S-wave arrival times were chosen by visual inspection of the three-component records used during the time-history processing. An example of a horizontal acceleration time history with noise and S-wave windows is presented in Figure 3.10.

### 3.4 Generalized Inversion Technique

Once the database was developed and the time histories had been processed, the analysis of records could commence. Several methods of analysis were considered. The Generalized Inversion Technique (GIT) was developed by Andrews (1986) and has been subsequently used in a variety of microzonation studies worldwide to evaluate variation of local site amplification. GIT utilizes a system of equations to determine the source, path, and site terms for the analysis of earthquake ground motions. Further, and more in-depth description of GIT is provided in the following chapter, including a presentation of the system of equations, descriptions of the source, path, and site terms, as well as the parameters utilized in this study. The MATLAB software package, GITANES, developed by Dr. Peter Klin (2019), was used for this study.

A reference station is selected as a neutral location when using GIT to establish a baseline which allows the remaining site to be compared. The reference station is often selected as a rock site where amplifications due to soil behavior are minimized, allowing for a comparison among other sites where site amplification can be observed (Steidl et al. 1996). In this study, the strong-motion station K216 is utilized as the reference station. This selection is consistent with previous studies such as Dutta et al. (2003).

An evaluation of the horizontal to vertical spectral ratio (HVSr) was performed to verify the selection of the K216 strong-motion station as a reference station for this study. The HVSr results are presented in Figure 3.11. Lower horizontal site amplifications are observed at a site when HVSr is near unity. The K216 station provides generally the lowest bound HVSr ratio among the stations (black line in Figure 3.11). As an example, the blue line in Figure 3.10 presents the HVSr ratio for Station 8040. There are significant horizontal amplifications at this site, showing why it would not be an effective reference station. This study noticed, as did others (Martirosyan 2002), that at frequencies above 7Hz, station K216 appears to have significant site amplification, especially when compared to other stations used in this study. Lower frequencies, especially around 1 and 5Hz are more important for the built environment in Anchorage and hence this high-frequency response is not particularly important for this study. While it may be possible to establish a different reference site in the future, the K216 strong-motion station provides the most consistent HVSr ratio, especially below about 5.5Hz.

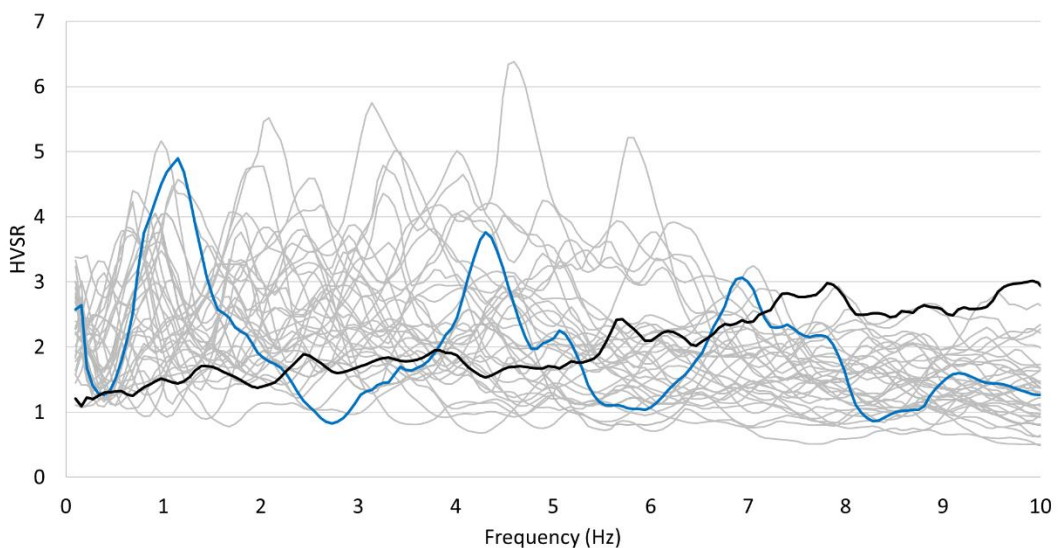


Figure 3.11. HVSr of the strong-motion stations used in this study. K216, the selected reference station, is the black line and 8040 is the blue line.

The following chapters present additional characteristics about the strong-motion database used in this study, greater detail on the methods of analysis, and the results which can be utilized to develop a greater understanding of the microzonation of Anchorage.

## **4.0 In-Situ Shear Wave Velocity Measurements at the Delaney Park Downhole Array, Anchorage, Alaska**

Authors: John Thornley, Utpal Dutta, Peter Fahringer, and Zhaohui (Joey) Yang

*Seismological Research Letters, Volume 90, Number 1, January/February 2019 (p 395-400)*

The following article presents the results of shear-wave velocity measurements recorded at the DPDA to a depth of 60m. The shear-wave velocity measurements were then used to help calibrate a one-dimensional equivalent linear model of the DPDA and several earthquake records were used to validate the calibration. I organized and led the field work, developed and calibrated the model, and wrote the article. My coauthors Utpal Dutta and Joey Yang provided support during the field work and edited the manuscript. Peter Fahringer processed the field data to calculate the shear-wave velocity profile and reviewed the manuscript.

### [4.1 Abstract](#)

Many studies are ongoing within Alaska's most populous city to understand better its unique seismogenic setting as well as its seismic hazard and risk. With its relative proximity to the Aleutian Megathrust subduction zone and other earthquake sources, Anchorage has been subjected to regular earthquakes, including the 1964 Great Alaska Earthquake. In 2004 a downhole array was installed near downtown Anchorage within the Bootlegger Cove Formation, which was responsible for much of the ground failure during the 1964 earthquake. This study provides new information regarding the downhole array and the dynamic soil properties found at the array site. Shear and compression wave velocities were measured at the site. Evaluation of the transfer function of the new velocity model is compared with the measured response at the site. In addition, several comparisons are

performed utilizing nearby historic cone penetration test (CPT) and standard penetration test (SPT) data measured during installation of the deepest accelerometer at the site. A significant improvement in the theoretical modeling of the site is achieved utilizing the new shear wave velocity profile.

## 4.2 Introduction

Anchorage, home to approximately half of Alaska's population, is located within a highly seismogenic zone. This zone is comprised of the Pacific plate underthrusting the North American plate at a rate of greater than 50 mm per year. Anchorage is situated in a region of complex geology that consists of a sedimentary basin abutting metamorphic bedrock exposed in the Chugach Mountains, located on the eastern side of the city. One of the most important features affecting the ground response in Anchorage is the Bootlegger Cove Formation, consisting of glacial and glaciofluvial deposits of interbedded clay, silt, and sand (Schmoll and Debrovlny 1972). Significant ground loss and slope failures within this formation resulted in the northern portion of the city during the 1964 Great Alaska Earthquake (MW 9.2). Significant effort by seismologists and engineers has been placed in understanding the anticipated ground response resulting from the next major earthquake because of the population density and unique seismic setting of the Anchorage area.

## 4.3 Background

A downhole array, with three component accelerometers placed at seven depths from the surface to 61 meters below ground (Figure 4.1) is located in Delaney Park, part of downtown Anchorage, Alaska, and has been recording strong ground motions since 2004 (Figure 4.2 and inset figure top left). The site is located on level ground approximately 800 meters south and 800 meters east of the 1964 Great Alaska Earthquake 4<sup>th</sup> Avenue and K Street ground failures, respectively. Recorded ground motions at the borehole array have been analyzed as part of

a systematic approach to develop a ground-motion model and to measure the impedance characteristics of the soil column located at the borehole array. The soil column at the array site is similar to the soils encountered north of the array, where significant damage resulted from the 1964 Great Alaska Earthquake. The general subsurface conditions consist of alluvium over glacial outwash and the Bootlegger Cove Formation (a stratified sequence of clastic sediments). Very dense glacial till lies below the Bootlegger Cove Formation and, because of its high shear (S) wave velocity ( $V_s > 760\text{m/sec}$ ), acts as a Seismic Site Class B/C boundary (Dutta et al. 2009).

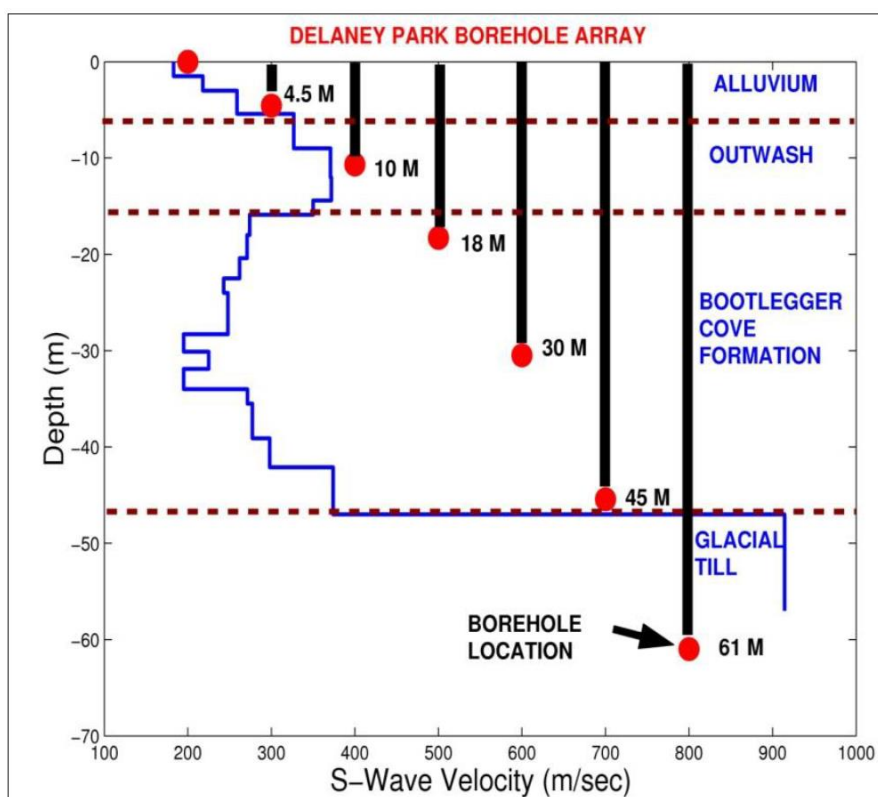


Figure 4.1. Delaney Park Borehole Array sensor layout and generalized geology with the previously assumed shear wave velocity profile.



Figure 4.2. Location of the Delaney Park Downhole Array. Inset Figure (Upper Left) shows the location of the array site adjacent to Delaney Park in downtown Anchorage. Inset Figure (Lower Right) shows the relative locations of the two earthquake events used in this study.

During the installation of the downhole array 7.5-cm casing was installed into boreholes, but very little is published about the exact makeup and engineering properties of the soils at the site. Several efforts have been made to characterize the thicknesses of the soil layers and their key engineering properties, such as shear wave velocity, shear modulus and damping, and unit weight (Thornley et al. 2014a, Thornley et al. 2014b, Thornley et al. 2013). As shown in Figure 4.1, an assumed shear wave velocity profile, measured for a geotechnical study at a building approximately 250 meters northwest, was suggested for the site prior to this study, as there was no shear wave velocity data collected at the downhole array. Comparisons between the instrument recordings and modeled ground motions did not show a good fit when evaluating the transfer functions of modeled earthquake ground motions between instruments, when compared to the suggested profile. Several models were developed and



refined to modify the estimated shear wave velocity profile to better model measured ground motions between instruments at the array site. However, the results of the models suggested that collecting in-situ measurements at the downhole array site would be necessary to gain additional improvements.

#### 4.4 Field Study

To capture in-situ measurements at the downhole array site, the deepest accelerometer (61 meters below ground surface) was removed from the casing and shear wave velocity profiling was performed. Upon removal of the accelerometer the groundwater level was measured within the casing. Its depth is estimated to be approximately 21 meters below ground surface.

#### 4.5 Vertical Seismic Profiling of the Casing

Vertical seismic profiling is a single borehole geophysical method. Seismic energy is generated at the ground surface by an active seismic source and recorded by a geophone located a known depth below ground surface. The time required for energy to reach the geophone along a path of known distance, between the source and receiver, provides a measurement of average seismic wave velocity of the medium between the source and receiver. Data obtained from different geophone depths is used to calculate a detailed seismic wave velocity profile of the subsurface in the immediate vicinity of the accelerometer casing.

The seismic source used for this study was a wooden beam, 3.7 meters in length, laid horizontally on the ground in close vicinity to the casing. The beam was coupled to the ground by parking a vehicle on the beam. A 7.3-kilogram sledge hammer was used to strike alternate ends of the beam to induce polarized shear waves. A three-component borehole geophone was lowered in the casing and clamped against the casing.

For data acquisition, the team utilized a Geostuff BG2 3-axis (triaxial) borehole geophone, a Geometrics Geode multichannel seismograph with an accelerometer electronic trigger, a field laptop computer and Geometrics Seismodule software. Data was processed using Geometrics SeisImager software.

The borehole geophone was suspended downhole at a maximum depth of 59.7 meters. For each depth where data was recorded, three seismic records were acquired separately (two shear waves of opposing polarity and a compressional wave). Each record was comprised of multiple stacks to minimize the influence of background seismic noise. Data collection commenced at a depth of 59.7 meters, continued at 0.91-meter intervals, and ended at 0.3 meters below the ground surface.

The recorded data was subsequently analyzed by splitting the three recorded components (vertical, longitudinal, and transverse) into depth-wave trains. P- and S-wave first arrivals were then picked and were best fit to a model to derive layer thicknesses and compression and shear wave velocities at the site.

#### 4.6 Summary of Results

The P- and S-wave velocity profiles ( $V_p$  and  $V_s$ , respectively) are presented in Figures 4.3 and 4.4, respectively. Because of the density of the measurements and relative scatter from one measurement to another, a five-point moving average has been applied to the data. In general, the shapes of the velocity profiles are similar. It is observed that the measured P-wave velocities do not seem to have been affected by the water in the casing at approximately 21 meters.

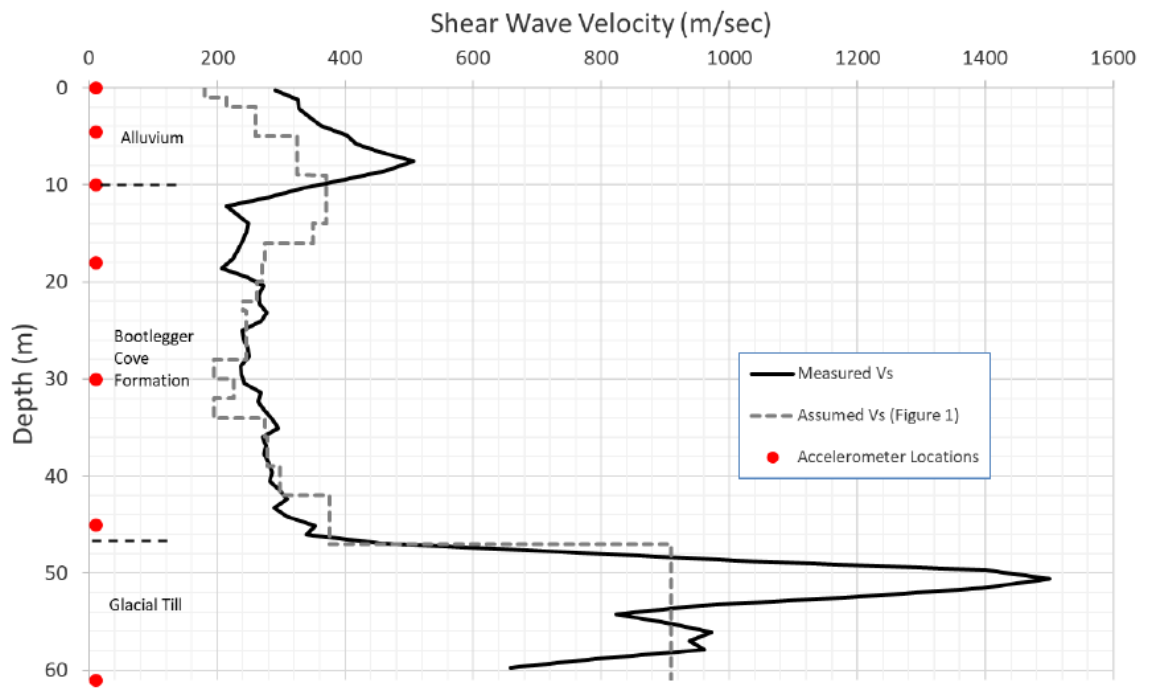


Figure 4.3. Measured Five-Point Moving Average Shear Wave Velocity Profile.

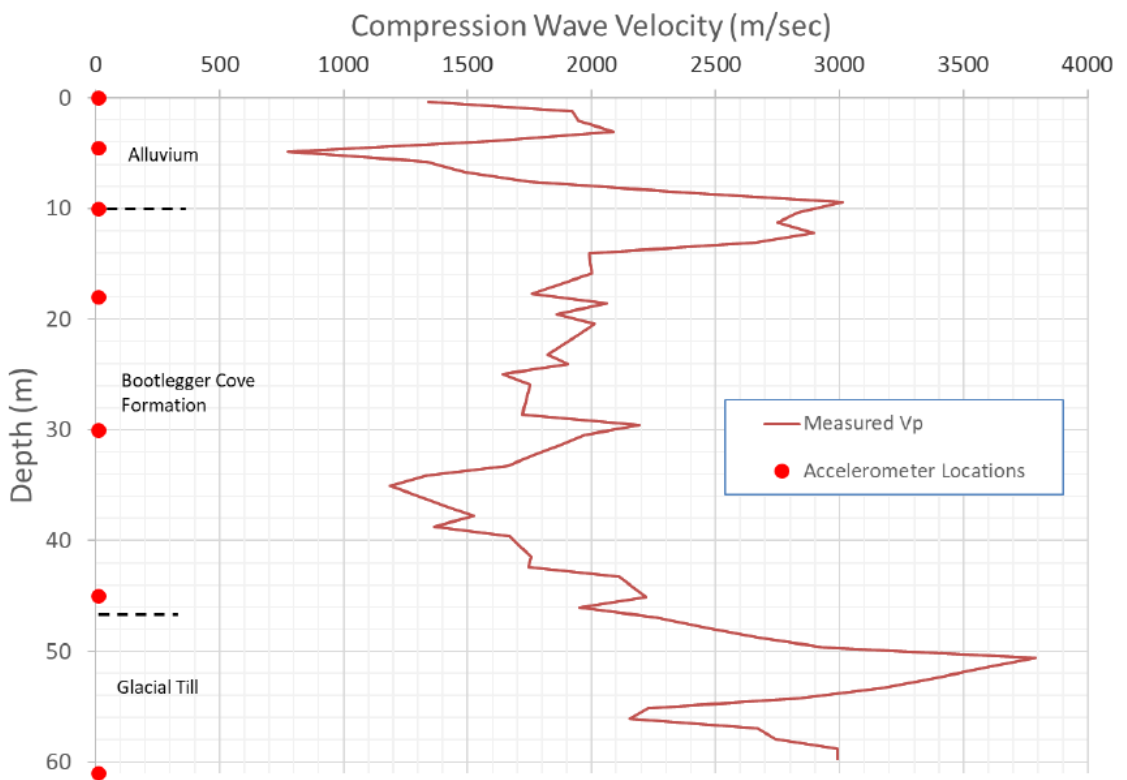


Figure 4.4. Measured Five-point Moving Average Compression Wave Velocity Profile.

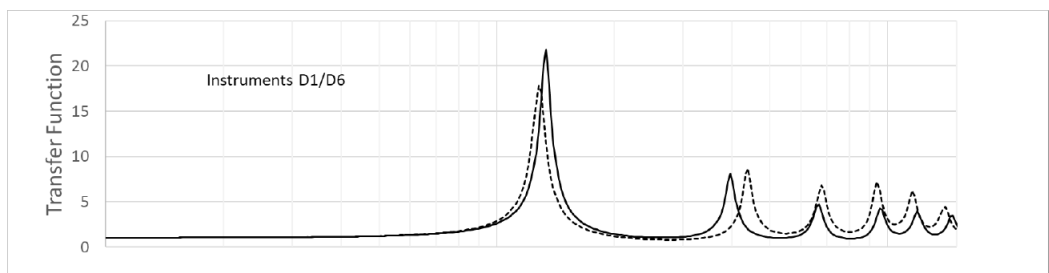
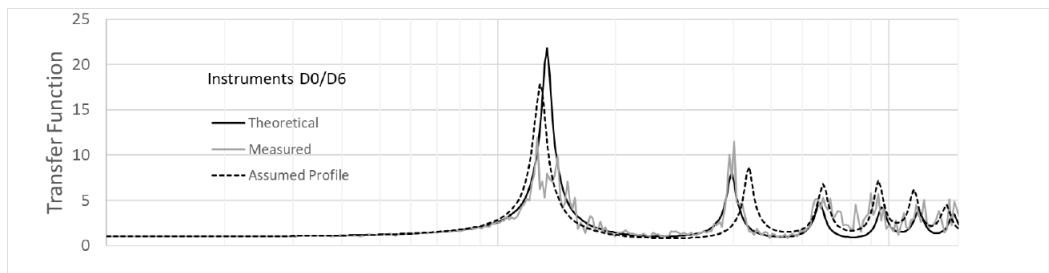
To evaluate the  $V_s$  profile further, Figure 4.3 presents the  $V_s$  profile, including the depths of the accelerometer sensors at the array site. The previous shear wave velocity profile that

was assumed for the downhole array site has been included in Figure 4.3 to illustrate the changes between the measured and assumed profiles. When comparing the generalized geology of Figure 4.1 and site-specific measurements of Figure 4.3, there are some notable observations that can be made. The higher velocity alluvium and outwash materials estimated in the Figure 4.1 profile appear to be thinner at this site and the lower velocity structure of the Bootlegger Cove Formation appears to begin closer to the 10-meter accelerometer. The lowest velocity portion of the subsurface appears to be at a depth of 12 to 18 meters, while velocity does not substantially increase until the interface with the underlying glacial till material at approximately 47 meters. The linear increase in velocity near the surface is a feature that peaks at a much higher velocity than that measured at the nearby site and is higher than would be anticipated for typical alluvial sands and gravels. The glacial till material was observed to have high velocity values, which is in line with other studies within Anchorage.

#### 4.7 Transfer Function Evaluation

An evaluation of the transfer functions of the measured DPDA ground motions compared to the theoretical transfer function using the measured shear wave velocity profile was performed using the program Strata v0.5.9 (Kottke 2013 and Strata 2017). The theoretical transfer functions were compared to the measured transfer function for two recently recorded earthquake ground motions. The earthquake ground motions selected were the 24 January 2016 Iniskin Earthquake (M7.1) and the 25 September 2014 Willow Earthquake (M6.2), located roughly 260 km south and 130 km north of the DPDA site, respectively (see Figure 4.2, inset figure bottom right and Data and Resources below). The instrument at the bottom of the array (D6) and the instrument at the surface (D0) were used to calculate the measured transfer function. The same depths within the theoretical Strata model were used to calculate the theoretical transfer function. Figure 4.5 presents the average horizontal

component results for several transfer functions. The theoretical transfer functions for both the assumed and measured shear wave velocity profiles are presented for instruments at each depth using the deepest instrument for comparison. The surface theoretical transfer functions are compared with the measured transfer function at the surface instrument. The theoretical transfer function from the measured shear wave velocity profile shows a promising match to the measured transfer function. While the amplitude is slightly higher than the measured transfer function, the peaks generally match well.



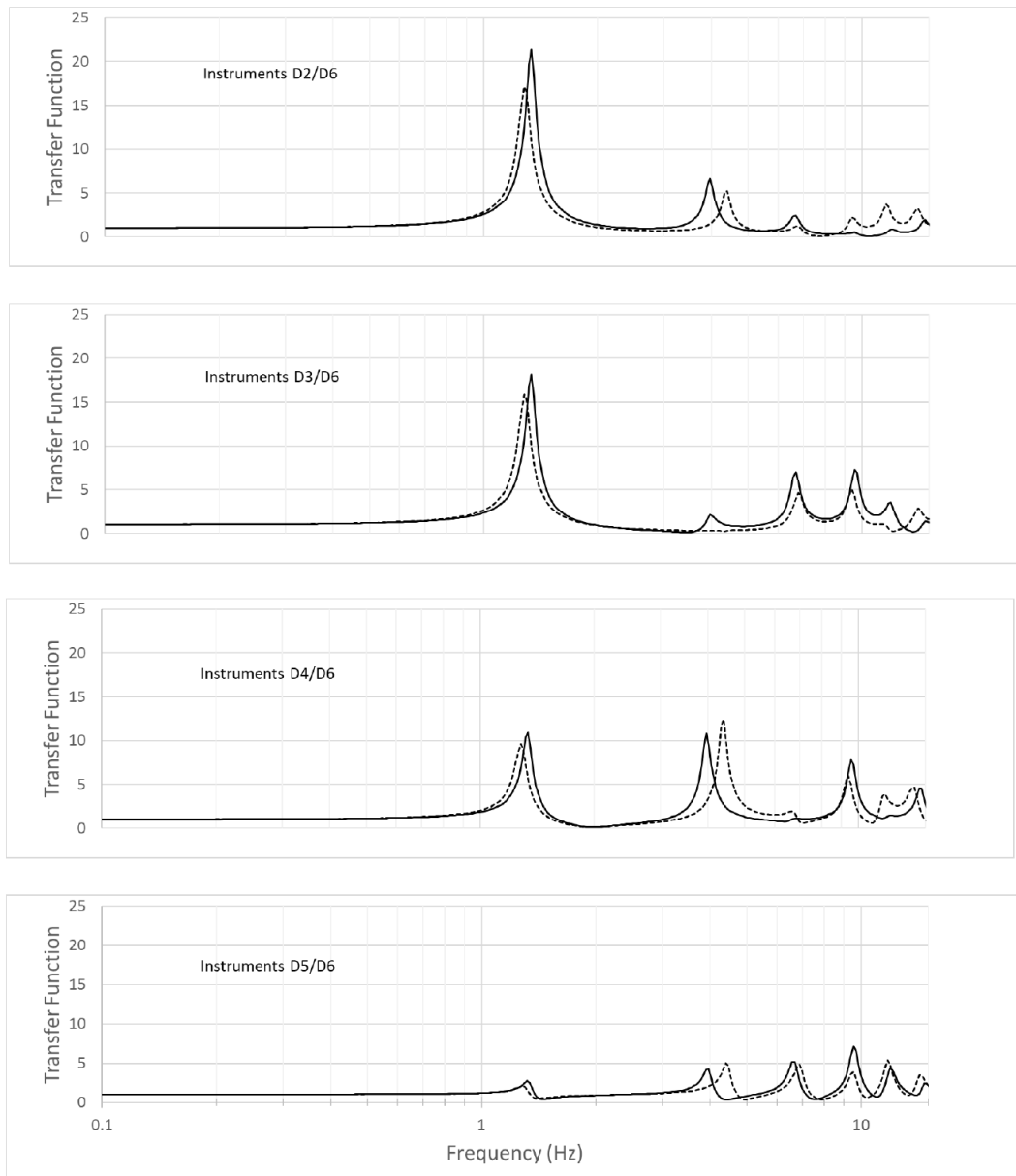


Figure 4.5. Comparison of theoretical transfer functions of the assumed and measured shear wave velocity profiles using two recent earthquakes.

Nonlinear behavior was not evaluated in this effort. The shear strain index ( $I_\gamma$ ) (Idriss 2011) was below 0.3% for both ground motions and is estimated to have little influence of the one-dimensional site response analysis methods used in this study (Kim et al. 2016). This is likely due to the great distance of the ground motions from the site, as detailed in Table 4.1.

Table 4.1. Earthquake Event Details.

Event	Latitude (degrees N)	Longitude (degrees W)	Depth (km)	Hypocentral Distance (km)	Azimuth (degrees)	Moment Magnitude (M)	PGA (g)	PGV (cm/sec)
Iniskin	59.620	153.339	125.6	261	310	7.1	0.071	11.66
Willow	61.945	151.816	108.9	130	230	6.2	0.073	5.81

#### 4.8 Comparison of Results to those for Nearby Sites

A literature review was performed to compare the findings from this study to other near-by data. Very few buildings in downtown Anchorage have available  $V_s$  data. However, in the 1980s the State of Alaska Department of Natural Resources performed cone penetration testing (CPT) along Delaney Park (Updike and Ulery 1986). Cone Penetrometer Sounding PS-C-08 was advanced in 1982 and is located approximately 45 meters southwest of the downhole array. Measurements of the friction resistance and cone tip resistance were recorded on 0.3-meter intervals to the depth of approximately 47 meters, with refusal on the underlying glacial till. Using the results of that study several correlations were applied to empirically calculate the  $V_s$  profile. Several different correlations were applied, based on the guidance of Wair et al. (2012). In addition, the data, processed using software by GeoLogismiki (2014) which uses the correlation by Robertson (2009) was evaluated. The correlation presented by Robertson (2009) is Equation 10 within that paper and is presented here:

$$V_s = \sqrt{\frac{\alpha_{vs}(q_t - \sigma_v)}{p_a}}$$

where  $\alpha_{vs}$  is the shear-wave velocity cone factor,  $q_t$  is the cone tip resistance,  $\sigma_v$  is the vertical stress, and  $p_a$  is the atmospheric pressure. Because the evaluation of the CPT data was

strictly for comparison to the measured data at the downhole array, the Robertson (2009) correlation was used to compare the results of the study.

Figure 4.6 presents several  $V_s$  profiles, including the five-point moving average values measured at the downhole array and the calculated  $V_s$  profile utilizing the CPT data presented by Updike and Ulery (1986) using  $V_s$  correlations by Robertson (2009). In general, the profiles are in good agreement. The measured  $V_s$  profile appears to estimate higher values in the upper 10 meters with relatively good agreement between profiles down to the glacial till at approximately 45 to 47 meters below existing ground.

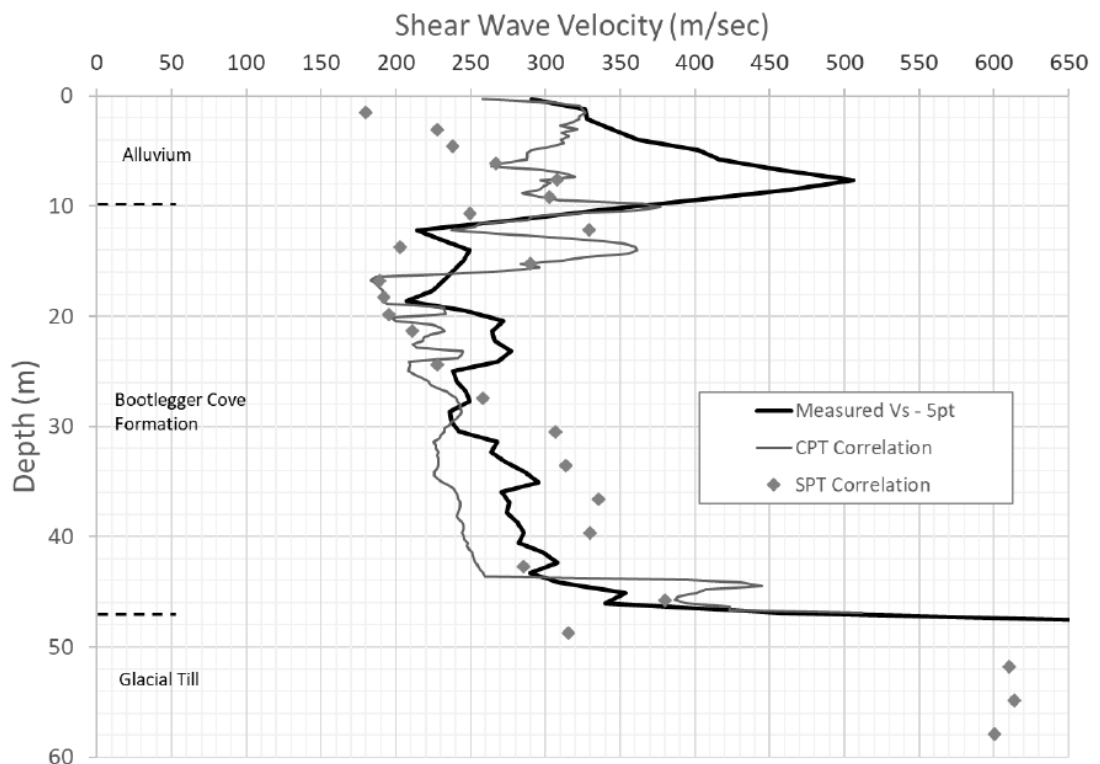


Figure 4.6. Comparison of Measured Shear Wave Velocity and Estimated Shear Wave Velocity through CPT and SPT.

Recently a borehole log was found, which had been collected during the drilling and installation of the instrumentation (personal communication with Dave Cole, December 2017). Using geotechnical drilling and logging methods, the soil lithology was recorded, and relative density relations were collected by driving a sampler and recording blow counts, also



referred to as the Standard Penetration Test (SPT). As part of this study the blow counts were corrected and a correlation to  $V_s$  was calculated using methods presented in Wair et al. (2012). The basic equation for all soils was used without modification of the blow counts, other than geotechnical corrections. The results of the SPT correlation of  $V_s$  at the site is also presented in Figure 4.6.

#### 4.9 Relevant Engineering Properties

Using the small strain velocity data collected at the site, several other properties have been calculated, including the shear modulus values with depth. The equation  $G=\rho V_s^2$ , where  $G$  is the shear modulus and  $\rho$  is the mass density (which typically ranges from 19 to 21.5 kN/m<sup>3</sup>), was used to estimate the shear modulus from measured  $V_s$  data. The Idriss (1990) shear modulus reduction and damping curves were utilized for the previously discussed transfer function analysis. To further evaluate the shear modulus estimate we utilized the CPT data previously discussed and utilized the correlation by Robertson (2009). The transformation can be done but is not presented here to save space. As with the velocity profiles discussed above, the fit is relatively good, especially considering the period of collection for the CPT data (Updike and Ulery 1986) and the potential variabilities. From these relationships one can develop average values that can be used in the evaluation of estimating site response at the Anchorage downhole array.

#### 4.10 Conclusions

The results of the downhole velocity profiling measurements have provided a significant improvement on the understanding of the dynamic properties of the soils at the Delaney Park Downhole Array site. While  $V_s$  velocity profiles near the site have been used in the past to model site response, it has proved difficult to match modeled results using these profiles to actual recorded earthquake ground motions, as shown in the transfer functions for a

recent earthquake. The comparisons of the velocity profiling results to other nearby data, including CPT and SPT measurements, gives further confidence that the  $V_s$  profile is representative of the in-situ velocities down to 60 meters at the site. These new data should allow for improved modeling of site response at the downhole array site.

## **5.0 Site Response Analysis of Anchorage, Alaska Using Generalized Inversions of Strong-Motion Data (2004-2019)**

Authors: John Thornley, John Douglas, Utpal Dutta, Zhaohui (Joey) Yang

*Geophysical Journal International (In Review)*

The following article presents the earthquake record dataset used throughout the research. The Generalized Inversion Technique (GIT) is described and the Fourier spectral amplification results for the strong-motion stations are presented. The spectral amplification results are then compared to the spatial variability of geologic conditions in Anchorage.

### **5.1 Abstract**

Anchorage, Alaska, is located in one of the most active tectonic settings in the world. The city and region were significantly impacted by the  $M_w$  9.2 Great Alaska Earthquake in 1964, and they were recently shaken by a  $M_w$  7.1 event in 2018. The city was developed in an area underlain by complex soil deposits of varied geological origins and stiffnesses, with the deposits' thicknesses increasing east to west. Situated at the edge of the North American Plate, with the actively subducting Pacific Plate below, Anchorage is susceptible to both intraslab and interface earthquakes, along with crustal earthquakes. Strong-motion stations were installed across the city in an attempt to capture the variability in site response. Several studies have been performed to evaluate that variability but have not included larger magnitude events and have not benefited from the current density of instrumentation. The work presented here provides background information on the geology and tectonic setting of Anchorage and presents details related to the dataset and methods used to perform the site-response analysis. This study has collected strong-motion recordings from 35 surface stations across Anchorage for 95 events spanning from 2004 to 2019, including the  $M_w$  7.1

Anchorage Earthquake in 2018. The more than 1,700 three-component recordings from those 95 events with moment magnitudes ranging from 4.5 to 7.1 were used to evaluate site response variability across the city. Using the Generalized Inversion Technique and a reference rock site, spectral amplifications were calculated and analyzed for frequencies between 0.25 and 10 Hz for each strong-motion station. The study results were used to develop contour maps at 1 Hz and 5 Hz, using logarithmic band averages, to describe the variability of spectral amplifications at these two frequencies of interest. The results were also compared to geologic conditions across Anchorage, and the overlaying of different soil deposits can be seen to have an impact on the spectral amplification at the sites. The results of this study provide improvements on past microzonation studies and, using sensitivity analyses, offer support for the use of small and moderate earthquakes to evaluate spectral amplifications.

#### Keywords

Earthquake ground motions, Earthquake hazards, Site effects, Spectral amplification

## 5.2 Introduction

Southcentral Alaska is one of the most seismically active regions of the world. It is located at the convergence of the Pacific and North American tectonic plates, which results in a variety of seismic sources, including deep subduction intraslab and interface earthquakes, as well as crustal earthquakes (Wesson et al. 2007). Southcentral Alaska also has approximately half of the state's population, primarily living and working in Anchorage. The 1964 Great Alaska Earthquake ( $M_w$  9.2), which is the second-largest earthquake recorded in modern history (USGS.gov 2020), affected southcentral Alaska, including Anchorage, and resulted in significant ground failure. While Anchorage's population in the 1960s was approximately

44,000 (U.S. Bureau of the Census 1963), the current population has grown to 291,000 (Census.gov 2020); since the earthquake hazard has not reduced, the risk remains high.

The Anchorage area sits in a geologically complex area of southcentral Alaska. Mountain building at the edge of the subduction zone and episodic glaciation have affected the geology and created a basin of soft sediments composed of sands, gravels, and clay overlying a steeply dipping Tertiary rock (Combellick 1999). An initial microzonation study was started in the 1990s by Biswas et al. (2003) within Anchorage, and several digital seismic strong-motion stations were installed across Anchorage to measure the variability of ground motions across the city (Dutta et al. 2003, Martirosyan et al. 2002, Biswas et al. 2004, EERI 2019, Franke et al. 2019). Since then, several strong-motion stations have been added to the network by a variety of working groups. The network now consists of more than 30 surface strong-motion stations and a downhole array. Additionally, several buildings and bridges were instrumented to measure their structural response (e.g., Yang et al. 2004, Xiong and Yang 2008).

This study presents the findings from the site response analysis of 35 surface strong-motion stations located in Anchorage, including the development of the database, methodology for performing the site response analysis for the selected stations, and initial results. This study represents a substantial improvement of the previous seismic microzonation studies for Anchorage, Alaska, as it uses data from more seismic stations representing various geological units and more and larger-amplitude strong-motion records than used in previous studies.

Microzonation studies like this consider the varied site response across Anchorage and allow the development of more resilient infrastructure that will suffer less damage and will recover more quickly after the next large earthquake. Anchorage serves a strategic community for a variety of services and operations such as the fifth busiest cargo airport in the world; United

States military installations; and a deep-water port that receives 75% of the goods arriving in Alaska. Impacts on infrastructure due to earthquakes can be significant, and mitigation of the earthquake risk is critical to the continued operation of these facilities.

### 5.3 Tectonic Setting and Seismicity of the Southcentral Alaska

Southcentral Alaska is on the North American Plate, with the Pacific Plate subducting below at a rate of 55 mm/yr (Haeussler 2008). As shown in Figure 5.1, the depth of the interface between the two plates (identified in the figure as Subduction Zone Interface Depth contours) ranges from 25 to 40 km in the region around Anchorage (Wesson et al. 2007, Hayes et al. 2018). Both intraslab and interface earthquakes occur in this region. The most notable interface earthquake was the 1964  $M_w$  9.2 Great Alaska Earthquake, which ruptured approximately 800km of the Alaska-Aleutian megathrust (Freymueller et al. 2008). An example of a notable recent intraslab earthquake is the 2018  $M_w$  7.1 Anchorage Earthquake, which caused extensive damage to infrastructure in southcentral Alaska (West et al. 2019). The 2018 Anchorage Earthquake occurred at a depth of more than 40km, representing a common observation that the subduction-zone earthquakes are quite deep in this region.

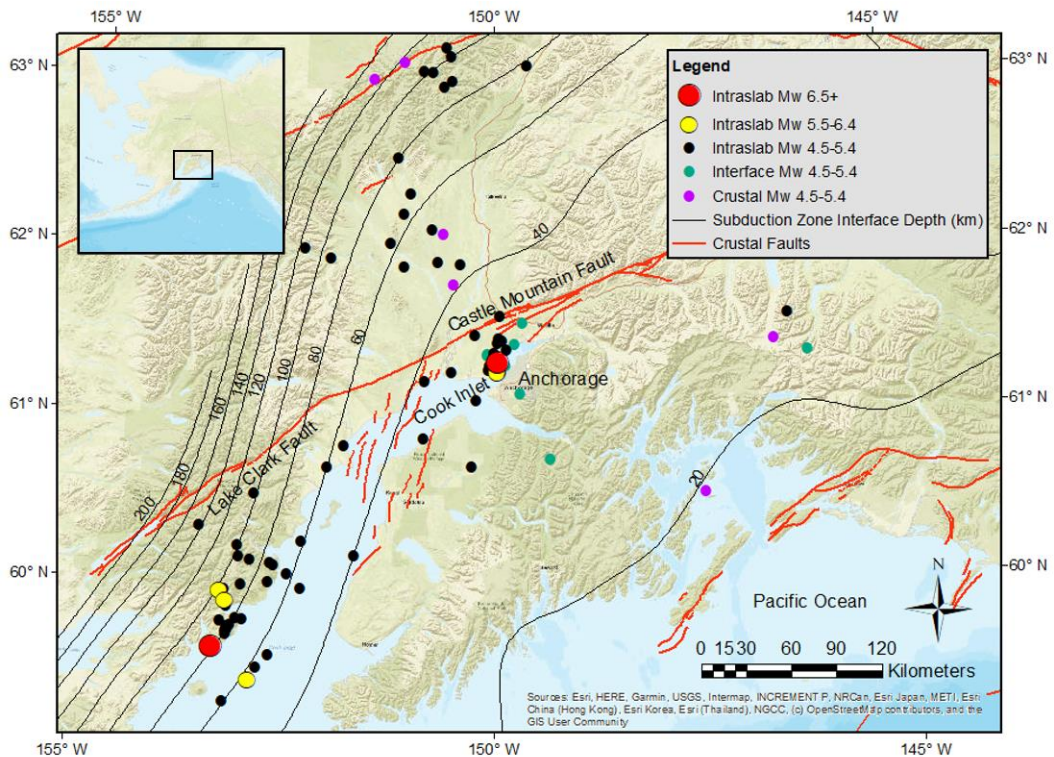


Figure 5.1. Southcentral Alaska tectonics and earthquake epicenters used in this study. Subduction zone depth contours in black using Slab 2.0 (Hayes 2018) and active crustal faults in red (Koehler 2013). The inset map indicates the location of the study in Alaska. The large red dot in the southwest corner of the figure presents the epicentral location of the January 24, 2016  $M_w$ 7.1 Inskin Earthquake. The red dot located near the center of the figure presents the location of the November 30, 2018  $M_w$ 7.1 Anchorage Earthquake. In addition to the subduction-zone earthquakes, additional seismic sources include shallow crustal faults and folds (Figure 5.1) in the Cook Inlet west and southwest of Anchorage and those in the northwest of Anchorage, including the Castle Mountain fault (Koehler et al. 2012). While the Cook Inlet crustal faults and folds are not likely to generate earthquakes of similar magnitude to the interface and intraslab earthquakes, they are much shallower than the subduction events and can potentially cause significant damage to the built environment. The Castle Mountain fault complex, which includes the Lake Clark fault to the west, can produce earthquakes up to  $M_w$  7.1 to 7.5 (Wesson et al. 2007, Haeussler et al. 2002).

## 5.4 Geology

The geology of Anchorage varies significantly from east to west (Figure 5.2). The Chugach Mountains, an accreted and lightly metamorphosed greywacke, border the city to the east (Wilson et al. 2012). Glacial valleys trend through the mountains in a northwest orientation and glacial outwash materials are found at the base of the mountains. The Chugach Mountains dip steeply to the northwest, and the sedimentary soil thickness reaches a depth of 500m overlying Tertiary sandstone at the western edge of the city (Glass 1988, Combellick 1999, Schmoll and Barnwell 1984). The soil overlying bedrock consists of a range of soils, from dense glacial outwash and till with shear wave velocities greater than 1,000 m/s (Thornley et al. 2019) to soft, cohesive lacustrine soil with shear wave velocities of 150 m/s (Updike et al. 1988). Erosional events related to several glaciation events have affected the thickness and lateral deposition of these different soils (Ulery and Updike 1983, Combellick 1999). Such marine transgressions and glacial advance and retreat cause soil heterogeneities, and hence significant variability in the amplification of earthquake ground motions across Anchorage.



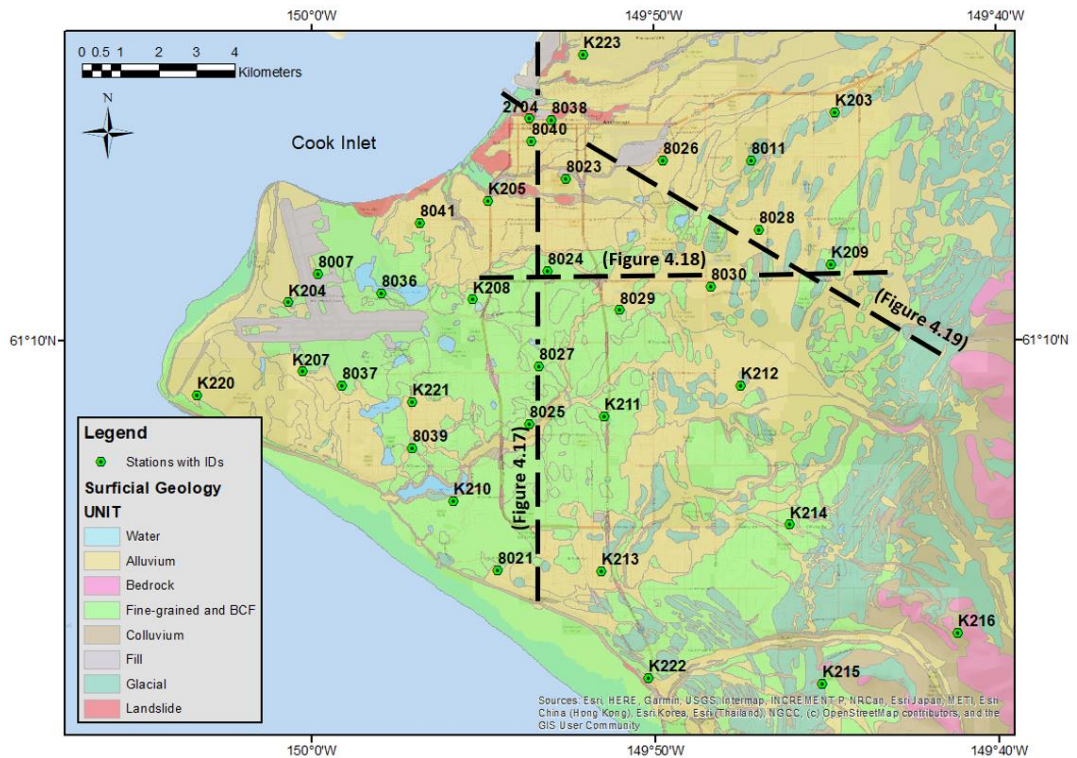


Figure 5.2. Strong motion station locations in Anchorage, Alaska. The generalized surficial geology is provided in the background to show variability, along with cross-section locations (dashed black lines) with figure references described in subsequent sections.

The surficial geology consists of several soil units, including dense glacial till, glacial outwash, alluvium, and lacustrine deposits (Schmoll and Dobrovolsky 1972). The dense glacial till extends across the city and is near the surface in the eastern portion of the city. In the northern part of the city, the glacial till is overlain by glacial outwash deposits. Overlying the glacial till in the central and western portions of the city are alluvial deposits of varying thickness. The main soil unit that has been found to have a significant impact on ground motions and site response is the Bootlegger Cove Formation (BCF). The BCF has several facies, including sand, silt, and clay. One of the sensitive clay facies is responsible for the significant ground failures in the 1964 Great Alaska Earthquake. The BCF is generally centered in the middle portion of the city, with the more sensitive clay facies located in the north and overlain by silt and sand in the south (Updike and Ulery 1986, Combellik 1999).

## 5.5 Anchorage Strong Motion Network

At the time of the Great Alaska Earthquake, March 27, 1964, there were only two seismograph stations located within Alaska. These included one station in Sitka and one in Fairbanks. The Sitka Observatory was established in 1904, located 950km southeast of Anchorage. In Fairbanks, the University of Alaska College Observatory was established in 1935. Fairbanks was the closer of the two stations to Anchorage, but it was over 400 kilometers north of Anchorage. As a result, no local strong-motion records of the Great Alaska Earthquake exist (Hansen 1965). In the years following this monumental event, numerous seismograph stations were installed and operated by the U.S. Geological Survey, U.S. Army Corps of Engineers, and others. By 1976 there were more than 40 stations across Alaska, including five stations in Anchorage (Porcella 1979).

As mentioned previously, in 1993, an effort was launched to provide a further understanding of the variability in Anchorage's seismicity through a multi-agency seismic microzonation study. Twenty-two digital surface strong-motion stations were established across the Anchorage metropolitan area (Biswas et al. 2004). Several studies have been performed using data from those stations, including those by Biswas et al. (2003) and Dutta et al. (2003). In comparison to the current work, these previous studies were achieved with fewer stations (Alaska Science and Technology Foundation stations identified as K2XX Stations) and strong-motion records of small ( $M_w$  3.3) to moderate earthquakes ( $M_w$  6.5). The recent growth of the network, including the stations of the USGS National Strong Motion Program (NSMP Stations) and the Delaney Park Downhole Array (DPDA), dating from 2004, allows characterization of the variability in response due to Anchorage's complex geology. In the early 2000s, the strong-motion data from the K2XX and NSMP stations started being collected at a single location, the Alaska Earthquake Center (AEC). Figure 5.2 presents the stations included in this analysis, and the latitude and longitude of each of the stations are

included in Appendix A-1. This study uses ground motions recorded by this network to update and refine the microzonation work performed previously by others.

## 5.6 Strong Motion Data Used in the Current Study

The strong-motion data used in this study are of earthquakes between 2004 and 2019, including the November 30, 2018  $M_w$  7.1 Anchorage Earthquake, which was recorded by 28 of the stations used in this study. Except for the DPDA data, the strong-motion records were primarily provided by the AEC. The AEC provided date, time, hypocentral location, and magnitude for the strong-motion records. The DPDA data were downloaded from the University of California, Santa Barbara (<http://www.nees.ucsb.edu/>), while the data from the  $M_w$  7.1 Anchorage Earthquake and larger aftershocks were downloaded from IRIS (<https://www.iris.edu/hq/>). The study includes recorded earthquakes with local magnitudes ( $M_L$ ) greater than 4.5 and at epicentral distances less than 300 km. The cut-off distance of 300 km was chosen to include the  $M_w$  7.1 Iniskin Earthquake (January 24, 2016), identified in Figure 5.1. A summary of the events used in this study is provided in Appendix A-2.

The database included records that were characterized in local magnitude ( $M_L$ ), body-wave magnitude ( $m_b$ ), and moment magnitude ( $M_w$ ) scales. The magnitude scales were unified to  $M_w$ . Magnitudes in  $m_b$  and  $M_L$  scales were considered equal because of their relatively low magnitudes (typically below  $M$  6) and based on research by Ruppert and Hansen (2010). These magnitudes were then converted to the  $M_w$  scale using the correlation by Dutta et al. (2003) which was developed for southcentral Alaska (Equation 5.1). Larger magnitude events in the database were characterized in the  $M_w$  scale and did not require conversion.

$$M_w = (0.855 \pm 0.04)M_L + (0.58 \pm 0.17) \quad (\text{Equation 5.1})$$

## Seismic Sensor and Data Collection

The strong-motion stations located across Anchorage primarily consist of Kinemetrics sensors. Many of these stations started with Altus K2 sensors and most have been upgraded over time to Basalt sensors. Most stations record at a sampling rate of 200 Hz, and, with the exception of the DPDA, all of the stations used in the study provide continuous data and are monitored by the AEC. The data used in this study was in the SAC format with a typical acceleration time history record length of around 300 seconds, including, in most cases, at least 20 seconds of pre-event (noise) data. The Seismic Analysis Code (SAC) (Goldstein and Snoke 2005) was selected to process the strong-motion data. The general processing included updating key metadata and selecting P and S wave arrivals.

Figure 5.1 presents the distribution of earthquakes used in this study and identifies the crustal, interface, and intraslab events, as determined by using the depth and geometry of the subduction zone defined by Hayes et al. (2018). Figure 5.4 presents the epicentral distance versus the magnitude of the events in the database. Note that the DPDA Station 8040, with latitude and longitude given in Appendix A-1, was chosen as the point in Anchorage used to define a general epicentral distance from the city, although site-specific distances were used in the analyses. The database consists primarily of  $M_w$  4.5 to 5.5 events (Figure 5.5a). Additional information describing the distribution of data across epicentral distance, depth, and azimuth from Anchorage is presented in Figures 5.5b through 5.5d.

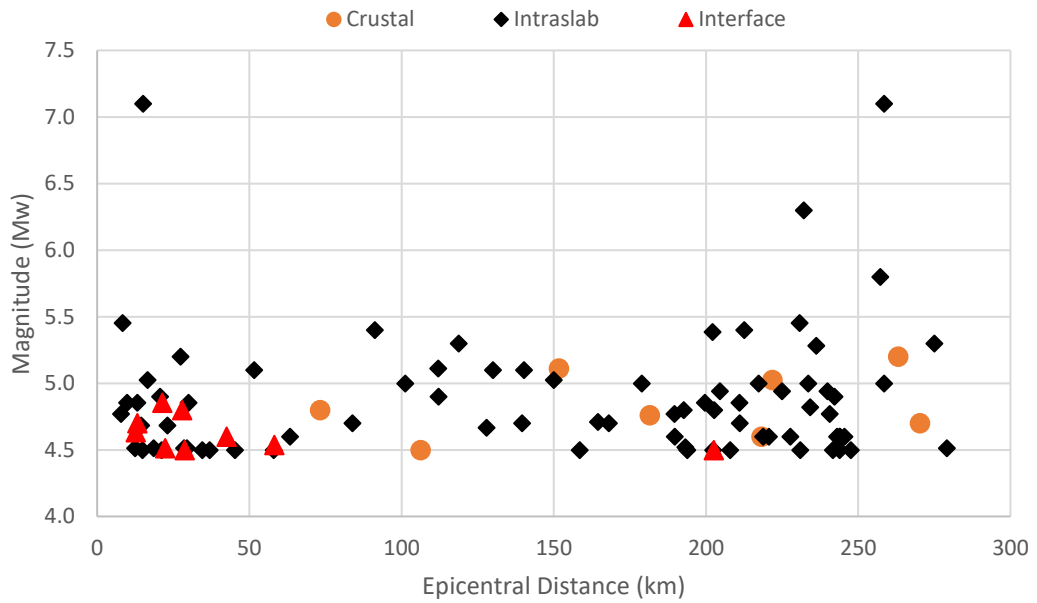


Figure 5.4. Epicentral distance versus magnitude with crustal, intraslab, and interface events identified.

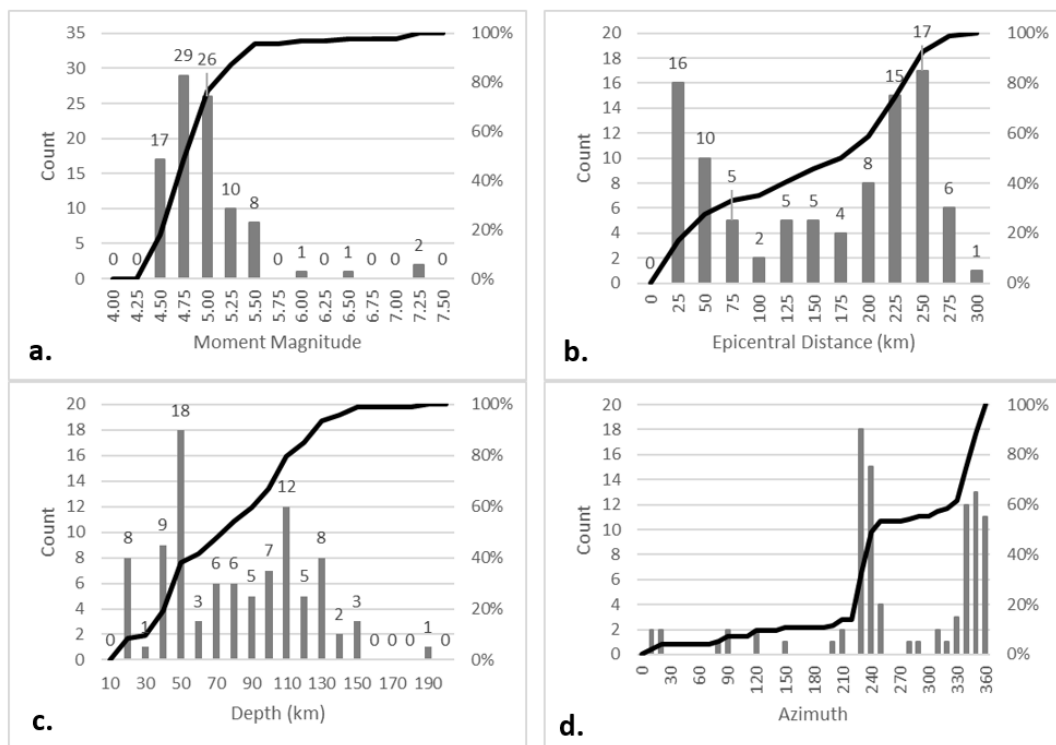


Figure 5.5. Summary of Database Event Parameters. (a) Magnitude Distribution, (b) Epicentral Distance to Anchorage, (c) Event Depth, (d) Azimuthal Direction from Anchorage. The mean value for each bin is presented on the x-axis.

Not all stations recorded all the events in the database. In some cases, the station was not functioning and in others the SNR was less than 3 over the frequency range of interest and,

hence, the record was not useful for this study. The station with the most recordings (70 in total) was K213 and the station with the fewest (only 6) was K207. The 35 stations had an average of 48 records each. The number of events recorded at each station and used in this study is presented in Figure 5.6.

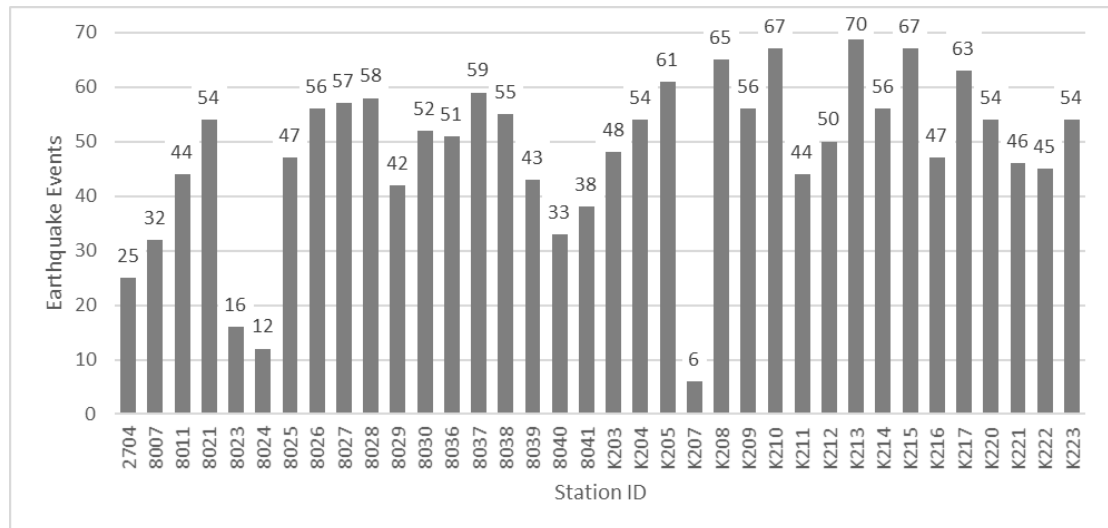


Figure 5.6. Number of earthquake recordings per station from 2004 to 2019 used in this study.

### 5.7 Site Response Evaluation

For this study records from 95 earthquakes recorded at 35 stations have been used. However, not all events were recorded at every station. To include as many strong-motion stations as possible the Generalized Inversion Technique (GIT) was used to evaluate the spectral amplifications (site response) for a site (Andrews 1986, Castro et al. 2004, Priolo et al. 2019). The GIT methodology allows for gaps in the completeness of the dataset, providing a way to incorporate as many sites as practicable.

#### GIT Background Information

The use of GIT in site response analysis has become more common since the original article by Andrews (1986), e.g., Parolai et al. (2000), Dutta et al. (2003), Oth et al. (2009), Bindi et al. (2017), and Laurenzano et al. (2018). Constraints applied to the source, path, and site terms

in the spectral domain allows the indeterminate matrix to be solved. One constraint, such as the selection of a reference site, provides a simple way to constrain the matrix within microzonation studies (Klin et al. 2018). The main assumption of GIT is that in the frequency domain, the logarithmic value of the observed amplitude spectrum at any site due to a source is the logarithmic summation of the source, site, and path spectra.

For this study, GITANES (Version 1.3) developed in MATLAB by Klin (2019) was used. Selected SAC format three-component time histories described in previous sections are loaded into GITANES. The program uses the data in the headers to select the S-wave portion of the time history (10 seconds as shown in Figure 5.3) and performs a fast Fourier transform of the data. The logarithmic value of the spectral amplitude of the S-wave data can be expressed as:

$$\log A(r_{ij}, f) = \log S_{o_i}(f) + \log S_{l_j}(f) + \log P(r_{ij}, f) \quad (\text{Equation 5.2})$$

where the amplitude spectrum of the recorded S-wave data,  $A$ , is a function of the hypocentral distance,  $r$ , and frequency,  $f$ .  $S_{o_i}(f)$  is the source for the  $i$ th source term,  $S_{l_j}(f)$  is the site term for the  $j$ th site, and  $P$  is the path effect describing the attenuation of the source hypocentral distance  $r_{ij}$  for the  $i$ th earthquake event to the  $j$ th site.

The path term ( $P$ ) can be written as:

$$P(r_{ij}, f) = \frac{1}{r_{ij}^\gamma} e^{-\frac{\pi r_{ij} f}{V_s Q_0 f}} \quad (\text{Equation 5.3})$$

Taking the logarithm of the path term:

$$\log P(r_{ij}, f) = -\gamma \log(r_{ij}) - \frac{\pi r_{ij} f}{V_s Q_0 f^\eta} \quad (\text{Equation 5.4})$$

where  $r_{ij}$  and  $f$  are the distance and frequency, respectively, and  $\gamma$  is the geometric spreading coefficient. The parameters  $V_s$ ,  $Q_0$ , and  $\eta$  are the average shear wave velocity, quality factor at 1 Hz, and exponent, respectively.

One of the tradeoffs when using GITANES is that the path terms defined in Equation 5.4 are constrained. For this study, the average shear wave velocity is assumed to be 3.2 km/s, due to the range of shallow to deep earthquakes. The quality factor,  $Q_0$ , of 150 was used for this study and  $\eta$  was set at one. Several regional studies, including Boore (2013), McNamara (2000), and Stachnik et al. (2004) show the values of  $Q_0$  often to range between approximately 100 to 300 for various models of surface, coda, and shear waves. A sensitivity analysis was performed to select the  $Q_0$  and  $\eta$  values and it was found that varying them had an insignificant effect on spectral amplification. The results of the sensitivity analysis for Station 8040 are presented in Figure 5.7, as an example of a typical result. It has been observed that the choice of  $Q_0$  does not significantly affect the results of site response studies such as this one. Still, it does impact source spectra estimates (Parolai et al. 2000), which is supported by the results of the sensitivity analysis performed for this study.

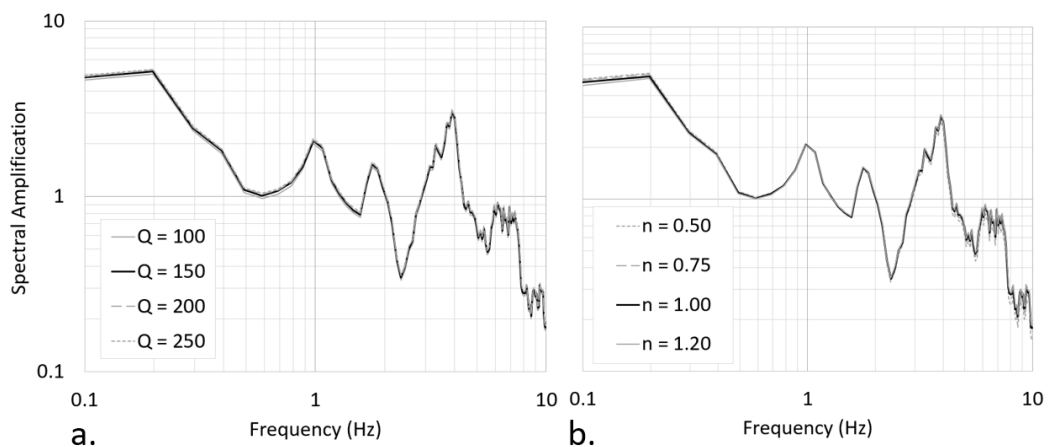


Figure 5.7. Sensitivity of  $Q_0$  and  $\eta$  on spectral amplification for Station 8040. (a.) Range of  $Q_0$  from 100 to 250 holding  $\eta$  at 1.00. (b.) Range of  $\eta$  from 0.5 to 1.2 holding  $Q_0$  at 150. The geometric spreading coefficient,  $\gamma$ , was assumed to be equal to 1 (spherical waves) for distances less than 100 km and 0.5 (cylindrical waves) for distances greater than 100 km, which is similar to the assumption of Dutta et al. (2003) and used for earthquakes with epicentral distances of 75 to 500km in a southcentral Alaska study by McNamara (2000). The geometric spreading coefficients are also recommended by Havskov and Ottemoller (2010)



when using simplified geometric spreading parameters, such as those used in GITANES. The distance,  $r_{ij}$ , was collected from header information for each event. A sensitivity analysis, using a range for each coefficient and visual evaluation on the effects of the coefficient values on the site results, was performed before settling on these values.

Rewriting Equation 5.2 as:

$$\log A(r_{ij}, f) - \log P(r_{ij}, f) = \log S_{o_i}(f) + \log S_{I_j}(f) \quad (\text{Equation 5.5})$$

And substituting Equation 5.4:

$$\log A(r_{ij}, f) + \gamma \log(r_{ij}) + \frac{\pi r_{ij} f}{v_s Q_0 f^\eta} = \log S_{o_i}(f) + \log S_{I_j}(f) \quad (\text{Equation 5.6})$$

For a particular frequency we denote:

$$d_{ij} = \log A(r_{ij}, f) + \gamma \log(r_{ij}) + \frac{\pi r_{ij} f}{v_s Q_0 f^\eta} \quad (\text{Equation 5.7})$$

Where  $d_{ij}$  is the weighted vector with path spectrum added to the amplitude spectrum and  $\log S_{o_i}(f) = s_{o_i}$  and  $\log S_{I_j}(f) = s_{I_j}$ . Equation 5.6 can be expressed as:

$$d_{ij} = s_{o_i} + s_{I_j} \quad (\text{Equation 5.8})$$

The matrix form of Equation 8 can be expressed as:

$$\begin{pmatrix} G \\ S \end{pmatrix} m = \begin{pmatrix} d \\ 0 \end{pmatrix} \quad (\text{Equation 5.9})$$

Where  $G$  is the sparse matrix that relates  $m$ , the model vector of unknown source and site terms (logarithmic values), to  $d$ , defined in Equation 5.7; and  $S$  is the row matrix that is appended to matrix  $G$  with reference site terms. These matrices are solved independently for each frequency of interest.

As mentioned above the path term is constrained in GITANES but does not have an appreciable effect on the site response results. While the source spectra results are not the primary focus of this study, the source spectra have been evaluated to understand the effects of path terms  $Q_0$  and  $\eta$  and to verify their appropriateness and physical meaning. The sensitivity analysis results of  $Q_0$  and  $\eta$  on the source spectrum for the  $M_w7.1$  Anchorage Earthquake are presented in Figure 5.8. The variability of the source spectrum with respect to  $Q_0$ , holding  $\eta$  at unity with similar results for  $Q_0$  ranging from 150 to 250 (Figure 5.8a). Figure 5.8b shows that the variation of  $\eta$  using values between 0.5 and 1.2, while maintaining  $Q_0$  at 150, produces little impact for  $\eta$  ranging between 0.75 and 1.2. These sensitivity results support the use of  $Q_0$  and  $\eta$  values described in the site amplification discussion above.

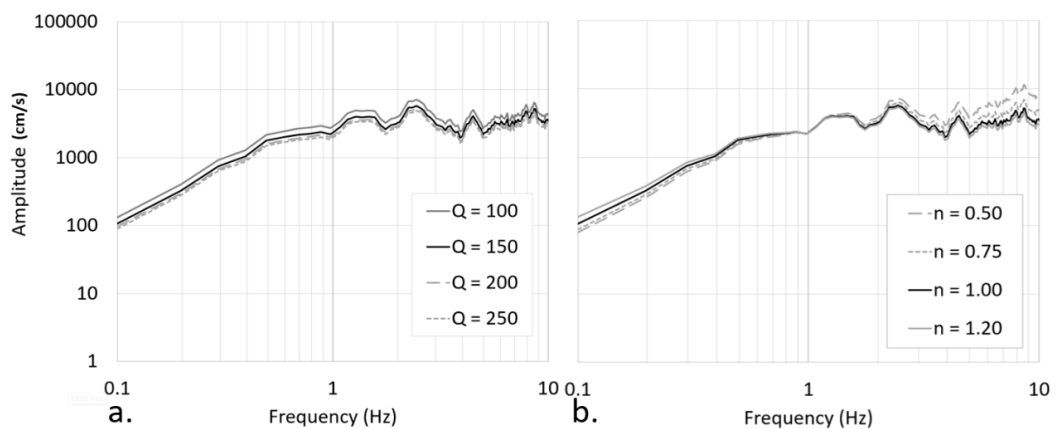


Figure 5.8. Sensitivity of  $Q_0$  and  $\eta$  on source spectra for the  $M_w7.1$  Anchorage Earthquake. (a.) Range of  $Q_0$  from 100 to 250 holding  $\eta$  at 1.00. (b.) Range of  $\eta$  from 0.5 to 1.2 holding  $Q_0$  at 150.

As shown in Figure 5.9a, source spectra from the 95 earthquakes have been plotted. The source spectrum in black at the top of Figure 5.9a is replotted in Figure 5.9b using  $Q_0$  of 150 and three values of  $\eta$ , including 0.5, 0.75, and 1.0. Figure 5.9b also presents Brune's omega square model (Brune 1970) with stress drops of 2 and 5 MPa, and a seismic moment of  $5.02 \times 10^{19}$  Nm to evaluate the source spectral shape. Estimates of stress drop range from 2.7 to 3.9 MPa and a seismic moment of  $5.02 \times 10^{19}$  Nm by Liu et al. (2019) for the  $M_w7.1$  Anchorage

Earthquake. The results presented in Figure 5.9b indicate the Brune's omega square model fits the source spectral shape for this event well, further supporting the path parameters selected for this study, given the range of earthquakes in the database.

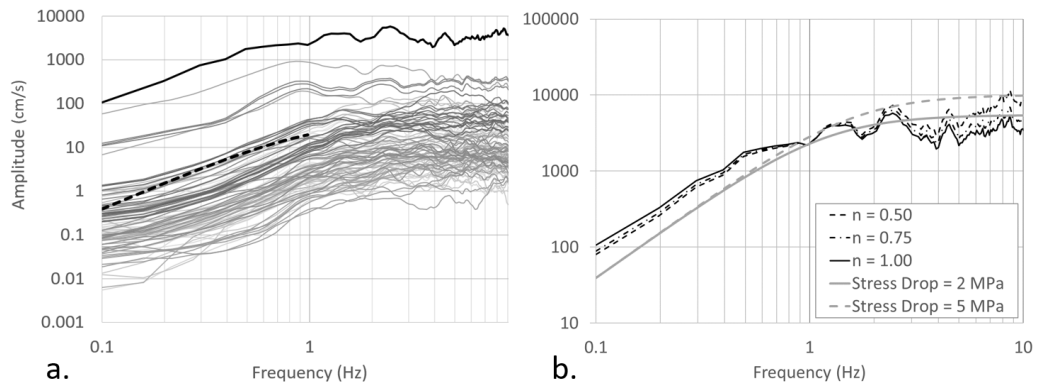


Figure 5.9. Source spectra calculated for this study. (a.) Source spectra for the 95 events with the  $M_w 7.1$  earthquake source spectrum in black and the others in grey. The dashed black line shows the general slope of Brune's omega square model. (b.) The  $M_w 7.1$  source Spectrum with  $Q_0$  of 150 and a range of  $n$  values between 0.5 and 1.0 in black. The omega square model for the event (Brune 1970) for two stress drops in grey. Note, the y-axis scales in a. and b. are different.

The results of the GIT provide spectral amplification functions (SAFs) for the two horizontal components of each station from the two orthogonal components based on a selected reference station. In this study, the K216 surface station was used as the reference station. This station is located at the eastern edge of Anchorage and is in the Chugach Mountain Range on a rock outcrop. The site is underlain by glacially-carved and metamorphosed greywacke rock and is within the vicinity of the other stations. It is the best reference station available for the network as it is the stiffest site with respect to its shear-wave velocity. The other strong-motion stations are underlain by soil and were not deemed to be more effective than K216 as a reference station for this study.

The frequencies of interest for this project range from 0.25 to 10 Hz for reasons noted earlier. The spectral amplification at several stiffer soil sites shows ratios below unity at frequencies greater than 7 Hz, suggesting that the K216 station amplifies seismic waves above 7 Hz, which

means it may not be an ideal reference site for the entire range of frequencies used in this study. Similar findings were reported by Martirosyan et al. (2002).

The two orthogonal horizontal component SAFs and their standard errors are provided as output from GITANES. An averaging technique, as proposed by Goulet et al. (2018), was applied to the resulting orthogonal horizontal site amplification ratios to calculate a single site amplification ratio at each station that is independent of instrument orientation. The equation:

$$EAF(f) = \sqrt{\frac{1}{2} [SAF_{E-W}(f)^2 + SAF_{N-S}(f)^2]} \quad (\text{Equation 5.10})$$

in which the EAF is the average site amplitude spectrum calculated at each frequency of interest ( $f$ ), and  $SAF_{E-W}$  and  $SAF_{N-S}$  are the site amplification functions for the east-west and north-south orthogonal horizontal components, respectively. This is similar to what is done for Fourier amplitude spectra (FAS) for orthogonal components within ground-motion models (Bayless and Abrahamson 2019). From this point forward the spectral amplifications for each site have been calculated using Equation 5.10.

## 5.8 Sensitivity of Model

A wide variety of earthquakes are used in this study, ranging in magnitude, epicentral distance, depth, and source type. An effort has been made to better understand the impacts of these elements in the dataset on the results of the site response analysis. As an example, more than 70% of the earthquakes in the database are smaller than  $M_w$  5.0 (Figure 5.5a). The dataset was subdivided into earthquakes smaller than  $M_w$  5.0 and those equal to or greater than  $M_w$  5.0. The two subdivided sets were evaluated using GIT, and the results were compared. An analysis of the residuals was performed to evaluate the bias one dataset has compared to the other by using Equation 5.11, where AmpA is the larger dataset, which in

this case is the events less than  $M_w$  5.0, and AmpB is defined as the smaller dataset, with  $i$  and  $j$  being the number of the recording station and frequency, respectively. The results of the magnitude sensitivity analysis are presented in Figure 5.10, with the average and the bounds of  $\pm 1$  standard deviation indicated.

$$R_{i,j} = \log(\text{Amp}A_{i,j}) - \log(\text{Amp}B_{i,j}) \quad (\text{Equation 5.11})$$

The results of the magnitude analysis suggest that there is some influence of the lower magnitude data set on the results; however, zero is within one standard deviation for most of the frequencies of interest. Only for 1.8 Hz to 3 Hz and 4.1 Hz to 5.6 Hz is the mean more than one standard deviation above zero.

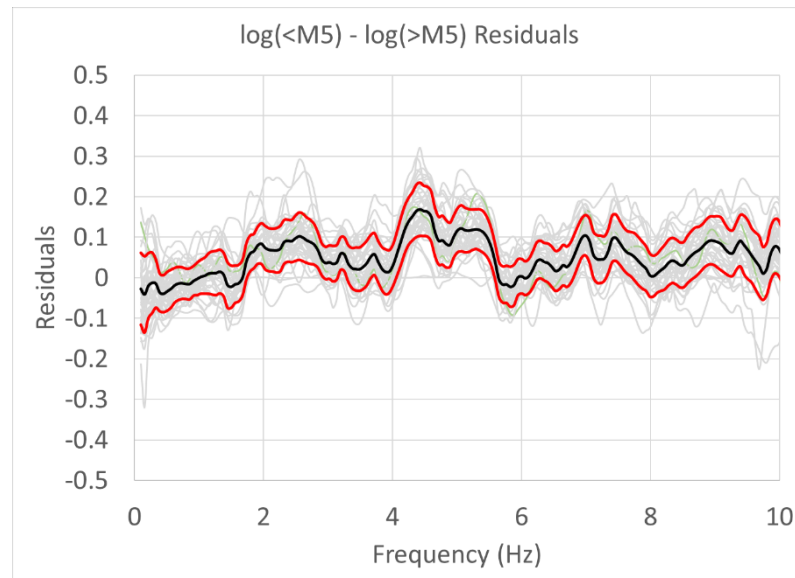


Figure 5.10. Residual plot of magnitudes less than and greater than  $M_w$ 5.0. The black line indicates the average and the red lines  $\pm 1$  standard deviation.

The residual analysis was also performed for epicentral distance where the division is between earthquakes less than 100km (36%) from Anchorage versus those at distances between 100 and 300km (64%). Sensitivity analysis considering the focal depth was also undertaken, especially given the range of earthquake depths is from 10 to 189km. A division point was selected at a depth of 50 km, where 61% of the events were at depths greater than

50 km, and 39% are less than 50 km. It was found that, in general, there was no significant impact related to epicentral distance or depth as identified by the residual analysis.

An additional analysis considered the impact of azimuth on the results. As shown in Figure 5.5d and can be observed from the visual inspection of Figure 5.1, there are two predominant azimuthal zones in the dataset. The first is the earthquakes to the southwest of Anchorage with azimuths between 225 and 250 degrees, and the second includes the earthquakes north-northwest of Anchorage with an azimuthal range of 330 to 360 degrees. It was found that there was minimal impact related to whether the earthquake originated in either of these locations. Figure 5.11 presents the results of the residual analysis for the northern azimuthal range versus the events not in that range. Similar results were observed for the southern azimuthal range. Additional sensitivity analyses were performed to evaluate the impact on the results of event type, the November 2018  $M_w7.1$  earthquake, and other factors. These analyses suggest that the results are not sensitive to these factors. It is interesting to note that there were likely nonlinear site effects at some of the stations that recorded the November 2018  $M_w7.1$  earthquake (Thornley et al. 2021c). To evaluate the effects of this event on the overall results of the study, the GIT was repeated on the full database and the full database without the data from the  $M_w7.1$  event. The two sets of results were compared for each strong-motion station where the  $M_w7.1$  event was recorded and it was found that there was very little change (less than 4%) in the overall results, which is attributed to the large number of events in the database. Figure 5.12 presents the results for three stations, one in each of Site Classes C, CD, and D. The site classes are defined by time-averaged shear wave velocities in the upper 30m ( $V_{s30}$ ), where Site Class C is 440 to 640 m/s, Site Class CD is 300 to 440 m/s, and Site Class D is 215 to 300 m/s (BSSC 2019). Site Class D sites showed nonlinear response from the  $M_w7.1$  event; however, none of the stations

show any significant difference between the database with and without the  $M_w7.1$  event (less than four percent difference at any frequency).

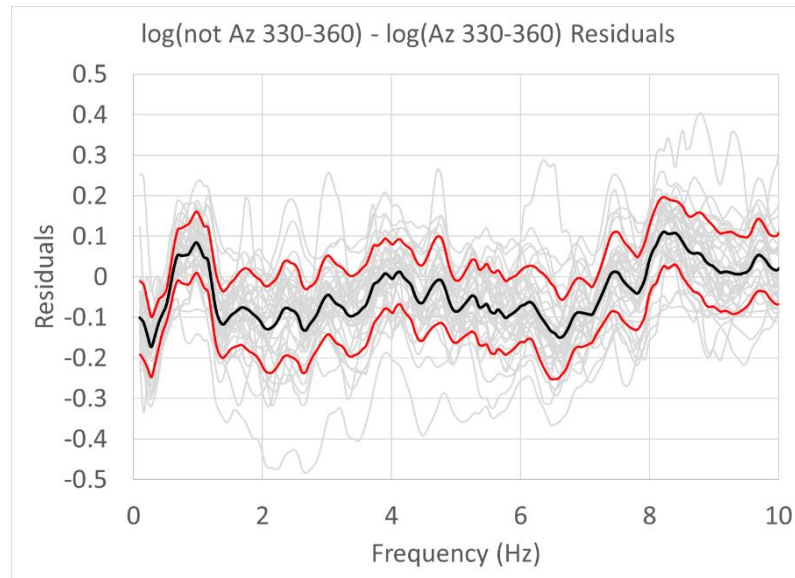


Figure 5.11. Azimuthal residual results for the azimuth range between 330 and 360 degrees. The black line indicates the average, and the red lines are  $\pm 1$  standard deviation.

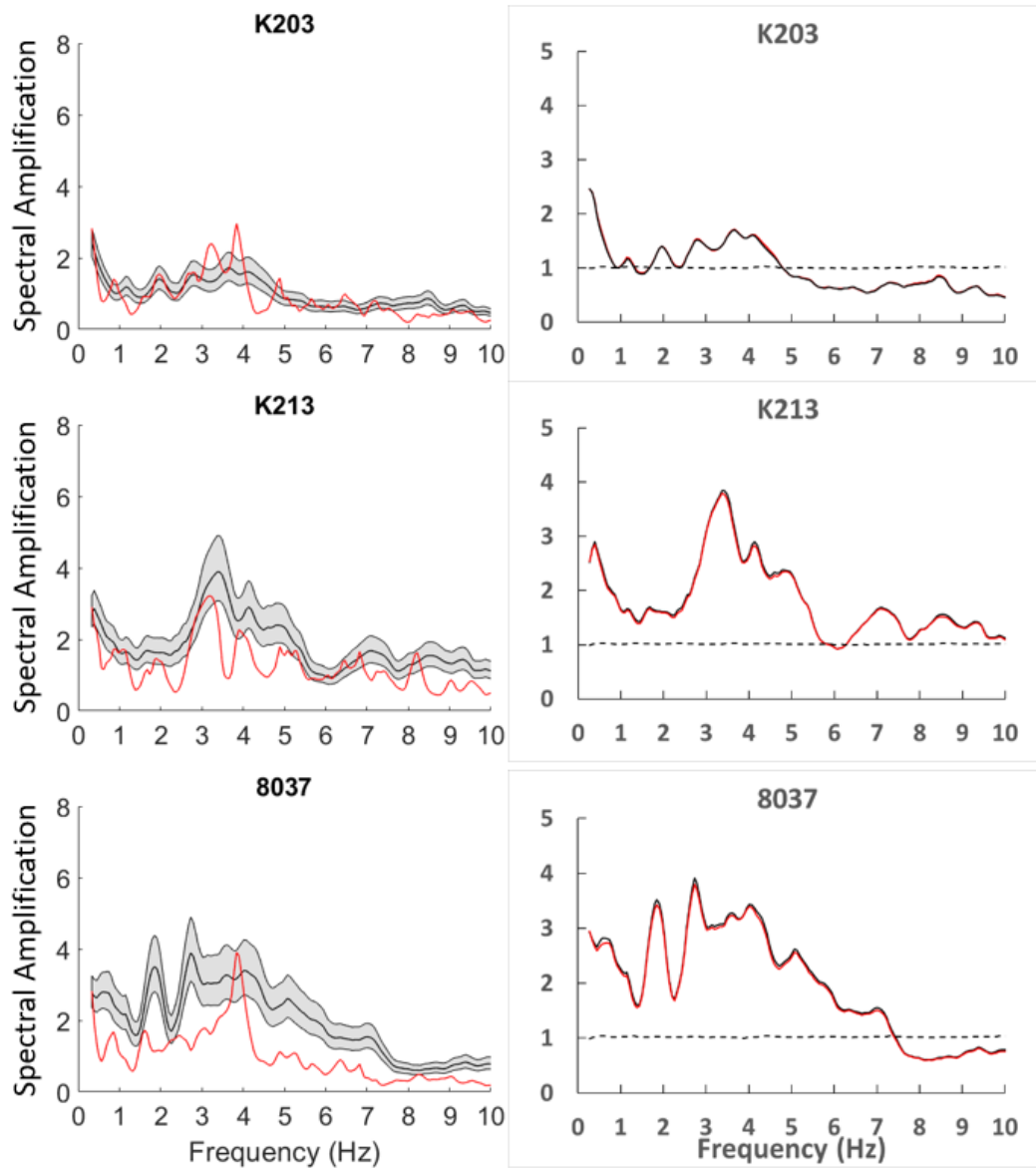


Figure 5.12. Spectral amplification results for Stations K203 (Site Class C), K213 (Site Class CD), and 8037 (Site Class D). On the left-hand side, the spectral amplifications for all events excluding the  $M_w7.1$  event are in black with the grey shading presenting the standard error and the red line presenting the spectral amplification from the  $M_w7.1$  event. On the right-hand side the spectral amplifications of the database with and without the  $M_w7.1$  event included (red line with and black line without), and the dashed line the ratio of the two (i.e., database without/database with).

### 5.9 Site Response

As described above, there is significant geologic variability across Anchorage, which as shown by others including Souriau et al (2007) can impact site effects across a region. That geologic variability results in nonuniform site response, where different areas of the city behave



differently during strong shaking. There is a need to understand and model this variability so that better risk-mitigation decisions can be made by policymakers, engineers, and emergency response teams. The results from the GIT provide insights into those differences. For example, as shown in Figure 5.13, there are significant differences in site response, as indicated by spectral amplification, between a site (K209) located in east Anchorage where the near-surface soils are dense glacial till overlying rock versus the DPDA site (8040), located in the center-north portion of the city, where there are more than 45 m of alluvium and BCF silts and clays overlying glacial till (Thornley et al. 2019). The spectral amplitude results for each station are included in Appendix A-1. Twelve of the 35 stations presented in this study were evaluated by Dutta et al. (2003) using the GIT methodology, but with a different database of earthquakes, as described earlier. The results of that study for those stations are compared with the spectral amplification results from this study in Appendix A-1. In general, there is a good fit between the results from Dutta et al. (2003) and this study, where the average spectral amplification results of the past study stay within the standard error of the results of this study. There are three stations, K203, K220, and K221 where there is a difference at one frequency, but the results across the other frequencies at these stations also fit well within the standard error of the results from this study.

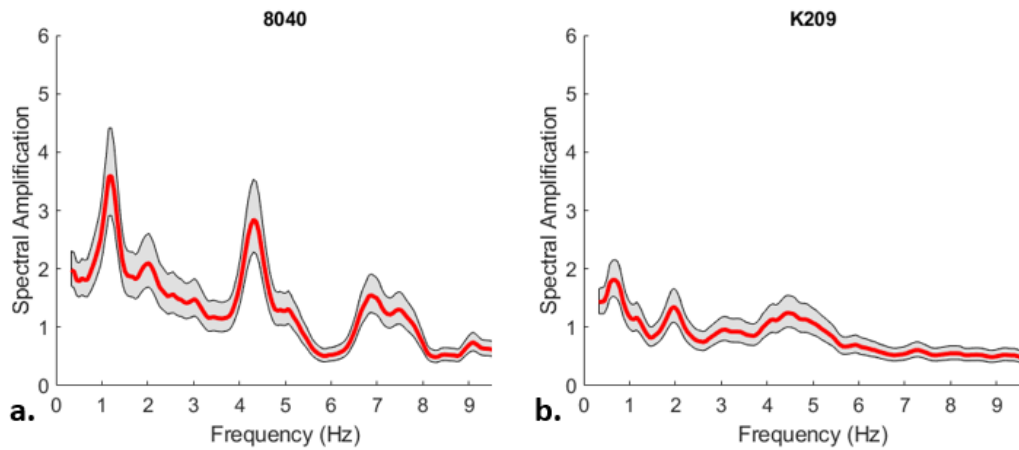


Figure 5.13. Spectral amplifications of two sites (a) DPDA station (8040) in north-central Anchorage and (b) Station K209 in east Anchorage. The average spectral amplification is indicated by the red line and the standard error is indicated by the shaded area above and below the average. Amplifications are relative to the reference station.

While acknowledging the geologic variability across Anchorage, it is important to identify areas of similarity among specific frequencies of interest. The focus of this study was to evaluate the spectral amplitudes for a range of frequencies between 0.25 Hz and 10 Hz, with the understanding that frequencies above 7 Hz may be artificially low because of potential site amplifications at K216. To more clearly show similarities and differences across Anchorage the 1 Hz and 5 Hz frequencies were considered for further evaluation. These two frequencies of interest were selected because of their use in engineering studies; these frequencies are often used in engineering studies to define design response spectra (American Society of Civil Engineers, 2017). As shown in Figure 5.14, there is a chance that the value at exactly 1 Hz may not be representative of the values above and below 1 Hz. A logarithmic band average of the computed spectral amplifications was, therefore, used between 0.5 and 2.5 Hz for the 1 Hz band and logarithmic band average between 4 and 6.5 Hz for the 5 Hz band, which is also shown in Figure 5.14.

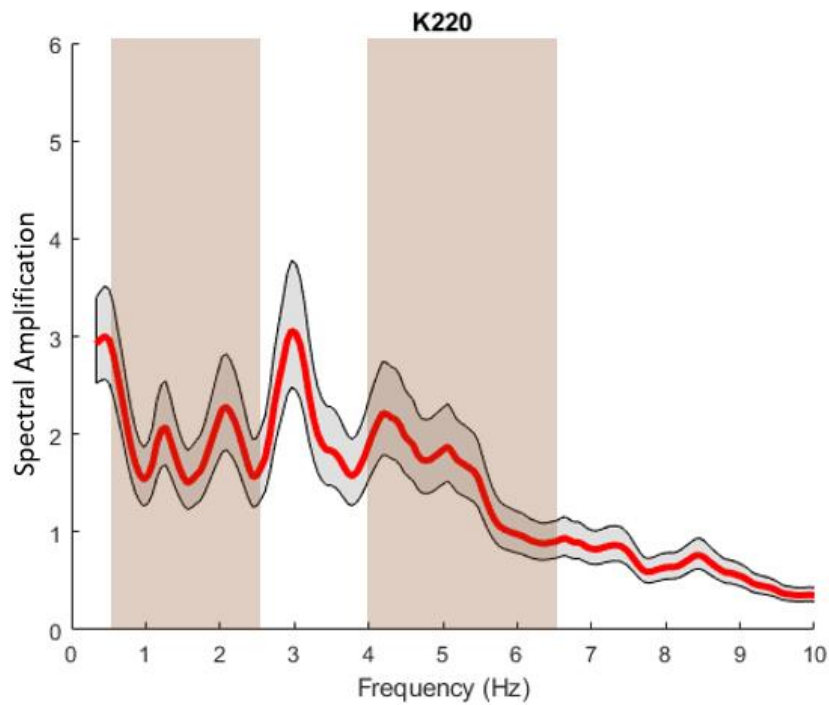


Figure 5.14. Spectral amplification at the K220 Station – the western-most station used in this study. The vertical left shaded band is the range of the 1 Hz band average and the vertical right shaded band is the range of the 5 Hz band average.

#### 5.10 Spectral Amplification Variability Across Anchorage

The strong-motion stations are roughly uniformly distributed across Anchorage, from shallow soil over the rock in the eastern portion of the city to the deep soil deposits in the mid to western portions of the city. To highlight the changes in spectral amplification across the city for the specific frequency ranges, two contour maps are drawn. The contours were created using GIS software by applying an inverse distance weighting with a power of three. No smoothing was applied. The contours have not been modified to account for known changes in surficial geology between stations. Due to the high density of the strong-motion stations across Anchorage the variability of subsurface geology is generally accounted for by these contours. Trends in the contours can be seen, and initial conclusions are drawn below; however, it is acknowledged that location-specific responses may be different due to

variability of surficial geology. Contour maps for 1 Hz and 5 Hz are presented in Figures 5.15 and 5.16.

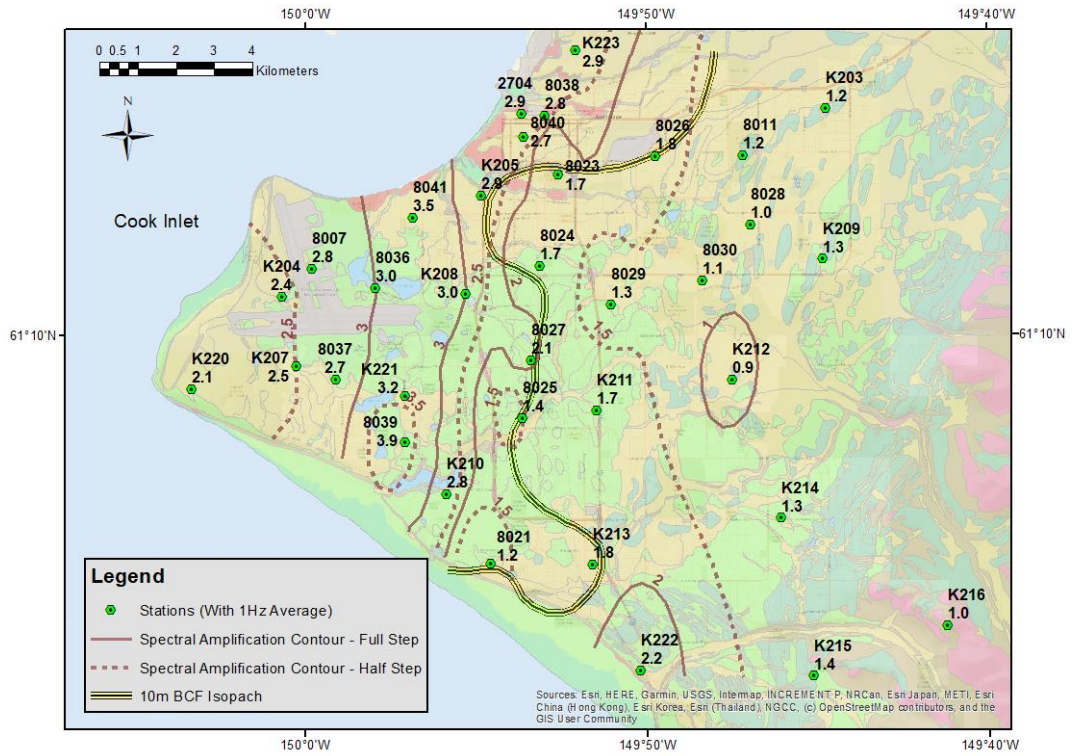


Figure 5.15. 1 Hz band-averaged spectral amplification contour map. Contours are in 0.5 spectral amplification units. The stations are indicated along with their band average spectral amplification for 1 Hz frequency.

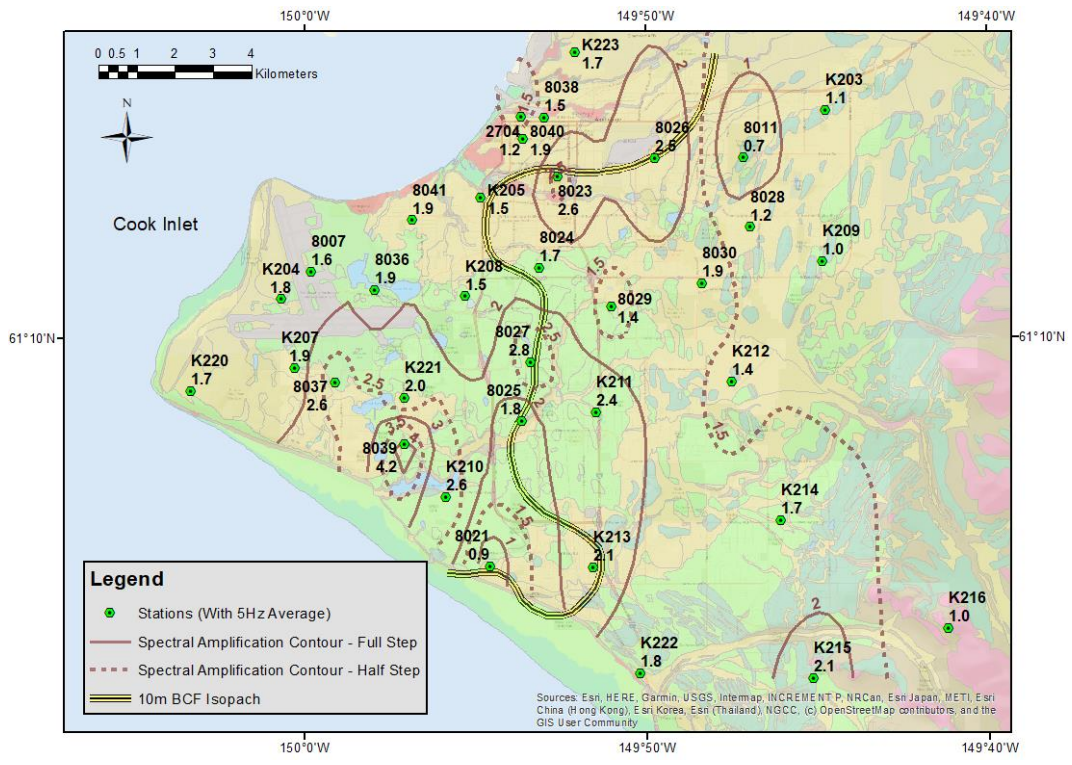


Figure 5.16. 5 Hz band-averaged spectral amplification contour map. Contours are in 0.5 spectral amplification units. The stations are indicated along with their band average spectral amplification for 5 Hz frequency.

There is a general trend across Anchorage for the 1 Hz band-averaged spectral amplification. The spectral amplification of the stations compared to the reference station is less than 1.5 in the eastern portion of the city and increases to the west. Combellick (1999) presents a line that estimates the eastern extent where the BCF (primarily silt and clay) becomes less than 10m thick. That estimated line is shown in Figures 5.15 and 5.16. The thickness increases to the west and then decreases in thickness again at the western edge of the city as indicated by Ulery and Updike (1986). In general, the spectral amplification at 1 Hz appears to increase as the BCF increases with depth and then decreases again at the western edge of the city.

Boreholes near Stations K221 and K208 indicate cohesive soil depths of 25 and 20 m, respectively. The amplifications observed at 1 Hz for Stations K208 and K221 are similar in both this study and that of Dutta et al. (2003). Similarities like this show that, despite two

different datasets, the estimated low-frequency amplification tends to be similar. However, Station 8039, a newer station not included in Dutta et al. (2003), in southwest Anchorage, has the highest spectral amplification (3.9) at 1 Hz. Ulery and Updike (1983) indicate the BCF has deeper regions of cohesive soil in the vicinity of this site. Station 8039 is located in an area that has approximately 55m of cohesive BCF soil below it. Interestingly, Station 8041 is located in another area with a deeper cohesive soil deposit of 45m and a band-average spectral amplification of 3.5 at 1 Hz. The results at the western edge of the city tend to show lower amplifications (e.g., K220 in this study has a spectral amplification of 2.1 while Dutta et al. (2003) shows a spectral amplification of 2.7), which is also where the soft portions of the BCF become thinner and stiffer soil becomes more predominant (Updike and Ulery 1986). Based on the findings from this study, the thickness of the BCF directly impacts the spectral amplification at 1 Hz, indicating that for sites located in central to western Anchorage there is a spectral amplification of more than a factor of two.

For the higher frequency band surrounding 5 Hz, there is less of an east-west contrast (Figure 5.16). On the east side of Anchorage, the spectral amplification is similar to the reference site. There are two areas where the spectral amplification is above 2. The northern area is located in the Chester Creek basin (identified in Figure 5.2) where the stations are located in an area with a mixture of alluvium and glacio-fluvial surficial soil. The second area is found in southwestern Anchorage where the surficial soils tend to consist of lacustrine or eolian silt, fine sand, and clay related to glacio-estuarine deposition (Combellick 1999). The additional strong-motion stations that have been included in this study offer a significant improvement in the 5 Hz results compared to Dutta et al. (2003). This is particularly true in southwestern Anchorage where there are more significant amplifications (greater than 4) than were estimated by the previous study (approximately 2). The differences presented in this study are primarily related to the additional strong-motion stations installed in key

geologic conditions, further underscoring the importance of establishing and maintaining dense networks in urban areas with complex geologic conditions.

### 5.11 Geological impacts on Spectral Amplification

To further evaluate the impact of geology, the spectral amplifications are plotted and compared with geologic cross-sections developed by Combellick (1999). Figures 5.17 and 5.18 present the spectral amplification for several stations along a north-south and east-west geologic section, respectively. The locations of the cross-sections are indicated as dashed lines in Figure 5.2. The glacial till is represented in blue, BCF soil in green and pink indicates the estimated bedrock. Other colors represent the mixture of alluvial and other surficial soil deposits. The spectral amplification plots are centered at the locations of the strong-motion stations located along the cross-section. In areas where glacial till is shallow there is a distinct difference in the shape of the spectral amplification, especially when compared to areas where the glacial till is deep.

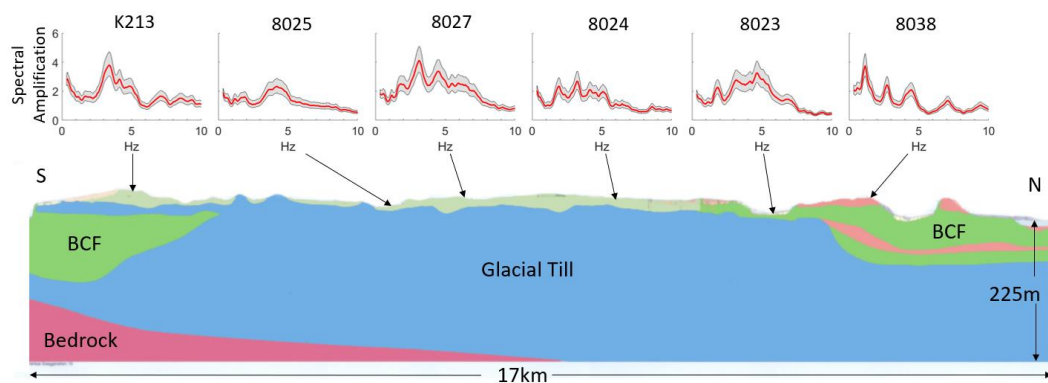


Figure 5.17. North-South Geologic Cross Section (South is on the left side of the figure). Geologic Cross Section from Combellick (1999) C Street section. Vertical and horizontal spectral amplification plot axes are the same on all plots.

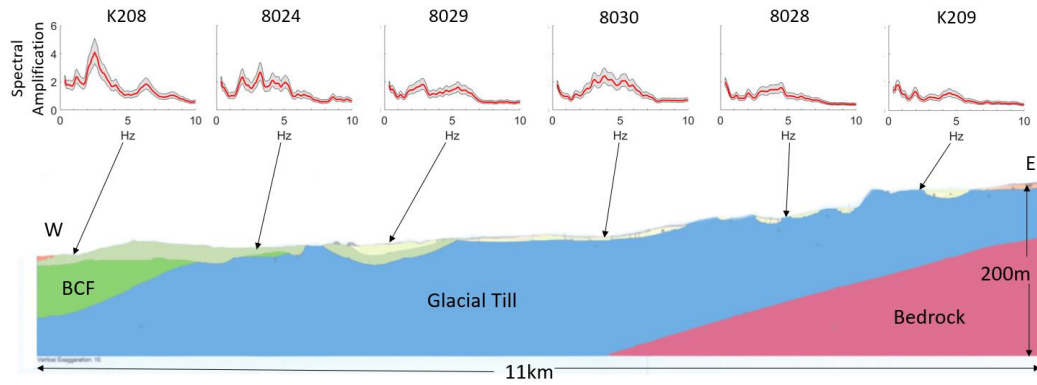


Figure 5.18. East-West Geologic Cross Section (West is on the left side of the figure). Geologic Cross Section from Combellick (1999) Tudor section.

A third cross-section is presented in Figure 5.19. This represents the NW/SE cross-section by Combellick (1999), with its location identified in Figure 5.2. It offers an excellent example of the impact of soil thickness and change in response based on the type of soil. The spectral amplification starts increasing significantly in the northwest portion of the cross-section at stations located over the BCF (green) subsurface soil. This contrasts with the stations in the southeast, where the stations are located with dense to very dense glacial till close to the surface.

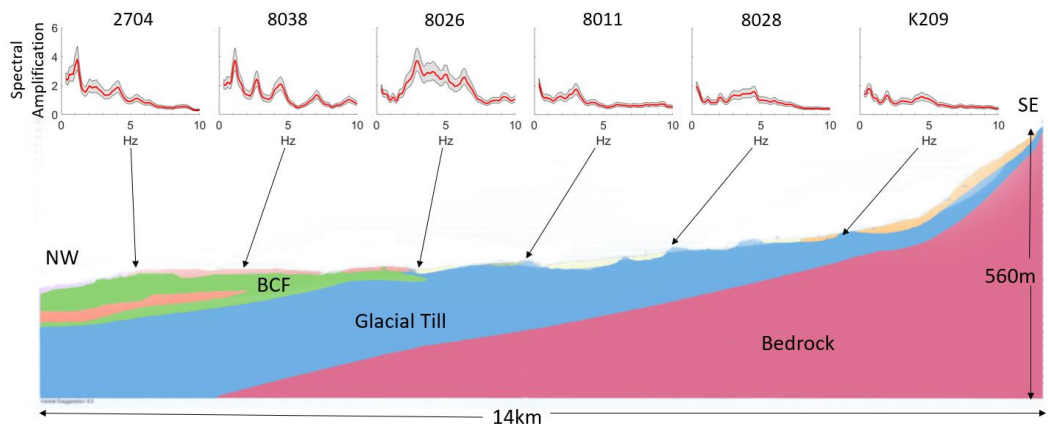


Figure 5.19. Northwest-Southeast Geologic Cross Section (northwest is on the left side of the figure). Geologic Cross Section from Combellick (1999) NW/SE section.



## 5.12 Conclusions

The results of this study build on past studies and provide further insight into the variability of site response through an evaluation of the spectral amplification of ground motions at strong-motion stations in Anchorage. The dataset used in this study is independent of previous studies and includes various events from magnitudes  $M_w$  4.5 to 7.1. There is a strong geological effect on the response of different areas in Anchorage. As seen in Figures 5.15 and 5.16, there will be distinct impacts on structures with varying frequencies of response in future earthquakes. The results provide additional insight into which areas in Anchorage are susceptible to higher ground motions, due to the subsurface conditions present.

The findings of this study further indicate that the BCF substantially impacts site response, especially at frequencies around 1 Hz. The results fit well with the geologic observations related to the extent and variable thickness of that deposit. Furthermore, the results from the 5 Hz study also match well with the surficial geology, where in the southern portion of the city, the BCF is overlain by silt and sand and was in a different depositional environment compared to the northern and eastern portions of the city.

As presented in the discussion of the model sensitivity, the inclusion of a wide variety of data appears not to bias the study results. While it is acknowledged that the dataset would be better if larger and closer earthquakes were included, no such data exists at this time. The sensitivity study indicates that, for several different parameters, impacts on the results were not observed. This gives confidence that the results can be used to evaluate the potential response related to larger and more damaging events.

In general, the current study agrees well with previous studies, including Dutta et al. (2003). The previous work and this one are based on very different earthquake datasets and using

different software, so in that way, this study validated the work performed by the previous study. This study does provide additional refinement and identifies areas where higher amplifications have been recently measured through the inclusion of additional strong-motion stations as well. Further investigation will be required to evaluate the impact of the site amplifications on the built environment - this study provides the support to perform those analyses.

## 6.0 Nonlinear Site Effects from the 30 November 2018 Anchorage, Alaska, Earthquake

Authors: John Thornley, Utpal Dutta, John Douglas, Zhaohui (Joey) Yang

*Bulletin of the Seismological Society of America; in publication. doi: 10.1785/0120200347*

The 30 November 2018  $M_w7.1$  Anchorage Earthquake offered a very timely event, with respect to this research, that could be used to evaluate the nonlinear site response at several strong-motion stations in Anchorage. The database presented in Chapter 5 is used to compare site response between lower-intensity earthquakes and the  $M_w7.1$  event.

### 6.1 Abstract

Anchorage, Alaska, is a natural laboratory for recording strong ground motions from a variety of earthquake sources. The city is situated in a tectonic region that includes the interface and intraslab earthquakes related to the subducting Pacific plate and crustal earthquakes from the upper North American plate. The Generalized Inversion Technique was used with a local rock reference station to develop site response at more than 20 strong-motion stations in Anchorage. A database of 94 events recorded at these sites from 2005 to 2019 was also compiled and processed to compare their site response to those in the 2018  $M_w7.1$  event (main event). The database is divided into three datasets including 75 events prior to the main event, the main event, and 19 aftershocks. The stations were subdivided into the site classes defined in the National Earthquake Hazard Reduction Program, based on estimated average shear wave velocity in of the upper 30 m ( $VS_{30}$ ), and site response results from the datasets were compared. Nonlinear site response was observed at class D and DE sites ( $VS_{30}$  of 215 to 300 m/s and 150 to 215 m/s, respectively), but not at class CD and C sites ( $VS_{30}$  of 300 to 440 m/s and 440 to 640 m/s, respectively). The relationship of peak ground acceleration versus peak ground velocity divided by  $VS_{30}$  (shear strain proxy) was

shown to further support the observation that sites with lower  $V_{s30}$  experienced nonlinear site response.

## 6.2 Introduction

Southcentral Alaska is one of the most active tectonic regions in the world. Since the 1964  $M_w$ 9.2 Great Alaska Earthquake, a dense array of strong-motion sensors has been installed across the area. Over the past several decades, strong-motion recording stations have recorded numerous earthquakes in the region. On 30 November 2018, at approximately 8:30 am (Alaska time), Southcentral Alaska shook because of a  $M_w$ 7.1 earthquake, which caused damage to schools, residential and commercial buildings, utilities, and roads throughout the region (epicenter shown in Figure 6.1). The impacts were widely felt, with slope failures, soil liquefaction, and ground settlement causing significant structural damage. Within Anchorage, Alaska's most populous city, the peak ground acceleration (PGA) ranged between 0.12 and 0.56g (Center for Engineering Strong Motion Data 2020) with many records of around 0.3g. The focus of this article is to evaluate the nature of the ground motions at 23 strong-motion stations across Anchorage during the 2018  $M_w$ 7.1 earthquake and how it differs from the observed site response estimated from records of smaller magnitude earthquakes.

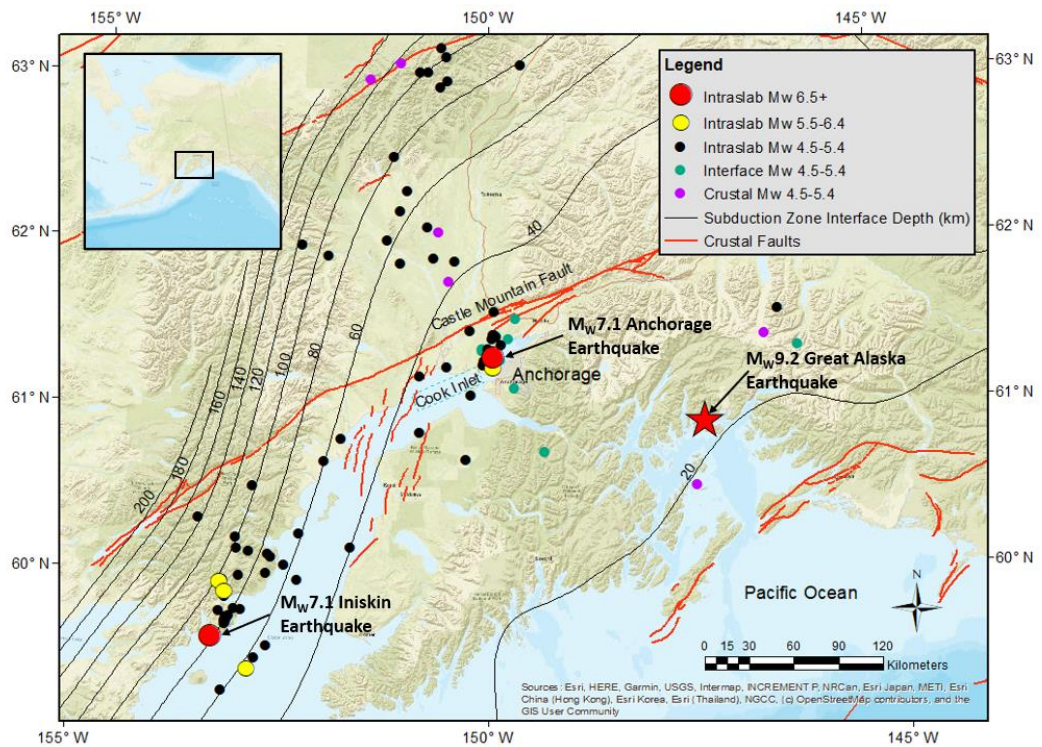


Figure 6.1. The tectonic setting of Southcentral Alaska along with the contours of the interface between the subducting Pacific plate and the North American plate using Slab 2.0 (Hayes 2018) and crustal faults as identified by Koehler (2013). The earthquake epicentral locations used in this study are shown as circles and have been further divided into intraslab, interface, and crustal events. For reference the epicenter of the  $M_w$ 9.2 Great Alaska Earthquake is identified, although the rupture area of this event was very large and hence its epicenter is a relatively poor representation of its location.

### 6.3 Seismotectonic Setting and Geology of Southcentral Alaska

The  $M_w$ 7.1 event resulted from a normal fault rupture on the Pacific plate, and it has been classified as an intraslab event (West et al. 2020). Within Southcentral Alaska, several sources of earthquakes are present, including interface and intraslab subduction zone events resulting from the Pacific plate subducting under the North American plate at a rate of 55 mm/yr (Haeussler 2008), as depicted by Smith and Tape (2020) in Figure 1c of their paper. Several active crustal sources can also produce moderate to large earthquakes (Koehler 2013). The  $M_w$ 7.1 event occurred at a depth of approximately 42 km, and it was located about 20 km north of Anchorage (West et al. 2020). The ground motions at three of the stations used in this study may have induced liquefaction, including Stations 8036, 8027, and

K211 (Franke et al. 2020), with station locations shown on Figure 6.2. Additional research is underway to evaluate the occurrence of liquefaction at these sites, as there were sand boils observed at the surface near Station K211 and settlement of a building near Station 8027.

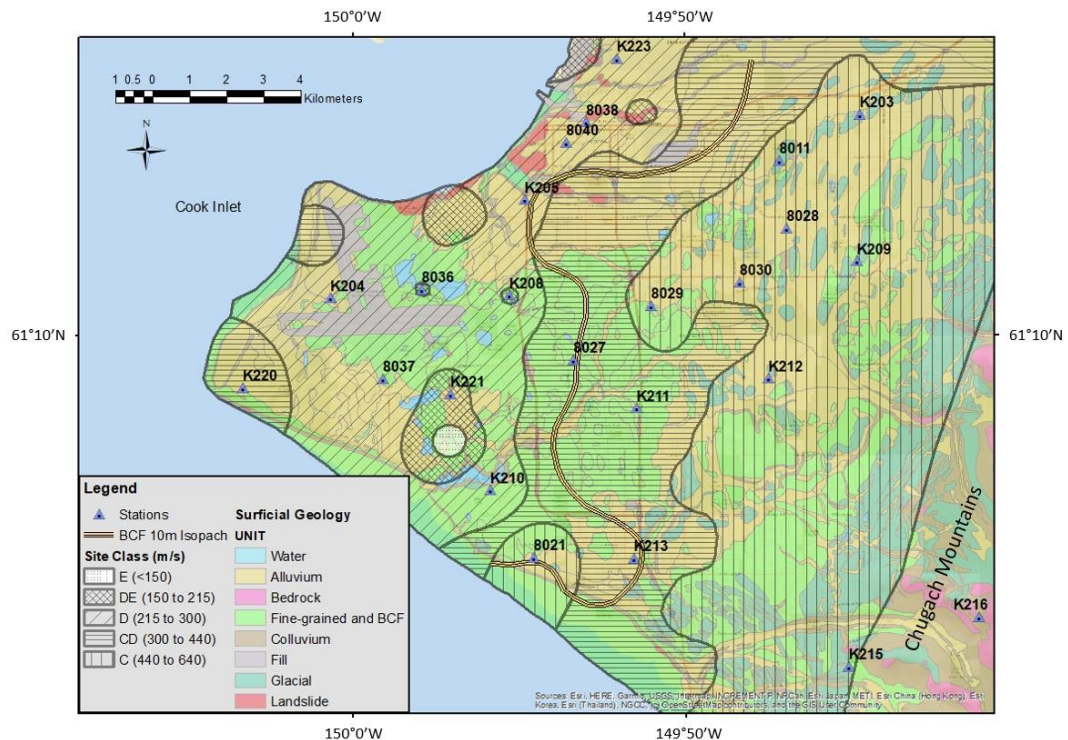


Figure 6.2. A simplified geologic map of Anchorage with strong-motion station locations. Hatching identifies the site class based on estimated  $V_{S30}$ . A 10-m isopach line is added from Combellick (1999) to show the geologic break in BCF thickness, where the BCF becomes thinner to the east of the line.

Due to the region's high tectonic activity, numerous strong-motion stations have recorded various events over the past several decades, including another  $M_w 7.1$  event approximately 300 km southeast of Anchorage in January 2016. However, the 30 November 2018 earthquake was the largest event close to Anchorage since the  $M_w 9.2$  Great Alaska Earthquake (West et al. 2020). The epicenters of these earthquakes, along with other events used in this study, are presented in Figure 6.1. This figure also shows the subducting Pacific plate's interface contours from the Slab 2.0 model (Hayes 2018) and several active crustal faults in the region (Koehler 2013). This large magnitude earthquake allows us to evaluate the site response observed at several sites across Anchorage. These effects can be compared

to those estimated from smaller magnitude earthquakes recorded in Anchorage at the same strong-motion stations to understand site response in different geologic conditions.

The subsurface soil and rock makeup are critical aspects affecting seismically-induced site response. The geologic setting is complex within the city of Anchorage. The Chugach Mountains, comprised of lightly metamorphosed greywacke, located at the eastern edge of the city, dipping steeply to the west (Wilson et al. 2012). An exploratory boring at the western edge of the city encountered bedrock at 500m, borings in the central portion of the town observed bedrock at depths greater than 200m, while borings at the eastern side encountered bedrock at depths of less than 100m (Glass 1988; Combelick 1999; Schmoll and Barnwell 1984). The bedrock consists of greywacke overlying tertiary sandstone (Combelick 1999). Dense glacial till is encountered above the greywacke across most of Anchorage and is known to have rock-like shear wave velocities (i.e., shear wave velocities above 760 m/s) as measured by Thornley et al. (2019). The city is located between the Chugach Mountains to the east and wrapping around the Cook Inlet to the south and west (Figure 6.2). The soil derived from different glacial and erosional events cover the area. Anchorage's northern and eastern parts consist of alluvial and outwash deposits over dense glacial till and bedrock. The central portion of the city sits atop fine-grained silt and clay deposits [Bootlegger Cove Formation (BCF)] derived from a glaciolacustrine environment related to the Naptown glacial advance approximately 10,000 years ago (Ulery and Updike 1983). The western edge transitions to denser sand and stiffer silt. Figure 6.2 represents a simplified geological map of Anchorage.

Site response is sensitive to geology in several ways. It is common to use the time-averaged shear-wave velocity in the upper 30 m ( $V_{s30}$ ) as a method to estimate soil behavior due to earthquakes. The practice is so common that it is included in the building code used across

the United States. Only one strong-motion station used in this study has a direct measure of  $V_{S30}$  (Thornley et al. 2019). Other studies including Dutta et al. (2000) and Martirosyan et al. (2002), also utilized surface measurements and near-surface geology to estimate  $V_{S30}$  across Anchorage. An update to these studies, which include a collection of numerous downhole measures, horizontal to vertical ratios (HVR) based on noise ratios, and site response results, are presented in Thornley et al. (2021b) have been used to estimate  $V_{S30}$  at the strong-motion stations. The city was divided into seismic site classes (described hereafter as site class), as defined in the National Earthquake Hazard Reduction Program (NEHRP) guidelines, based on the  $V_{S30}$  estimates at each site and other available  $V_{S30}$  data (BSSC 2019). Figure 6.2 shows the variability of site class, which can be seen to transition east to west in a similar fashion to the changing depth of soil from east to west.

#### 6.4 Strong-Motion Network and Data

The installation of strong-motion stations in Anchorage began in the 1970s. Early stations were analog stations using instruments such as the Kinometrics SMA-1 (Porcella 1979). In the 1990s, there was an effort to replace analog devices with digital strong-motion instruments such as the Kinometrics Altus K2 sensors with sampling rates of 200 Hz (Biswas et al. 2003). The network now consists entirely of modern digital accelerometers (primarily Kinometrics Basalt sensors).

Earthquake ground motion recordings for this study comprise data recorded at 24 strong-motion stations within Anchorage, including a reference site located within the Chugach Mountains at the eastern edge of Anchorage, identified as K216. The K216 station is the only rock site in the Anchorage network of strong-motion stations, resulting in its selection as a reference station (Steidl et al. 1996). The locations of the strong-motion stations used in this study cover various site classes reasonably well, allowing for an evaluation of nonlinear site



response if present (Figure 6.2). The locations of the strong-motion stations are provided in Thornley et al. (2021a).

The strong-motion data used in this study were obtained from the Alaska Earthquake Center (AEC). The strong-motion data for Station 8040, the Delaney Park Downhole Array, are available from the University of California, Santa Barbara (<http://www.nees.ucsb.edu/>). Strong-motion records at several stations were downloaded from IRIS (<https://www.iris.edu/hq/>) for the  $M_w7.1$  event. The full dataset can be divided into three distinct groups: 75 events prior to the  $M_w7.1$  Anchorage Earthquake, the records from the  $M_w7.1$  event, and 19 aftershocks. The PGA values of the 75 earthquakes prior to the  $M_w7.1$  main event ranged from 0.001g to 0.1g, with the average less than 0.01g. The smaller and more distant earthquakes before the main event provide an estimate of a linear site response because of their low PGA values (Regnier et al., 2013). The earthquakes range from  $M_w$  4.5 to 7.1, with epicentral distances up to 300 km for the period ranging from February 2005 to November 2018, prior to the main event. The earthquakes before the  $M_w7.1$  event consist of a mixture of the crustal, interface, and intraslab events, with the latter being predominant. Additional information on the database is presented in Thornley et al. (2021a). The aftershocks utilized in this study were recorded between November 2018 and February 2019, with magnitudes ranging between  $M_w$  4.5 and 5.7 and PGAs ranging between 0.005g and 0.1g. Epicentral locations and types of events are presented in Figure 6.1.

## 6.5 Methodology

The Generalized Inversion Technique (GIT) was utilized in this study to evaluate the spectral amplifications (site response) at each station. The use of GIT in site response analysis has become common since the original article by Andrews (1986), e.g., Parolai et al. (2000), Dutta et al. (2003), Oth et al. (2009), Bindi et al. (2017), and Laurenzano et al. (2018). The GIT site

response analysis for the three datasets were calculated separately using GITANES (Version 1.3) developed in MATLAB (Klin 2019), to maintain the independence of the results. GITANES requires the user to provide path propagation terms, including the quality factor,  $Q$ , for path attenuation and  $\eta$  for the frequency dependent exponent of the attenuation. Values of 150 and 1.0 have been selected for path propagation terms  $Q$  and  $\eta$ , respectively (Dutta et al. 2004). Before finalizing the path terms, the authors performed sensitivity analyses and found negligible to minor impacts on the site response results within the frequencies of interest for this study. This finding was also observed by Parolai et al. (2000) for their Italian dataset. It has been observed by Bonilla et al. (1997), Oth et al. (2009), and others that surface waves can impact site amplification studies. To reduce the interference of the surface waves, the S-wave window length was kept to 10 seconds. The noise portion of the record was identified as the signal before the arrival of the P-wave. Further information regarding GIT is provided by Klin et al. (2018) and others and is not included here for brevity.

The orthogonal horizontal component-time history data is used as an input, with GITANES calculating spectral amplification functions (SAFs) and standard error results for each station. The resulting orthogonal SAFs were combined using Equation 6.1 to calculate an equivalent average spectral amplification function (EAF) at each frequency ( $f$ ) of interest for each station:

$$EAF(f) = \sqrt{\frac{1}{2} [SAF_{E-W}(f)^2 + SAF_{N-S}(f)^2]} \quad \text{(Equation 6.1)}$$

For engineering studies of site response, such as this one, a range of 0.25 to 10Hz is generally adequate to evaluate earthquakes' impacts on the built environment. Figure 6.3 presents an example of the site spectral amplification at two stations, with the K216 record used as a reference motion. The solid black line with shading shows the site amplification of the database of 94 events (pre and post main event), excluding the  $M_w$ 7.1 Anchorage Earthquake

and the range of the standard error. The dotted line is the site amplification of the  $M_w7.1$  Anchorage Earthquake. The results of the site response analysis for each station are presented in Appendix A-6.

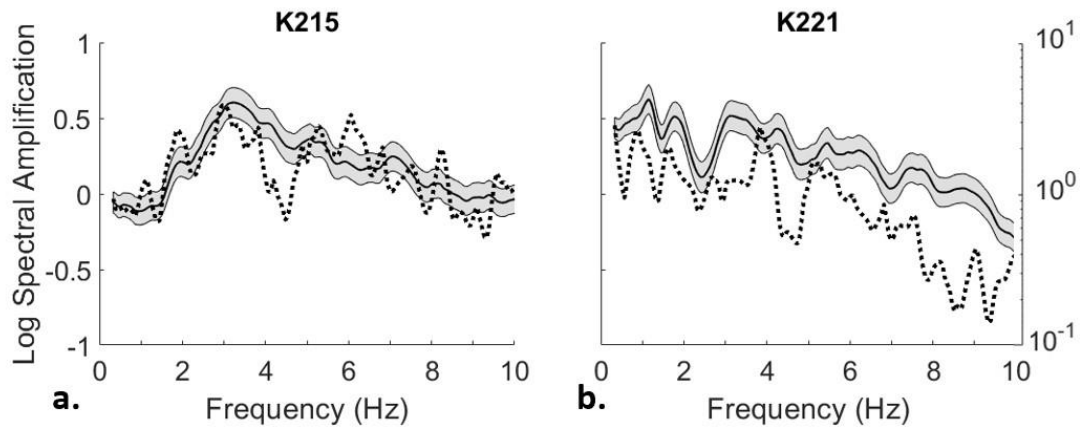


Figure 6.3. An example of site response results for two stations. The solid black line with grey shading provides the average site response and standard error for the database of 94 events. The dotted line is the spectral amplification result from the 2018  $M_w7.1$  event. All sites utilized in this study have been included in the electronic supplement.

As described above, the geology across Anchorage varies significantly. There is shallow, dense glacial till over the steeply dipping rock in the city's eastern limits. The deeper soil deposits consist of stiffer sands and gravels associated with glacial outwash and alluvial deposition. There are also soft silts and clays resulting from the BCF glaciolacustrine deposition. As seen in Dutta et al. (2000), Thornley et al. (2021a), and Thornley et al. (2021b), the geological variability has a significant effect on Anchorage's ground response. Figure 6.3a shows the results for a stiffer site on the eastern side of Anchorage and Figure 6.3b the site's results in the city's central portion. Figure 6-3 also shows a key observation where K215 (Figure 6.3a) is on a stiffer site. The site response of the 2018 Anchorage Earthquake generally matches well with the site amplification estimates provided by the database of other events (mainly small to moderate  $M_w4.5$  to 5 earthquakes). Station K221 (Figure 6.3b) is on a deep deposit of BCF soil materials below it to depths greater than 20m (Ulery and Updike 1983)

and shows a reduction in site amplification during the Anchorage Earthquake across nearly all frequencies of interest.

## 6.6 Site Response and Nonlinear Effects

Several studies, including the seminal work by Field et al. (1997), have indicated a reduction in amplification (including deamplification) when evaluating site response from mainshocks compared to aftershocks. Field et al. (1997) found, using Northridge 1994 records, that there was a reduction in amplification of the main event compared to the smaller magnitude aftershocks at alluvial sites across frequencies from 0.5 to 10 Hz. Frankel et al. (2002) observed a reduced amplification in site response values for the 2001 Nisqually Earthquake. In the Frankel study, the results of several different frequency bands were presented, and it was found that between 2 to 8 Hz the main event had lower amplification than the aftershock for softer soil sites (i.e. lower  $V_{S30}$  sites) and the reduced amplification was attributed to nonlinear site response. In addition to the reduced amplification, the mainshock amplification was compared to aftershocks and it was observed that at frequencies of 1 and 5Hz there was less amplification at lower  $V_{S30}$  and differences became less apparent at higher  $V_{S30}$  sites.

To further understand the changes in amplification and impacts on the site response across Anchorage, stations were divided by site class. As discussed previously, in Thornley et al. (2021b) the stations were divided into site class bins using Horizontal to Vertical Spectral Ratios (HVSr) and spectral amplification-derived estimates of  $V_{S30}$ . The HVSr and spectral amplification data were utilized to estimate  $V_{S30}$  at each of the strong-motion stations. The  $V_{S30}$  estimation using spectral amplification followed the technique proposed by Dutta et al. (2003). The HVSr- $V_{S30}$  classification was similar to the categorization that would have resulted using the approaches of Ghofrani and Atkinson (2104), Hassani and Atkinson (2016),

and Yaghmaei-Sabegh and Hassani (2020), where the peaks of the ratios can be used to estimate  $V_{S30}$ ; however, as with the studies above, sites with soil deposits deeper than 30m may not be adequately described by  $V_{S30}$  from a site response perspective. There is also a general assumption when using  $V_{S30}$  that shear wave velocity increases with depth, which is not likely the case with several sites located over deep BCF soil deposits. The site class contours across Anchorage are shown in Figure 6.2. Table 6.1 provides a list of the stations per site class.

Table 6-1. Stations with November 2018  $M_w$ 7.1 event estimated shear strain proxy ( $PGV/V_{S30}$ ) divided by site class using the corresponding  $V_{S30}$  ranges (ranges based on BSSC 2019). Estimates of  $V_{S30}$  are presented in Thornley et al. (2021b). PGA and PGV values are found in Center for Engineering Strong Motion Data (2020).

Site Class	Station IDs	$V_{S30}$ (m/s)	PGA (g)	PGV (cm/s)	$PGV/V_{S30}$ (%)
C	8011	513	0.33	31.5	0.06
	8021	513	0.12	16.3	0.03
	8028	565	0.21	21.1	0.04
	8029	488	0.24	22.4	0.05
	8030	538	0.29	21.8	0.04
	K203	513	0.30	30.4	0.06
	K209	488	0.19	18.8	0.04
	K212	594	0.21	15.8	0.03
	K215	465	0.56	20.7	0.04
CD	8027	330	0.47	29.5	0.09
	K211	402	0.46	30.3	0.08
	K213	383	0.34	28.5	0.07
	K220	330	0.33	22.0	0.07
D	8037	246	0.36	25.0	0.10
	8038	235	0.29	24.7	0.10
	8040	265	0.25	21.7	0.08
	K204	285	0.19	20.9	0.07
	K205	224	0.26	26.7	0.12
	K210	235	0.24	31.0	0.13
	K223	224	0.27	29.5	0.13
DE	8036	213	0.41	31.6	0.15
	K208	213	0.26	33.9	0.16
	K221	193	0.24	26.8	0.14

The average and standard deviation of the site amplification was calculated for each site class for both the database of 94 other events (pre- and post-main event) and for the  $M_w$ 7.1 Anchorage Earthquake. Figure 6.4 (a-d) presents the two sets of results for each site class.

Figure 6.4a presents the site class C results ( $V_{S30}$  of 440 to 640 m/s) from both sets of data and shows significant overlap, indicating that there was little difference across most frequencies for the  $M_w7.1$  event. As a particular example, Station K215 presented in Figure 6.3a is one of the stations in site class C.

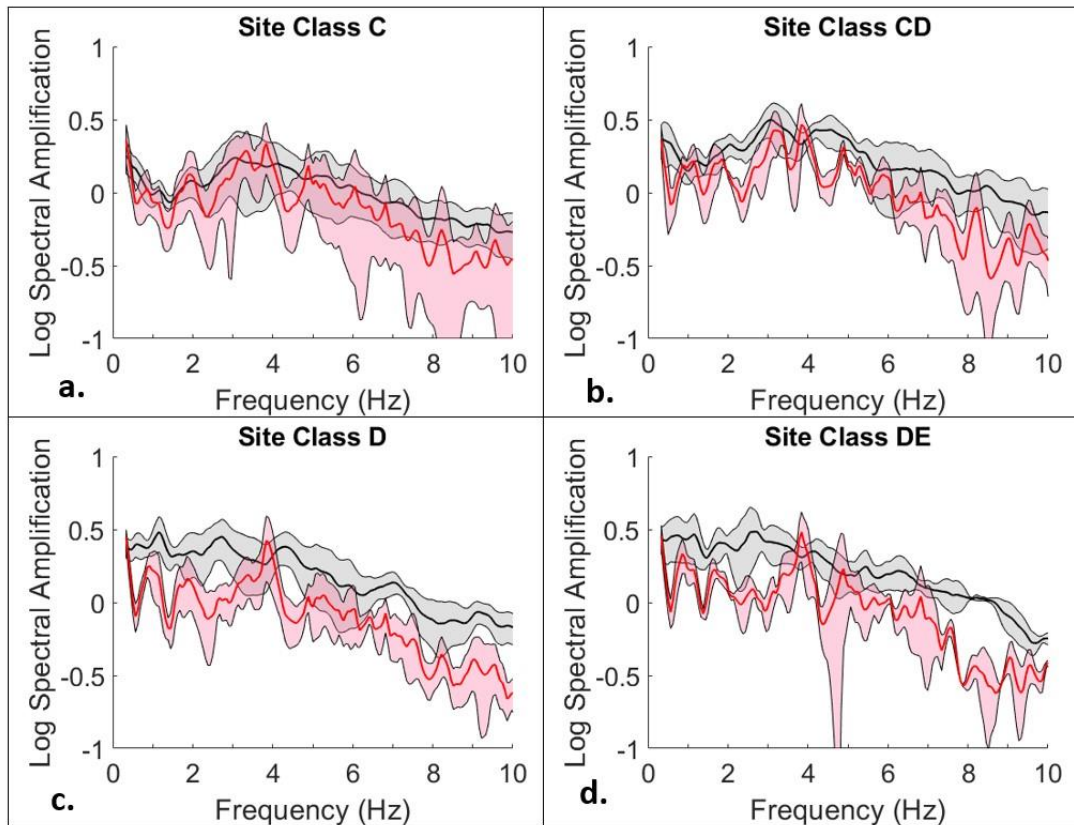


Figure 6.4. Logarithmic spectral amplification based on site class for the full dataset in grey and the  $M_w7.1$  event in red. The shading shows the range of  $\pm 1$  standard deviation for each dataset. There is more variability in the standard deviations for the  $M_w7.1$  event because it is based on the range of site class amplification from one event, whereas the full dataset is much more constrained.

A general trend of deamplification at frequencies above 7 Hz is noticed for each site class bins, which could be related to possible high-frequency site amplification at the reference station, K216, as observed by Martirosyan et al. (2002). In the visual observation of Figures 6.4a through 6.4d the general trend across all frequencies is that the site amplification decreases between the two datasets from site class C (stiffer sites) to DE (softer sites).

There were numerous aftershocks related to the  $M_w7.1$  earthquake. Further evaluation of these aftershock events was performed to understand if the ground response from these events also suggests a similar reduction in site response. If so, then it would call into question whether the observations presented in Figure 6.4 were related nonlinear site response or other attributes, such as location. The recorded data from 19 aftershocks ranging from  $M_w$  4.5 to 5.7 were used separately for this evaluation of site response. Figure 6.5a and 6.5b present the response obtained for the class D ( $V_{s30}$  of 215 to 300 m/s) and DE sites ( $V_{s30}$  of 150 to 215 m/s), respectively. The overlap of the site response results from the pre-main event dataset and the aftershocks support the finding that the  $M_w7.1$  event did result in nonlinear site response behavior, especially at class D and DE sites.

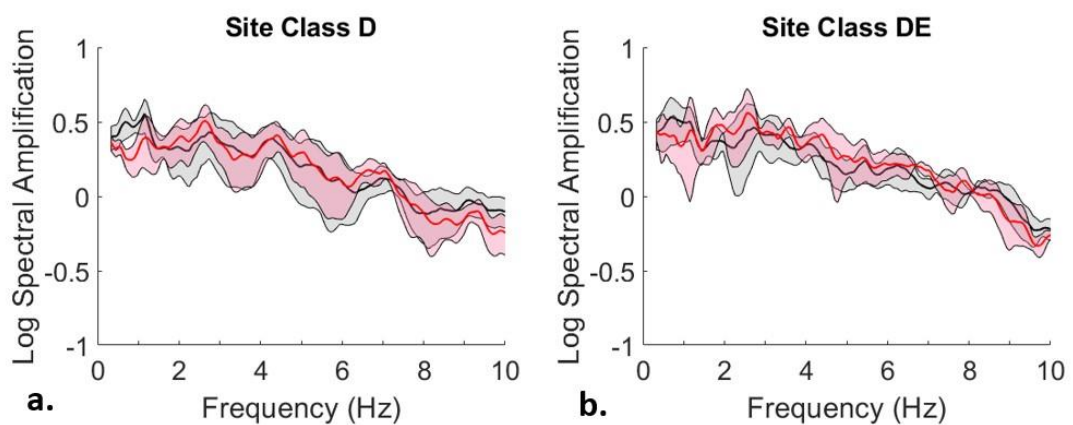


Figure 6.5. The site database (in grey) and the aftershock events (in red) with  $\pm 1$  standard deviation for site class D and DE.

One of the nonlinear effects that is observed in soil under dynamic loading is a reduction of shear strain modulus and an increase in shear strain. As mentioned previously, only one site has a properly characterized subsurface that can be modeled using one-dimensional equivalent linear or nonlinear modeling (Thornley et al. 2020). Therefore, it is necessary to utilize a shear strain proxy to evaluate nonlinear site effects. Using the peak ground velocity (PGV), the shear strain proxy of  $PGV/V_{s30}$  can be calculated to assess nonlinear site effects (Idriss 2011). Chandra et al. (2015, 2016) found a good relationship between PGA and the

shear strain proxy when predicting nonlinear site response. These methods provide an excellent first-order prediction that can be improved with the additional characterization of a particular site.

Using the methodology presented by Gueguen et al. (2018), a plot of PGA versus  $PGV/V_{S30}$  can be used to approximate the stress-strain curve that indicates linear and nonlinear soil response. The nonlinear response can be further evaluated utilizing the  $V_{S30}$  estimates for the strong-motion stations and the PGA and PGV values from the  $M_w7.1$  event. Using the PGA and shear strain proxy, four stations, each from a different site class have been plotted in Figure 6-6 using the events included in the database. The highest PGA data points for each site is the  $M_w7.1$  event. In the case of Station 8030 (site class C) the slope of the PGA versus strain proxy is much steeper than the other stations, indicating that the site is much stiffer. It is clear from this figure that the  $M_w7.1$  event resulted in a more significant nonlinear response at softer soil sites, which further supports the findings presented in Figure 6.4. This pattern can also be seen in the shear strain proxy results presented in Table 6.1, where the highest shear strain proxy values are estimated at the softest sites.



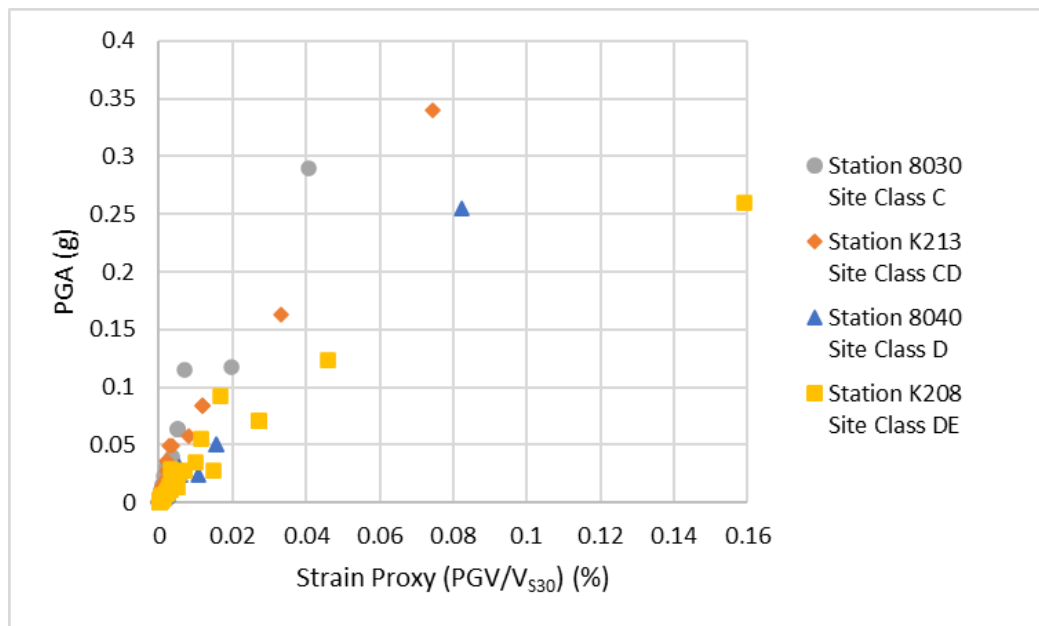


Figure 6.6. Strain proxy estimates at four stations representative of each site class versus PGA. The highest PGA values and strain proxies correspond to the  $M_w7.1$  event.

## 6.7 Conclusions

Even though the 2018  $M_w7.1$  intraslab earthquake occurred at a depth of more than 40 km, sites with deeper and softer deposits showed nonlinear soil behavior. This nonlinear behavior was much less apparent at stations with higher estimated  $V_{s30}$  (i.e. site class C). As  $V_{s30}$  decreases there is reduction in site amplification across frequencies of engineering interest. It should be noted that there is more work to be done to evaluate the effects of varied velocity layers and their impacts on site response, especially at soil sites deeper than 30 m. The nonlinearity observed at some of these deeper soil sites could result from a combination of deep soil and soft soil layers interbedded with stiffer soil layers. The findings here support the current generalized classification of strong-motion sites. Further evaluation should be conducted to evaluate the adequacy of the building code by site class. Additional characterization on a site-by-site basis may help improve the site class contours and allows for more site-specific refinements.

## 7.0 Evaluation of Horizontal to Vertical Spectral Ratio and Standard Spectral Ratio Methods for Mapping Shear Wave Velocity Across Anchorage, Alaska

Authors: John D. Thornley, Utpal Dutta, John Douglas, Zhaohui (Joey) Yang

*Soil Dynamics and Earthquake Engineering (Resubmitted with revisions – in review)*

The use of shear wave velocity, especially  $V_{S30}$ , as a tool to estimate site response in local building codes. The strong-motion dataset is used to calculate the horizontal to vertical spectral ratio (HVR) and the peak amplification ratio is used to develop a regional  $V_{S30}$  equation for strong-motion stations and compared to standard spectral ratio  $V_{S30}$  correlations. A  $V_{S30}$  contour map of Anchorage is then presented.

### 7.1 Abstract

The use of horizontal to vertical spectral ratios (HVR) of earthquake ground motions has become a standard technique to characterize sites, especially those lacking subsurface measurements. Several studies have developed relationships between HVR results and time-averaged shear-wave velocity in the upper 30m ( $V_{S30}$ ). Other studies have utilized standard spectral ratios calculated from horizontal ground motion Fourier amplitude spectra to estimate  $V_{S30}$ . Anchorage, Alaska (USA), has a network of strong-motion recording stations, many of which have no site-specific subsurface characterization. This study compares measured  $V_{S30}$  and HVR results from 18 strong-motion stations to four regional models developed by others. A relationship between the 1 Hz band-averaged (0.5 to 2.5 Hz) spectral amplification results and  $V_{S30}$  is presented.  $V_{S30}$  estimates for the strong-motion stations are made, and a regional model is developed between HVR and  $V_{S30}$ , both in terms of  $f_{\text{peak}}$  (the frequency of the peak HVR amplitude) and  $A_{\text{peak}}$  (the amplitude of the peak). In addition to the regional model, additional  $V_{S30}$  data from other sites in Anchorage, including

19 downhole  $V_{S30}$  measurements and 22 microtremor  $V_{S30}$  estimates from others, are used with the strong-motion station  $V_{S30}$  estimates to develop a  $V_{S30}$  contour map of Anchorage. The contouring represents the spatial distribution of the site classes of the local building code, which are based on  $V_{S30}$ . This map may be incorporated into planning documents for future developments in the city.

#### Key Words

Horizontal to Vertical Spectral Ratio, Standard Spectral Ratio, Shear Wave Velocity, Microzonation, Site response

### 7.2 Introduction

Anchorage (USA) is home to approximately half the State of Alaska's population (approximately 300,000 people) and is located in a highly active tectonic setting. Anchorage was devastated by the 1964 Great Alaska Earthquake, which is the world's second-largest earthquake in recorded history, with a moment magnitude ( $M_w$ ) of 9.2 (USGS 2020). More recently, an  $M_w$ 7.1 earthquake struck southcentral Alaska in November 2018, resulting in damage throughout the region, including Anchorage (West et al. 2020). As shown in Figure 7.1, seismicity around Anchorage is attributed to earthquakes originating from several sources including interface and intraslab events (Wesson et al. 2007) related to the subducting Pacific plate diving below the North American plate at a rate of 55mm/yr (Haeussler 2008). There are also several crustal faults within the region (Koehler et al. 2012).

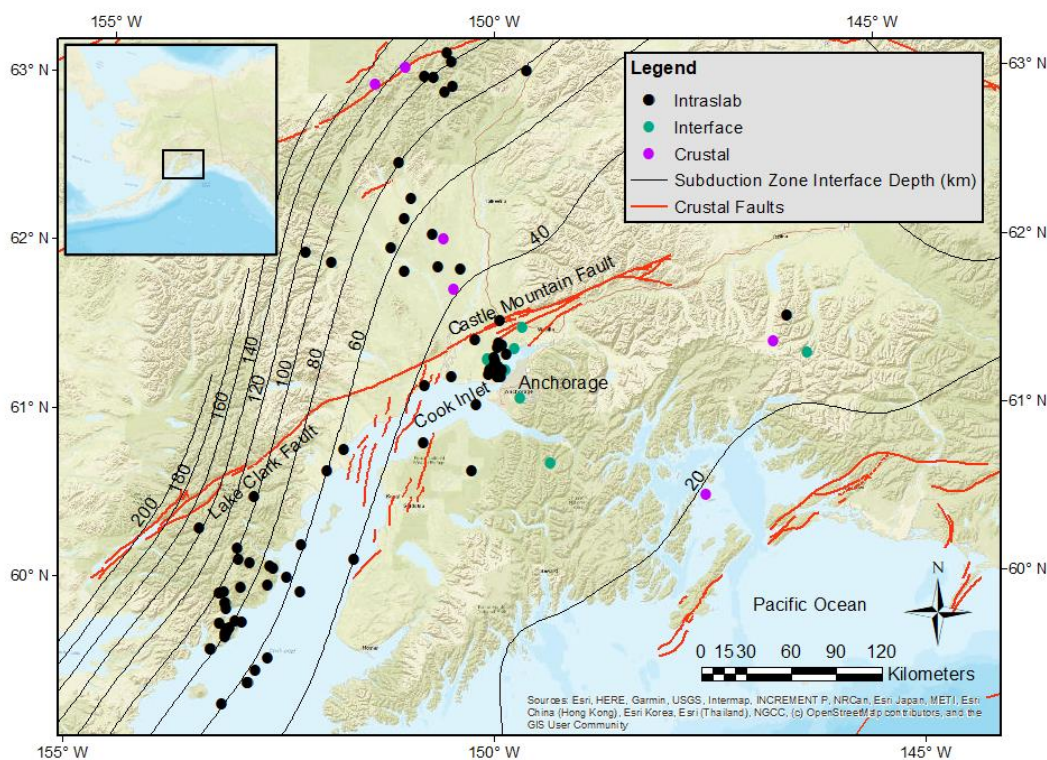


Figure 7.1. Southcentral Alaska’s tectonic setting. The contours indicate the depth of the interface between the subducting Pacific plate and the North American plate and regional crustal faults (Koehler et al. 2021). The earthquake epicentral locations used in this study are shown as circles and have been further divided into intraslab, interface, and crustal events. The inset figure indicates the location in Alaska considered for this study.

Due to frequent earthquakes in the region, numerous strong-motion sensors have been installed in and around Anchorage to better assess ground motion characteristics in the area. Thornley et al. (2021a) have utilized recent recordings from 35 strong-motion stations to evaluate the variability of spectral amplification across Anchorage, using standard spectral ratio (SSR) techniques, defined as Fourier amplitude spectral ratio between each site and a reference site. While analyses using SSR data are useful for site response studies, other methods have also been found to offer efficiencies. A tool that has been found to be effective in estimating site response (Field and Jacob 1995; Bonilla et al. 1997), especially in determining a site’s fundamental frequency of vibration, is the horizontal to vertical spectral ratio (HVSr), where the horizontal ground response from an earthquake ground motion is divided by the vertical response at frequencies of interest.

HVSR analysis is useful in several ways. The results can be used to interpret the soil layering from a velocity perspective (e.g., Ibs-von Seht and Wohlenberg 1999; Castellaro and Mulargia 2009; Mundepe et al. 2009), and the results can provide the fundamental frequency of a site (e.g., Parolai and Richwalski 2004; Zhu et al. 2020). HVSR has also been used to estimate the time-averaged shear-wave velocity in the upper 30m ( $V_{S30}$ ) of a site for engineering applications. For example, the NEHRP site classifications have recently been divided into eight new groups based on  $V_{S30}$  (BSSC 2019), which adds three categories to the previous classification system. These classifications are used to calculate the site amplification based on  $V_{S30}$  in building standards and codes throughout the United States. Table 7.1 provides the  $V_{S30}$  ranges for each of the seismic site classes based on the changes to Table 20.3-1 of the 2020 NEHRP recommendations.

Table 7.1. Seismic Site Classification (modified from BSSC 2019)

Site Class	$V_{S30}$ range (m/s)
A: Hard rock	> 1,500
B: Rock	915 to 1,500
BC: Soft rock	640 to 915
C: Very dense soil and soft rock	440 to 640
CD: Very stiff soil	300 to 440
D: Stiff soil	215 to 300
DE: Soft soil	150 to 215
E: Soft clay soil	< 150

The HVSR are often easier to compute than SSR data because HVSR results do not require a reference-rock site. Therefore, the technique has been adopted widely when carrying out microtremor analysis using surface waves for site characterization in less active tectonic regions. However, it is noted that HVSR data used in this study were calculated using the S-

wave portion of the earthquake records (rather than microtremors) collected at 35 strong-motion stations in Anchorage.

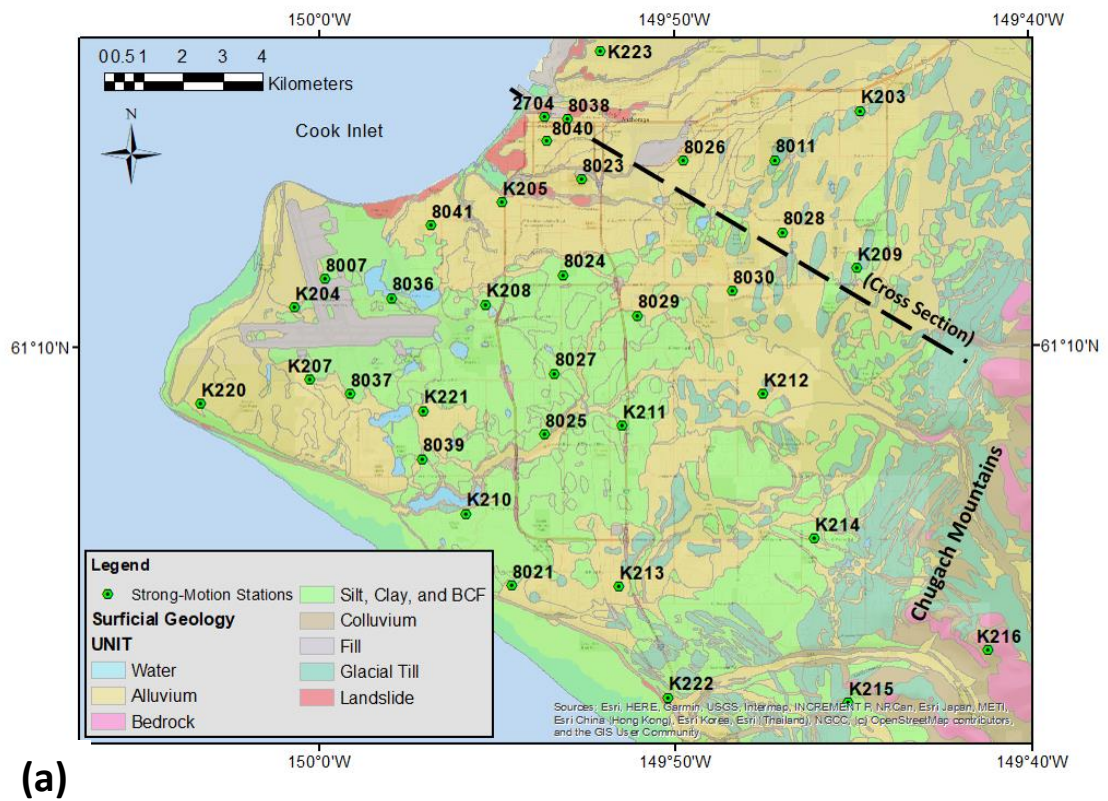
Studies by Nath et al. (1997), Dutta et al. (2001), Biswas et al. (2003), Thornley et al. (2019), and others have utilized a variety of methods to estimate seismic characterization of several sites in the Anchorage basin. Nevertheless, there are still numerous strong-motion station sites in the Anchorage area where deep subsurface information is not available. These studies rely on methods to characterize Anchorage sites using shear-wave velocity, which is a fundamental property of the soil (Hashash 2014). While  $V_{S30}$  is not a physical characteristic of site response (Idriss 2011), it is a common term used in ground motion prediction equations such as NGA-West2 (Boore et al. 2013) and NGA-Subduction (Bozorgnia 2020), and code-based site characterization (ASCE 2017). However, many have cautioned against the use of  $V_{S30}$  to describe deep soil deposits (e.g., Ghofrani and Atkinson 2014). The western portion of Anchorage consists of deeper soil deposits, and in some cases soil deposits that have low shear-wave velocities below 30m depth. Thornley et al. (2019) have shown shear-wave velocities less than 300 m/s deeper than 40m at one site, where the profiling extended below 30m. Considering these deeper deposits were shown to be more effective for site response analyses of this deep soil site in Anchorage. Other areas in Anchorage are likely to fit a model based on an average of more than 30m. The lack of available subsurface data requires consideration of various other methods including HSVR and SSR to estimate  $V_{S30}$ . This is necessary because of the adoption in Anchorage of the International Building Code, which classifies sites based on  $V_{S30}$ .

This article presents the results of the HSVR calculations for the strong-motion sites in Anchorage using a dataset from 2004-2019. Then the study provides a relationship between HSVR results and  $V_{S30}$  and its comparison to several studies from other parts of the world. A

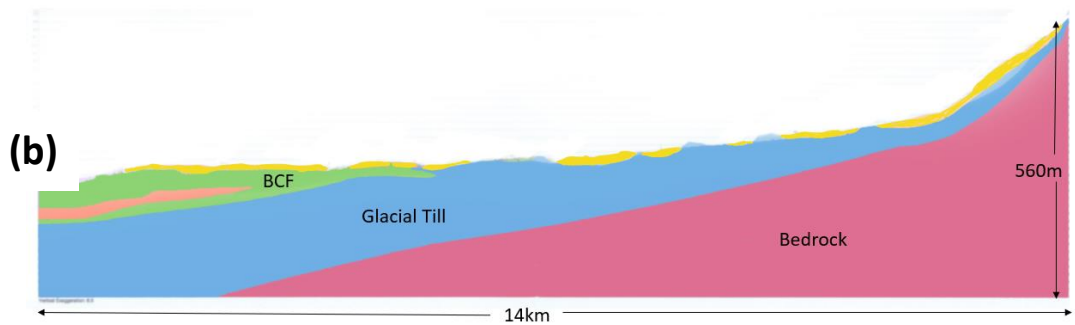
comparison of the HVSR and SSR results for the current dataset is also presented here. As a result of this analysis and the collection of other site-specific shear wave velocity data, a map showing the spatial distribution of  $V_{s30}$  in Anchorage is also presented.

### 7.3 Geology

Anchorage is bounded by the Cook Inlet (Pacific Ocean) on three sides with the Chugach Mountains rising at the eastern flank of the city. The Chugach Mountains, consisting of an accreted and lightly metamorphosed greywacke (Wilson et al. 2012), dip steeply to the northwest. Anchorage has experienced several glacial episodes that have advanced and deposited various materials, from glacial outwash consisting of coarse sand and gravel to glaciolacustrine fine-grained silt and clay, which has created an area of complex geology. A simplified summary of the surficial geology is presented in Figure 7.2a. Sedimentary soil thickness reaches a depth of 500m overlying bedrock at the city's western border (Glass 1988; Combellick 1999; Schmoll and Barnwell 1984). The overlying deposits consist of a range of soils, from dense glacial till with shear-wave velocities greater than 1,000 m/s (Thornley et al. 2019) to soft, cohesive lacustrine soil with shear wave velocities of 150 m/s (Updike and Ulery 1986b). Erosional events related to several glaciation events have affected the thickness and lateral deposition of these different soils (Ulery and Updike 1983; Combellick 1999). The complex geology across Anchorage results in significant variability in ground shaking from earthquakes.



(a)



(b)

Figure 7.2. Strong-motion station locations in Anchorage, Alaska. (a) The generalized surficial geology is provided in the background along with a cross-section location (dashed black line). Notably, the Bootlegger Cove Formation (BCF) is in green. (b) A simplified geologic cross-section depicting the variability of subsurface conditions across Anchorage (modified from Combellick (1999)). Note the vertical exaggeration.

A layer of dense glacial till overlies the dipping bedrock across the city and is near the surface in the eastern portion of the city (Figure 7.2b). Glacial till is overlain by glacial outwash in the northern part of the city. Overlying the glacial till in the central and western portions of the city are varying thicknesses of alluvium. The central soil unit that has a significant impact on ground motions and site response is the Bootlegger Cove Formation (BCF). The BCF was deposited 10,000 to 14,000 years ago over multiple glacial episodes in



the region and has several facies of varying stiffness and makeup, including sand, silt, and clay (Ulery and Updike 1983). One of the more sensitive clay facies was responsible for the 1964 Great Alaska Earthquake's significant ground failures. These failures included significant slope failures (Hansen 1965) and the formation of grabens (Shannon & Wilson 1964). A ground failure susceptibility map of the city, focused primarily on the anticipated effects of the BCF from future earthquakes, as published by Harding-Lawson Associates (1979). The BCF is generally centered in the city's middle portion with the more sensitive clay facies located in the north. The BCF is overlain by silt and sand in the south, depicted by fine-grained (silt and clay) and alluvial soil in Fig. 2a (Updike and Ulery 1986; Combellick 1999; Schmoll and Dobrovolny 1972). There is also some fill soil, such as in the western portion of the city at the Ted Stevens Anchorage International Airport, which is anthropogenic in nature.

#### 7.4 Strong-Motion Stations and Dataset

Many strong-motion stations have been installed in south-central Alaska since the Great Alaska Earthquake in 1964. The current study utilizes strong-motion records of 95 earthquakes (locations shown in Figure 7.1) measured at 35 stations across Anchorage (Figure 7.2a). Appendix A-1 provides the locations of the strong-motion stations and Appendix A-2 provides the epicentral locations, depths, and magnitudes of the events used. The stations are primarily Kinematics force-balanced accelerometers with sampling rates of 200 Hz. The stations are set to record continuously. The stations are monitored by the Alaska Earthquake Center (AEC).

The dataset used in this study is described in considerable detail by Thornley et al. (2021a). A total of 1,727 three-component recordings are used in the HVSr analysis. These records were collected between 2004 and 2019 and include the November 30, 2018,  $M_w$ 7.1 Anchorage Earthquake. A large majority of the data was provided by AEC, with the Delaney

Park Downhole Array (DPDA) data from the University of California, Santa Barbara (<http://www.nees.ucsb.edu/>), and some additional records from IRIS (<https://www.iris.edu/hq/>).

As mentioned in the introduction, there are three primary sources of earthquakes in the region. These include crustal, intraslab, and interface earthquakes, with the latter two being related to the subducting North American plate. The magnitude-epicentral distance relationship of the events used in this study is shown in Figure 7.3. Additional information related to processing is presented in Chapter 3.

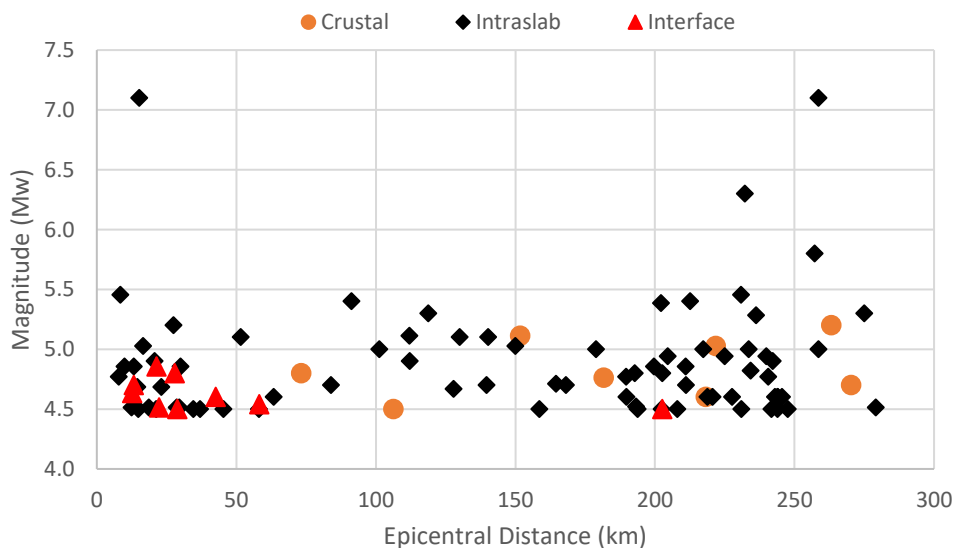


Figure 7.3. Epicentral distances of the 95 events used in this study to central Anchorage versus magnitude with crustal, intraslab, and interface events identified. Distances are calculated from Station 8040 (Figure 7.1) located in downtown Anchorage (location presented in Appendix A-1).

### 7.5 HVSR Analysis

The earthquake records selected for this study were analyzed using the GITANES program in MATLAB, which was developed by Klin (2019). The program utilizes the generalized inversion technique (GIT) to produce SSRs, where the stations are compared to a reference site. In this case, the reference site was the K216 rock site in southeast Anchorage (Figure 7.2a). In

addition to the SSR results, GITANES calculated the HVSR receiver function results from each station's input earthquake time histories. In Thornley et al. (2021a), the GIT approach is used to evaluate the variability of site response at 1 Hz and 5 Hz across Anchorage. In that study, little attention is paid to the ability of SSR to evaluate site response through estimates of  $V_{S30}$ . In GITANES, the logarithmic mean of the Fourier amplitude spectra (FAS) of the two horizontal components is divided by the FAS of the vertical component for each frequency of interest. This method is preferred to the pseudo-spectral acceleration ratio method by Zhu et al. (2020) because it avoids potential bias at sites with multiple peaks. The standard error is also calculated when several time histories are included for a station. In this study, the HVSR was calculated for each station over the 0.25 to 10 Hz frequency range, which provides for the fundamental frequencies of buildings and infrastructure typical in Anchorage. The HVSR results for each station are presented in Appendix A-4.

Because HVSR and SSR data provide overlapping information regarding a site, including the fundamental frequency and insight into site amplification, a comparison of the two datasets is presented in this study. It should be noted that HVSR data can be used to estimate the frequencies where site amplification occurs, but in many cases, there is no clear indication of the amplitude of the ground amplification (Field and Jacob 1995), which is why SSR results derived from GIT or other means are often preferred.

The use of HVSR starts with the selection of the frequency where the peak amplification occurs, identified as  $f_{\text{peak}}$  throughout this study. Another term that is of importance is  $A_{\text{peak}}$ , defined as the amplitude corresponding to  $f_{\text{peak}}$ . Often this is recognized as the first peak (Ghofrani and Atkinson 2014) but has also been identified as the point where the highest peak is observed Hassani and Atkinson (2016), which may not be the first peak. The following three examples demonstrate the situations that may lead to different peaks being selected.

In the case of Figure 7.4a, there is a clear peak, while in Figure 7.4b the highest peak is not the first peak. The third case is where there is no clear highest peak, as shown in Figure 7.4c. Studies including Zhu et al. (2020) have evaluated the selection of peaks and found the highest peak is preferred to the first peak in characterizing site resonant frequencies. In this study, the highest peak is selected and used as  $f_{\text{peak}}$ .

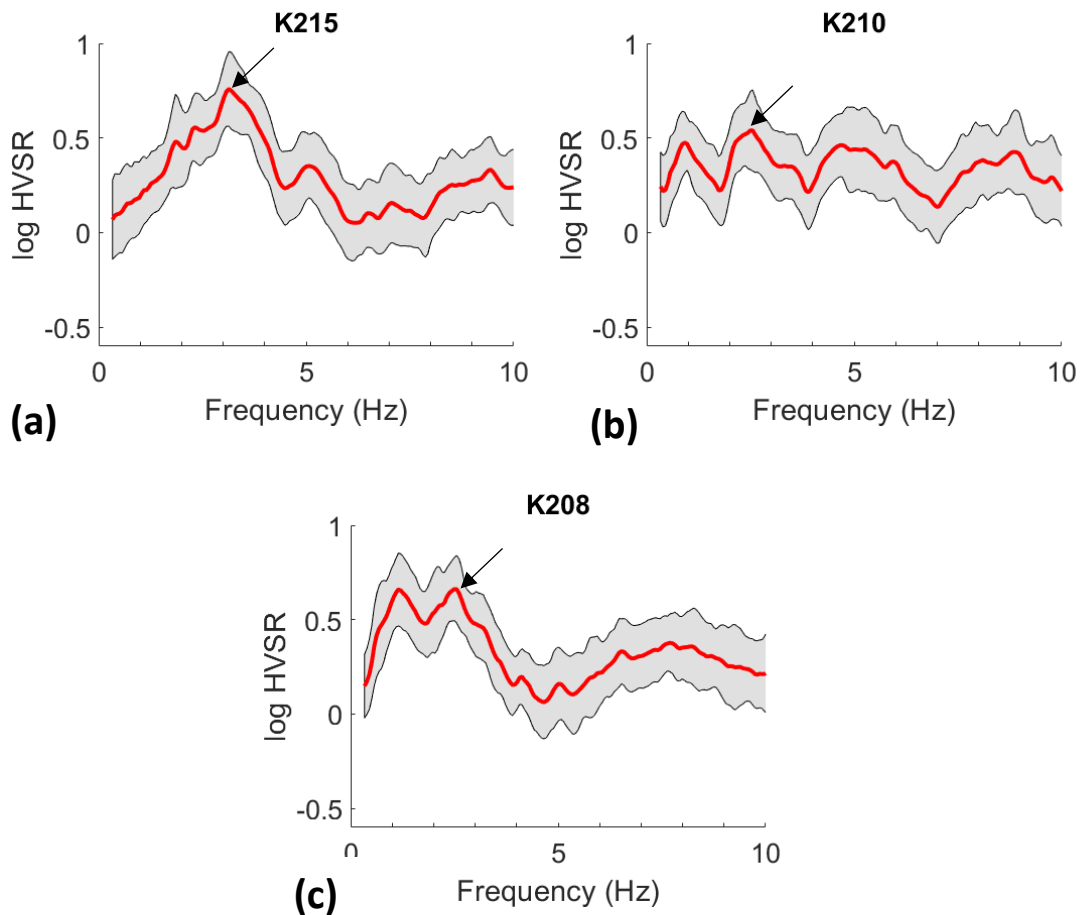


Figure 7.4. HVSR data presenting three conditions where the selected peak may vary. (a) shows a single peak where the peak frequency is approximately 3Hz. (b) shows multiple peaks where the second peak is the highest peak. (c) shows double peaks where there are two peaks, and the amplitude of the highest peak is not much different from the amplitude of the second peak. Arrows indicate selected peaks.

## 7.6 Evaluation of $V_{S30}$ by HVSR (an evaluation of several methods)

One of the main challenges with the Anchorage strong-motion network is the lack of subsurface characterization at many recording sites. Few sites have geotechnical data

deeper than 10m, either at the site or nearby. This lack of information supports the need for studies like this to better estimate site characteristics and better understand the observed site response in Anchorage.

The  $V_{S30}$  for several strong-motion sites in Anchorage has been measured. Of the 35 stations evaluated in this study, 16 stations have an estimate of  $V_{S30}$ , 15 include surface measurements and only one has a downhole  $V_s$  profile. In Dutta et al. (2000) 15 strong-motion sites that are included in this study were evaluated using Rayleigh waves from an electromagnetic vibrator and  $V_{S30}$  was estimated. As mentioned previously, Thornley et al. (2019) performed downhole testing at the DPDA to measure the time-averaged shear-wave velocity profile to a depth of 60m below ground surface. The  $V_{S30}$  measurements for these stations are included in Appendix A-1.

The use of  $f_{peak}$  from HVSr data to estimate  $V_{S30}$  for a site has been proposed in several studies, including regional studies using data from NGA-West2 and Japan (Ghofrani and Atkinson 2014), central and eastern portions of the United States (CEUS) by Hassani and Atkinson (2016), and the study by Yaghmaei-Sabegh and Hassani (2020) identified throughout this paper as the “Iran” study, among others. The study presented by Hassani and Atkinson (2016) is focused on the CEUS where soft soils overlay hard bedrock. The eastern portion of Anchorage has some similarities to CEUS sites, where the loose sand and gravel overlies dense glacial till which can have shear-wave velocities greater than 1,000 m/s (Thornley et al. 2019). Because the  $V_s$  of these geologic units is greater than 760 m/s it is considered to be engineering bedrock from a shear-wave velocity perspective (ASCE 2017). Figure 7.5 presents the above-referenced models comparing  $f_{peak}$  from the HVSr data to measured  $V_{S30}$  for the stations shown in Appendix A-1.

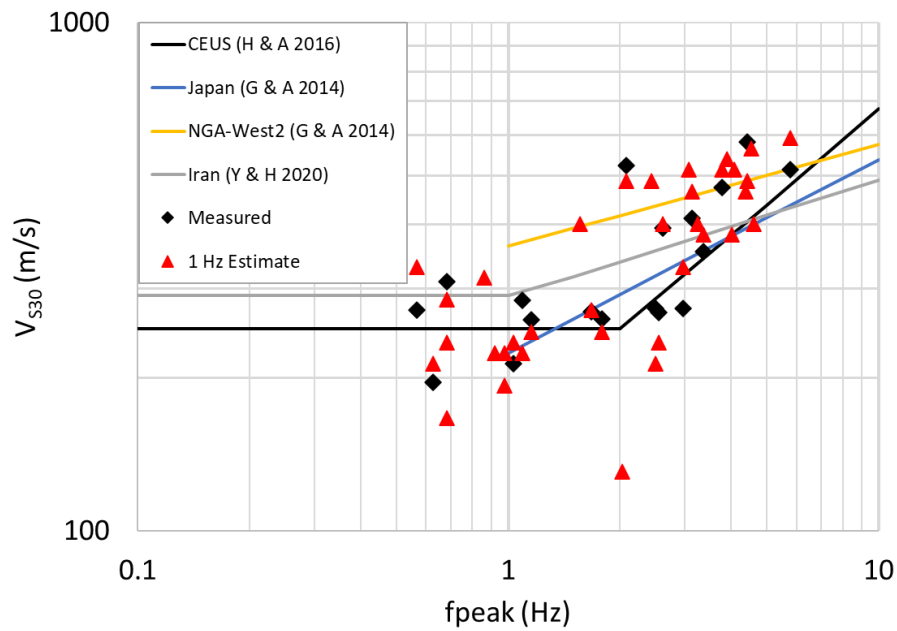


Figure 7.5.  $V_{S30}$  data for several strong-motion stations in Anchorage and the HVS  $f_{peaks}$  for those sites plotted with models from four different studies. The black diamonds represent measured  $V_{S30}$  data and the red triangles (“1 Hz Estimate”) represent the results from an SSR estimate of  $V_{S30}$  (introduced subsequently). NGA-West2 and Japan models are only applicable from 1 to 10 Hz.

Locally, Dutta et al. (2003) created a relationship between the SSR at 1 Hz and  $V_{S30}$ . To evaluate this relationship for the current dataset the logarithmic band-averaged SSR results for 1 Hz from Thornley et al. (2021a) have been used. The SSR results were calculated using the Fourier amplitude spectral ratios at each station with respect to the reference station, which is consistent with Dutta et al. (2003). The logarithmic band-averaged results cover the 0.5 to 2.5 Hz frequency range of HVS and SSR. It is observed that both studies yield similar results with independent datasets (Figure 7.6).

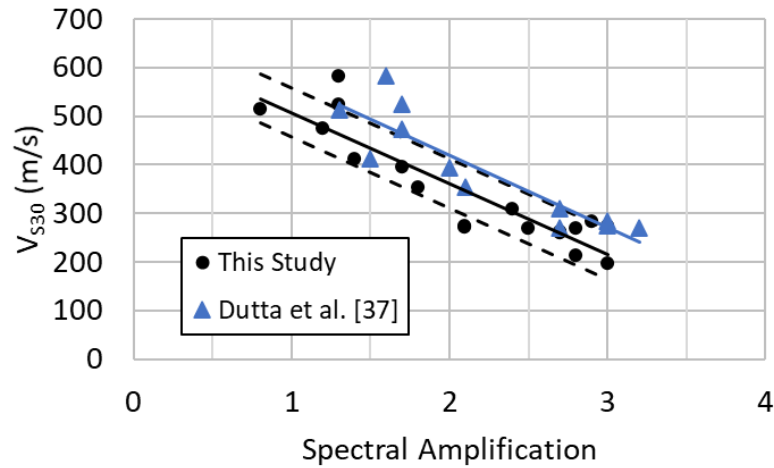


Figure 7.6. Plot of the relationship between 1 Hz logarithmic band-averaged spectral amplification and measured  $V_{s30}$  profiles. The SSR values plotted for this study are from the results presented in Thornley et al. (2021a). The dashed black lines present  $\pm 1$  standard deviation for the data used in this study.

The relationship between  $V_{s30}$  and SSR at 1Hz is shown in the following equation obtained using least-squares regression:

$$V_{s30} = -145.9 (\pm 17.1)(SSR_{1Hz}) + 652.9 (\pm 38.4) \quad (\text{Equation 7.1})$$

where  $SSR_{1Hz}$  is the spectral amplification of the logarithmic band average about 1Hz. The model standard deviation is 50.4.

The 1 Hz band-averaged range is lower than the  $f_{peak}$  for the stiffer sites (Appendix A-1). In Anchorage, the sites with higher shear-wave velocity are located on the east side of the city and have estimated depths to engineering bedrock of less than 30m (Combellick 1999). When comparing the SSR results presented by Thornley et al. (2021a) and HVSR results, it is observed that the amplitudes across the frequencies of interest tend to overlap more for sites in central and western Anchorage (Figure 7.7). A comparison of the HVSR and SSR plots for each station is included in Appendix A-4. For sites in the eastern portion of the city, where the depth to engineering bedrock is shallower, the frequency peaks are generally well aligned between the SSR and HVSR data. Still, the amplitudes of the HVSR curves tend to be higher within most of the 0.25 to 10 Hz range. SSR peak amplitudes range from 8% higher to 99%

lower than  $A_{\text{peak}}$  values with an average of 25% lower (standard deviation of 29%). The stiffer sites such as K212 and K214 appear to have higher SSR peak amplitudes while the softer sites appear to have higher  $A_{\text{peak}}$  values.

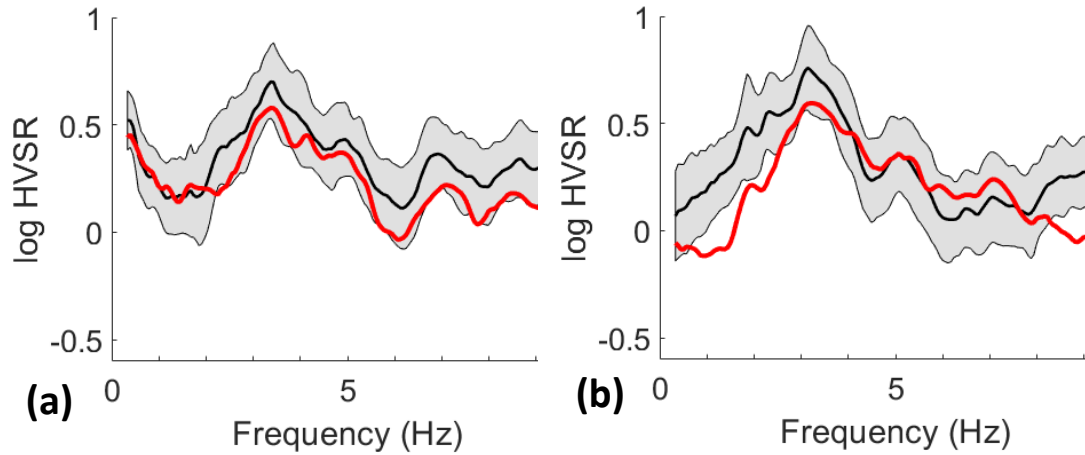


Figure 7.7. HVSR (black line and grey shaded area is standard error range) and SSR (red line) plots of a station in (a) central Anchorage (K213) and (b) a site in eastern Anchorage (K215). To further evaluate the relationship between HVSR and SSR the logarithmic band-averaged 1 Hz (0.5 to 2.5 Hz) and 5 Hz (4 to 6.5 Hz) values have been calculated and compared. The comparison utilizes a Bland-Altman difference plot (Bland and Altman 1986) where the x-axis is the average of the two models and y-axis is the difference between the two models as summarized by the following relationship:

$$M(x, y) = \left( \frac{M_1 + M_2}{2}, M_1 - M_2 \right) \quad (\text{Equation 7.2})$$

where  $M_1$  and  $M_2$  are the HVSR and SSR band-averaged values, respectively, for the frequencies of interest. Figure 7.8 presents the plots of the function  $M(x, y)$  for two different frequencies (1 and 5 Hz) color-coded for corresponding  $V_{S30}$  ranges presented in Table 7.1. Points that plot closer to zero on the y-axis indicate a better fit between models. The median and  $\pm$  one standard deviation values for the full dataset are included. In general, the sites with  $V_{S30}$  of less than 300 m/s appear to lead to a better fit between models for both 1 Hz and 5 Hz band-averages.



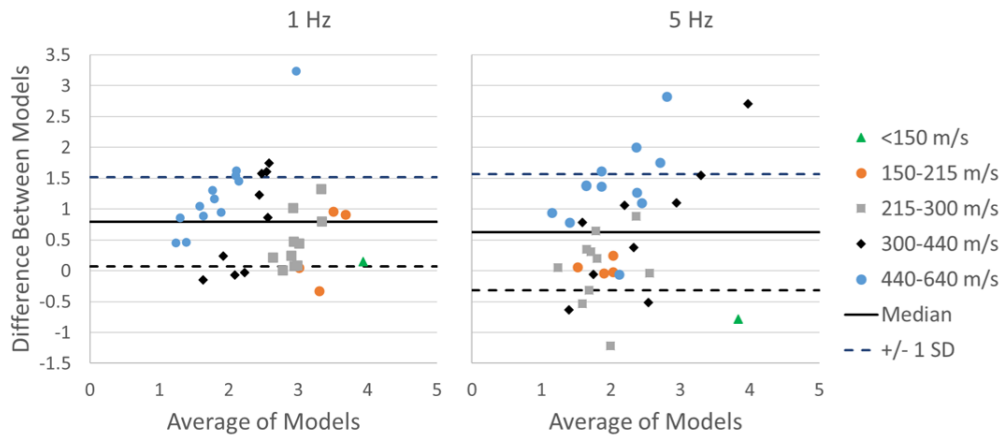


Figure 7.8. Comparison between band-averaged SSR and band-averaged HVSr data at 1 and 5 Hz using a Bland-Altman difference plot for Anchorage data for the 35 stations in this study. The median and  $\pm$  one standard deviation range of the dataset are shown as solid and dashed lines, respectively.

### 7.7 Relationship Between $V_{s30}$ and HVSr

As noted above, several models may be used to estimate  $V_{s30}$  at strong-motion sites using either SSR or HVSr from earthquake records. The HVSr-based  $V_{s30}$  models by others presented in Figure 7.5 show significant variability. These models have been developed from independent datasets for different tectonic regions. The CEUS model is for a relatively quiet tectonic region of the United States (Dutta et al. 2003), particularly when compared to south-central Alaska. As noted previously, some similarities related to soil depth over stiffer material make the CEUS model useful in eastern Anchorage where the  $V_{s30}$  estimates are higher. Visual inspection of Figure 7.5 suggests that the slope of the CEUS model at  $f_{peak}$  frequencies greater than 2 Hz tends to match the Anchorage data better than the other three models. To select the most appropriate model for estimating  $V_{s30}$  using HVSr data at strong-motion stations in Anchorage, a comparison is performed between the HVSr-based models (shown graphically in Figure 7-5) and the band-averaged SSR model (Figure 7.6). Figure 7.9 presents the comparisons between the SSR model presented in Figure 7.5 (red triangles) and the CEUS, Iran, Japan, and NGA-West2 models. A Bland-Altman difference plot described in Equation 7.2 is used to explore the differences.

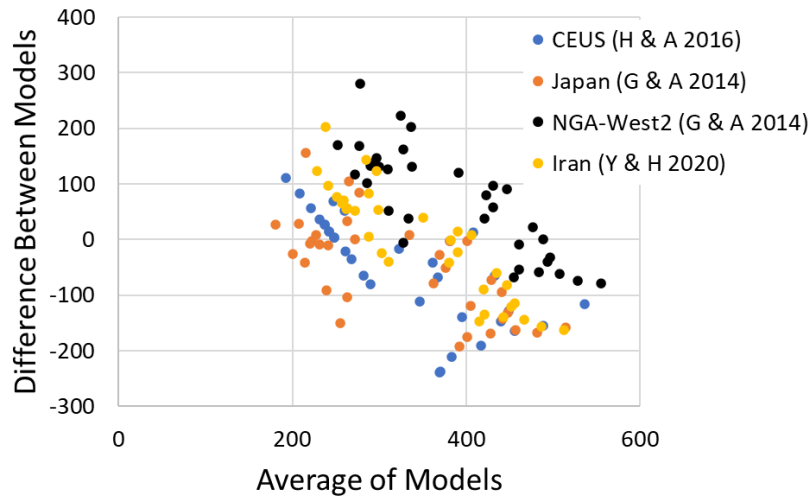


Figure 7.9. Comparison of  $V_{S30}$  results for the 1 Hz band-averaged SSR and four HVSR-based models. (a) CEUS model, (b) Iran model, (c) Japan model, and (d) NGA-West2 model.

Several observations for Anchorage can be made based on the results presented in Figure 7.9. The CEUS and Japan models tend to underpredict  $V_{S30}$  when compared to the 1 Hz band-averaged SSR model. The Iran model tends to overpredict lower  $V_{S30}$  values, which is partially a function of the lower bound of the model set to 290 m/s for  $f_{peaks}$  less than 1 Hz. The Iran model also tends to underpredict higher  $V_{S30}$  values. While the NGA-West2 model matches higher  $V_{S30}$  values more closely, there is a general overprediction of lower  $V_{S30}$  values than the 1 Hz band-averaged SSR model. These observations suggest that the other regional models considered are not as effective as the SSR model for estimating  $V_{S30}$  in Anchorage.

### 7.8 Comparison of $f_{peak}$ and $A_{peak}$ $V_{S30}$ relationships to global models

Ghofrani and Atkinson (2014) present a relationship between  $V_{S30}$  and  $f_{peak}$ . In that study, there was also a relationship presented between the peak amplitude of the H/V data and  $V_{S30}$ . While the Anchorage  $V_{S30}$  data at strong-motion stations are limited, the  $V_{S30}$  estimates developed from the 1 Hz SSR estimates can be used in conjunction with the  $f_{peak}$  and  $A_{peak}$

HVSR results to further evaluate the appropriateness of the model when compared to global estimates.

In Ghofrani and Atkinson (2014) the NGA-West2 dataset is used to develop the following equations:

$$\log(V_{S30}) = 0.20 \log(f_{peak}) + 2.56 \text{ for } f_{peak} \geq 1\text{Hz} \quad (\text{Equation 7.3})$$

and

$$\log(V_{S30}) = -0.46 \log(A_{peak}) + 2.86 \quad (\text{Equation 7.4})$$

with  $\pm$  one standard deviation estimates of 0.16 and 0.15 log units for  $f_{peak}$  and  $A_{peak}$ , respectively. The  $V_{S30}$  estimates based on the 1 Hz spectral amplitude model, along with HVSR  $f_{peak}$  and  $A_{peak}$  results have been used to estimate local relationships between estimated  $V_{S30}$  and the HVSR  $f_{peak}$  and  $A_{peak}$  values. Figure 7.10 presents the Anchorage data and provides a comparison with the NGA-West2 dataset. The relationship developed in the NGA-West2 study had a lower bound for  $f_{peak}$  of 1 Hz. The current study utilizes data below 1 Hz because there is no strong indication that 1 Hz was the appropriate cutoff.

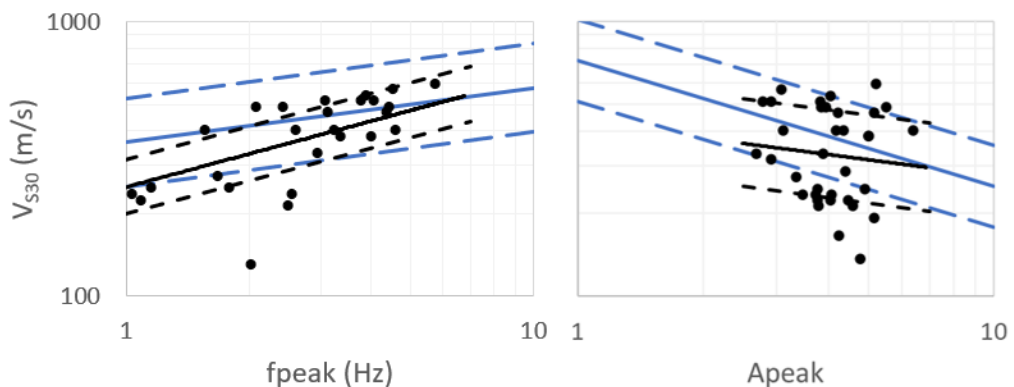


Figure 7.10. Estimated  $V_{S30}$  relationship with HVSR  $f_{peak}$  and  $A_{peak}$  results, black circles. The regression line (solid black line with  $\pm$  one standard deviation in black dashed lines) shows that the results generally fit within the median  $\pm$  one standard deviation (blue solid and dashed lines, respectively) for the NGA-West2 dataset, as presented in Figure 7-8 of Ghofrani and Atkinson (2014).

The resulting equations (Equations 7.5 and 7.6) have been developed to describe the estimated  $V_{S30}$  for Anchorage from HVSR  $f_{peak}$  and  $A_{peak}$  values:

$$\log(V_{S30}) = (0.40 \pm 0.03) \log(f_{peak}) + (2.40 \pm 0.09) \quad (\text{Equation 7.5})$$

and

$$\log(V_{S30}) = -(0.20 \pm 0.08) \log(A_{peak}) + (2.64 \pm 0.3) \quad (\text{Equation 7.6})$$

The following relationship is developed through multivariate linear regression to estimate  $V_{S30}$  with both  $f_{peak}$  and  $A_{peak}$ :

$$\log(V_{S30}) = (0.37 \pm 0.04) \log(f_{peak}) - (0.36 \pm 0.1) \log(A_{peak}) + (2.72 \pm 0.2)$$

(Equation 7.7)

The standard deviations for Equations 7.5 through 7.7 are 0.10, 0.16, and 0.09 log units, respectively. Equations 7.5 and 7.7 are only valid for values of  $f_{peak} \geq 1$  Hz. The results of the relationship between the estimated  $V_{S30}$  and HVSR values for  $f_{peak}$  and  $A_{peak}$  are generally similar to the NGA-West2 dataset, especially at higher  $V_{S30}$ . However, the slope of  $f_{peak}$  with  $V_{S30}$  is steeper than the NGA-West2 slope. This result agrees well with the visual observation that can be made in Figure 7.5. While it does not appear to be particularly strong due to the wide spread of data points, the relationship with  $A_{peak}$  is similar to the NGA-West2 dataset but with the slope of the current dataset being flatter than the NGA-West2 trend. These results suggest that as the  $V_{S30}$  increases, the  $f_{peak}$  increases at a higher rate indicating that the underlying glacial till in the eastern portion of Anchorage has a high shear-wave velocity, which is in better agreement with the CEUS model presented in Figure 7.5. However, the shallow slope of the trendline of the  $A_{peak}$  relationship suggests that the amplitude of the HVSR results does not reduce as quickly, indicating that  $A_{peak}$  may not be as sensitive an indicator of  $V_{S30}$  in Anchorage as it is in other regions.

## 7.9 $V_{S30}$ Map of Anchorage

The subsurface geology of Anchorage is complex and varies significantly, especially from east to west. One indicator of this variability is  $V_{S30}$  at the strong-motion stations, which represent 35 locations where  $V_{S30}$  can be estimated, based on the models presented above. In addition to these data points, we have also collected  $V_{S30}$  estimates from public and private projects across Anchorage to provide a higher density of data points. The private projects represent a large collection of downhole  $V_{S30}$  estimates, which are presented as black triangles in Figure 7.10, but are not publicly available, except for Thornley et al. (2019). Additionally, Dutta et al. (2000) performed  $V_{S30}$  assessments at several additional locations that were collocated with current and previous strong-motion stations and other selected locations. These data were not used in the development of the correlations above because the strong-motion stations had been dismantled did not record events used in this study. The compilation of these data provides more than 70 discrete locations where  $V_{S30}$  has been estimated in Anchorage. A contour map showing the variability of  $V_{S30}$  across Anchorage is presented in Figure 7.11. The  $V_{S30}$  values used at the strong-motion stations have been calculated utilizing the SSR relationship illustrated in Figure 7.6 and are included in Appendix A-1. Additional sites presented by Dutta et al. (2000) are provided in Appendix A-5. When comparing this map to that of Dutta et al. (2003) there is a general trend moving from east to west that is the same on both maps. However, with an additional 34 locations where  $V_{S30}$  has been estimated, additional granularity is developed by the newer map. This is especially evident in areas where  $V_{S30}$  estimates are less than 215m/s, which agree with the local geologic conditions, and are discussed further below.

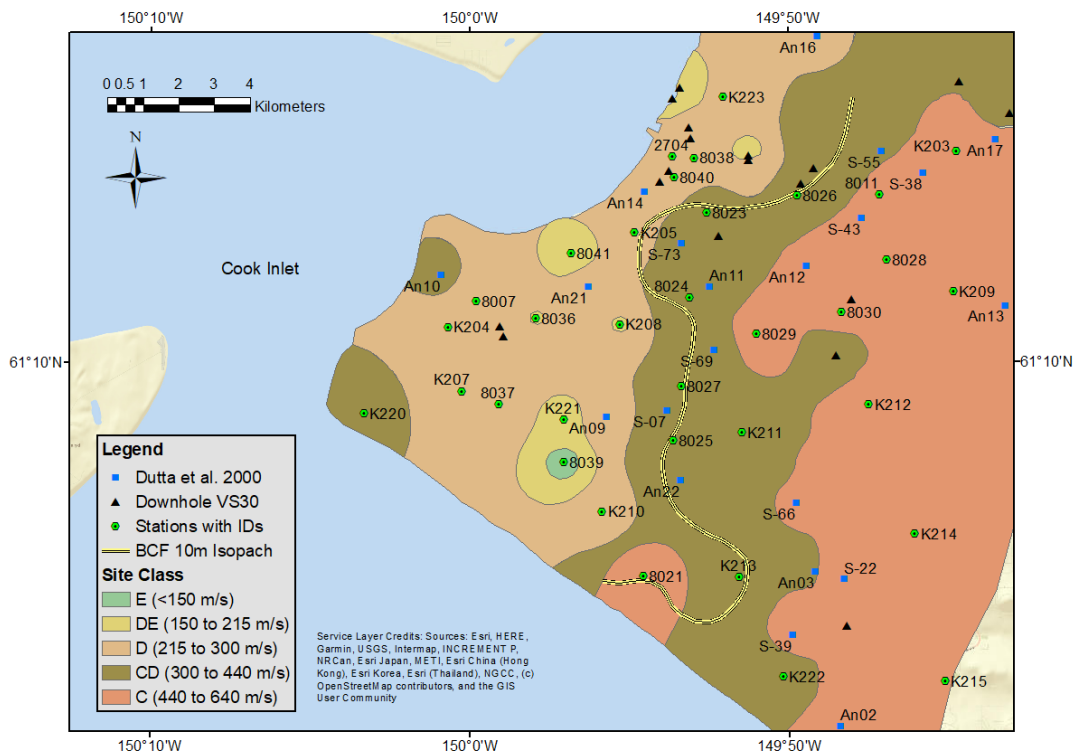


Figure 7.11. Contour map of BSSC (2019) Seismic Site Class, based on  $V_{S30}$  estimates at strong-motion stations and measurements at other locations across Anchorage.

The contour lines used for Figure 7.11 have been calculated utilizing the inverse distance weighting to a power gridding method in Surfer (version 17.1.288) from Golden Software, LLC (goldensoftware.com) with a power exponent of three and no smoothing. The site classes are those in the revised seismic site classifications presented in the 2020 National Earthquake Hazard Reduction Program (NEHRP) guidelines by BSSC (2019). Site classes have been color-coded in Figure 7.11, identifying areas expected to have similar  $V_{S30}$ . This contour map may be useful for planning within Anchorage and could be used as the first estimate of seismic site classification when planning geotechnical investigations. As expected, the stiffer soil with higher site classes is found on the east side of Anchorage. The interface between site class C soil and the stiffer BC and B sites (Table 7.1) to the east has not been estimated due to a lack of information other than surficial geology. Still, this area on the east side of Anchorage is much less inhabited and is typically reserved as parkland.

There is a clear area just west of the site class C zone that can be defined as a site class CD. This zone indicates a transition between the glacial tills to the east and the BCF soils in central and western Anchorage. Site class D regions agree well with regions of deeper BCF soil [Ulery and Updike 1983; Updike and Ulery 1986b; Combellick 1999]. There are two zones of site class D/E in western Anchorage (i.e., at Stations 8039 and 8041). These areas are indicative of deeper, and softer soil areas, as also described by Updike and Ulery (1986b). In these two regions there are deeper pockets of BCF silts and clays. The results from this study suggest that deeper BCF deposits indicate a softer site class as well. At the western edge of Anchorage, the site class increases to site class CD, which is in general agreement with other studies showing that the western edge, despite having deep soil deposits, is generally stiffer than the middle portions of Anchorage. This area is also at the western fringe of the BCF, with only thin pockets of soft soil.

As mentioned previously, one of the assumptions for using  $f_{peak}$  as an indicator of  $V_{S30}$  is that the shear-wave velocity increases with depth. Station 8040, located in northern Anchorage, was found by Thornley et al. (2019) to have BCF soil to depths greater than 40m with higher shear-wave velocity overlying zones of soil with lower shear-wave velocity and then increasing again. The estimates of  $V_{S30}$  and the measured  $V_{S30}$  show general agreement and the site is classified as a site class D in both cases. Strong-motion stations 8039 and 8041 indicate areas of lower  $V_{S30}$ , and it is possible that the surficial soil has a higher shear-wave velocity than the BCF deposits at depth, indicating that  $f_{peak}$  or SSR methods may not provide an adequate estimate of  $V_{S30}$  in these areas. Additional study at these sites is necessary to understand the impact of this potential velocity inversion on  $f_{peak}$  and other HVSr parameters. This may also be important for other areas in the city where deeper soil deposits, significantly deeper BCF deposits, are encountered. Figure 7.11 presents regions where similar shear wave velocity is estimated. There is likely to be additional variability,

related to the geologic variability and the built environment that may shift or modify the site class boundaries. Further study will help define the lateral changes in  $V_{S30}$  across Anchorage. However, because  $V_{S30}$  is an important parameter in site response analysis for engineering design when using the building code, this map provides the most up-to-date estimate of the variability of  $V_{S30}$  across Anchorage. It should be noted that it does not attempt to identify sites where liquefaction may occur (i.e., site class F) so proper site characterization of the near surface is still required for future developments.

### 7.10 Concluding Remarks

Anchorage, Alaska, is situated in an active tectonic region experiencing both crustal and subduction earthquakes. Earthquake records from 35 strong-motion stations have been utilized to evaluate relationships between HVSr and site response, especially the site maximum peak frequency and its relationship to  $V_{S30}$ . Two regional relationships have been established including one between  $f_{peak}$ ,  $A_{peak}$ , and  $V_{S30}$  and a second relationship between SSR and  $V_{S30}$  (Figure 7.6), which can be utilized for future studies in the region.

In addition to the HVSr relationship, a  $V_{S30}$  contour map of Anchorage indicating estimated seismic site classes for all locations has been developed. This map can be utilized by planners and engineers as it can be used to provide first-order estimates of earthquake site amplification within Anchorage. There are areas within the confines of the map that lack data, such as the eastern edge where the site class boundary between site class C and site class BC has not been established, despite the likelihood of shallow bedrock. There are additional areas in western Anchorage where further study may validate the relationship between the geologic conditions and  $V_{S30}$ . As noted throughout the text, there are limitations with the use of  $V_{S30}$  to estimate site response. Further study is needed to evaluate methods that may be more dependable for site response characterization in deeper and more variable



soil deposits. Additionally, the findings presented here can be further improved in the future through the incorporation of uncertainties related to the data and methodologies used. This uncertainty should address the different techniques used in collecting measured  $V_{S30}$  data and the uncertainties captured in the analysis. The  $V_{S30}$  map will have blended edges between the  $V_{S30}$  ranges presented in Figure 7.11 as a result rather than the hard lines between the different site classes.

## 8.0 Engineering Site Response Analysis of Anchorage, Alaska Using Site Amplifications and Random Vibration Theory

John Thornley, John Douglas, Utpal Dutta, and Zhaohui (Joey) Yang

*Earthquake Spectra (In review)*

One of the main issues with the Anchorage strong-motion dataset is that it consists primarily of low-intensity ground motions, not allowing for direct accountability of nonlinear soil behavior. The following presents a methodology to use Fourier spectral amplification results to calculate engineering response spectra and account for nonlinear site effects.

### 8.1 Abstract

Earthquake records collected at dense arrays of strong-motion stations are often utilized in microzonation studies to evaluate the changes in site response due to variability in site conditions across a region. These studies typically begin with calculating Fourier spectral amplification and then transition to performing engineering site response analyses. It has proven difficult to utilize Fourier spectral amplification to define the appropriate elastic response spectrum for a site or sites. This is because the ground motions recorded at these strong-motion stations have lower intensity and do not show the nonlinear site effects observed during higher-intensity earthquakes and because Fourier and response spectral amplitudes measure different aspects of ground motions. The strong-motion stations in Anchorage, Alaska have been recording earthquakes in the region for the last three decades. This study utilizes a database of 95 events from 2004 to 2019 to calculate Fourier spectral amplifications at 35 stations using the generalized inversion technique (GIT). Estimated response spectra have been evaluated at each site by applying those Fourier spectral amplifications to a response spectrum of a reference station through random vibration

theory (RVT). Correction factors are also applied within the approach to account for nonlinear site effects. This RVT-based approach is tested using ground motions recorded during the M7.1 2018 Anchorage Earthquake and close matches between measured and predicted response spectra are found. The method is then compared to site response analyses using a calibrated 1D equivalent linear (EQL) model of the Delaney Park Downhole Array site. Estimated spectra using the RVT-based approach are, finally, compared to those using NGA-Subduction and NGA-West2 ground-motion models. The proposed method provides a coherent and straightforward way to use GIT-derived Fourier spectral amplifications to directly estimate site-specific response spectra, accounting for nonlinear site effects without requiring engineering characterization of subsurface soil conditions.

Key words: Earthquake site response analysis, random vibration theory, spectral amplification, microzonation

## 8.2 Introduction

The city of Anchorage, located in southcentral Alaska, is Alaska's most populous city, with approximately half of the State's population. Southcentral Alaska is situated in a very active tectonic region near the edges of the North American and the subducting Pacific plates. This region was significantly impacted by the 1964 Moment Magnitude ( $M_w$ ) 9.2 Great Alaska Earthquake (Hansen 1965), the second-largest earthquake on record (USGS 2020). Since the 1970s strong-motion sensors have been installed for a better understanding of ground-motion variability across Anchorage. Several studies have performed site-response analyses in the frequency domain through methods such as standard spectral ratio (SSR) and horizontal to vertical spectral ratio (HVSr) (see, e.g., Borchardt 1970 and Ghofrani and Atkinson 2014, for a discussion of these techniques) using the recorded ground motions at strong-motion stations. However, many of these stations have not been appropriately

characterized through subsurface soil studies. Fourier amplitude spectra (FAS) of the recorded ground motions are used to compute SSR and HVSR. Although newer ground motion models and other tools are utilizing FAS more (e.g., Bayless and Abrahamson 2019), engineers often prefer response spectra, rather than FAS, because it better predicts building and other structural responses. This article aims to provide a methodology to utilize the results from spectral amplification studies, even from those that primarily consist of low-magnitude earthquakes, to estimate site response spectra that accounts for nonlinear soil behavior without requiring detailed soil characterization. This will allow the engineering community to utilize, more efficiently, years of measured ground motions to understand engineering site response, especially at sites with poorly characterized soil conditions.

The following sections begin by presenting the tectonic setting and geologic conditions in Anchorage, followed by a description of the strong-motion dataset used in this study. A brief description of the time-history processing and Fourier spectral amplification analysis of the dataset is provided. Then the methodology to calculate site response spectra utilizing Fourier spectral amplification results, combined with random vibration theory (RVT), is described. Several examples of its use are then presented and evaluated, with a final discussion on other potential applications.

### 8.3 Tectonic Setting and Seismicity

Alaska is situated in one of the most tectonically active regions globally with, for example, the Alaska Earthquake Center (AEC) recording more than 54,000 earthquakes across the state in 2018 (AEC 2021), including the  $M_w$ 7.1 Anchorage Earthquake (locations shown on Figure 8.1). Anchorage sits at the edge of the North American plate, where the Pacific plate converges at a rate of 55 mm/year (Haeussler 2008). This region, known as the Alaska-

Aleutian megathrust, experiences, on average, an M7 or greater earthquake every 11 years (West et al. 2020).

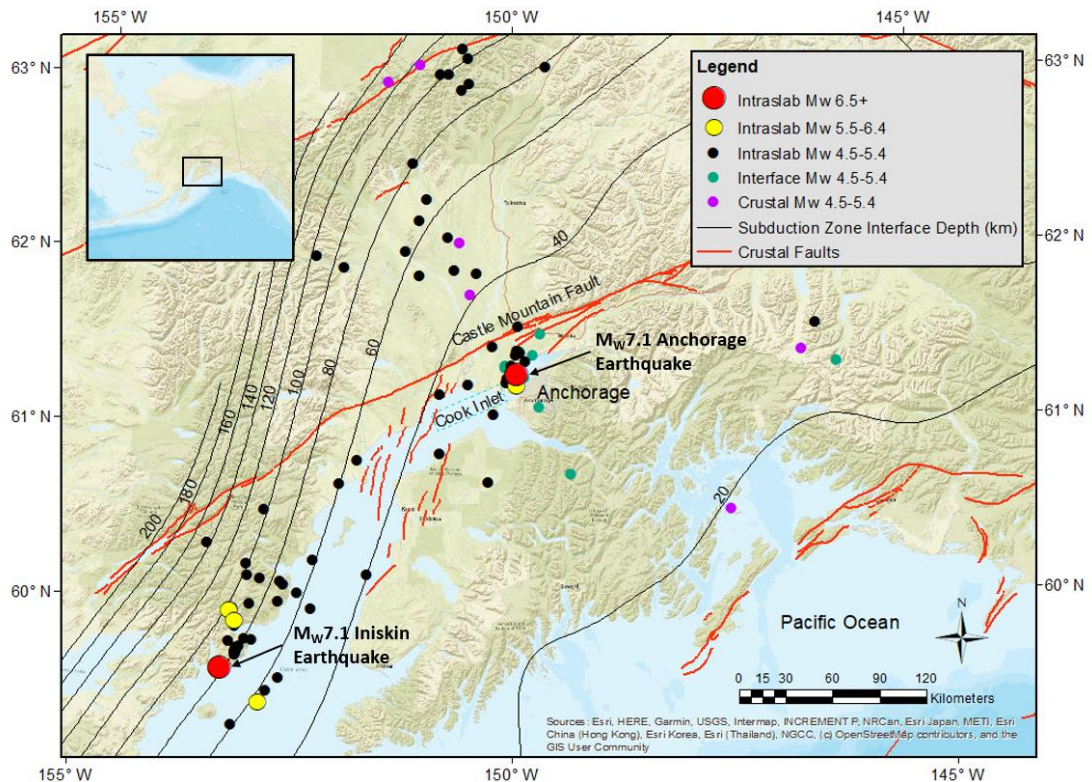


Figure 8.1. The tectonic setting of Southcentral Alaska, including contours of the interface between the North American and the subducting Pacific plates (using Slab 2.0; Hayes 2018) and crustal faults as identified by Koehler (2013). The colored circles indicate the epicenters of the earthquakes used in this study, which have been divided into intraslab, interface, and crustal events.

Several sources, including the interface, intraslab, and crustal sources, are responsible for these earthquakes (Wesson et al. 2007). The intraslab events within the Pacific plate are the most common. Additionally, several crustal sources can impact Anchorage, including the Castle Mountain Fault north of Anchorage (Figure 8.1), which is estimated to be capable of an M7 to 7.5 earthquake (Wesson et al. 2007; Koehler 2013).

#### 8.4 Geology

The geologic setting below Anchorage is as intricate as the tectonic setting, as it has been greatly affected by the advances and retreats of various glaciers in the region, resulting in a

complex soil stratigraphy. The simplified surficial geology is presented in Figure 8.2. The Chugach Mountains, comprised of lightly metamorphosed greywacke, rise at the city's eastern border (Wilson et al. 2012). Dense glacial till overlies the greywacke and is found at the surface in the lower reaches of the Chugach Mountains to the east, but it is encountered at depth to the west (Updike and Ulery 1986, Combellick 1999). Glacial outwash and alluvial deposits are found in the northern portion of Anchorage, often overlying glacial till.

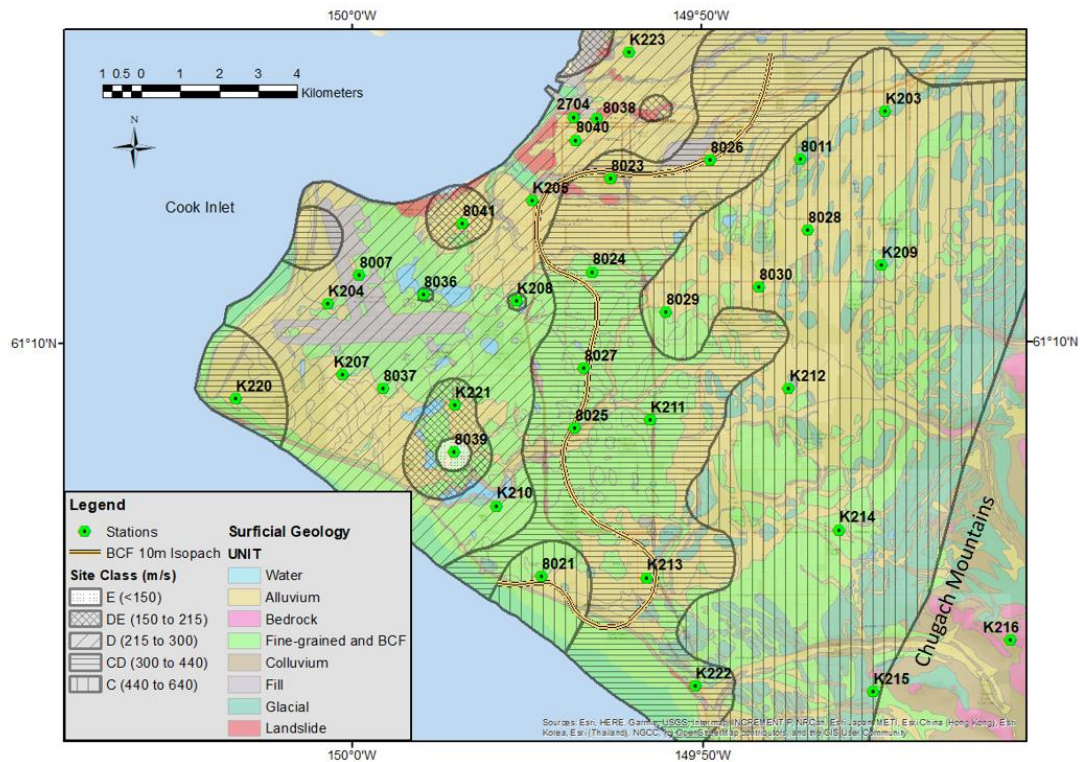


Figure 8.2. A simplified geologic map of Anchorage with strong-motion station locations. Hatching identifies the site class based on estimated  $V_{S30}$  (Thornley et al. 2021b). A 10-m isopach line is added from Combellick (1999) to show the geologic break in BCF thickness, where the BCF becomes thinner to the east of the line.

The Bootlegger Cove Formation (BCF), due to glaciolacustrine deposition, consists of various facies of sand, silt, and clay (Updike and Ulery 1986). The BCF is found in the city's central and western portions. The more sensitive clay layers of the BCF have been identified as the weak soil that caused significant deformations and slope failures in the 1964 Great Alaska Earthquake. The BCF ranges in thickness up to 60m, with its deepest portions found in the city's western-central part (Ulery and Updike 1983). The BCF grades to deltaic deposits of silt

and fine sand on the western edge of Anchorage. The variability of these subsurface soil conditions affects the site response across Anchorage (Thornley et al. 2021a).

### 8.5 Strong-motion Stations and Dataset

The current Anchorage network consists entirely of modern digital accelerometers (mostly Kinemetrics Basalt sensors) with sampling rates of 200 Hz. The 35 strong-motion stations used for this study are distributed across various surficial geologic conditions, as shown in Figure 8.2. In addition to surface strong-motion stations, the Delaney Park Downhole Array (DPDA), identified as Station 8040, was installed in 2004 (Figure 8.2), with a surface sensor and six subsurface accelerometers sensors at varying depths of up to 60 m below the ground surface. Between 2005 and early 2019 approximately 95 earthquakes within 300 km, ranging from  $M_w$ 4.5 to  $M_w$ 7.1, have been recorded at the strong-motion stations across Anchorage. The acceleration time-histories were processed prior to performing data analysis. A detailed description of the full processing of the data is described in Thornley et al. (2021a). In all, 1,727 three-component records from the 95 events were retained after processing for this analysis.

### 8.6 Site Spectral Amplification Evaluation

Once processed, the dataset for the 35 strong-motion stations and 95 events was used to evaluate the site response variability across Anchorage. The Generalized Inversion Technique (GIT), which was first developed by Andrews (1986), was utilized to perform the analysis. GIT is an efficient method for estimating the spectral amplification of many sites compared to a selected reference site (e.g., Parolai et al., 2000; Dutta et al., 2003; Oth et al., 2009; Bindi et al., 2017; Laurenzano et al., 2019). One of the benefits of GIT is its ability to use a large number of earthquakes at a large number of stations and obtain spectral amplification results

at each station, even when not all stations recorded all earthquakes. The GITANES (Version 1.3) package, implemented in MATLAB by Klin (2019), was used for this analysis.

While three-component time histories are used as inputs to GITANES, only the horizontal orthogonal components are used to calculate the spectral amplification functions (SAFs). The two orthogonal SAFs were combined using the following equation to calculate an equivalent average spectral amplification function (EAF) over the selected range of frequencies ( $f$ ) for each station evaluated.

$$EAF(f) = \sqrt{\frac{1}{2} [SAF_{E-W}(f)^2 + SAF_{N-S}(f)^2]} \quad (\text{Equation 8.1})$$

The EAF for each station represents the spectral amplification compared to the selected reference station (Station K216 in this study). The range of frequencies utilized in this study ranged from 0.25 to 10 Hz or 0.1 to 4 seconds, which roughly covers the natural periods of buildings between 1 and 40 stories, the range of building types in Anchorage.

Once the spectral amplifications are calculated for each of the strong-motion stations, they can be used to understand the variability of site response across Anchorage, which is related to the changes in geologic conditions, especially from east to west (Thornley et al. 2021a). For example, the EAF for a site in eastern Anchorage (K212), with a shallow soil layer over dense glacial till (Combellick 1999), is presented in Figure 8.3a and the EAF for a station in western Anchorage with a BCF thickness of more than 20 m and more than 40 m to dense glacial till (Updike and Ulery 1986), is presented in Figure 8.3b. In general, the stations in the eastern portion of the city have higher spectral amplification at higher frequencies, indicating stiff sites (higher shear-wave velocities), while the western portion has much higher spectral amplification at lower frequencies, indicating softer sites (thick soil sites with lower shear-wave velocities).



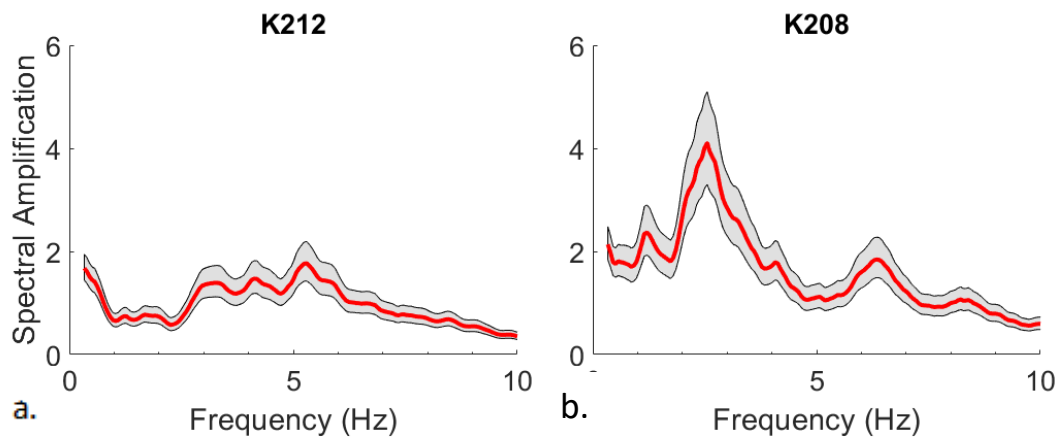


Figure 8.3. Spectral amplification for a station located on a shallow soil deposit over dense glacial till (a) and a station with more than 40m of variable soil, including soft silts and clays, over dense glacial till (b).

In addition to the spectral amplifications presented in Thornley et al. (2021a), estimates of  $V_{S30}$  have also been estimated for the strong-motion stations (Thornley et al. 2021b). The  $V_{S30}$  estimates allow the city to be subdivided into different site classes based on the building code categories. The work presented in this article builds on the results of Thornley et al. (2021a and 2021b). The interested reader is referred to those articles for further details related to the database, methods, and results.

### 8.7 Engineering Site Response Using Random Vibration Theory

Engineering site response analyses commonly use tools such as equivalent linear (EQL) and nonlinear analyses to estimate how earthquake ground motions are amplified as they travel through the soil profile (NASEM 2012, Stewart et al. 2014, Hashash et al. 2015, Regnier et al. 2018). EQL analyses using computer programs such as SHAKE91 (Idriss and Sun 1992) take input ground motions in the time domain and use frequency-domain transfer functions to calculate the soil effects on the ground motion. This approach's main advantages are its simplicity and that it requires few parameters, principally shear-wave velocity, unit weight, and shear modulus reduction and damping curves, to be defined for the discrete soil layers at a site. Rathje and Kottke (2008) explained that performing EQL analyses requires a large

number of input ground motions at the base of the soil deposit to get a robust estimate of site amplification. Introducing RVT allows using a single input FAS to calculate the site response (Rathje and Kottke 2008). The input FAS is still transferred through the soil column, but the transfer function outputs a surface FAS, which is converted through RVT to a response spectrum for the site.

RVT was introduced into seismology by Hanks and McGuire (1981). Since that time, developments by Boore (1983), Boore and Joyner (1984), and Boore (2003), among others, have allowed for improved implementation in EQL software such as Strata (Kottke and Rathje 2008). These improvements account for differences in duration and tectonic regime. At its basic level, RVT utilizes Parseval's theorem and extreme value statistics to transfer ground motions between the frequency domain and time domain and provide a median site response estimate (Kottke et al. 2019). While RVT allows the calculation of response spectra from FAS, inverse RVT (IRVT) calculates FAS from response spectra.

#### Proposed Methodology

To perform EQL analyses, it is critical to understand the subsurface soil conditions at a site. Thornley et al. (2019) calibrate an EQL model for the DPDA site, and Thornley et al. (2020) showed that this calibrated model could successfully match measured site response for the 2018  $M_w7.1$  Anchorage earthquake using both EQL and nonlinear methods. However, the calibration required knowledge of the subsurface profile and testing of several shear modulus and damping curves. In EQL analysis using RVT, a soil column is still required to estimate the profile's transfer function. As mentioned previously, few strong-motion stations in Anchorage have subsurface characterization for depths greater than 10 m, and these sites, especially in western Anchorage, have soil deposits with depths of more than 50 m.

Therefore, it is not appropriate to perform EQL analysis using shallow borings and  $V_{S30}$  estimates.

Site spectral amplification studies provide a means to estimate the missing link at sites that do not have adequate characterization to perform microzonation with EQL or nonlinear methods. These studies commonly use a reference site and calculate the amplification at each site with respect to that reference. These spectral amplifications are an analog of the transfer function used in an EQL analysis for a site. Using an input FAS, RVT techniques can provide a tool for evaluating the site response at a strong-motion station regardless of quality or availability of soil characterization. This technique offers a method to estimate site response that does not require the same level of site characterization as is required for EQL analysis. This may be especially beneficial for sites with complex subsurface conditions.

When calculating spectral amplifications in GIT, a reference station is selected, which is often a rock site with a  $V_{S30}$  greater than 760 m/s (site class BC). The spectral amplification for each site with respect to the reference site provides an approach to estimate the site response anticipated in a subsequent earthquake. However, because these results are in the frequency domain, it is challenging to utilize standard engineering choices of input spectra (e.g., uniform hazard spectra, UHS), such as those presented in building codes that provide the basis of estimating seismic demand for design.

### Generalized Approach

The RVT approach proposed in this study can be used for site response analyses at sites where strong ground motions have been recorded. The following describes the general process. This is followed by examples of the approach's use in several applications. As a starting point, a rock-outcrop ground motion is selected as the input response spectrum. IRVT converts the selected input response spectrum from either an outcrop or within motion

to a FAS ( $FAS_{Within}$ ). Once in the frequency domain, the spectral amplification results from GIT for a select site is applied to the  $FAS_{Within}$  to estimate the surface FAS ( $FAS_{Surface}$ ) using the following equation:

$$FAS_{Surface,i,j} = EAF_{i,j} \times FAS_{Within,ref,j} \quad (\text{Equation 8.2})$$

where  $i$  is the site,  $j$  is the frequency of interest, and  $ref$  is the reference site. Then RVT is used to convert the site response from the  $FAS_{Surface}$  to obtain the site-specific response spectrum.

This process allows the utilization of spectral amplifications calculated with GIT to be utilized directly into engineering studies without geotechnical characterization of the typical soil properties, as is required by EQL analysis. The process is shown graphically in Figure 8.4.

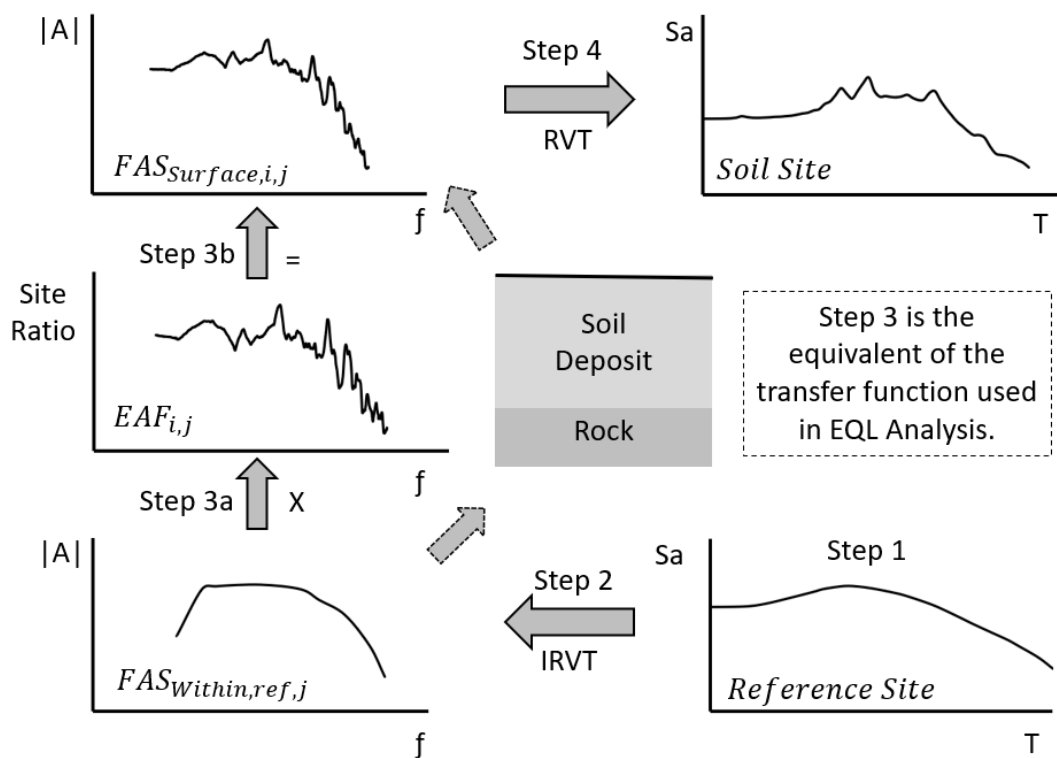


Figure 8.4. Process for using RVT and IRVT to utilize spectral amplifications to estimate site-specific response spectra given the response spectrum for a reference site. Step 1 begins in the lower right-hand corner. Step 3 is similar to the process used in standard EQL analysis (dashed arrows).

## Application of the Proposed Methodology

To test this methodology, ground motions recorded during the 2018  $M_w7.1$  Anchorage Earthquake at Station K216 and several strong-motion stations in Anchorage are used. The orthogonal response spectra at Station K216 (Step 1) are converted to FAS using IRVT (Step 2). In this instance, the two orthogonal horizontal components were combined after performing IRVT using Equation 8.1. The GIT spectral amplifications for the event, also presented by Thornley et al. (2021c) for each site, are applied to Station K216's FAS ( $FAS_{\text{Within}}$ ) to calculate each site's FAS ( $FAS_{\text{Surface}}$ ), as described in Step 3. Using RVT, the site FAS is converted to the response spectrum for the site (Step 4). It should be noted that there are several options to modify the duration, magnitude, damping, and other parameters in Strata. Provided, however, the user consistently uses the same parameters for IRVT and RVT calculations, the results achieved in Step 4 remain unaffected. The results are compared in Figure 8.5 to the response spectra calculated from the ground motions recorded at each site. This process was performed for several other earthquakes of lower magnitudes recorded in Anchorage, and similar good matches were achieved.

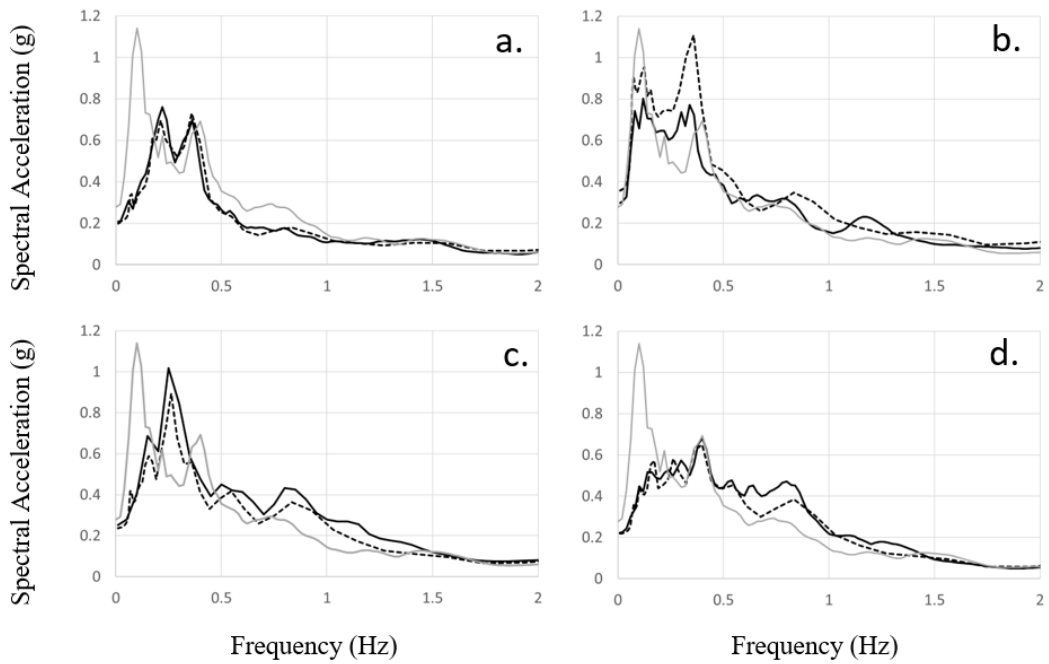


Figure 8.5. a. Station K212 (site class C), b. Station K213 (site class CD), c. Station 8040 (site class D), d. Station K208 (site class DE), where the measured response spectrum at each site is presented as the solid line and RVT-based response spectrum calculated from the K216 reference site is presented as the dashed line. For reference, the grey line indicates the K216 (reference site) geometric-mean response spectrum.

In general, the match between observed and the RVT-approach response spectra is close, although not exact. The locations of the peaks and their amplitudes are generally similar. As an example, Station 8040 (Figure 8.5c) has a maximum difference of 39% at 1.3s, but an average difference less than 16%. Station K212 (Figure 8.5a) has a maximum difference of less than 20% with an average of 5%. These differences may be attributed to several reasons, including the potential effects of using the EAF (Equation 8.1) to combine the two orthogonal components.

An evaluation was also performed to consider the results of the EAF (with frequency converted to period) applied directly to the reference site response spectrum. A comparison of the measured response spectrum and the EAF-based response spectrum is presented in Figure 8.6. EAF-based response spectrum does not provide a reasonable fit, as there are several periods where the spectra differ by factors of two or more, which is supported by

differences in FAS and response spectra (e.g., Bora et al. 2016). The RVT-based approach provides consistently similar results to the measured response spectra.

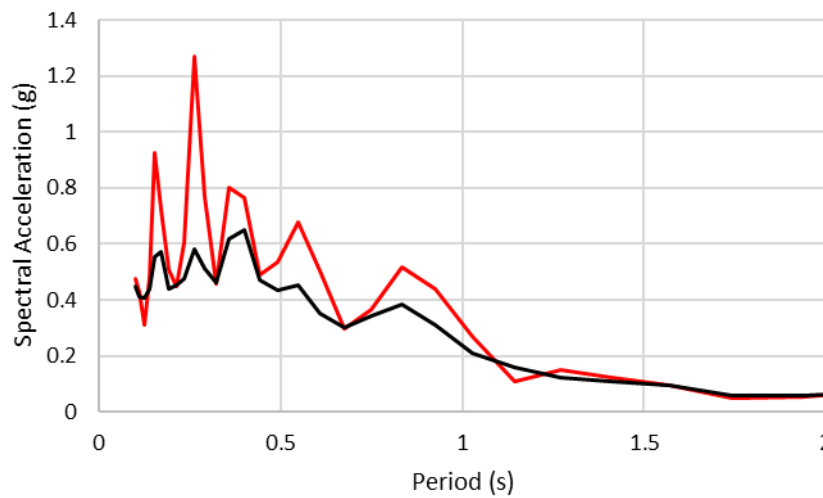


Figure 8.6. Response spectra at Station K208. The measured response spectrum is shown in black, and the EAF-based response spectrum is in red.

### 8.8 Nonlinear Site Effects

Nonlinear site response, due to the response of soil undergoing large strains, is an important aspect of any model for large earthquakes. As described in Thornley et al. (2021c), the 2018 Mw7.1 Anchorage Earthquake resulted in nonlinear site response at the strong-motion stations with lower  $V_{s30}$ . Numerous ground-motion models (GMMs) attempt to include both linear and nonlinear site responses. Several current GMMs do this by using the following equation:

$$F_S = \ln(F_{lin}) + \ln(F_{nl}) \quad (\text{Equation 8.3})$$

where  $F_S$  is the site amplification;  $F_{lin}$  is the linear term of the site amplification as a result of small shear strain; and  $F_{nl}$  is the nonlinear term that accounts for the large shear strain response of the soil at the site. This combination of terms is discussed in Seyhan and Stewart (2014), Harmon et al. (2019), and Parker et al. (2020), among others.

As presented by Hashash et al. (2018), site response analyses within the western United States (WUS) show that the  $F_{nl}$  term has a greater impact on the response spectrum at periods less than one second. The impacts of nonlinear site response tend to affect softer sites (i.e., sites with smaller  $V_{s30}$ ). Seyhan and Stewart (2014) found that the  $F_{nl}$  term has the largest impact at a period of approximately 0.3s. As shown below, the  $F_{nl}$  term results in a reduction of the spectral accelerations for the Anchorage study, especially at sites in classes D and DE.

The response spectra for each station calculated by the RVT-based approach have been developed using numerous moderate-magnitude earthquakes. As suggested previously, only one or two events may have caused nonlinear response at some of the strong-motion stations. Due to their great epicentral distances and/or small magnitudes, the other events caused minor or no nonlinear site response at the stations evaluated. The spectral amplification used in this study is considered to be the  $F_{lin}$  term. Accounting for potential nonlinearity using terms such as those provided by Seyhan and Stewart (2014) will reduce the likelihood of overestimating short-period spectral accelerations using the RVT-based approach.

### 8.9 Comparison to EQL Site Response Modeling

As mentioned previously, a calibrated EQL model has been developed for the DPDA, which is used here to further evaluate the validity of the proposed method. Four ground motions recorded at surface sites with  $V_{s30}$  greater than 700 m/s were selected from the PEER (2021) databased (Table 8.1), to use records from sites that may be considered reference sites and from large earthquakes. The response spectrum was calculated for each time history and utilized in Step 1 of the RVT-based analysis as the reference station, and the surface response for Station 8040 was calculated. The same time history was applied as an outcrop motion for



use in the DPDA model. In addition to the  $F_{in}$  response term, the RVT-based response spectrum was adjusted to account for  $F_{nl}$ , as described above.

Table 8.1. Ground motions utilized for DPDA calibrated model comparison with the RVT-based technique. Time histories and station data from PEER (2021). Maximum shear strain and surface PGA are calculated in the Strata DPDA model.

Event <sup>1</sup>	Station <sup>1</sup>	Magnitude <sup>1</sup>	$V_{S30}$ (m/s) <sup>1</sup>	Maximum Shear Strain (%) <sup>2</sup>	Shear Strain Index (%) <sup>2</sup>	Surface PGA (g) <sup>2</sup>
Duzce, Turkey	Lamont 1060	7.14	782	0.020	0.022	0.06
Chi-Chi, Taiwan	TTN025	7.62	705	0.019	0.016	0.06
Hector Mine	Hector	7.13	726	0.202	0.170	0.33
Kocaeli, Turkey	Gebze	7.51	792	0.091	0.124	0.17

1. Data from PEER NGA-West2 Ground Motion Database (2021).

2. Results from the DPDA EQL.

The resulting response spectra for the RVT-based approach and the EQL analysis are presented in Figure 8.7. The input response spectrum for each event is also plotted to provide a comparison of input and output spectra. The model presented by Thornley et al. (2019) and Thornley et al. (2020) was not modified and the EAF, as presented in Thornley et al. (2021a), was used for the RVT-based approach. The results presented in Figure 8.7 show that the periods of the peaks match and that accounting for nonlinear effects reduces the spectral accelerations to better match the amplitude of the EQL results. Between periods of about 0.3s and 0.6s, the RVT-based model tends to overpredict the site response, when compared to the DPDA model. This may reflect the ground motions used to develop the EAF but is more likely related to more complex site response being captured by the RVT-based approach than can be captured by a 1-D EQL analysis. In addition to characteristics related to the ground motions, the maximum shear strain within the soil column and ground surface PGA are

presented in Table 8.1. The shear strain index ( $I_v$ ), estimated by  $PGV_{in}/V_{S30}$  (Idriss 2011), is calculated to verify the appropriateness of the EQL model. Kim et al. (2016) found that EQL results with  $I_v < 0.1\%$  provide similar results to nonlinear analyses. The results in Figure 8.7c and 8.7d may be better approximated using a nonlinear model. However, for the purposes of this study, the results show that the DPDA EQL model provides a similar response. The PGAs presented in Table 8.1 were used to calculate the nonlinear site modifications.

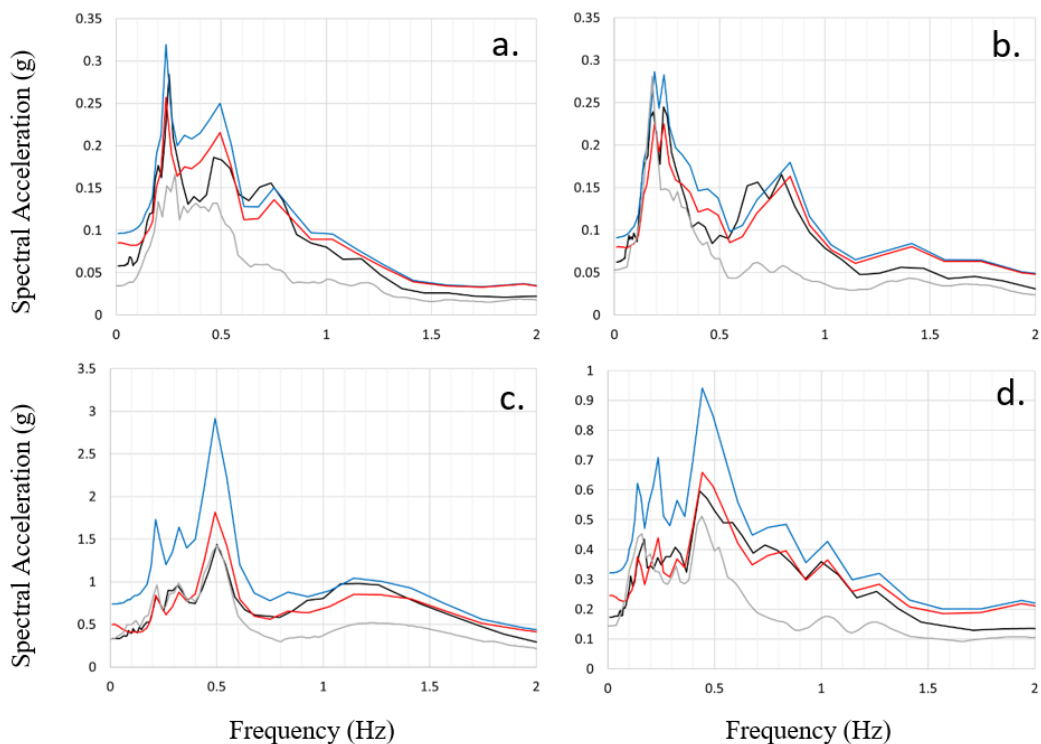


Figure 8.7. The results of the comparison between the DPDA EQL model and the RVT-based approach using the 1999 Chi-Chi record (a.), 1999 Duzce, Turkey record (b.), 1999 Hector Mine record (c.), and the 1999 Kocaeli, Turkey record as input motions (grey line). The DPDA EQL model is shown in black. The linear and nonlinear results from the RVT approach are shown in blue and red, respectively. Note the change in vertical scale in c) and d.).

### 8.10 Ground Motion Model Comparison

Recently, two Next Generation Attenuation Subduction (NGA-Sub) GMMs were released by Parker et al. (2020) and Kuehn et al. (2020). Because of the proximity of Anchorage to the subduction zone, the high rate of earthquake activity, and the likelihood of damaging earthquakes, subduction interface earthquakes account for 36% of the earthquake hazard

for Anchorage, according to the disaggregated hazard of the “Dynamic: Alaska 2007 (v2.1.2)” hazard model presented by USGS (2021). This model indicates a  $M_w$ 9.2 interface earthquake at a rupture depth ( $r_{RUP}$ ) of 36 km as the key scenario. Using this earthquake as a test case, site response spectra estimated using the NGA-Sub GMMs are compared here to response spectra using the RVT-based technique.

The NGA-Sub hazard characterization tool (Mazzoni 2020) was used to calculate the response spectrum for the site class BC, where the  $V_{S30}$  is 760 m/s, and at the strong-motion stations using their estimated  $V_{S30}$ . The Parker et al. (2020) and Kuehn et al. (2020) models (Global variants) were equally weighted. The site class BC response spectrum was used in Step 1 (Figure 8.4) as the reference site response spectra. The  $EAF_{i,j}$  for each station (Step 3) was used to calculate the soil site response spectra. The PGA estimated by the GMMs is then used to calculate  $F_{nl}$  using the approach presented by Parker et al. (2020) and the soil site response spectra are adjusted to account for nonlinear site response. The comparison between the two approaches is presented in Figure 8.8.

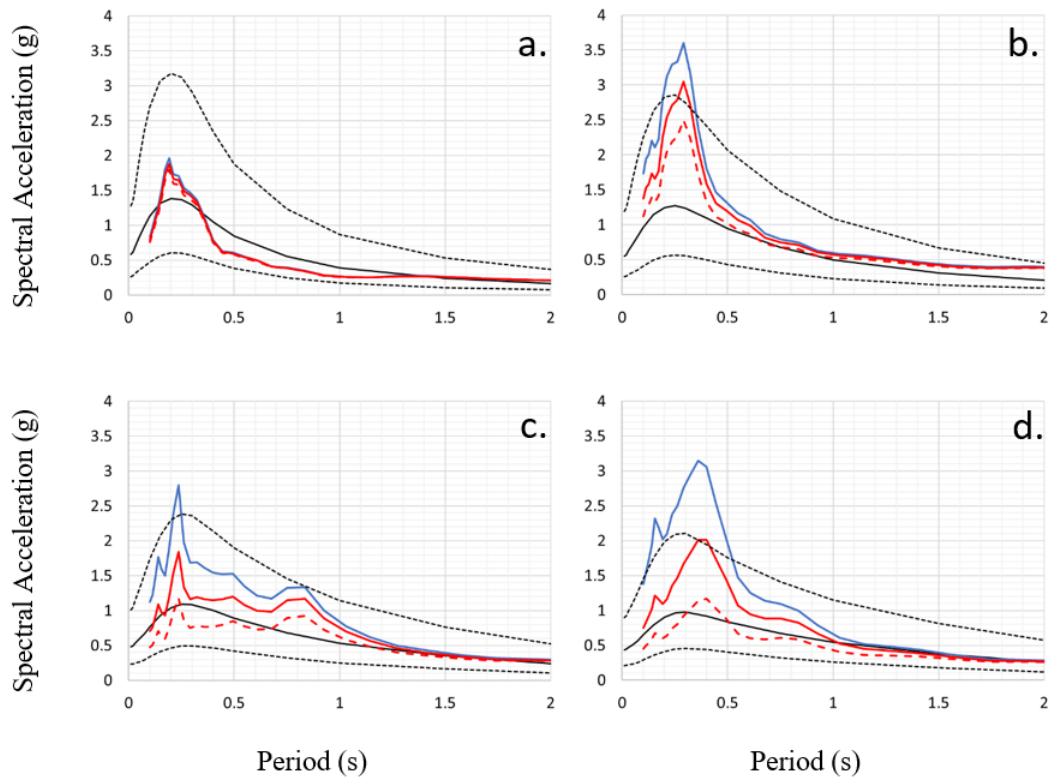


Figure 8.8. a. Station K212 (site class C), b. Station K213 (site class CD). c. Station 8040 (site class D), d. Station K208 (site class DE) where the black line with dotted lines indicates the median and  $\pm 1$  standard deviation response spectra for the NGA-Sub GMMs for the Mw9.2 event. The blue line is the RVT-based median response spectrum without the correction for nonlinearity and the solid red line corrects for nonlinearity using the factors recommended by Parker et al. (2020) and the dashed red lines using the factors of Seyhan and Stewart (2014).

The results indicate that the RVT technique provides similar results to the NGA-Sub estimates, but because they are site-specific, they provide details related to amplification behavior at each site. Utilizing the nonlinear modification, the RVT-based spectral accelerations are reduced at shorter periods and the shapes of the overall spectra are similar to those estimated by NGA-Sub. Even when the nonlinear response is accounted for, the site-specific response spectra tend to be above the median GMM estimate for the periods below 1s. However, the response spectra are within one standard deviation of the median, indicating a reasonable match. Modification of the factors utilized in the calculation of  $F_{nl}$  may help improve the fit. Figure 8.8 shows the differences when using  $F_{nl}$  factors recommended Parker et al. (2020) and Seyhan and Stewart (2014), indicated by the solid red

lines and dashed red lines, respectively. A fit closer to the NGA-Sub GMM median values is achieved using the Seyhan and Stewart (2014)  $F_{nl}$  term, especially at softer sites (i.e., site class D and DE).

The EAF results from the strong-motion stations were also divided by site class [defined by  $V_{s30}$  estimated by Thornley et al. (2021b)]. The range of response spectra for the strong-motion stations, divided by site class, is presented in Figure 8.9 along with the median and  $\pm 1$  standard deviation (shaded region) spectra. The response spectra in Figure 8.9 have not been adjusted to account for possible nonlinear site effects.

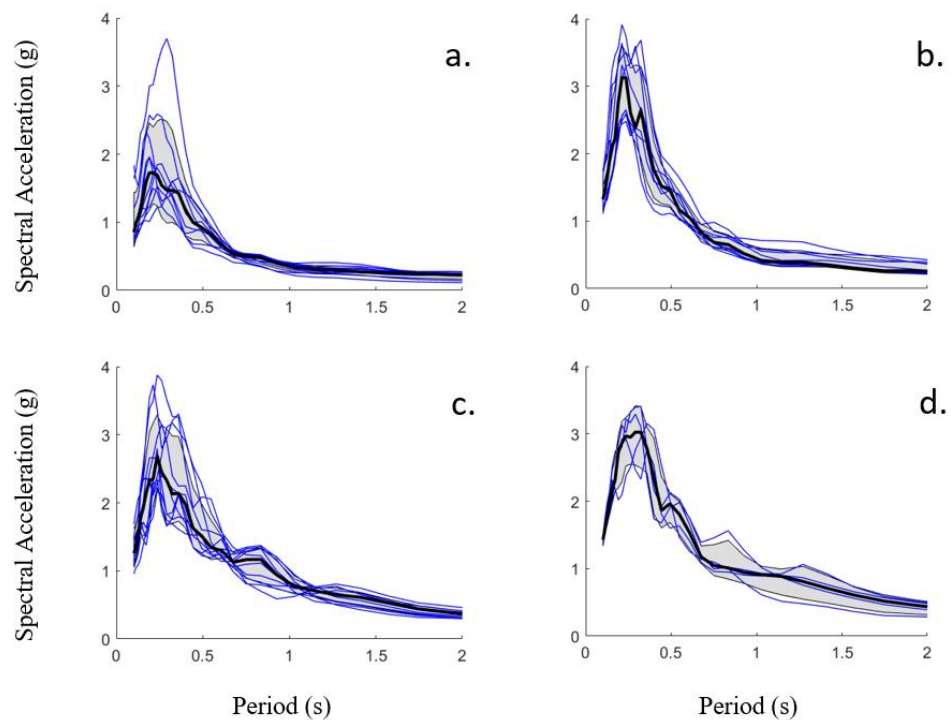


Figure 8.9. Response spectra for strong-motion stations in Anchorage by site class (frames a. through d. presents site class C, CD, D, and DE, respectively). The median is the black line and the  $\pm 1$  standard is shaded.

The average EAF for each site class was then used to estimate an average response spectrum for each site class similar to the process described above. The average  $V_{s30}$  for each site class was used to calculate the NGA-Sub GMM response spectra (Table 8.2). The results for the

four site classes are presented in Figure 8.10. The Seyhan and Stewart (2014) nonlinear adjustment provides a closer fit between the site class response spectra and the NGA-Sub GMM response spectra.

Table 8.2.  $V_{S30}$  ranges by site class proposed by BSSC (2020) and Anchorage strong-motion station estimates used in this study.

Site Class	$V_{S30}$ Range (BSSC 2020) (m/s)	Strong-motion Station $V_{S30}$ Range (m/s)	Strong-motion Station $V_{S30}$ Average (m/s)	Number of Strong-motion Stations
C	440 – 640	465 – 594	516	10
CD	300 – 440	315 – 439	376	9
D	215 – 300	224 – 285	244	10
DE	150 – 215	167 – 213	196	4

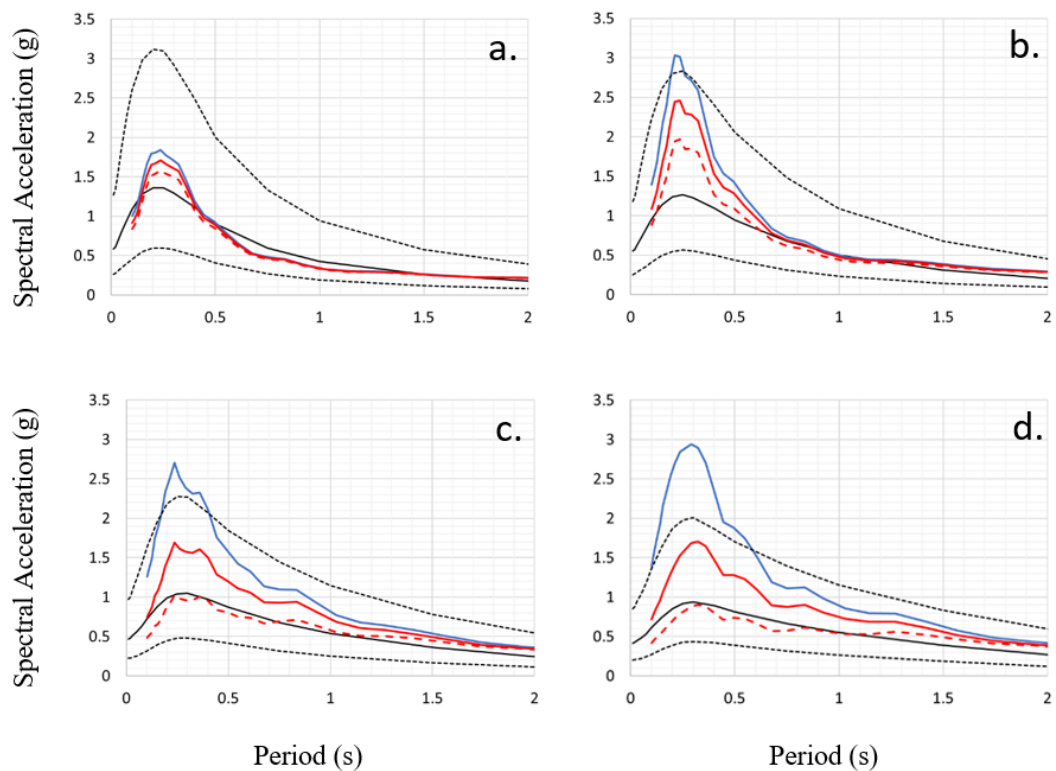


Figure 8.10. Response spectra for the combination of strong-motion stations in Anchorage by site class (frames a. through d. present site class C, CD, D, and DE, respectively). The black line with dotted lines indicates the median and  $\pm 1$  standard deviation response spectra for the NGA-Sub GMMs for the M9.2 event. The blue line is the RVT-based median response spectrum without the correction for nonlinearity, and the solid red line corrects for nonlinearity using the factors recommended by Parker et al. (2020) and the dashed red lines for Seyhan and Stewart (2014).

Crustal earthquake sources have also been included in the Alaska hazard model. The Castle Mountain Fault, north of Anchorage (Figure 8.1), is estimated to produce strike-slip events up to  $M_w7.5$  (Wesson et al. 2007). This scenario earthquake was used to compare the results of the four equally weighted soil-site NGA-West2 GMMs (Abrahamson et al. 2014, Boore et al. 2014, Campbell and Bozorgnia 2014, and Chiou and Youngs 2014) and the RVT technique. This is evaluated in a similar fashion to the site class approach presented above. The  $F_{nl}$  term is developed using the factors suggested by Seyhan and Stewart (2014) for crustal earthquakes. The results of this comparison are provided in Figure 8.11. The nonlinear effects for a  $M_w7.5$  crustal earthquake 65 km from Anchorage may not be as prevalent as suggested by the substantial reduction in spectral accelerations at shorter periods.

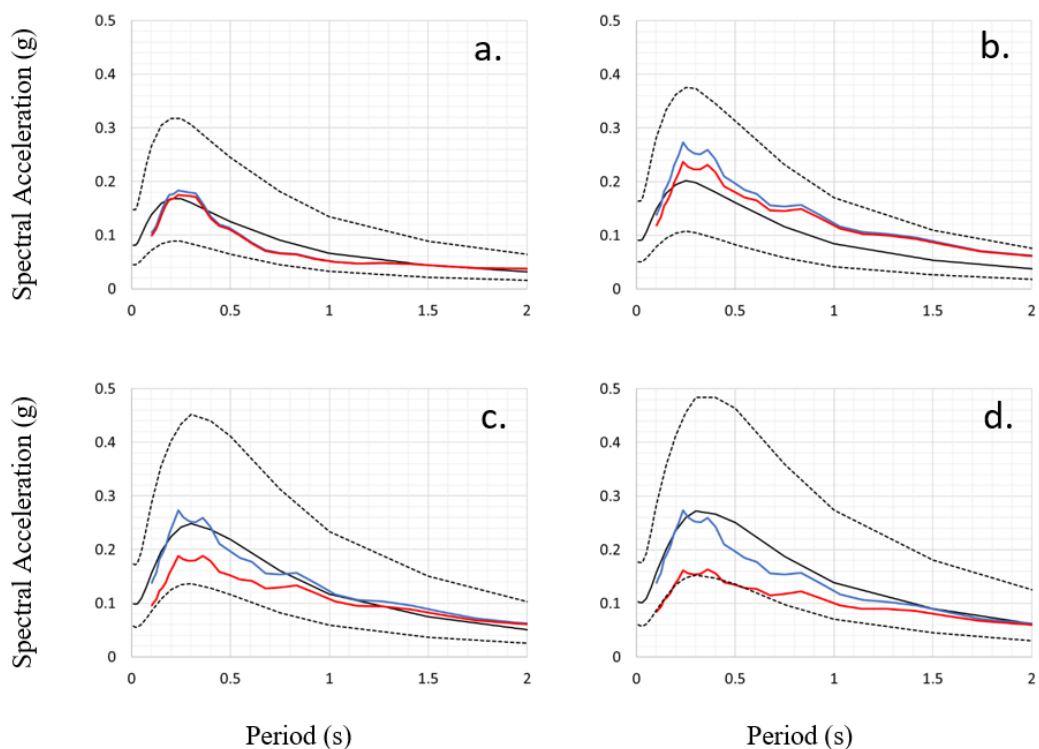


Figure 8.11. Response Spectra for the combination of Anchorage site classes (frames a. through d. present site class C, CD, D, and DE, respectively). The black line with dotted lines indicates the median and  $\pm 1$  standard deviation response spectra for the NGA-West2 GMMs for the  $M_w7.5$  event. The blue line is the RVT-based median response spectrum without the correction for nonlinearity, and the red line corrects for nonlinearity.

## 8.11 Discussion and Application

One of the limitations of microzonation studies is the need for proper engineering characterization of the subsurface soil, especially at strong-motion stations, to draw conclusions about sites within the vicinity that have similar subsurface conditions. As described here, the Anchorage strong-motion network does not have this level of characterization, but unlike regional strong-motion networks, such as in the central and eastern United States (CEUS), the Anchorage network has recorded numerous moderate to strong earthquakes. The use of RVT techniques with GIT-derived spectral amplification allows the characterization of site response without additional subsurface characterization, as shown in Figure 5. This is especially beneficial because even with the proper characterization of subsurface conditions, the selection of shear modulus reduction and damping curves can have a significant impact on the results of EQL analyses.

As mentioned previously, one of the benefits of the use of spectral amplification measured at the strong-motion stations is that the site response, especially in the linear range, is accounted for in the results. This is beneficial when performing site response analysis, whether EQL or nonlinear. The results allow for calibration of site models under small strain before extending those models to the nonlinear realm. This can also support a methodology for selecting and applying shear modulus reduction and damping curves for regional soil types so that a model for a strong-motion station can be applied to other sites within a region.

When utilizing this methodology, several aspects should be considered. As presented in Kottke et al. (2019), care should be taken when calculating input FAS from response spectra. Reference site response spectra may need to be upsampled to achieve appropriate FAS representation. In addition, unlike GMM applications using RVT, parameters such as magnitude, duration, and other modifications do not need to be accounted for in this



method, provided that the parameters used in Step 2 and Step 4 (Figure 8.4) are the same. Lastly, the spectral amplification used in this study resulted primarily from smaller-magnitude earthquakes that provide linear site response, allowing for the application of the  $F_{nl}$  term. Care should be given to the selection of earthquakes for the GIT analysis so that nonlinear response is not accounted for twice. On the other hand, if the ground motions used in the GIT analysis account for nonlinear response (Figure 8.5) then  $F_{nl}$  may not need to be applied.

## 8.12 Conclusions

The use of Fourier spectral amplification results directly in geotechnical engineering studies has been limited. This is because there has been no coherent and simple approach to transfer the Fourier spectral amplification results to the response spectral-domain more common in engineering studies. The methodology presented in this study provides the opportunity to directly utilize Fourier spectral amplification to estimate response spectra for strong-motion stations without the need for engineering characterization of subsurface conditions. The methodology, shown here to be compatible with individual earthquakes, can be extended to incorporate the results from numerous earthquakes to capture average site response. While the initial results provide the linear response, the application of a nonlinear term allows for the correction of site response to include nonlinear effects on the response spectrum.

## 9.0 Conclusions and Future Research

Earthquake records from 2004 to 2019 were collected from the AEC, and after processing, resulted in a database of 95 three-component time-histories with magnitudes of  $M_w$  4.5 and greater within 300km of Anchorage. The earthquake records were predominantly intraslab events, but the dataset included subduction interface and crustal earthquakes as well. More than 90% of the events were  $M_w$  5.5 or less and approximately 40% of the earthquake records had epicentral distances greater than 200km from Anchorage, suggesting a majority of the database consists of low-intensity ground motions. The time-histories were processed for use, which included updating key header data, picking P and S-wave arrivals, removing trends, and filtering to improve the SNR. Filtering was performed using a fourth-order Butterworth band-pass filter with lower and upper limits of 0.1 and 30 Hz, respectively, resulting in a range of useful frequencies between 0.25 and 10 Hz. Further details of these efforts are presented in detail in Chapters 3 and 5.

Thirty-five strong-motion stations were included in this study. Unfortunately, due to a variety of reasons, the 95 earthquakes in the database were not recorded at each station each time. For example, of the 95 events used in the database, Station K213 had the most recordings at 70 events and Station K207 had the least, at seven recordings. The average number of records for the 35 strong-motion stations was 48. However, the Generalized Inversion technique (GIT) provides a methodology for estimating Fourier spectral amplification for each station, even when a complete set of records is not available. GIT utilizes a reference site for evaluating site amplification. Station K216, a rock site located in the Chugach Mountains on the eastern edge of the city, was used as the reference site. HVSR calculations were performed to evaluate  $f_{\text{peak}}$  and estimate  $V_{S30}$  for each of the strong-motion stations and develop a regional relationship between  $f_{\text{peak}}$  and  $V_{S30}$ .

While most of the database consists of low-intensity earthquake records, the inclusion of the  $M_w$ 7.1 Anchorage Earthquake from 30 November 2018 allows for the evaluation of nonlinear soil behavior due to a higher-intensity earthquake and comparisons between linear and nonlinear site response become possible. In addition to the evaluation of site amplification and nonlinear site response studies, the database was also used to develop a method to utilize Fourier spectral amplification to calculate engineering response spectra using Random Vibration Theory (RVT). The following section provides a summary of key findings related to the utilization of this database followed by a section describing some additional potential avenues of future research that can be explored.

### 9.1 Key Take-Aways

- Shear wave velocity profiling is a critical aspect in the development of an engineering site response model. As shown at the DPDA, utilization of the recorded data, along with proper site characterization, allows for calibration of a one-dimensional equivalent linear model. Without proper site characterization, it can be difficult to select the appropriate shear modulus reduction and damping curves (Chapter 4). Once a calibrated model is developed, it can be used to effectively estimate site response using nonlinear site response models (Appendix B).
- Given the wide variety of geologic soil units in Anchorage, site response across Anchorage changes, particularly from east to west, as the soils transition from dense glacial till to deep soft BCF deposits and then to stiffer silt and sand at the far western portion of the city. This finding is consistent with previous research, but now utilizes a larger set of strong-motion stations and higher intensity earthquakes (Chapter 5).
- The spectral amplifications vary greatly across Anchorage. For this study, the logarithmic band-average for 1 Hz and 5 Hz were evaluated because of the range of

common infrastructure (approximate fundamental periods of 10 and 2-story buildings, respectively) considered to be typical of Anchorage. The spectral amplification ranges from one to almost four times the reference site for the 1 Hz band-averaged results. The higher amplifications primarily coincide with areas with underlying BCF deposits, where higher amplifications are related to deeper soft soil deposits in the central portion of Anchorage. The 5 Hz band-average results range from one to over four, where the lower amplifications are related to denser alluvial and glacial till deposits in the east, west and north of Anchorage, while the southcentral portion of Anchorage consists of softer surficial deposits of silt and clay, over deep BCF deposits. The effects of these subsurface conditions on spectral amplification are shown especially well in Figures 5.18 and 5.19.

- The earthquake records used in this study account for wide distribution of azimuths, with higher concentrations of earthquakes recorded between 225 and 250 degrees and 330 to 360 degrees. A sensitivity analysis was performed, and the results of the study did not show bias based on azimuth. Similar sensitivity analyses were performed to evaluate the effects of magnitude, event depth, and epicentral distance, with similar results. There is a possibility that with higher-intensity earthquakes, a basin-related effect may affect site response, but this was not apparent from the sensitivity studies performed using this database (Chapter 5).
- One of the events that was included in the database was the 30 November 2018  $M_w$ 7.1 Anchorage Earthquake, which caused widespread damage across southcentral Alaska. An analysis of the recorded ground motions indicate that nonlinear site response occurred at sites with lower  $V_{s30}$ , while stiffer sites (higher  $V_{s30}$ ) showed little to no nonlinear response. This was shown comparing the spectral amplification results from the low-intensity events compared to the  $M_w$ 7.1 event

and using the relationship of  $PGV/V_{S30}$  as a proxy for shear strain. Both methods indicated the same site response behavior (Chapter 6).

- As noted previously, little to no subsurface characterization has been performed at a majority of strong-motion stations in Anchorage. Calculation of the HVSr for the strong-motion stations has allowed for an initial estimate of  $V_{S30}$  for the strong-motion stations used in this study. Two regional equations have been developed to assist in estimating  $V_{S30}$  for other strong-motion stations in the future. These include:

$$V_{S30} = -145.9 (\pm 17.1)(SSR_{1Hz}) + 652.9 (\pm 38.4) \quad (\text{Equation 7.1})$$

and

$$\log(V_{S30}) = (0.40 \pm 0.03) \log(f_{peak}) + (2.40 \pm 0.09) \quad (\text{Equation 7.5})$$

where  $SSR_{1Hz}$  and  $f_{peak}$  are results of the standard spectral ratio (SSR) and frequency peak of the HVSr results, respectively. The local building code utilizes  $V_{S30}$  for establishing seismic site classification to estimate earthquake loading on structures. A contour map estimating seismic site class across Anchorage has been developed using a combination of sites with  $V_{S30}$  measurements and  $V_{S30}$  estimates for the strong-motion stations using the relationships presented above (Chapter 7).

- The use of Fourier spectral amplification has long been challenging to incorporate into traditional engineering site response analysis. In addition, a large portion of earthquakes recorded at strong-motion stations tend to have lower-intensity earthquakes and do not capture nonlinear site response behavior. A method has been developed to estimate engineering response spectra using Fourier spectral amplification calculated at each strong-motion station and RVT methods. In cases where the input Fourier spectral amplification is captures linear response, the nonlinear response can be accounted for in similar fashion to the practice utilized by

recent GMMs. While this was developed using Anchorage data, its application is not limited to Alaska. It is reasonable to expect that spectral amplifications calculated at other strong-motion networks can be used to estimate site response or calibrate site response models (Chapter 8).

## 9.2 Further Research Opportunities

- As shown in Figure 2.3, several earthquakes greater than  $M_w 5.5$  have been recorded by accelerograph stations prior to 1993. These earthquake time-histories could not be utilized in this study because a digitized version of the records could not be found. If those records can be secured, their spectral amplifications could be compared to the results of this study and provide additional understanding of site response in Anchorage.
- The current dataset should continue to be updated and evaluated, especially when higher-intensity earthquakes occur. At the time of writing this section a  $M_w 6.1$  event occurred 170km north of Anchorage and was strongly felt. The inclusion of additional large earthquakes will allow for comparison of subsets of the data such that linear and nonlinear response behavior can be further understood.
- One of the recent focuses in the development of GMMs is the attempt to capture basin behavior for different regions. With further development and characterization of the basin structure in southcentral Alaska, additional terms may be added to adjust for that behavior in site response characterization. Further consideration of the basin behavior using the current database would assist in the characterization of the basin.
- Additional refinement can likely be achieved to further refine the  $V_{S30}$  map of Anchorage. Key elements that could be improved include additional incorporation

of surficial geology, subsurface data, and anthropogenic effects. Regardless of the limitations of  $V_{S30}$  (especially in the site response characterization of deeper soil sites), current plans include continued use of  $V_{S30}$  for seismic site classification in updates to the 2024 International Building Code. This map could be adopted by the Municipality of Anchorage for use as a planning and development document.

- Additional planning and development products can be supported using the current dataset. One such product that will be especially useful for the Municipality of Anchorage is a liquefaction susceptibility map. This can be accomplished through the combination of surficial geologic mapping,  $V_{S30}$  mapping, and simplified liquefaction screening procedures. It should be noted that one of the biggest challenges of such a product is the anthropogenic causes of liquefaction (i.e., poor compaction of saturated soil backfill below a structure). This issue was observed in the  $M_w7.1$  Anchorage Earthquake and will be difficult to capture in such a product.
- One of the challenges of this study is the lack of subsurface characterization of the strong-motion stations (i.e., depth to engineering bedrock,  $V_s$  profile, soil stratigraphy, etc.). Further characterization could provide extensions of the findings presented in this study. As an example, additional strong-motion site characterization may allow for further extension of the HVSR results, which may allow improvements related to the use of H/V data collected at sites where infrastructure projects are planned, and no strong-motion records have been collected. This may also allow for the development of characterization terms other than  $V_{S30}$  for sites where soft soil extends deeper than 30m.
- While the RVT-based approach was developed using the Fourier spectral amplification results from this study, its use may be extended beyond Anchorage.

Evaluation of its use with similar studies performed in other regions should be performed to further improve the method. Additionally, site response modeling could incorporate this method to improve on the models developed at strong-motion stations, potentially even assisting in characterization of three-dimensional site response. Machine learning techniques could be incorporated into this to add efficiency to model development and calibration.

- Additionally, using the RVT-based approach, it may become possible to collect H/V information at a site and develop a relationship to Fourier spectral amplification that can then be used to develop a site response model. One of the challenges, as noted in Chapter 7, is the differences in amplitude between HVSr and SSR data. The current dataset could be used to develop that relationship. This would then allow for better site characterization and more effective site response modelling.

Lastly, the importance of strong-motion networks cannot be understated and is critical in earthquake research, especially towards risk mitigation. Without the continued support and modernization of networks like the one used in this study, research like this cannot occur. The lack of strong-motion data in Eagle River, the community just north of Anchorage, resulted in numerous hypotheses regarding the disproportionate damage following the 30 November 2018  $M_w$ 7.1 Anchorage Earthquake. Further expansion and use of networks like the one in Anchorage will allow for a better understanding of site response in Alaska and beyond, resulting in benefits through new research, positively impacting others living in regions with earthquake hazards.



## 10.0 References

- Abrahamson NA, Silva WJ, Kamai R. Summary of the ASK14 Ground Motion Relation for Active Crustal Regions. *Earthquake Spectra*. 2014;30(3):1025-1055. doi:10.1193/070913EQS198M
- Akkar, S. and J.J. Bommer, 2006, Influence of long-period filter cut-off on elastic spectral displacements. *Earthquake Engineering Structural Dynamics*, 35: 1145-1165. doi:10.1002/eqe.577
- Alaska Earthquake Center (AEC), 2021, <https://earthquake.alaska.edu/earthquakes/about>, last referenced 6 February 2021.
- Andrews, D.J., 1986, Objective determination of source parameters and similarity of earthquakes of different size, in *Earthquake source mechanics*. In: Das S, Boatwright J, Scholz CH (eds) *American Geophysical Monograph 37*, vol 6, pp 259–267.
- American Society of Civil Engineers (ASCE), 2017, *ASCE/SEI 7-16 Minimum Design Loads and Associated Criteria for Buildings and Other Structures*, American Society of Civil Engineers.
- Bayless, J., N. A. Abrahamson, 2019, An Empirical Model for the Interfrequency Correlation of Epsilon for Fourier Amplitude Spectra, *Bulletin of the Seismological Society of America*; 109 (3): 1058–1070. doi: <https://doi.org/10.1785/0120180238>
- Beavan J., K.H. Jacob, 1984, *Processed Strong-Motion Data from Subduction Zones: Alaska*. Columbia University, Palisades, New York: Lamont-Doherty Geological Observatory; 1984.
- Bindi, D., D. Spallarossa, F. Pacor, 2017, Between-event and Between-station Variability Observed in the Fourier and Response Spectra Domains: Comparison with Seismological Models, *Geophysical Journal International*, 210, 1092-1104. Doi: 10.1093/gji/ggx217.
- Biswas, N., A. Martirosyan, U. Dutta, A. Papageorgiou, and R. Combellick, 2003, *Seismic Microzonation: Metropolitan area of Anchorage. Part A and B. Final Report prepared for Alaska Science and Technology Foundation, Geophysical Institute, University of Alaska Fairbanks, Fairbanks, AK.*
- Biswas, N., A. Martirosyan, U. Dutta, M. Dravinski, and A. Papageorgiou, 2004, *Investigation for Seismic Zonation of Anchorage, in Earthquake Hazard, Risk, and Strong Ground Motion*, Y. T. Chen, G.F. Panza, and Z.L.Wu (Editors), IUGG Special Volume, Seismological Press, Beijing, 243-257. (ISBN 7-5028-2506-1).

Bland, J.M., and D.G. Altman, 1986, Statistical Methods for Assessing Agreement Between Two Methods of Clinical Measurement, *Lancet* 327 (8476): 307-10.

Bonilla, L.F., J. H. Steidl, G. T. Lindley, A. G. Tumarkin, R. J. Archuleta, 1997, Site amplification in the San Fernando Valley, California: Variability of site-effect estimation using the S-wave, coda, and H/V methods. *Bulletin of the Seismological Society of America*; 87 (3): 710–730.

Boore, D., 1983, Stochastic simulation of high-frequency ground motions based on seismological models of the radiated spectra. *Bulletin of the Seismological Society of America*, Vol. 73, No. 6, pp. 1865-1894.

Boore, D., 2003, Simulation of ground motion using the stochastic method. *Pure Appl. Geophys.*, Vol. 160, No. 3-4, pp. 635-676.

Boore, D., 2013, ROSE School Engineering Seismology Lecture Notes: ROSE\_2013\_W2D3L1\_ground\_motions\_from\_simulations, [http://www.daveboore.com/short\\_course\\_lectures\\_and\\_labs.html](http://www.daveboore.com/short_course_lectures_and_labs.html) last accessed May 2020.

Boore, D. M. and W.B. Joyner, 1984 A note on the use of random vibration theory to predict peak amplitudes of transient signals. *Bulletin of the Seismological Society of America*, Vol. 74, No. 5, pp. 2035-2039.

Boore D.M., J.P. Stewart, E. Seyhan, G.M. Atkinson, 2014. NGA-West2 Equations for Predicting PGA, PGV, and 5% Damped PSA for Shallow Crustal Earthquakes. *Earthquake Spectra*. 2014;30(3):1057-1085. doi:10.1193/070113EQS184M

Bora, S.S, F. Scherbaum, N. Kuehn, P. Stafford, 2016. On the Relationship between Fourier and Response Spectra: Implications for the Adjustment of Empirical Ground-Motion Prediction Equations (GMPEs). *Bulletin of the Seismological Society of America*, Vol. 106, No. 3, pp. 1235-1253. doi: 10.1785/0120150129

Borcherdt R. D. 1970, Effects of local geology on ground motion near San Francisco Bay. *Bulletin of the Seismological Society of America* 1970, 60 (1): 29–61.

Bozorgnia, Y., 2020, Data Resources for NGA-Subduction Project, Pacific Earthquake Engineering Research Center Report 2020/02.

Building Sciences Safety Council (BSSC), 2019, BSSC Project Final Report: Development of the Next Generation of Seismic Design Value Maps for the 2020 NEHRP Provisions, National Institute of Building Sciences.

Brune, J.N., 1970, Tectonic Stress and the Spectra of Seismic Shear Waves from Earthquakes, *Journal of Geophysical Research*, Vol. 75, No. 26, September 10, 1970.

Building Sciences Safety Council (BSSC), 2019, BSSC Project Final Report: Development of the Next Generation of Seismic Design Value Maps for the 2020 NEHRP Provisions, National Institute of Building Sciences.

Campbell K.W. and Y. Bozorgnia, 2014. NGA-West2 Ground Motion Model for the Average Horizontal Components of PGA, PGV, and 5% Damped Linear Acceleration Response Spectra. *Earthquake Spectra*. 2014;30(3):1087-1115. doi:10.1193/062913EQS175M

Castellaro S., F. Mulargia, 2009, VS30 estimates using constrained H/V measurements. *Bulletin of the Seismological Society of America* 99:761–773. <https://doi.org/10.1785/0120080179>

Castro RR, F. Pacor, D. Bindi, L. Luzi, 2004, Site response of strong motion stations in the Umbria, Central Italy, Region. *Bulletin of the Seismological Society of America*, 94(2):576–590. <https://doi.org/10.1785/0120030114>.

Census.gov <https://www.census.gov/quickfacts/anchorageunicipalityalaskacounty> Last accessed February 23, 2020.

Chandra J., P. Gueguen, J.H. Steidl, L.F. Bonilla, 2015, In Situ Assessment of the G- $\gamma$  Curve for Characterizing the Nonlinear Response of Soil: Application to the Garner Valley Downhole Array and the Wildlife Liquefaction Array, *Bulletin of the Seismological Society of America*; 105 (2A): 993-1010. Doi: 10.1785/0120140209

Chandra, J. P. Gueguen, L.F. Bonilla, 2016, PGA-PGV/Vs considered as a stress-strain proxy for predicting nonlinear soil response, *Soil Dynamics and Earthquake Engineering*, 85, 146-160. <http://dx.doi.org/10.1016/j.soildyn.2016.03.020>

Chiou B.S-J. and R.R. Youngs, 2014. Update of the Chiou and Youngs NGA Model for the Average Horizontal Component of Peak Ground Motion and Response Spectra. *Earthquake Spectra*. 2014;30(3):1117-1153. doi:10.1193/072813EQS219M

Center for Strong Motion Data (CESMD) 2020, [https://strongmotioncenter.org/cgi-bin/CESMD/iqr\\_dist\\_DM2.pl?IQRID=us1000hyfh&SFlag=0&Flag=2](https://strongmotioncenter.org/cgi-bin/CESMD/iqr_dist_DM2.pl?IQRID=us1000hyfh&SFlag=0&Flag=2) last accessed October 2020.

Center for Strong Motion Data (CESMD) 2021, [https://www.strongmotioncenter.org/cgi-bin/CESMD/iqr\\_dist\\_DM2.pl?IQRID=IniskinAlaska\\_24Jan2016\\_10004gqp&SFlag=0&Flag=2](https://www.strongmotioncenter.org/cgi-bin/CESMD/iqr_dist_DM2.pl?IQRID=IniskinAlaska_24Jan2016_10004gqp&SFlag=0&Flag=2), last accessed April 2021.

Combellick, R.A., 1999, Simplified geologic map and cross sections of central and east Anchorage, Alaska, Alaska Division of Geological & Geophysical Surveys Preliminary Interpretive Report 1999-1, 13 p., 2 sheets. <http://doi.org/10.14509/2243>

Douglas, J., D.M. Boore, 2011, High-frequency filtering of strong-motion records, *Bulletin of Earthquake Engineering* 9, 395–409 (2011). <https://doi.org/10.1007/s10518-010-9208-4>

Dutta, U., N. Biswas, A. Martirosyan, S. Nath, M. Dravinski, A. Papageorgiou, R. Combellick, 2000, Delineation of Spatial Variation of Shear Wave Velocity with High-Frequency Rayleigh Waves in Anchorage, Alaska, *Geophysical Journal International* (2000) 143, 365-375.

Dutta, U., A. Martirosyan, N. Biswas, A. Papageorgiou, R. Combellick, 2001, Estimation of S-Wave Site Response in Anchorage, Alaska, from Weak-Motion Data Using Generalized Inversion Method, *Bulletin of the Seismological Society of America*, 91, 2, pp. 335-346, April 2001.

Dutta, U., N. Biswas, A. Martirosyan, A. Papageorgiou, S. Kinoshita, 2003, Estimation of Earthquake Source Parameters and Site Response in Anchorage, Alaska from Strong-Motion Network Data Using Generalized Inversion Method, *Physics of the Planetary Interiors*, 137 (2003) pp. 13-29. doi:10.1016/S0031-9201(03)00005-0

Dutta, U., N. Biswas, D. Adams, A. Papageorgiou, 2004, Analysis of S-Wave Attenuation in South-Central Alaska, *Bulletin of the Seismological Society of America*; 94 (1): 16-28. Doi: 10.1785/0120030072.

Dutta, U., M.K. Sen, N. Biswas, Z. Yang, 2009, Investigation of Shallow Sedimentary Structure of the Anchorage Basin, Alaska, Using Simulated Annealing Inversion of Site Response. *Bulletin of the Seismological Society of America*, Vol 99, No. 1, pp. 326-339, February 2009.

EERI, 2019, Webinar Recording: Anchorage, Alaska Reconnaissance Briefing, February 14, 2019, [http://www.learningfromearthquakes.org/2018-11-30-anchorage-alaska/index.php?option=com\\_content&view=article&id=68](http://www.learningfromearthquakes.org/2018-11-30-anchorage-alaska/index.php?option=com_content&view=article&id=68) last accessed May 14, 2020.

Field, E.H., and K.H. Jacob, 1995, A Comparison and Test of Various Site-Response Estimation Techniques, Including Three that are not Reference-Site Dependent, *Bulletin of the Seismological Society of America*, 85, 1127-1143.

Field, E.H., P.A. Johnson, I.A. Beresnov, Y. Zeng, (1997), Nonlinear ground-motion amplification by sediments during the 1994 Northridge earthquake. *Nature*, Vol. 390, 11 December 1997.

Franke, K. W., R. D. Koehler, C. Z. Beyzaei, A. Cabas, I. Pierce, A. Stuedlein, and Z. Yang, 2020, Geotechnical engineering reconnaissance of the 30 November 2018 Mw 7.1 Anchorage, Alaska Earthquake, Version 2.1, GEER Rept. GEER-059, Geotechnical Extreme Events Association, 1 pp., doi: 10.18118/G6P07F.

Frankel A.D., D.L. Carver, R.A. Williams (2002), Nonlinear and Linear Site Response and Basin Effects in Seattle for the M 6.8 Nisqually, Washington, Earthquake. *Bulletin of the Seismological Society of America*; 92 (6): 2090–2109. doi: <https://doi.org/10.1785/0120010254>

Freymueller, J.T., H. Woodward, S.C. Cohen, R. Cross, J. Elliot, C.F. Larsen, S. Hreinsdóttir, and C. Zweck, 2008, Active Deformation Processes in Alaska, Based on 15 Years of GPS Measurements, in: Freymueller, J.T., Haeussler, P.J., Wesson, R.L., and Ekström, G., eds., *Active Tectonics and Seismic Potential of Alaska: American Geophysical Union Geophysical Monograph Series 179*, p. 1-42.

GeoLogismiki Geotechnical Software CPeT-IT Version 2.0, 2014, [Software] Available from [geologismiki.gr](http://geologismiki.gr).

Ghofrani H., G.M. Atkinson, (2014), Site condition evaluation using horizontal-to-vertical response spectral ratios of earthquakes in the NGA-West 2 and Japanese databases. *Soil Dynamics and Earthquake Engineering*, Vol. 67, 2014.

Glass, R.L., 1988, Map Showing Depth to Bedrock, Anchorage, Alaska. Open File Report 88-198, USGS. 1988. doi: 10.3133/ofr88198

Goldstein, P., A. Snoke, 2005, "SAC Availability for the IRIS Community", Incorporated Institutions for Seismology Data Management Center Electronic Newsletter.

Goldstein, P., D. Dodge, M. Firpo, L. Minner, 2003, SAC2000: Signal processing and analysis tools for seismologists and engineers, Invited contribution to The IASPEI International Handbook of Earthquake and Engineering Seismology, Edited by WHK Lee, H. Kanamori, P.C. Jennings, and C. Kisslinger, Academic Press, London.

Goulet, C., Y. Bozorgnia, N. Abrahamson, N. Kuehn, L. Al Atik, R. Youngs, R. Graves, G. Atkinson, 2018, Central and Eastern North America Ground-Motion Characterization, NGA-East Final Report, Pacific Earthquake Engineering Research Center, PEER Report No. 2018/08.

Guéguen, P., L.F. Bonilla, J. Douglas, 2018, Comparison of Soil Nonlinearity (In Situ Stress–Strain Relation and  $G/G_{max}$  Reduction) Observed in Strong-Motion Databases and Modeled in Ground-Motion Prediction Equations. *Bulletin of the Seismological Society of America*; 109 (1): 178–186. doi: <https://doi.org/10.1785/0120180169>

Haeussler, P. J. 2008. An overview of the neotectonics of interior Alaska: Far-field deformation from the Yakutat microplate collision, in *Active Tectonics and Seismic Potential in Alaska*, J. T. Freymueller, P. J. Haeussler, R. Wesson, and G. Ekström (Editors), *Geophysics Monograph Series*, Vol. 179, American Geophysical Union, Washington, D.C., 83–108, doi: 10.1029/179GM05.

Haeussler, P.J., Bruhn, R.L., and Pratt, T.L, 2000, Potential seismic hazards and tectonics of the upper Cook Inlet basin, Alaska, based on analysis of Pliocene and younger deformation: *Geological Society of America Bulletin*, vol. 112, no. 9, p. 1414-1429.

Haessler, P.J, T.C. Best, and C.F. Waythomas, 2002, Paleoseismicity at high latitudes: Seismic disturbance of late Quaternary deposits along the Castle Mountain fault near Houston, Alaska, *Geological Society of America Bulletin*, 114, 1296-1310.

Hanks, T. and R. McGuire, 1981. "The character of high-frequency strong ground motion." *Bulletin of the Seismological Society of America*, Vol. 71, No. 6, pp. 2071-2095.

Hansen, W. R. 1965. Effects of the earthquake of March 27, 1964, at Anchorage, Alaska, U.S. Geol. Surv. Profess. Pap. (542-A), 68 pp.

Harding-Lawson Associates, 1979, "Seismically-Induced Ground Failure Susceptibility", Geotechnical Report for Municipality of Anchorage, Alaska.

Harmon J, Y.M.A Hashash, J.P Stewart, E.M. Rathje, K.W. Campbell, W.J. Silva, O. Ilhan, 2019, Site Amplification Functions for Central and Eastern North America – Part II: Modular Simulation-Based Models. *Earthquake Spectra*. 2019;35(2):815-847. doi:10.1193/091117EQS179M

Hashash, Y. 2014, 2014 Ralph B. Peck Lecture: Innovations in Modeling and Monitoring Technology for Response of Deep Urban Excavations, American Society of Civil Engineers Geo-Congress, Atlanta, GA, 2014.

Hashash, Y.M.A., S. Dashti, M.I. Romero, M. Ghayoomi, M. Musgrove, Evaluation of 1-D seismic site response modeling of sand using centrifuge experiments, *Soil Dynamics and Earthquake Engineering*, Volume 78, 2015, Pages 19-31, doi: 10.1016/j.soildyn.2015.07.003.

Hashash, Y.M.A., J. Harmin, O. Ilhan, J.P. Stewart, E.M. Rathje, K.W. Campbell, W.J. Silva, C.A. Goulet, 2018, Modelling of Site Amplifications via Large Scale Nonlinear Simulations with Applications to North America, *Geotechnical Earthquake Engineering and Soil Dynamics V*, GSP 291, American Society of Civil Engineers, 2018.

Hassani, B., G.M. Atkinson, 2016, Applicability of the Site Fundamental Frequency as a VS30 Proxy for Central and Eastern North America. *Bulletin of the Seismological Society of America*; 106 (2): 653–664. doi: <https://doi.org/10.1785/0120150259>

Havskov, J. and L. Ottemoller, 2010, *Routine Data Processing in Earthquake Seismology*, Springer, 2010, DOI: 10.1007/978-90-481-8697-6.

Hayes, G., 2018, Slab2 - A Comprehensive Subduction Zone Geometry Model: U.S. Geological Survey data release, doi: 10.5066/F7PV6JNV.

Hayes, G., G. Moore, D. Portner, M. Hearne, et al., 2018, Slab2, a comprehensive subduction zone geometry model. *Science*, 362, p. 58-61, 2018.

Helffrich, G., J. Wookey, and I. Bastow, 2013. *The Seismic Analysis Code, A Primer and User's Guide*. Cambridge University Press, 2013.

Ibs-von Seht, M. and J. Wohlenberg, 1999, Microtremor Measurements Used to Map Thickness of Soft Sediments, *Bulletin of the Seismological Society of America* 89, 250-259.

Idriss, I.M., 1990, "Response of soft soil sites during earthquakes," in J.M. Duncan, ed Proceedings, H. Bolton Seed Memorial Symposium, BiTech Publishers, Vancouver, British Columbia, Vol. 2, pp. 273-289.

Idriss, I. M., 2011. Use of VS30 to represent local site conditions, in 4th LASPEI/IAEE International Symposium Effects of Surface Geology on Strong Ground Motions, Santa Barbara, CA.

Idriss, I.M. and J.I Sun, 1992. Shake91: A computer program for conducting equivalent linear seismic response analysis of horizontally layered soil deposits. User's Guide, Center for Geotechnical Modeling, Civil Engineering Department, UC Davis.

Kanamori, H., (1983). Magnitude scale and quantification of earthquakes. *Tectonophysics*, 93, 185-199.

Kim, B., Y.M. Hashash, J.P. Stewart, E.M. Rathje, J.A. Harmon, M.I. Musgrove, K. W. Campbell, W.J. Silva, 2016, Relative Differences between Nonlinear and Equivalent-Linear 1-D Site Response Analyses, *Earthquake Spectra*, Volume 32, No. 3, pp. 1845-1865, August 2016.

Klin, P., 2019, GITANES (<https://www.mathworks.com/matlabcentral/fileexchange/61711-gitanes>), MATLAB Central File Exchange. Retrieved August 2019.

Klin P, L. Laurenzano, E. Priolo, 2018, GITANES: a MATLAB package for joint estimation of site spectral amplification and seismic source spectra with the generalized inversion technique, *Seismological Research Letters* 89(1):182–190. <https://doi.org/10.1785/0220170080>.

Koehler, R.D., 2013, Quaternary Faults and Folds (QFF): Alaska Division of Geological & Geophysical Surveys Digital Data Series 3. Koehler, R.D., Burns, P.A.C., and Weakland, J.R., 2013, Digitized faults of the Neotectonic map of Alaska (Plafker and others, 1994), in Koehler, R.D., Quaternary Faults and Folds (QFF): Alaska Division of Geological & Geophysical Surveys Miscellaneous Publication 150, 1 p.

Koehler, R.D., R.E. Farrell, P.A.C. Burns, and R.A. Combellick, 2012, Quaternary faults and folds in Alaska: A digital database, in Koehler, R.D., Quaternary Faults and Folds (QFF): Alaska Division of Geological & Geophysical Surveys Miscellaneous Publication 141, 31 p., 1 sheet, scale 1:3,700,000. <http://doi.org/10.14509/23944>.

Kottke, Albert R., and Ellen M. Rathje. (2008). "Technical manual for Strata." Report No.: 2008/10. Pacific Earthquake Engineering Research Center, University of California, Berkeley.



Kottke, A.R., X. Wang, and E.M. Rathje, 2019, Strata Technical Manual, <https://github.com/arkottke/strata>, last accessed January 24, 2021.

Kuehn, N., Y. Bozorgnia, K.W. Campbell, N. Gregor, 2020. Partially Non-Ergodic Ground-Motion Model for Subduction Regions using the NGA-Subduction Database, Report No.: 2020/04. Pacific Earthquake Engineering Research Center, University of California, Berkeley, September 2020.

Laurenzano, G., C. Barnaba, M.A. Romano, et al., 2019, The Central Italy 2016–2017 seismic sequence: site response analysis based on seismological data in the Arquata del Tronto–Montegallo municipalities, *Bulletin of Earthquake Engineering* 17, 5449–5469 (2019). <https://doi.org/10.1007/s10518-018-0355-3>

Liu, C., T. Lay, Z. Xie, and X. Xiong, 2019, Intraslab Deformation in the 30 November 2018 Anchorage, Alaska, MW7.1 Earthquake, *Geophysical Research Letters*, 2019, DOI: 10.1029/2019GL082041.

Martirosyan, A., U. Dutta, N. Biswas, A. Papageorgiou, and R. Combellick, 2002, Determination of site response in Anchorage, Alaska, on the basis of spectral ratio methods, *Earthquake Spectra* 18, 85–104.

Mazzoni, S., 2020. NGA-Subduction Ground-Motion Characterization Tool (Excel Version: June 2020), <https://www.risksciences.ucla.edu/nhr3/gmtools?rq=NGA%20Subduction>, last accessed September 2020.

McNamara, D.E., 2000, Frequency Dependent Lg Attenuation in South-Central Alaska, *Geophysical Research Letters*, Vol. 27, No. 23, December 1, 2000.

Mundepi, A.K., C. Lindholm, and Kamal, 2009, Soft Soil Mapping Using Horizontal to Vertical Spectral Ratio (HVSr) for Seismic Hazard Assessment of Chandigarh City in Himalayan Foothills, North India, *Journal Geological Society of India*, Vol. 74, November 2009, pp. 551-558.

National Academies of Sciences, Engineering, and Medicine (NASEM), 2012, Practices and Procedures for Site-Specific Evaluations of Earthquake Ground Motions. Washington, DC: The National Academies Press. <https://doi.org/10.17226/14660>.

Nath S.K., D. Chatterjee, N.N. Biswas, M. Dravinski, D.A. Cole, A. Papageorgiou, J.A. Rodriguez, and C.J. Poran, 1997, Correlation Study of Shear Wave Velocity in Near Surface Geological Formations in Anchorage, Alaska, *Earthquake Spectra*, Vol. 13, No. 1, February 1997.

Nielson, J.D., F.A. Ellis, 1976, Seismic Engineering Program Report, April-June 1976. U.S. Department of the Interior Geological Survey; 1976.

Oth, A., S. Parolai, D. Bindi, F. Wenzel, 2009, Source Spectra and Site Response from S Waves of Intermediate-Depth Vrancea, Romania, Earthquakes. *Bulletin of the Seismological Society of America*; 99 (1): 235–254. doi: <https://doi.org/10.1785/0120080059>

Parker, G.A, J.P Stewart, D.M. Boore, G.M. Atkinson, B. Hassani, NGA-Subduction Global Ground-Motion Models with Regional Adjustment Factors, Report No.: 2020/03. Pacific Earthquake Engineering Research Center, University of California, Berkeley, August 2020.

Parolai, S., D. Bindi, P. Augliera, 2000, Application of the Generalized Inversion Technique (GIT) to a Microzonation Study: Numerical Simulations and Comparison with Different Site-Estimation Techniques, *Bulletin of the Seismological Society of America*, 90, 2, pp. 286-297, April 2000, doi: <https://doi.org/10.1785/0119990041>

PEER, 2021, Timothy D. Ancheta, Robert B. Darragh, Jonathan P. Stewart, Emel Seyhan, Walter J. Silva, Brian S.J. Chiou, Katie E. Wooddell, Robert W. Graves, Albert R. Kottke, David M. Boore, Tadahiro Kishida, and Jennifer L. Donahue. PEER 2013/03 – PEER NGA-West2 Database web portal: [https://ngawest2.berkeley.edu/spectras/new?sourceDb\\_flag=1](https://ngawest2.berkeley.edu/spectras/new?sourceDb_flag=1), last accessed May 2021.

Porcella, R.L., 1978, Seismic Engineering Program Report, September-December 1977. United States Department of the Interior Geological Survey; 1978.

Porcella, R.L., 1979, Seismic Engineering Program Report, January-April 1979. United States Department of the Interior Geological Survey; 1979.

Porcella, R.L., 1980, Seismic Engineering Program Report, September - December 1979. U.S. Department of the Interior Geological Survey; 1980.

Porcella, R.L., 1983, Strong-Motion Program Report, January - December 1981. United States Department of the Interior Geological Survey; 1983.

Porcella, R.L., 1985, Strong-Motion Program Report, January - December 1982. Department of the Interior - U.S. Geological Survey; 1985.

Porcella, R.L., 1986, Strong-Motion Program Report, January-December 1984. Department of the Interior U.S. Geological Survey; 1986.

Porcella, R.L., 1989, Strong-Motion Program Report, January-December 1985. Department of the Interior U.S. Geological Survey; 1989.

Porcella, R.L., J.C. Switzer, 1989, Catalogue of U.S. Geological Survey Strong-Motion Records, 1987. U.S. Geological Survey; 1989.

Rathje, E.M. and A.R. Kottke, 2008, "Procedures for Random Vibration Theory Based Seismic Site Response Analyses: A White Paper Prepared for the Nuclear Regulatory Commission," Geotechnical Engineering Report GR08-09, Geotechnical Engineering Center, Department of Civil, Architectural, and Environmental Engineering, University of Texas at Austin, Austin, TX.

Régnier, J., L. Bonilla, P. Bard, E. Bertrand, F. Hollender, H. Kawase, D. Sicilia, P. Arduino, A. Amorosi, D. Asimaki, D. Boldini, L. Chen, A. Chiaradonna, F. DeMartin, A. Elgamal, G. Falcone, E. Foerster, S. Foti, E. Garini, G. Gazetas, C. Gélis, A. Ghofrani, A. Giannakou, J. Gingery, N. Glinesky, J. Harmon, Y. Hashash, S. Iai, S. Kramer, S. Kontoe, J. Kristek, G. Lanzo, A. di Lernia, F. Lopez-Caballero, M. Marot, G. McAllister, E. Diego Mercerat, P. Moczo, S. Montoya-Noguera, M. Musgrove, A. Nieto-Ferro, A. Pagliaroli, F. Passeri, A. Richterova, S. Sajana, M. Paola Santisi d'Avila, J. Shi, F. Silvestri, M. Taiebat, G. Tropeano, D. Vandeputte, L. Verrucci; PRENOLIN: International Benchmark on 1D Nonlinear Site-Response Analysis—Validation Phase Exercise. *Bulletin of the Seismological Society of America*, 2018; 108 (2): 876–900. doi: <https://doi.org/10.1785/0120170210>

Regnier, J., H. Cadet, L.F. Bonilla, E. Bertrand, J.F. Semblat, 2013. Assessing Nonlinear Behavior of Soils in Seismic Site Response: Statistical Analysis on KiK-net Strong-Motion Data, *Bulletin of the Seismological Society of America*, 103(3):1750-1770.

Ristau, J., Rogers, G. C., and Cassidy, J. F. (2005). Moment magnitude-local magnitude calibration for earthquakes in Western Canada. *Bulletin of the Seismological Society of America*, 95, 5, 1994-2000.

Robertson, P.K., 2009, Interpretation of Cone Penetration Tests – A Unified Approach. *Canadian Geotechnical Journal*, Vol 46, pp. 1337-1355.

Rojahn, C., 1974, Seismic Engineering Program Report, October-December 1974. United States Department of the Interior Geological Survey; 1974.

Ruppert, N., and R. Hansen, 2010, Temporal and Spatial Variations of Local Magnitudes in Alaska and Aleutians and Comparison with Body-Wave and Moment Magnitudes, *Bulletin of the Seismological Society of America*, 100(3): 1174-1183. <http://dx.doi.org/10.1785/0120090172>

Schmoll, H.R. and W.W. Barnwell, 1984, East-west geologic cross section along the DeBarr Line, Anchorage, Alaska: U.S. Geological Survey Open-File Report 84-791, 10 p., 1 sheet.

Schmoll, H.R., E. Dobrovlny, 1972, Generalized geologic map of Anchorage and vicinity, Alaska. US Geologic Survey Misc. Geol. Invest. Map I-787-D.

Seekins, L.C., A.G. Brady, C. Carpenter, N. Brown, 1992, Digitized Strong-Motion Accelerograms of North and Central American Earthquakes 1933-1986. In: Survey USG, editor. 1992.

Seyhan E. and J.P. Stewart, 2014, Semi-Emperical Nonlinear Site Amplifiacation from NGA-West2 Data and Simulations, *Earthquake Spectra*, Vol. 30, No. 3, pages 1241-1256, August 2014.

Shannon & Wilson, 1964, "Anchorage Area Soil Studies," U.S. Army Engineer District, Alaska, Corps of Engineers.

Silverstein, B.L., A.G. Brady, P.N. Mork, 1986, Processed strong-motion records from the southern Alaska earthquake of January 1, 1975, 0355 GMT. Menlo Park, California: United States Department of the Interior Geologic Survey; 1986 February 1986.

Smith, K., C. Tape, 2020, Seismic Response of Cook Inlet Sedimentary Basin, Southern Alaska, *Seismological Research Letters*, 91, 33-55, DOI: 10.1785/0220190205.

Souriau, A., A. Roullé, C. Ponsolles, 2007, Site Effects in the City of Lourdes, France, from H/V Measurements: Implications for Seismic-Risk Evaluation. *Bulletin of the Seismological Society of America*; 97 (6): 2118–2136. doi: <https://doi.org/10.1785/0120060224>

Stachnik, J.C., G.A. Abers, D.H. Christensen, 2004, Seismic Attenuation and Mantle Wedge Temperatures in the Alaska Subduction Zone, *Journal of Geophysical Research*, Vol. 109, B10304, DOI:10.1029/2004JB003018.

Steidl, J.H., A.G. Tumarkin, R.J. Archuleta, 1996, What is a Reference Site?, Bulletin of the Seismological Society of America, 86, 6, pp. 1733-1748, December 1996.

Strata Equivalent Linear Site Response Software Version 0.5.9, 2017, [Software] Available from [github.com/arkottke/strata](https://github.com/arkottke/strata).

Stewart, J.P., K. Afshari, Y.M.A. Hashash, 2014, Guidelines for Performing Hazard-Consistent One-Dimensional Ground Response Analysis for Ground Motion Prediction, Pacific Earthquake Engineering Research Center, Report 2014/16, October 2014.

Switzer, J.C., R.L. Porcella, 1995, Catalogue of U.S. Geological Survey Strong-Motion Records, 1993. U.S. Geological Survey; 1995.

Switzer, J.C., R.L. Porcella, 1990, Catalogue of U.S. Geological Survey Strong-Motion Records, 1988. U.S. Geological Survey; 1990.

Thornley, J.D., U. Dutta and Z. Yang, 2013, Modeling the Site Response of a Downhole Array Site in Anchorage, Alaska. Seismological Society of America Annual Conference, April 2013. Salt Lake City, Utah. – Poster.

Thornley, J.D., U. Dutta and Z. Yang, 2014a, Modeling the Site Response of a Downhole Array Site in Anchorage, Alaska. 10th US National Conference on Earthquake Engineering, July. Anchorage, Alaska.

Thornley, J.D., U. Dutta and Z. Yang, 2014b, Calibration and Evaluation of Response Spectra in the Downtown Area of Anchorage, Alaska. Seismological Society of America Annual Conference, April 2014. Anchorage, Alaska. – Poster.

Thornley, J., Dutta, U., Fahringer, P., Yang, Z., 2019, In Situ Shear-Wave Velocity Measurements at the Delaney Park Downhole Array, Anchorage, Alaska. *Seismological Research Letters*, Volume 90, Number 1, January/February 2019 (p 395-400).

Thornley, J., U. Dutta, Z. Yang, J. Douglas, 2020, Nonlinear Site Response Analysis at the Delaney Park Downhole Array in Anchorage, Alaska, 17th World Conference on Earthquake Engineering, 17WCEE, Paper No. C004020.

Thornley, J., U. Dutta, J. Douglas, Z. Yang, 2021, Nonlinear Site Effects from the 30 November 2018 Anchorage, Alaska, Earthquake. Bulletin of the Seismological Society of America; in publication. doi: 10.1785/0120200347

Thornley, J., J. Douglas, U. Dutta, Z. Yang., 2021a, Site Response Analysis of Anchorage, Alaska Using Generalized Inversions of Strong-Motion Data (2014-2019), *Geophysical Journal International* (In Review).

Thornley, J., U. Dutta, J. Douglas, Z. Yang., 2021b, Evaluation of Horizontal to Vertical Spectral Ratio and Spectral Amplitude Methods for Estimating Shear Wave Velocity in Anchorage, (In Review).

Thornley, J., J. Douglas, U. Dutta, Z. Yang, 2021c, Engineering Site Response Analysis of Anchorage, Alaska Using Site Amplifications and Random Vibration Theory, *Earthquake Spectra* (In Review).

Ulery, C.A., and R.G. Updike, 1983, Subsurface structure of the cohesive facies of the Bootlegger Cove formation, southwest Anchorage: Alaska Division of Geological & Geophysical Surveys Professional Report 84, 5 p., 3 sheets, scale 1:15,840. <http://doi.org/10.14509/2257>

University of California Santa Barbara (UCSB), 2021, <http://www.nees.ucsb.edu/data-portal> last accessed March 2021.

Updike, R.G. and C.A. Ulery, 1986a, A Geotechnical Cross Section of Downtown Anchorage: An Assessment Using the Electric-Cone-Penetration Test, State of Alaska Department of Natural Resources Division of Geological and Geophysical Surveys, 45 pages, June 1986.

Updike, R.G. and C.A. Ulery, 1986b, Engineering-Geologic Map of Southwest Anchorage, Alaska. Alaska Division of Geological and Geophysical Surveys Professional Report 89, sheet 1 of 1.

U.S. Bureau of the Census, 1963, U.S. Census of Population: 1960, Vol. I, Characteristics of the Population. Part 3, Alaska. U.S. Government Printing Office, Washington, D.C., 1963.

USGS.gov, 2020, <https://earthquake.usgs.gov/earthquakes/events/alaska1964/>, last accessed May 30, 2020.

USGS.gov, 2021, <https://earthquake.usgs.gov/hazards/interactive/>, last accessed May 1, 2021.

Wair, B.R., J.T. DeJong, T. Shantz, 2012, Guidelines for Estimation of Shear Wave Velocity Profiles. Pacific Earthquake Engineering Research Center, PEER Report 2012/08, 95 pages, December 2012.

Wesson, R.L., O.S. Boyd, C.S. Mueller, C.G. Bufe, A.D. Frankel, M.D. Petersen, 2007, Revision of time-Independent probabilistic seismic hazard maps for Alaska: U.S. Geological Survey Open-File Report 2007-1043.

West, M. E., A. Bender, M. Gardine, L. Gardine, K. Gately, P. Haeussler, W. Hassan, F. Meyer, C. Richards, N.A. Ruppert, C. Tape, J. Thornley, and R.C. Witter, 2020, The 30 November 2018 Mw 7.1 Anchorage Earthquake. *Seismological Research Letters*, 91(1), 66–84. DOI: 10.1785/0220190176

Wilson, F. H.; C.P. Hults, H.R. Schmoll, P.J. Haeussler, 2012, Geologic map of the Cook Inlet region, Alaska, including parts of the Talkeetna, Talkeetna Mountains, Tyonek, Anchorage, Lake Clark, Kenai, Seward, Iliamna, Seldovia, Mount Katmai, and Afognak 1:250,000-scale quadrangles. Reston, VA, p. i-71. 2012. (3153).

Xiong, F., and Z. Yang, 2008, Effects of Seasonally Frozen Soil on the Seismic Behavior of Bridges, *Cold Regions Science and Technology*, 54 (2008) pp.44-53.

Yaghmaei-Sabegh, S., B. Hassani, 2020, Investigation of the relation between Vs30 and site characteristics of Iran based on horizontal-to-vertical spectral ratios. *Soil Dynamics and Earthquake Engineering*, Vol. 128, January 2020, <https://doi.org/10.1016/j.soildyn.2019.105899>

Yang, Z., U. Dutta, M. Celebi, H. Liu, N. Biswas, T. Kono, H. Benz, 2004, Strong-Motion Instrumentation and Structural Response at Atwood Building in Downtown Anchorage, Alaska, 13th World Conference on Earthquake Engineering, Vancouver, B.C., Canada, August 1-6, 2004, Paper No. 1136.

Zhu, C., F. Cotton, and M. Pilz, 2020, Detecting Site Resonant Frequency Using HVSR: Fourier versus Response Spectrum and the First versus the Highest Peak Frequency, *Bulletin of the Seismological Society of America* 110, 427–440, doi: 10.1785/0120190186

## Appendix A



Appendix A-1: List of Stations and  $V_{S30}$  Estimates and the  $f_{peak}$  and  $A_{peak}$  results from the HVSR analysis.

Station Code	Latitude (°N)	Longitude (°W)	$V_{S30}$ Estimate (m/s)	$V_{S30}$ Measured (m/s) <sup>1,2</sup>	$f_{peak}$ Hz	$A_{peak}$
K203	61.22007	149.7453	513	474 <sup>1</sup>	3.78	3.82
K204	61.17581	150.0114	285	309 <sup>1</sup>	0.68	4.40
K205	61.19963	149.9138	224	284 <sup>1</sup>	1.09	4.47
K207	61.15957	150.0044	272	270 <sup>1</sup>	1.68	3.35
K208	61.17646	149.9215	213	274 <sup>1</sup>	2.50	4.59
K209	61.18455	149.7471	488	582 <sup>1</sup>	4.42	3.85
K210	61.12923	149.9310	235	269 <sup>1</sup>	2.55	3.47
K211	61.14905	149.8578	402	394 <sup>1</sup>	2.61	4.18
K212	61.15622	149.7916	594	514 <sup>1</sup>	5.77	5.22
K213	61.11262	149.8595	383	354 <sup>1</sup>	3.37	5.01
K214	61.12353	149.7677	488	524 <sup>1</sup>	2.09	5.51
K215	61.08625	149.7521	465	412 <sup>1</sup>	3.14	5.15
K220	61.15404	150.0553	330		0.57	2.69
K221	61.15245	149.9510	193	277 <sup>1</sup>	0.98	5.16
K222	61.08757	149.8366	315		0.86	2.92
K223	61.2338	149.8675	224		0.92	4.05
2704	61.21883	149.8940	224		0.98	3.77
8007	61.18236	149.9968	235		0.68	3.73
8011	61.20898	149.7857	513		3.08	2.79
8021	61.11293	149.9095	513	428 <sup>1</sup>	4.07	2.91
8023	61.20469	149.8762	402		4.60	6.38
8024	61.18314	149.8853	402		3.26	4.36
8025	61.14716	149.8939	439		4.36	4.21
8026	61.20890	149.8289	383		4.01	5.01
8027	61.16087	149.8894	330		2.96	3.88
8028	61.19264	149.7823	565		4.54	3.08
8029	61.17392	149.8503	488	520 <sup>1</sup>	2.43	3.94
8030	61.17949	149.8058	538		3.90	4.05
8036	61.17794	149.9657	213		0.62	3.79
8037	61.15625	149.9850	246		1.79	3.76
8038	61.21844	149.8829	235		1.03	4.06
8039	61.14162	149.9512	137		20.3	4.78
8040	61.21350	149.8930	264	264 <sup>2</sup>	1.15	4.90
8041	61.19438	149.9471	167		0.68	4.23

Note: 1. Measurements from Dutta et al. 2000. 2. Measurement from Thornley et al. 2019.

Appendix A-2: List of Events

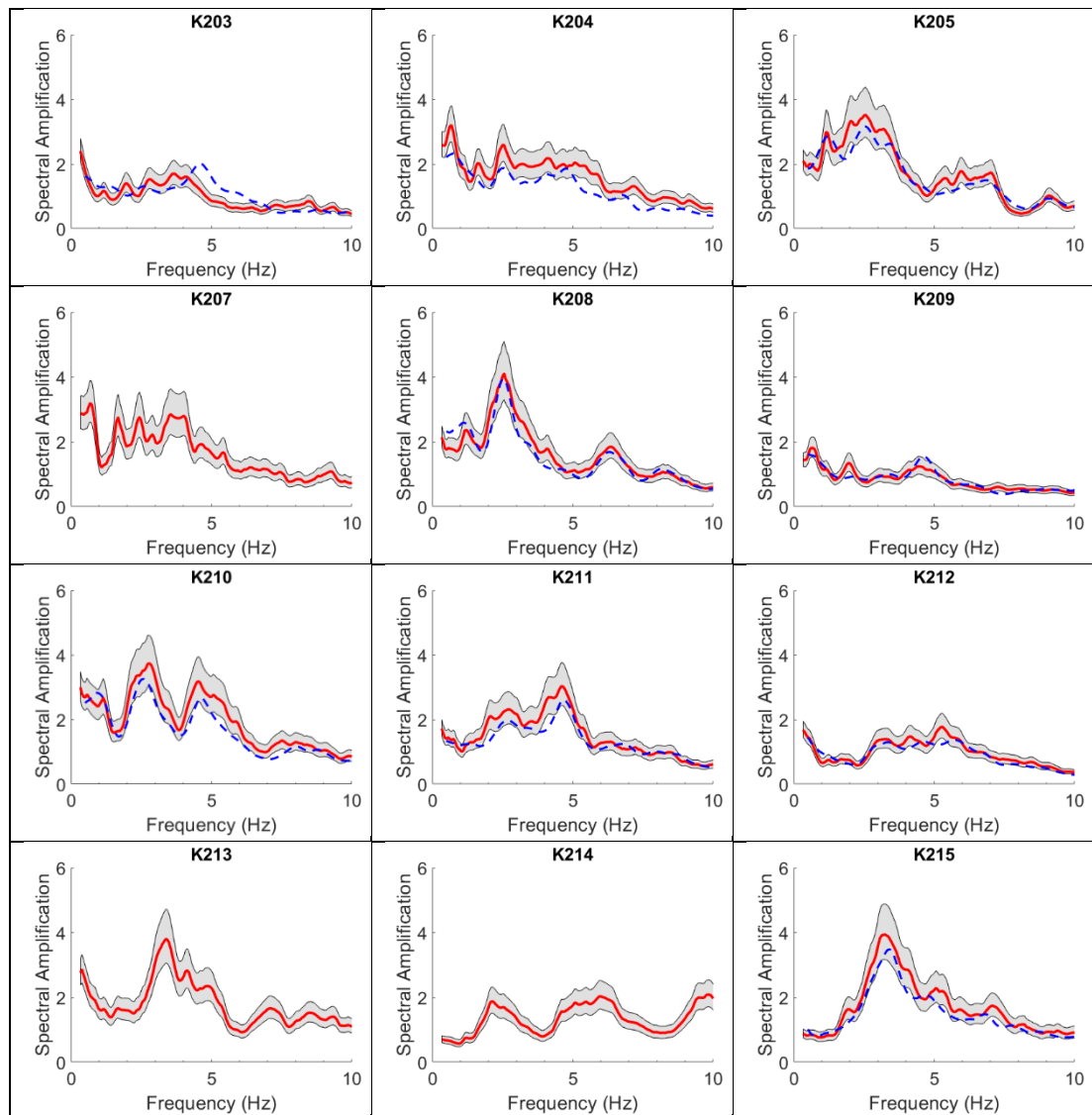
<b>Date (YYYY-MM-DD)</b>	<b>Latitude (°N)</b>	<b>Longitude (°W)</b>	<b>Depth (km)</b>	<b>Magnitude (M<sub>w</sub>)</b>
2005-02-16	61.326	149.853	35	4.6
2005-04-06	61.454	146.518	17	4.8
2005-04-17	60.771	149.311	27	4.5
2005-05-19	60.017	152.693	96	5.4
2005-08-15	60.130	152.675	103	4.5
2006-03-03	59.791	153.062	99	4.8
2006-03-17	60.706	152.024	81	4.7
2006-06-18	61.926	150.427	61	4.7
2006-07-27	61.155	149.678	36	4.7
2006-09-06	61.621	149.930	41	4.5
2007-09-19	61.375	146.105	31	4.5
2007-11-28	61.911	151.127	70	5.0
2008-03-27	59.010	152.169	69	5.3
2008-04-26	63.020	151.556	12	4.6
2008-09-18	59.503	152.793	90	4.5
2008-10-08	60.115	152.640	104	4.8
2008-10-12	63.161	150.553	123	4.6
2008-11-09	59.997	153.019	127	5.0
2008-11-29	63.111	149.577	95	4.7
2008-12-13	60.886	150.859	46	4.6
2008-12-28	62.346	151.055	89	4.7
2009-01-24	59.430	152.888	98	5.8
2009-02-15	61.603	146.334	37	4.5
2009-04-07	61.454	149.743	33	4.8
2009-04-10	63.495	151.737	14	4.7
2009-04-14	60.158	153.057	118	4.5
2009-04-30	58.993	151.311	53	5.0
2009-05-24	59.775	153.249	125	4.6
2009-06-22	61.939	150.704	65	5.4
2009-08-19	61.228	150.858	66	5.1
2010-04-07	61.580	149.652	35	4.6
2010-05-24	59.982	152.311	71	4.6
2010-07-08	61.805	150.505	15	4.8
2010-08-14	59.965	153.209	141	4.6
2010-09-15	59.861	153.176	121	5.0
2010-09-20	61.115	150.219	45	4.9

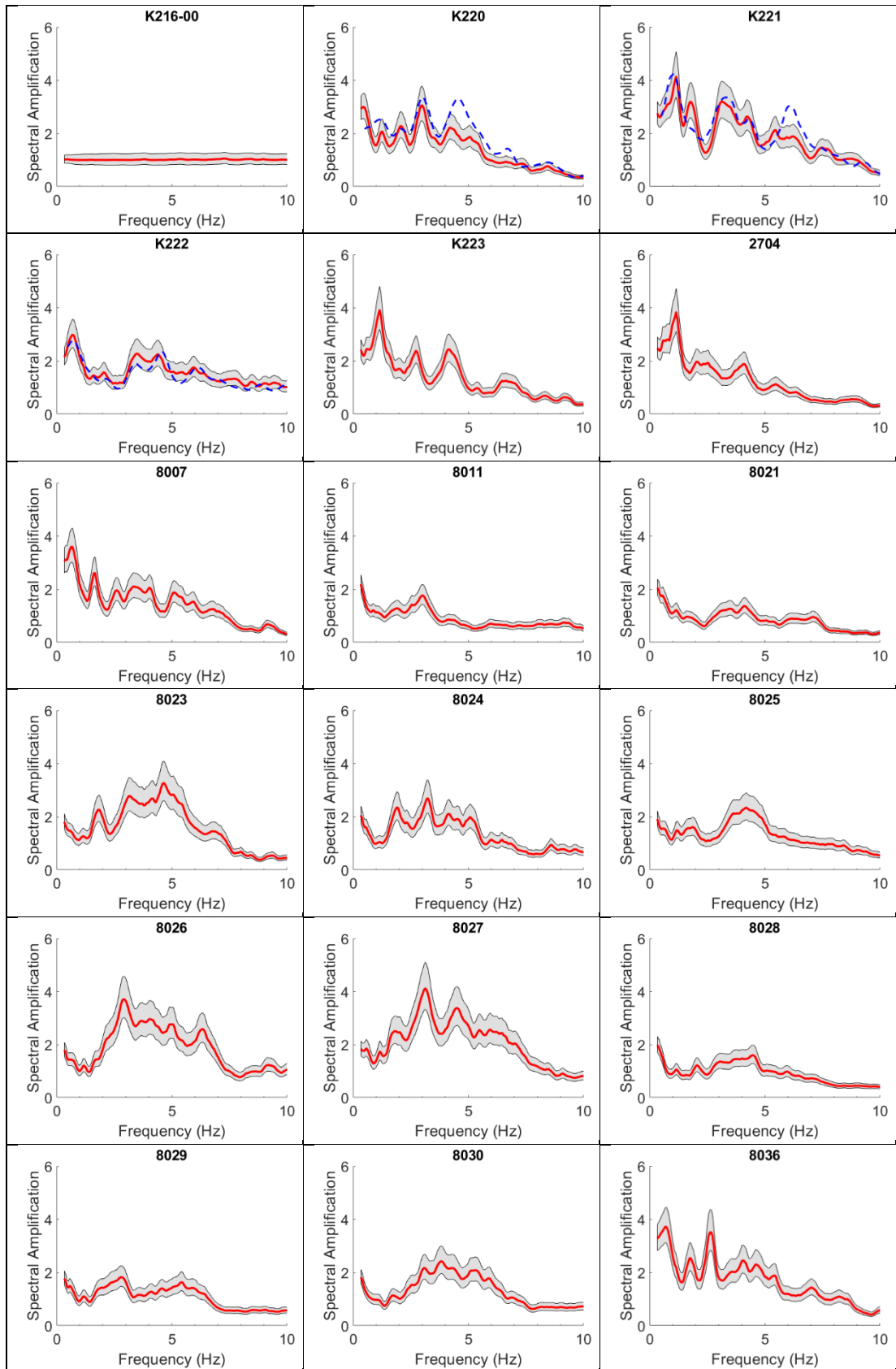
<b>Date (YYYY-MM-DD)</b>	<b>Latitude (°N)</b>	<b>Longitude (°W)</b>	<b>Depth (km)</b>	<b>Magnitude (M<sub>w</sub>)</b>
2011-01-23	63.542	150.865	16	5.2
2011-02-04	60.725	150.276	41	4.5
2011-07-28	62.049	151.303	87	5.3
2013-01-13	60.541	152.904	134	5.0
2013-03-13	62.556	151.230	84	4.7
2013-08-01	60.145	152.918	126	4.8
2013-08-27	63.213	150.624	128	4.9
2014-03-12	59.296	153.177	86	4.5
2014-03-30	62.224	151.144	72	5.1
2015-07-06	62.130	150.789	71	4.9
2015-07-25	61.949	152.052	126	5.1
2015-07-29	59.894	153.196	119	6.3
2016-01-18	62.103	150.640	10	4.5
2016-01-24	59.719	153.168	107	4.6
2016-01-24	59.731	153.146	107	4.9
2016-01-24	59.620	153.339	126	7.1
2016-01-25	59.744	153.158	108	4.5
2016-01-28	59.699	153.166	107	4.6
2016-02-03	60.333	153.546	189	4.6
2016-02-09	59.788	152.975	108	4.5
2016-02-10	59.719	153.166	106	4.5
2016-02-10	59.713	153.154	106	4.6
2016-03-12	60.261	152.304	100	4.7
2017-01-26	62.008	152.390	142	4.5
2017-01-31	63.071	150.906	117	5.4
2017-03-02	59.579	152.655	78	5.3
2017-04-29	63.123	151.166	12	5.0
2017-05-07	60.183	151.680	67	5.0
2017-05-30	60.838	151.828	78	5.1
2017-08-11	60.067	152.477	96	4.8
2017-08-31	63.012	150.538	105	4.5
2017-10-19	59.745	153.132	102	4.8
2017-11-05	60.225	153.076	140	4.9
2017-11-27	60.555	147.430	17	5.1
2018-03-09	59.751	153.126	100	4.9
2018-07-01	63.068	150.797	117	4.9
2018-07-10	62.979	150.636	113	4.9
2018-10-15	61.287	150.522	72	4.5

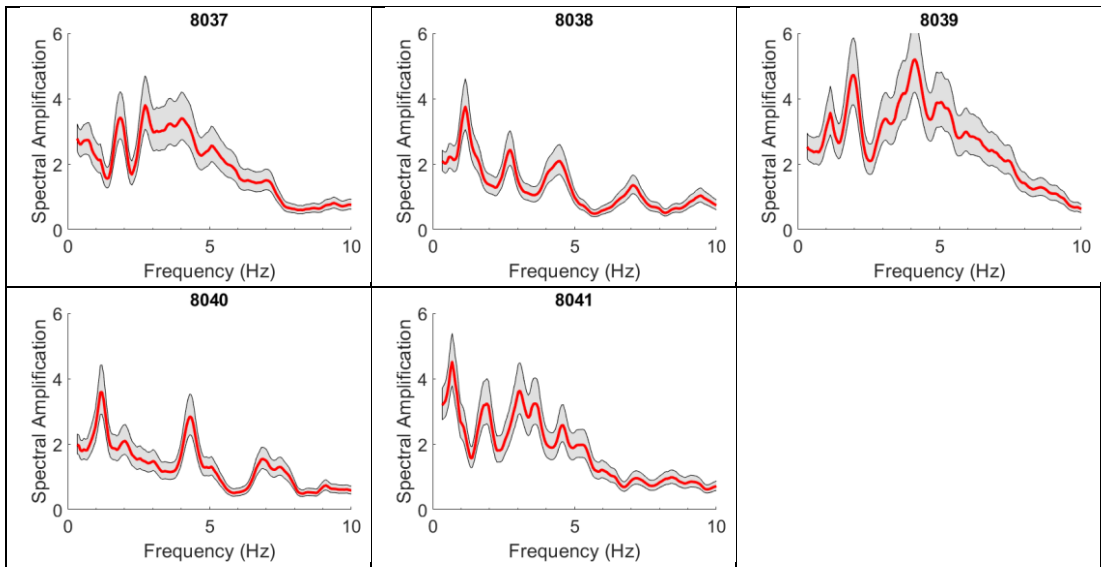
<b>Date (YYYY-MM-DD)</b>	<b>Latitude (°N)</b>	<b>Longitude (°W)</b>	<b>Depth (km)</b>	<b>Magnitude (M<sub>w</sub>)</b>
2018-11-21	59.955	153.266	143	5.5
2018-11-30	61.398	149.998	47	4.5
2018-11-30	61.479	149.923	37	4.5
2018-11-30	61.283	149.908	46	4.8
2018-11-30	61.384	150.080	38	4.9
2018-11-30	61.459	149.954	40	5.2
2018-11-30	61.282	149.957	41	5.5
2018-11-30	61.346	149.955	47	7.1
2018-12-01	61.473	149.898	34	4.5
2018-12-01	61.376	149.978	45	4.5
2018-12-01	61.483	149.936	51	4.9
2018-12-01	61.355	149.991	43	5.0
2018-12-02	61.325	149.901	52	4.5
2018-12-04	61.394	150.076	38	4.5
2018-12-05	61.323	150.053	42	4.5
2018-12-06	61.341	149.955	43	4.7
2018-12-09	61.420	149.837	41	4.7
2019-01-01	61.298	149.952	44	4.9
2019-01-11	61.471	149.899	50	4.5
2019-01-13	61.299	150.065	45	4.9
2019-01-23	61.503	150.237	46	4.5

### Appendix A-3: Strong-motion Station Spectral Amplification

Spectral Amplification Plots for the 35 Stations in this study. Twelve of the Stations in this study were also included in Dutta et al. (2003). The spectral amplification results from that study are included on the relevant Stations with a dashed blue line.

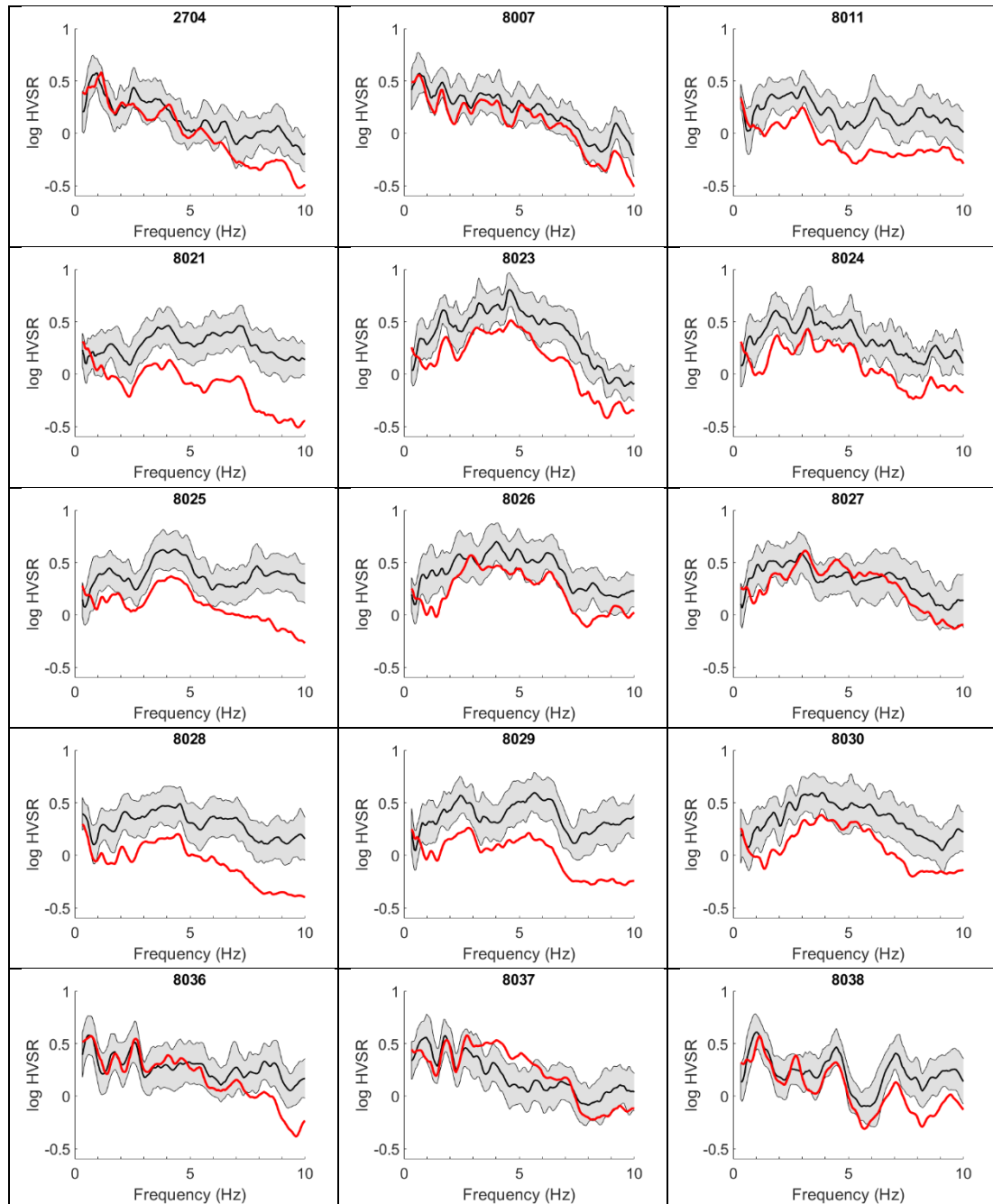




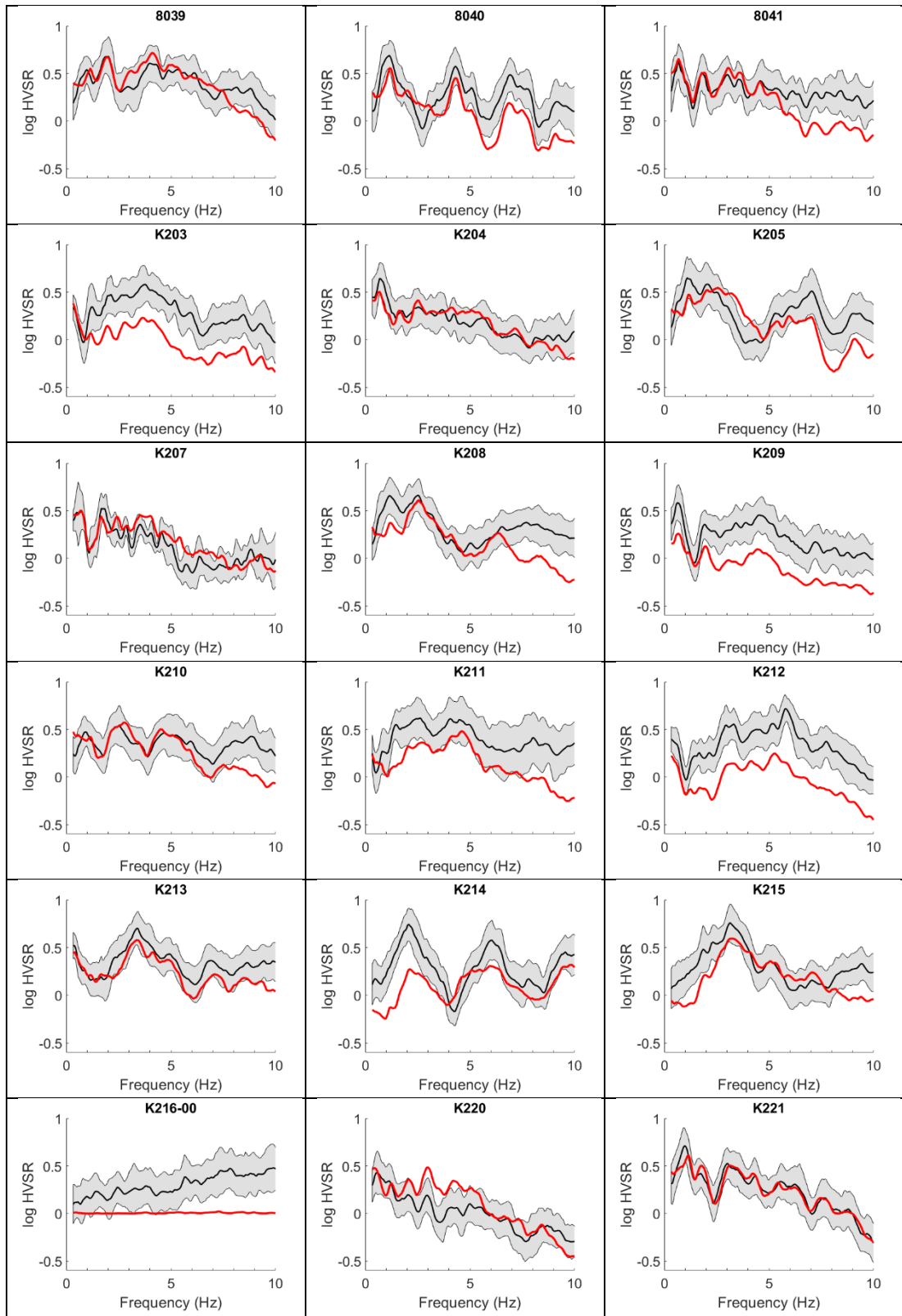


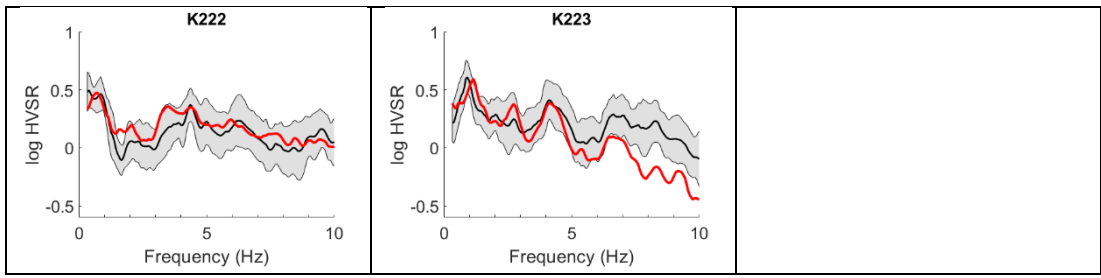
## Appendix A-4: Horizontal to Vertical Spectral Ratios

Strong-motion Station Horizontal to Vertical Spectral Ratio (HVSr) Plots, where the black line and grey shading are the median HVSr results with the standard error and the red line indicates the average SSR of each station.







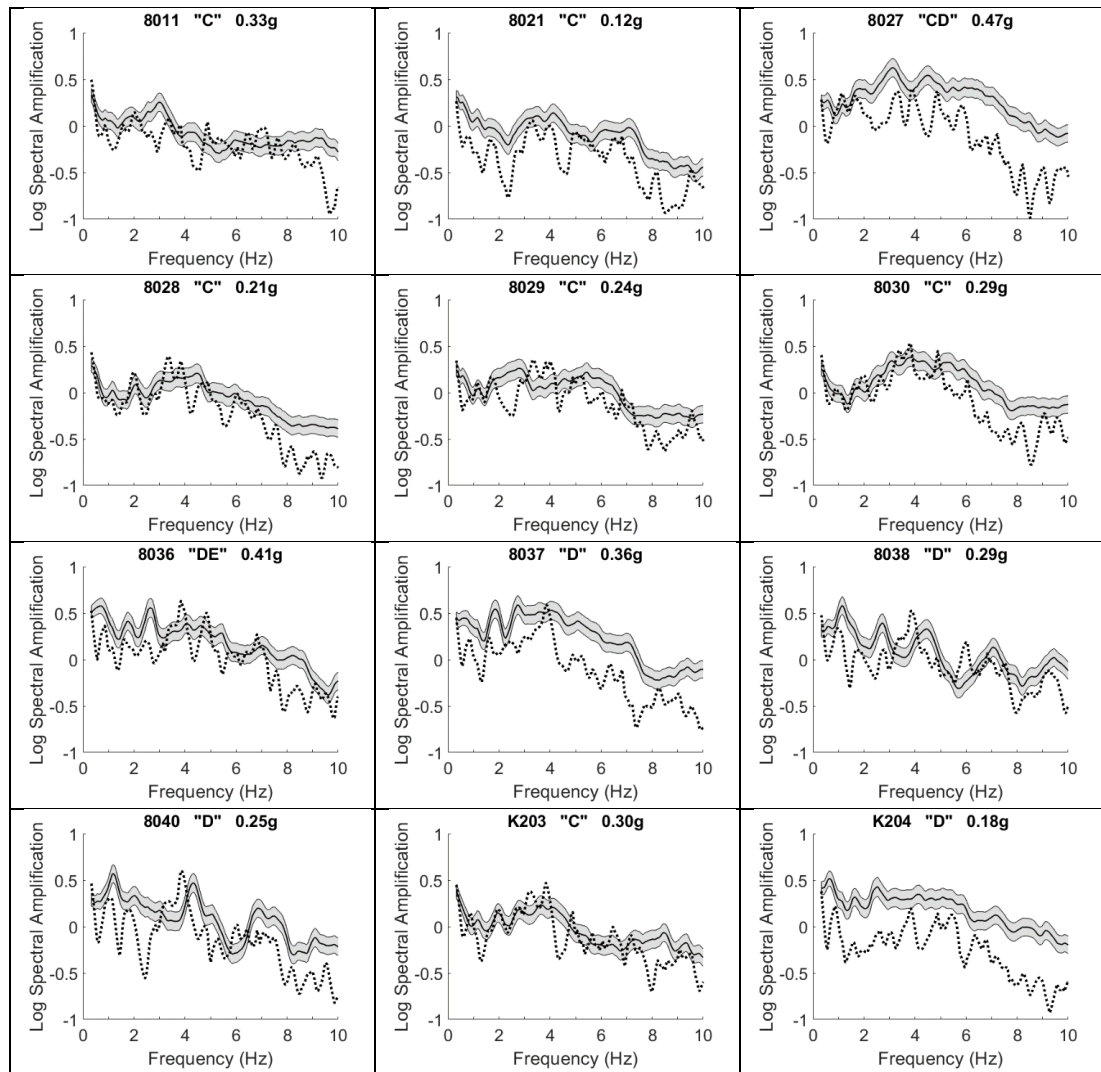


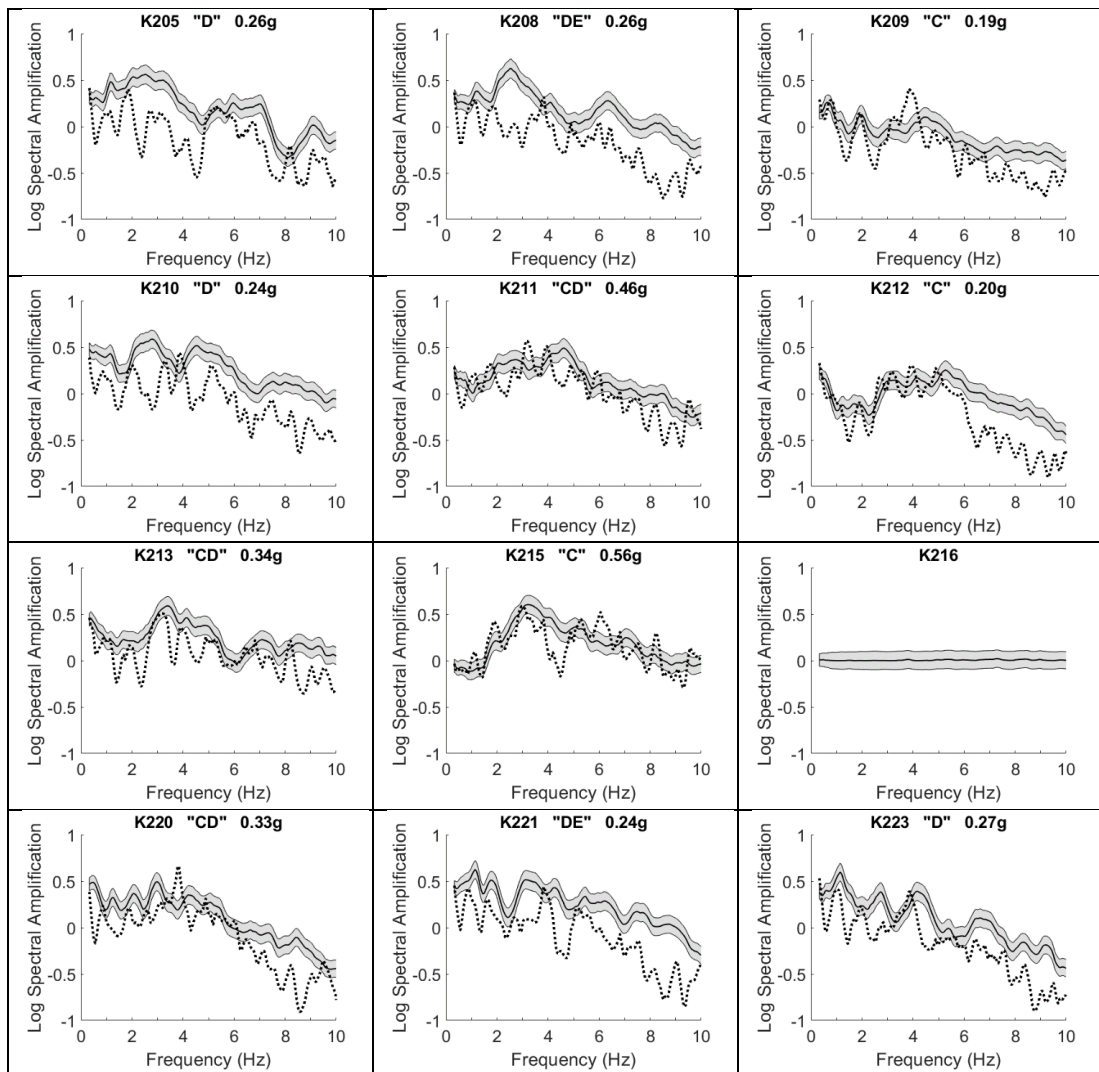
Appendix A-5:  $V_{S30}$  Data (Dutta et al. 2000)

Site ID	Latitude (°N)	Longitude (°W)	$V_{S30}$ (m/s)
An02	61.075	149.807	538
An03	61.114	149.820	420
An09	61.153	149.929	250
An10	61.189	150.015	315
An11	61.186	149.875	401
An12	61.191	149.824	499
An13	61.181	149.720	571
An14	61.210	149.909	253
An16	61.249	149.818	278
An17	61.223	149.725	453
An21	61.186	149.938	263
An22	61.137	149.890	380
S-07	61.155	149.897	313
S-22	61.112	149.805	504
S-38	61.215	149.763	448
S-39	61.098	149.832	514
S-43	61.203	149.795	451
S-55	61.220	149.785	408
S-66	61.131	149.830	445
S-69	61.170	149.873	376
S-73	61.197	149.890	404

## Appendix A-6: Spectral Amplifications – Nonlinear Site Response

Station spectral amplification results with database average and standard error shown with the solid black line and grey shading and  $M_w7.1$  Anchorage Earthquake shown with the dotted black line. K216 is the reference station for the study. The site class, from estimated  $V_{s30}$  and the PGA from the November 2018  $M_w7.1$  earthquake, are included with the station name for each station.





## **Appendix B: NONLINEAR SITE RESPONSE ANALYSIS AT THE DELANEY PARK DOWNHOLE ARRAY IN ANCHORAGE, ALASKA**

J.D. Thornley<sup>(1)</sup>, U. Dutta<sup>(2)</sup>, Z. Yang<sup>(3)</sup>, J. Douglas<sup>(4)</sup>

<sup>(1)</sup> Geotechnical Engineer, Golder Associates and University of Strathclyde Glasgow  
john\_thornley@golder.com

<sup>(2)</sup> Associate Professor, University of Alaska Anchorage, udutta2@alaska.edu

<sup>(3)</sup> Professor, University of Alaska Anchorage, zyang2@alaska.edu

<sup>(4)</sup> Senior Lecturer, University of Strathclyde Glasgow, john.douglas@strath.ac.uk

17<sup>th</sup> World Conference on Earthquake Engineering, 17WCEE, Paper No. C004020.

### **Abstract**

On November 30, 2018 Anchorage, Alaska was struck by a  $M_w$ 7.1 earthquake, the largest earthquake since the 1964 Great Alaska Earthquake to shake the city. Numerous strong motion instruments recorded the earthquake, including the Delaney Park Downhole Array (DPDA). The DPDA consists of seven strong-motion three-component accelerometers at depths ranging from the surface to 61 meters below ground, which includes the Bootlegger Cove formation, responsible for the significant ground failures in 1964. Significant improvements related to modeling ground response at the DPDA have been achieved by the authors over the past several years to better estimate the larger magnitude ground shaking, in the absence of larger events. With the data collected during the 2018 Anchorage Earthquake at the DPDA a comparison can now be made between the model, calibrated with earthquakes of lesser intensity, and the recent measured large ground motion.

The DPDA model provides a good fit of the large earthquake ground motion response and gives greater confidence for the analysis of site response within downtown Anchorage. There are some limitations to the equivalent-linear model with respect to nonlinear behavior of soil in large earthquakes where larger shear strains are developed. An evaluation of the modeled response with respect to estimation methods for nonlinear effects utilizing recent strain proxies is presented. The model is extended into a nonlinear analysis and verified to the measured ground motions. Once calibrated, the nonlinear model

was used to evaluate the attenuation behavior of the Bootlegger Cove formation using other measured earthquake ground motions. The results of these evaluations create the groundwork for changes proposed to local building codes related to slope stability analysis within Anchorage. Proposed Anchorage building code improvements are highlighted in the conclusions.

*Keywords: downhole array, nonlinear site response, model validation, Anchorage earthquake, strong ground motion*

## **1. Introduction**

The city of Anchorage is home to approximately half of Alaska's population and is located within a highly seismogenic zone. This zone is comprised of the Pacific plate underthrusting the North American plate at a rate of greater than 50 mm per year. Anchorage is situated in a region of complex geology that consists of a sedimentary basin abutting and overlying metamorphic bedrock exposed in the Chugach Mountains, located on the eastern side of the city. One of the most important features affecting the ground response in Anchorage is the Bootlegger Cove formation, consisting of glacial and glaciofluvial deposits of interbedded clay, silt, and sand [1]. Significant slope failures and ground loss within this formation resulted in the northern portion of the city during the 1964 Great Alaska Earthquake ( $M_w$  9.2). Due to the population density and unique seismic setting of the Anchorage area there has been a focused effort by seismologists and engineers to understand the anticipated ground response resulting from the next major earthquake.

## **2. Background**

One example of the effort that has been made includes the development of a downhole array to monitor ground motions. The instrumentation at the array includes three-component accelerometers placed at seven depths from the surface to 61 meters below ground (Figure 1) and is located in Delaney Park, part of downtown Anchorage, Alaska. The downhole array has been recording strong ground motions since 2004 (Figure 2 and inset figure top left). The

site is located on level ground approximately 800 meters south and 800 meters east of the 1964 Great Alaska Earthquake 4<sup>th</sup> Avenue and L Street ground failures, respectively. Recorded ground motions at the borehole array have been analyzed as part of a systematic approach to develop a ground-motion model and to measure the impedance characteristics of the soil column located at the borehole array. The soil column at the array site is similar to the soils encountered north of the array, where significant damage resulted from the 1964 Great Alaska Earthquake. The general subsurface conditions consist of alluvium over glacial outwash and the Bootlegger Cove Formation (a stratified sequence of clastic sediments). Very dense glacial till lies below the Bootlegger Cove Formation and, because of its high shear (S) wave velocity ( $V_s > 760\text{m/s}$ ), acts as a Seismic Site Class B/C boundary [2].

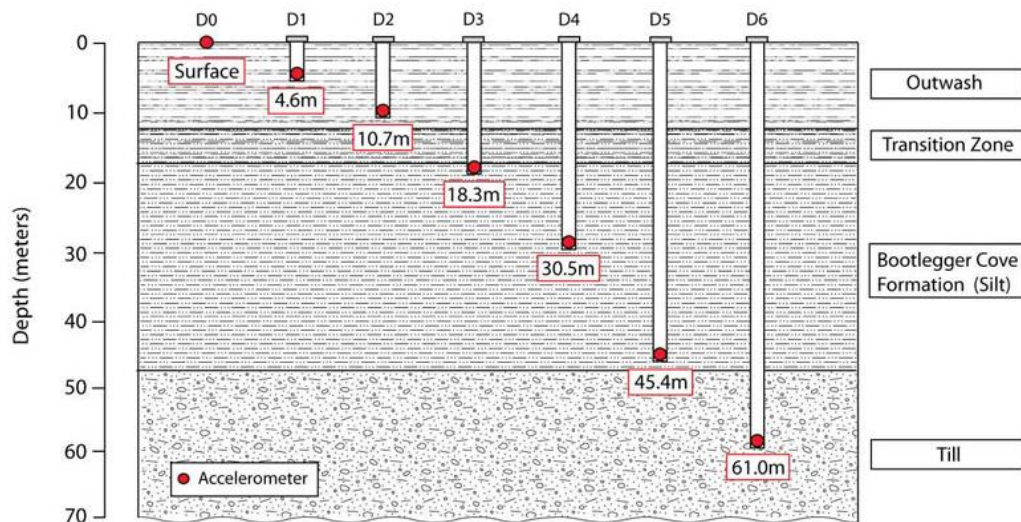


Fig. 7 – Delaney Park Downhole Array Instrument Depths [3].





Fig. 2 – Delaney Park Downhole Array Instrument Depths [4].

Shear wave velocity measurements at the site greatly improved the ability to estimate site response. The shear wave velocity at the site ranges from more than 900 m/s at the till to as low as 200 m/s in the upper Bootlegger Cove formation soils. The weighted average shear wave velocity at the site is calculated three different ways using the standard  $V_{S30}$  approach, averaging the upper 30-meter velocity profile,  $V_{S47}$ , averaging the upper soils above the till layer, and  $V_{S60}$ , using the full depth profile. The results along with the estimated fundamental periods, assuming quarter wavelength criteria are presented in Table 1.

Table 1 – Delaney Park Average Shear Wave Velocity Estimates

<b>Item</b>	<b>Weighted Average Shear Wave Velocity (m/s)</b>	<b>Fundamental Period (s)</b>
V <sub>S30</sub>	260	0.46
V <sub>S47</sub>	270	0.69
V <sub>S60</sub>	320	0.75

### 3. Site Modeling

As published in Thornley et al. [4], a soil model was developed to estimate the propagation of ground motions through a 1-D equivalent linear (EL) model of the DPDA site. The model was published a few weeks before the November 30, 2018 M<sub>w</sub>7.1 Anchorage Earthquake. The DPDA sensors recorded the event and these data were subsequently downloaded from the U.C. Santa Barbara Data portal [3]. The ground motions were processed using the SAC ground motion processing software. A bandpass Butterworth filter was applied with lower and upper filters at 0.1 and 30Hz. Ground motions records used had a signal-to-noise ratio greater than three. The processing was performed for the three components of each of the seven sensors.

Prior to evaluation of the ground motions with the EL model, shear strain levels were evaluated. This was performed because it has been observed that when shear strain levels are greater than about 0.3 to 1% the EL model begins to give erroneous results and a nonlinear (NL) model is considered more appropriate, as summarized by Kim et al. [5]. Using the methodology developed by Idriss [6] and further evaluated by Kim et al. [5], a shear strain index, as presented in Eq. (1) was used to calculate the maximum incident velocity that is allowable to maintain a shear index below 0.1%.

$$I_{\gamma} = PGV_{in}/V_{S30} \quad (1)$$

where  $I_\gamma$  is the shear strain index,  $PGV_{in}$  is the peak ground velocity of the incident motion, and  $V_{S30}$  is the weighted average site shear wave velocity for the upper 30 meters as defined by ASCE 7 [7]. The maximum  $PGV_{in}$  that maintains an appropriate shear index for EL models at this site is 28 cm/s or less. The November 30, 2018 recorded ground motions at the bottom of the DPDA were 20 cm/s, which supports the selection of an EL model for this event.

Once processed, the ground motions were used to test the previously mentioned 1-D equivalent linear model using STRATA [8]. The strong ground motion record measured at the bottom-most sensor, identified as D6 (Fig. 1), from the November 30, 2018 earthquake was used as the input motion. Both the North-South and East-West components were used individually. The ground motions were propagated through the model and the surface response spectra from the model were calculated. The calculated response spectra were then compared to the measured surface recording response spectra for both horizontal components. The measured and calculated response spectra at the surface (Instrument D0) are presented in Fig. 3a and 3b.

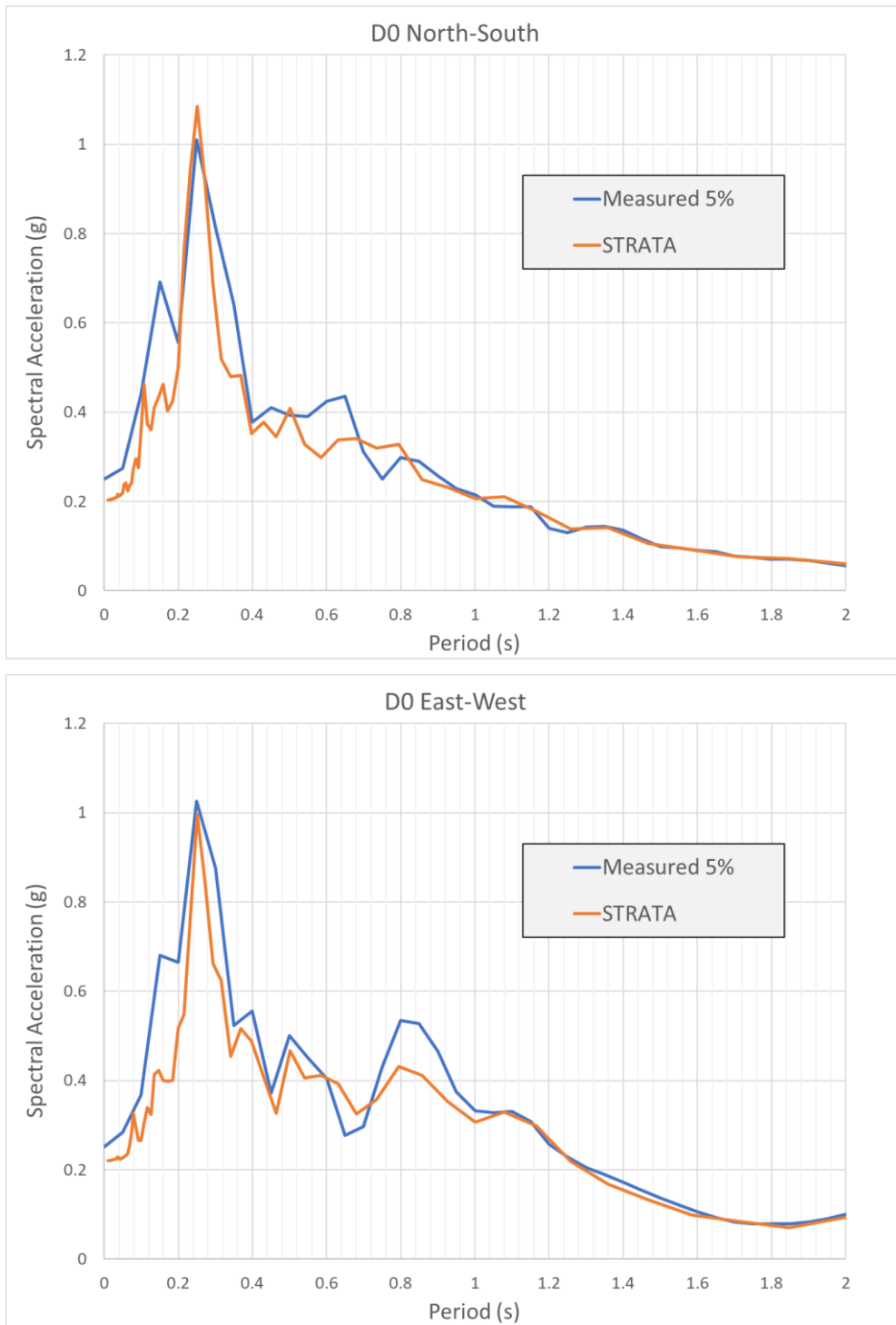


Fig. 3 – Measured and STRATA EL Response Spectra (a) (top) North-South Component (b) (bottom) East-West Component.

Based on visual observation the response spectra match well. The peaks, especially surrounding the peak period, are well matched, both by period and by amplitude. One

difference that is observed, both in the response spectra plots is the narrow peak at the peak period in the modeled spectra when compared to the measured spectra. This has been observed in modeling efforts at other sites by others as well (personal communication with Dr. Brady Cox [9]). Another interesting note is that, when comparing the results of the North-South component with the East-West component, the peaks have different amplitudes, but the EL model still performs well. This is an indicator that, at least for the November 30, 2018 earthquake, there was very little to no anisotropic effect. An evaluation of the measured versus modeled response for the five instruments located in the array between the bottom and the surface shows similar results and has not been included in this paper due to space constraints.

With the confidence in the results from the EL model, especially with respect to the shear modulus and damping curves, shear wave velocity profile, and other model parameters, a NL model was developed for the site. The NL software used for this effort was DEEPSOIL Version 7.0 [10] and the general quadratic/hyperbolic model (GQ/H) following Non-Masing Unload-Reload rules was used. The model was subdivided into the same 32 layers that were used for the STRATA EL model. Soil data collected from nearby sites, including standard penetration testing (SPT) and cone penetration testing (CPT), was used to estimate engineering parameters for appropriate curve fitting utilized in the DEEPSOIL model. DEEPSOIL provides both EL and NL results as part of the program's output. Because the strain index for the November 30, 2018 earthquake was appropriate for both EL and NL modeling, it is assumed that both models should give similar results. Figure 4 presents the response spectra for the measured ground motion for the North-South component and the results of the STRATA EL model (previously shown in Fig. 3) and the EL and NL DEEPSOIL models.

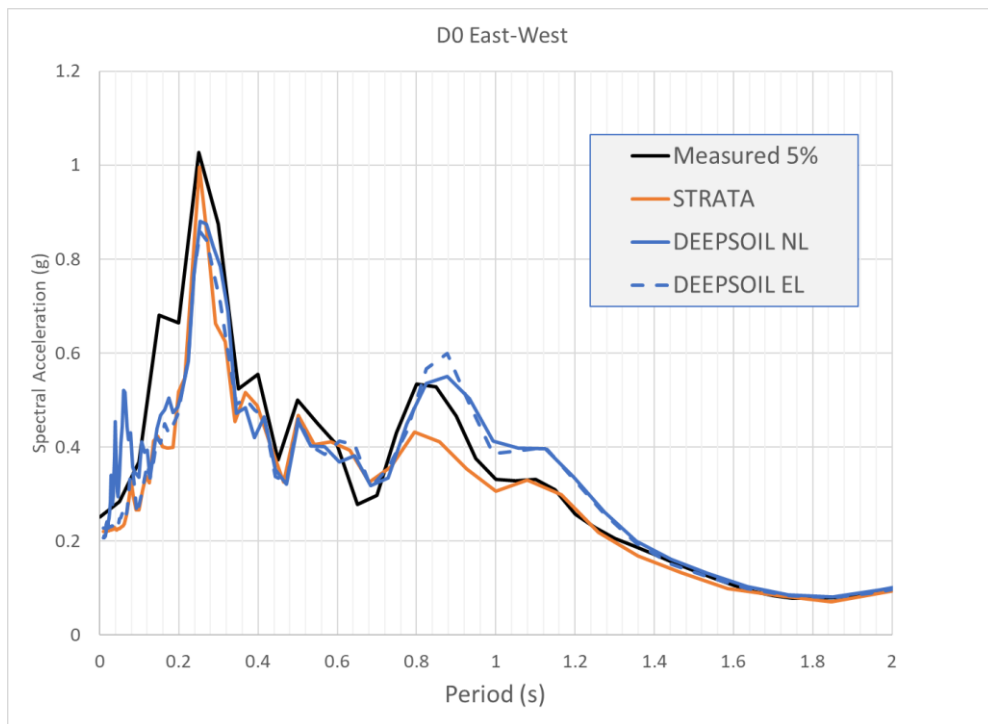


Fig. 4 – Measured and Modeled Response Spectra

The DEEPSOIL model provides results that match the measured response spectrum. The peak amplitude is slightly lower than the measured record, but the DEEPSOIL model provides a slightly broader peak, compared to the STRATA EL model. The DEEPSOIL model also matches additional peaks better (e.g. 0.75 to 1 s). The shear strains of the models are presented in Fig. 5. While the results indicate both models provide appropriate results for the November 30, 2018 earthquake for the response spectra, there are some differences between the shear strain estimates with depth. In general, within the Bootlegger Cove formation materials the DEEPSOIL model calculates the development of higher shear strain within the layers. It is interesting to note that the DEEPSOIL model requires additional fitting parameters during development when compared to the STRATA model, and differences between the two EL models may result. However, the results provide confidence that a suitable NL model has been calibrated to the DPDA site and the model can be used to evaluate site effects at the downhole array for larger ground motions.

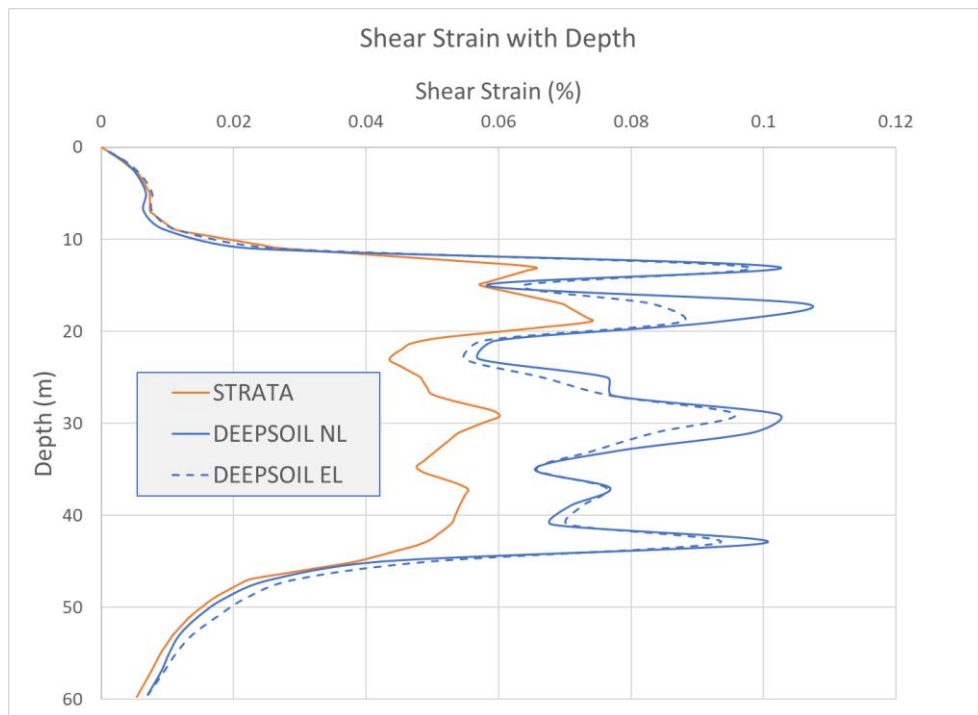


Fig. 5 – Shear Strain Estimates with Depth for STRATA and DEEPSOIL Models.

#### 4. Anchorage Engineering Considerations

Currently the Municipality of Anchorage has local amendments to the building code (2012 International Building Code) that provide direction to engineers performing slope stability modeling. It is common to perform limit equilibrium modeling using a pseudo-static approach for slope stability analyses. The pseudo-static approach requires a seismic coefficient ( $k_h$ ) that is applied to the horizontal portion of each slice in the limit equilibrium model [11]. The seismic coefficient is typically taken as a percentage of the site PGA. The percentage is adjusted based on several factors, including the tolerance for slope movement [12]. It is common engineering practice in Anchorage to use 50% of the peak ground acceleration (PGA) for slopes that can tolerate some movement under a design level earthquake. For a Seismic Site Class D soil in Anchorage, the code-based PGA is estimated to be 0.6g, using the current building code for a 2,475-year return period. In general, a  $k_h$  value of 0.3 is considered applicable within Anchorage for slope stability analyses. In areas within Anchorage near where significant slope failures have occurred, especially in areas where sloping ground has weaker zones of the Bootlegger Cove formation, a seismic coefficient of 0.2 is prescribed by

the local amendments to the building code. The general consensus of the local engineering community is that the Bootlegger Cove formation soils, when subjected to significant ground shaking, undergo large shear strains that provide damping of ground motions before they reach the ground surface.

While the November 30, 2018  $M_w 7.1$  earthquake was a significant event, larger earthquakes have occurred in southcentral Alaska and are anticipated in the future. There are several seismic sources that can be considered, including shallow crustal, intraplate, and subduction interface earthquakes [13]. One question that engineers continue to ask is whether the seismic coefficient assumption is correct. Using the model developed for the DPDA, we can help to evaluate this assumption. To test the effects of damping of the Bootlegger Cove formation on PGA, we assembled a series of time histories to evaluate the model. While this paper does not attempt to match the expected ground motions from a spectral analysis perspective, several time histories from crustal and subduction level events have been considered. Several readily available crustal earthquakes and scaled versions of the 2011 Tohoku earthquake have been used to evaluate the effects of scaled PGA at the DPDA.

*The Tohoku Earthquake time histories were scaled from the original PGA to new PGAs using the scaling function in DEEPSOIL. The ground motions were scaled using factors between 0.5 to 2 to develop a spread of data points that can be compared for input versus output ground motions.*

As noted previously, EL models are not effective at estimating 1-D site response when shear strains exceed 0.3 to 1%. The use of the calibrated NL model allows for further investigation of the assumption that greater damping is provided by the softer Bootlegger Cove formation soils and the lower  $k_h$  value is reasonable for use in slope stability analyses. The results of the site modeling provide some insights into the effects of the Bootlegger Cove formation soils on ground motion intensity measures such as PGA. Figure 6 presents the initial outcrop PGA and the modeled surface PGA at the DPDA using the NL model. These findings follow well



documented amplification and deamplification findings [14] where, at lower PGAs there is an amplification in the softer soil sites, but at larger PGAs there is a deamplification, when compared with reference rock sites.

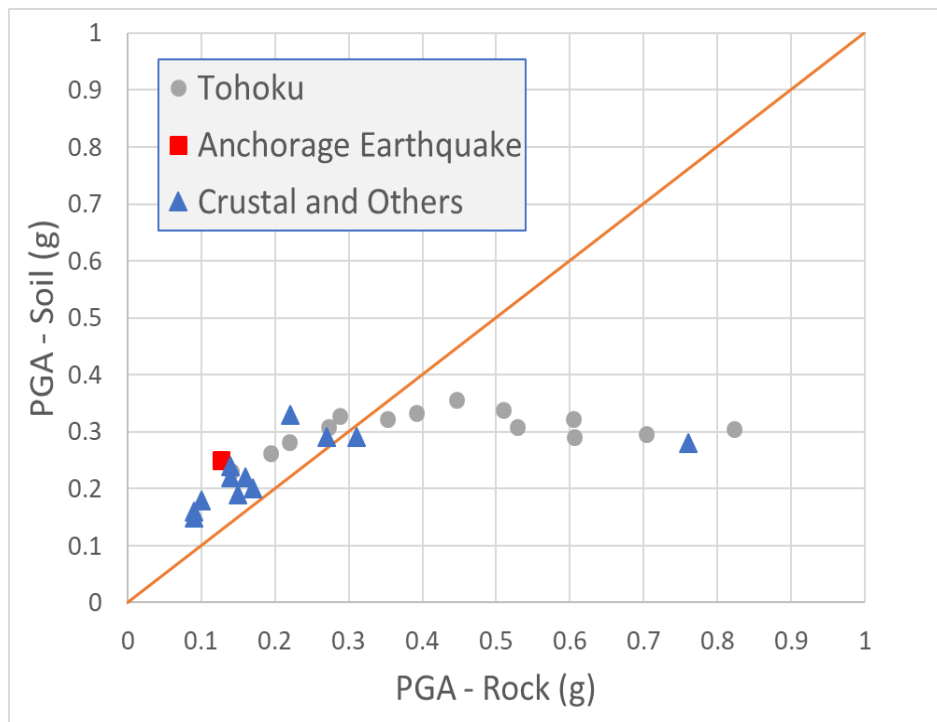


Fig. 6 – Soil Amplified PGA Compared to Outcrop PGA.

The shear strain with depth is presented in Fig. 7 for the 2011 Tohoku earthquake input motion at four different scaling factors between 0.5 and 2.0. The generalized soil lithology at the site is also presented. The shear strains within the Bootlegger Cove formation are significantly higher than the granular soils above and the glacial till below. The shear strains are greater than 1% at several depths and exceed 10% at one location at the higher scaling factors, which is in the realm of large shear strain and beyond the large shear strain failure of clay materials [15]. Figure 8 presents the calculated PGA with depth within the model. At scaling factors of 0.5 and 1.0 there are amplifications of the PGA. At larger scaling factors there is an alternating amplification and deamplification within the Bootlegger Cove formation, but as the ground motion approaches the interface with the overlying alluvium there is a significant reduction in PGA. These findings support the concept of utilizing a lower  $k_h$  value when evaluating the sites that have weaker Bootlegger Cove formation soils within Anchorage.

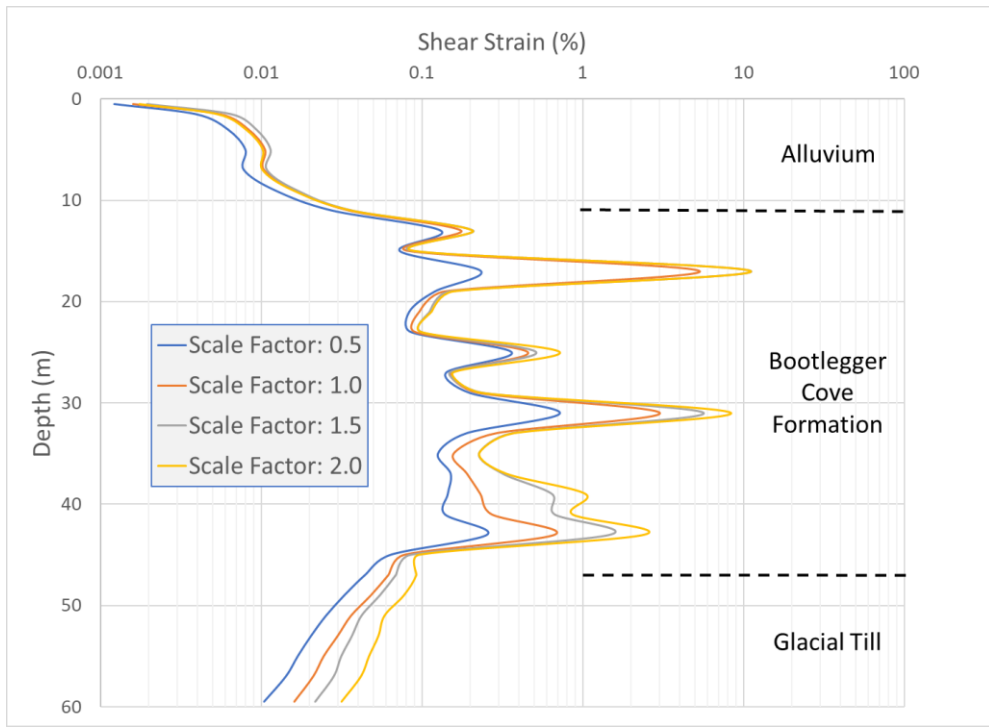


Fig. 7 – Shear Strain Estimates with Depth for the Scaled Tohoku Earthquakes with Generalized Soil Lithology

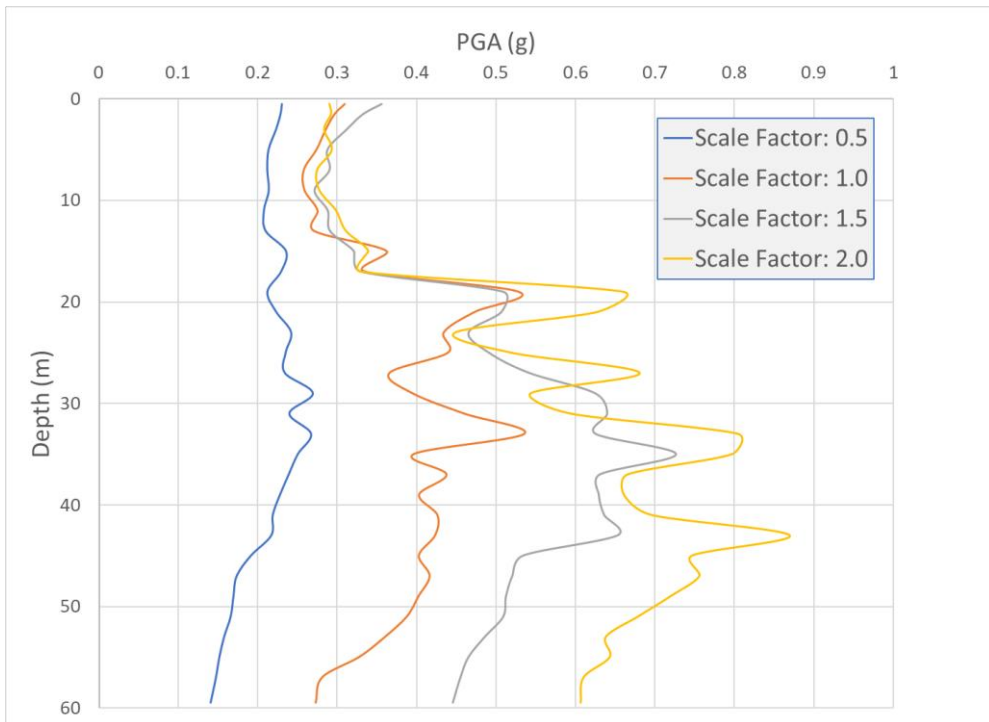


Fig. 8 – PGA Estimates with Depth for the Scaled Tohoku Earthquakes

## 5. Conclusions

The DPDA has provided useful ground motion recordings that have allowed for the opportunity to develop and calibrate 1-D EL and NL site response models. These models, especially the NL model, can be used for evaluating site response in downtown Anchorage where alluvial deposits overlie the Bootlegger Cove formation, which caused significant ground failure in the 1964 Great Alaska Earthquake. Based on the results presented in this paper, the response of the Bootlegger Cove formation is like other studies that have found deamplification of ground motions at larger ground shaking. This study supports previous efforts in the local building code to allow for a reduced seismic coefficient when performing simplified slope stability analyses using pseudo-static limit equilibrium approaches. It should be noted that a limited number of ground motions were utilized for this study and further assessment is likely necessary to develop definitive recommendations. Additionally, it should be noted that many of the slopes that are analyzed using the limit equilibrium approach result in factors of safety less than one and displacement-based approaches tend to be required. However, it is important to use appropriate input variables in engineering analyses and this study aims at supporting one aspect of that effort.

## **6. Acknowledgements**

The authors would like to acknowledge the numerous scientists and engineers that have worked in different ways to make this effort possible. Dr. Jamie Steidl has worked tirelessly to maintain a functional DPDA. Jessica Feenstra provided support in the time-history development. The Geotechnical Advisory Commission, especially Dave Cole and Buzz Scher, provided useful discussion throughout this evaluation. The support of these individuals, along with many others, has improved our understanding and ability to maintain high standards in public safety through earthquake engineering.

## 7. References

Schmoll, H.R., E. Dobrovolny, (1972). Generalized geologic map of Anchorage and vicinity, Alaska. US Geologic Survey Misc. Geol. Invest. Map I-787-D.

Dutta, U., M.K. Sen, N. Biswas, Z. Yang, (2009). Investigation of Shallow Sedimentary Structure of the Anchorage Basin, Alaska, Using Simulated Annealing Inversion of Site Response. *Bulletin of the Seismological Society of America*, Vol 99, No. 1, pp. 326-339, February 2009.

<http://www.nees.ucsb.edu/channel-maps#dpk/cross-section> (last accessed February 2020).

Thornley, J., Dutta, U., Fahringer, P., Yang, Z., (2019): In Situ Shear-Wave Velocity Measurements at the Delaney Park Downhole Array, Anchorage, Alaska. *Seismological Research Letters*, Volume 90, Number 1, January/February 2019 (p 395-400).

Kim, B., Y.M. Hashash, J.P. Stewart, E.M. Rathje, J.A. Harmon, M.I. Musgrove, K. W. Campbel, W.J. Silva, (2016). Relative Differences between Nonlinear and Equivalent-Linear 1-D Site Response Analyses, *Earthquake Spectra*, Volume 32, No. 3, pp. 1845-1865, August 2016.

Idriss, I. M., (2011). Use of Vs30 to represent local site conditions, in 4th LASPEI/IAEE International Symposium Effects of Surface Geology on Strong Ground Motions, Santa Barbara, CA.

American Society of Civil Engineers (ASCE). 2010. ASCE 7-10 Standard, Minimum Design Loads for Buildings and Other Structures, Reston VA.

Strata Equivalent Linear Site Response Software Version 0.5.9 (2017) [Software] Available from [github.com/arkottke/strata](https://github.com/arkottke/strata).

Cox, B. (2019). Personal communication.

Hashash, Y.M.A., Musgrove, M.I., Harmon, J.A., Ilhan, O., Groholski, D.R., Phillips, C.A., and Park, D. (2017) "DEEPSOIL 7.0, User Manual".

Duncan, J.M., Wright, S.G., Brandon, T.L. (2014). Soil Strength and Slope Stability, 2nd Edition. John Wiley & Sons, Inc.

Hynes-Griffin, M.E. and Franklin, A.G. (1984). "Rationalizing the Seismic Coefficient Method," Miscellaneous Paper GL-84-13, U.S. Army Corps of Engineers Waterways Experiment Station, Vicksburg, Mississippi, 21 pp.

Wesson, R.L., Boyd, O.S. Mueller, C.S., Bufe, C.G., Frankel, A.D., Petersen, M.D. (2007). Revision of Time-independent Probabilistic Seismic Hazard Maps of Alaska. U.S. Geological Survey Open-File Report 2007-1043.

Idriss, I.M. (1990). "Response of Soft Soil Sites During Earthquakes," J.M. Duncan, ed., Proceedings, H. Bolton Seed Memorial Symposium, BiTech Publishers, Vancouver, British Columbia, Vol. 2, pp. 273-289.

Dobry, R. and Vucetic, M. (1987). Dynamic Properties and Seismic Response of Soft Clay Deposits. Proceedings of the International Symposium on Geotechnical Engineering of Soft Soils, Mexico City, Volume 2, pp 57-87.

## **Appendix C: Relevant Coauthored Papers and Reports**



**EERI Earthquake Reconnaissance Report:  
M7.1 Anchorage Earthquake on Nov 30,  
2018**



Wael M. Hassan, John Thornley, Janise Rodgers, and Christopher Motter

April 2020

*A product of the EERI Learning from Earthquakes Program*

## INTRODUCTION

### Overview of the November 30, 2018, Anchorage Earthquake

On November 30, 2018, at 8:29 a.m., Alaska Standard Time (AKST), Southcentral Alaska, the most populous region in Alaska, was violently shaken by an Mw 7.1 earthquake that was 46 km (29 miles) deep with an epicenter at 61.346°N, 149.955°W, 12 km north of Anchorage and 19 km west of Eagle River. Shortly after, at 8:35 a.m., AKST, an Mw 5.8 aftershock and a widely broadcasted tsunami warning further terrified Alaskans and the nation, especially after early unconfirmed reports of widespread damage in the region. The event affected some 400,000 residents in the Anchorage Metropolitan Area in the Anchorage and Matanuska-Susitna (Mat-Su) Boroughs. The earthquake caused widespread damage to roads and highways, nonstructural components, non-engineered buildings (which do exist widely in the region), older buildings, and buildings and infrastructure on poorly compacted (and uncompacted) fills. Minor structural damage in newly engineered buildings was observed. The main shock generated a vigorous aftershock sequence with over 9,000 aftershocks within first 4.5 months. Over 300 aftershocks were felt.

Building stock diversity manifested the region as a large test bed to observe how building practices impacted their earthquake damage levels. The Anchorage Bowl is heavily free-field instrumented, and more than eight structures in Anchorage are well instrumented with structural arrays. The prevailing peak ground acceleration in the region was  $0.2g$ – $0.3g$ , although individual sites may have experienced stronger shaking due to local soil conditions or building configurations. In general, the ground motion at most sites was about 50%–60% of the design-based earthquake (DBE) acceleration.

After a year-long investigation following the earthquake, it can be confidently stated that Southcentral Alaska's built environment has not yet been seismically tested, even with a DBE, let alone the maximum considered event.

### EERI Reconnaissance Team Members

The Earthquake Engineering Research Institute (EERI) Field Reconnaissance Team comprised four members balanced between academics and professionals:

1. Wael M. Hassan, Associate Professor of Structural Engineering, University of Alaska, Anchorage, AK (team co-leader and leader of structural engineering reconnaissance)
2. John Thornley, Associate, Golder Associates, Anchorage, AK (team co-leader and leader of geotechnical engineering reconnaissance)
3. Janise Rodgers, Chief Operating Officer and Project Manager, GeoHazard International, Menlo Park, CA
4. Christopher Motter, Assistant Professor of Structural Engineering, Washington State University, Pullman, WA

Several other individuals facilitated and assisted the team in its mission, as outlined in the *Acknowledgments*.

### EERI Reconnaissance Team Activities

The EERI Reconnaissance Team started its mission a few days following the earthquake. Team co-leaders were already working on independent personal reconnaissance immediately



following the earthquake on November 30, 2018. The field mission comprised surveying, curb inspection, and thorough damage inspection of hundreds of structures over the course of 10 months following the event. The majority of field inspections took place in December 2018 and January 2019. However, significant field reconnaissance was performed by the team co-leaders in the spring and summer of 2019 following snow melting, which relatively exacerbated damage in the built environment and revealed original damage that was hidden by snow. Few field inspection activities were continued through September 2019 by the team co-leaders.

The EERI Reconnaissance Team co-leader Wael Hassan was in charge of leading the structural and nonstructural investigation, while the team co-leader John Thornley was in charge of leading the geotechnical and seismological investigation. The first phase of field reconnaissance (December 2018 to January 2019) by the team included 4 weeks of field reconnaissance by team co-leader Wael Hassan, 2 weeks of fieldwork by team co-leader John Thornley, and 1 week of field activity each by the team members Janise Rodgers and Christopher Motter. The second phase of field reconnaissance in spring and summer of 2019 comprised 2 weeks of fieldwork by each of the team co-leaders, Wael Hassan and John Thornley, while the third phase in September 2019 included 3 days of fieldwork by team co-leader Wael Hassan. The EERI Reconnaissance Team collected a significant amount of valuable perishable damage data firsthand throughout the reconnaissance mission, which were used to establish a damage database by the team. In addition, the team was able to secure other valuable damage databases and inspection reports by several governmental and private organizations involved in damage assessment and repair in both the Municipality of Anchorage and Mat-Su Borough. The EERI Reconnaissance Team conducted exploratory studies on building damage patterns, resilience and recovery, instrumented buildings, schools and hospitals, and bridges and lifelines that will appear in subsequent publications.

### **Coordination with Other Reconnaissance Teams**

The local EERI Learning from Earthquakes (LFE) co-leaders Wael Hassan and John Thornley provided assistance, contacts, coordination, access, and technical data to more than 16 different reconnaissance and inspection teams from December 2018 to September 2019. These teams include the Federal Emergency Management Agency; Applied Technology Council 20 local volunteers; Skidmore, Owings and Merrill, San Francisco; the University of Alaska, Anchorage; Simpson Gumpertz & Heger, San Francisco; the Electric Power Research Institute; the municipality of Anchorage; Thornton Tomasetti, Structural Engineering Extreme Event Reconnaissance; Geotechnical Engineering Extreme Event Reconnaissance; the EERI Virtual Reconnaissance Team; the EERI Business Resilience Team; the Pacific Earthquake Engineering Research Center; the U.S. Geological Survey; the National Institute for Standards and Technology; and Acceptable Risk, LLC, California, besides several other individuals.

### **EERI Clearinghouse Coordination**

Following the earthquake, EERI held 10 physical and virtual earthquake clearinghouses in Anchorage at Golder Associates through the end of January 2019. The clearinghouse notes can be found at <http://www.learningfromearthquakes.org/2018-11-30-anchorage-alaska/>. The first clearinghouses were held daily starting on December 1 for 5 days after the event then every 2 to 3 days until December 17. One more clearinghouse was held in January to follow up on the reconnaissance efforts after the holidays. The clearinghouses were very efficient in communicating and exchanging field reconnaissance data, reducing duplicate work, coordinating different teams' activities, securing building access for inspection, and focusing reconnaissance efforts on more perishable data sites/heavier damage sites. The

clearinghouse notes are one of the sources the EERI Field Reconnaissance Team used to confirm and document some damage observations.

### **EERI and LFE Program**

EERI was established in 1948. EERI is the leading nonprofit technical organization that connects those dedicated to reducing earthquake risk. The multidisciplinary membership includes engineers, geoscientists, social scientists, architects, planners, emergency managers, academics, students, and other like-minded professionals. The objective of EERI is to reduce earthquake risk by (1) advancing the science and practice of earthquake engineering; (2) improving understanding of the impact of earthquakes on the physical, social, economic, political, and cultural environment; and (3) advocating comprehensive and realistic measures for reducing the harmful effects of earthquakes.

The EERI LFE program was established in 1973, with a mission to accelerate and increase learning from earthquake-induced disasters that affect the natural, built, social, and political environments worldwide. The mission is accomplished through field reconnaissance, data collection and archiving, and dissemination of lessons and opportunities for reducing earthquake losses and increasing community resilience. Through LFE, EERI sends multidisciplinary reconnaissance teams of earthquake-risk-mitigation experts to investigate earthquake impacts. Reconnaissance teams travel to earthquake-impacted areas, document important observations, and identify topics in need of follow-up research. Increasingly, LFE has focused on capturing lessons for community resilience through earthquake reconnaissance. LFE has developed a framework for resilience reconnaissance and has begun conducting follow-up reconnaissance trips months and years after damaging earthquakes. Volunteer EERI field teams are deployed on trips that aim to document impacts, identify knowledge gaps for which further research is most needed, and identify practices that will improve mitigation measures, disaster preparedness, and emergency responses for future disasters.

### **EERI and LFE Program**

This report is a multidisciplinary seismological and engineering report that is organized in 10 chapters. The report is a first version that might be amended with subsequent versions and other independent publications should more information and lessons become available. Besides this introduction in Chapter 1, Chapter 2 presents the tectonic setting and seismological aspects of Southcentral Alaska. Chapter 3 presents the geotechnical impacts of the earthquake on the region. Chapter 4 portrays the structural damage observed in buildings along with the performance of instrumented buildings in Anchorage. Chapter 5 comprehensively depicts the observed nonstructural systems and equipment damage in buildings. Chapter 6 is dedicated to the performance of schools during the earthquake and their earthquake resiliency. Chapter 7 focuses on the impact of the earthquake on hospitals. Chapter 8 presents the impacts of the earthquake on the transportation system, including bridge structures, in Southcentral Alaska. Chapter 9 discusses the impacts of the earthquake on lifelines and utilities, and, finally, Chapter 10 presents concluding thoughts on the observations and lessons learned and recommendations and a vision to reduce earthquake losses on the basis of the results of this investigation.

Focus Section: 2018 Anchorage Earthquake

## The 30 November 2018 $M_w$ 7.1 Anchorage Earthquake

Michael E. West<sup>1</sup>, Adrian Bender<sup>2</sup>, Matthew Gardine<sup>1</sup>, Lea Gardine<sup>1</sup>, Kara Gately<sup>3</sup>, Peter Haeussler<sup>2</sup>, Wael Hassan<sup>4</sup>, Franz Meyer<sup>1</sup>, Cole Richards<sup>5</sup>, Natalia A. Ruppert<sup>1</sup>, Carl Tape<sup>1,5</sup>, John Thornley<sup>6</sup>, and Rob C. Witter<sup>2</sup>

### Abstract

The  $M_w$  7.1 47 km deep earthquake that occurred on 30 November 2018 had deep societal impacts across southcentral Alaska and exhibited phenomena of broad scientific interest. We document observations that point to future directions of research and hazard mitigation. The rupture mechanism, aftershocks, and deformation of the mainshock are consistent with extension inside the Pacific plate near the down-dip limit of flat-slab subduction. Peak ground motions  $>25\%$ g were observed across more than 8000 km<sup>2</sup>, though the most violent near-fault shaking was avoided because the hypocenter was nearly 50 km below the surface. The ground motions show substantial variation, highlighting the influence of regional geology and near-surface soil conditions. Aftershock activity was vigorous with roughly 300 felt events in the first six months, including two dozen aftershocks exceeding  $M$  4.5. Broad subsidence of up to 5 cm across the region is consistent with the rupture mechanism. The passage of seismic waves and possibly the coseismic subsidence mobilized ground waters, resulting in temporary increases in stream flow. Although there were many failures of natural slopes and soils, the shaking was insufficient to reactivate many of the failures observed during the 1964  $M$  9.2 earthquake. This is explained by the much shorter duration of shaking as well as the lower amplitude long-period motions in 2018. The majority of observed soil failures were in anthropogenically placed fill soils. Structural damage is attributed to both the failure of these emplaced soils as well as to the ground motion, which shows some spatial correlation to damage. However, the paucity of instrumental ground-motion recordings outside of downtown Anchorage makes these comparisons challenging. The earthquake demonstrated the challenge of issuing tsunami warnings in complex coastal geographies and highlights the need for a targeted tsunami hazard evaluation of the region. The event also demonstrates the challenge of estimating the probabilistic hazard posed by intraslab earthquakes.

Cite this article as West, M. E., A. Bender, M. Gardine, L. Gardine, K. Gately, P. Haeussler, W. Hassan, F. Meyer, C. Richards, N. A. Ruppert, et al. (2019). The 30 November 2018  $M_w$  7.1 Anchorage Earthquake, *Seismol. Res. Lett.* 91, 66–84, doi: 10.1785/0220190176.

[Supplemental Material](#)

### Introduction

On the morning of 30 November 2018, southcentral Alaska experienced the most societally significant earthquake in the region in half a century. The  $M_w$  7.1 earthquake occurred nearly 50 km beneath Anchorage inside the subducting slab as a result of tensional forces near the transition from flat to steeply dipping slab. Strong to severe shaking was felt by more than half of Alaska's population. Because the earthquake impacted so many sectors of society, it is arguably the best earthquake learning experience in Alaska since the  $M_w$  9.2 Great Alaska earthquake in 1964. The purpose of this article is to provide an introduction to the observations and impacts across disciplines.

Anchorage and southcentral Alaska experience frequent shaking from earthquakes occurring on the Alaska–Aleutian subduction zone interface. But earthquakes inside the subducting

slab and in the overlying crust add to the hazard. Magnitude 4 and 5 earthquakes are felt routinely, albeit lightly, by the majority of Alaskans. Even large earthquakes occur with some regularity. More than 80% of the  $M$  6+ earthquakes in the United States occur in Alaska and surrounding waters. Averaged over decades,  $M$  7+ earthquakes occur somewhere along the arc every other year, though the past few years have exceeded this rate.

1. Geophysical Institute, University of Alaska Fairbanks, Fairbanks, Alaska, U.S.A.;
2. Alaska Science Center, U.S. Geological Survey, Anchorage, Alaska, U.S.A.;
3. National Tsunami Warning Center, Palmer, Alaska, U.S.A.;
4. Civil Engineering Department, University of Alaska Anchorage, Anchorage, Alaska, U.S.A.;
5. Department of Geosciences, University of Alaska Fairbanks, Fairbanks, Alaska, U.S.A.;
6. Golder Associates Inc., Anchorage, Alaska, U.S.A.

\*Corresponding author: mewest@alaska.edu

© Seismological Society of America

## Impacts of the 2018 M7.1 Anchorage earthquake on schools

Earthquake Spectra

1–26

© The Author(s) 2021

Article reuse guidelines:

sagepub.com/journals-permissions

DOI: 10.1177/8755293020988022

journals.sagepub.com/home/eqs



Janise Rodgers, M.EERI<sup>1</sup>, Wael Hassan, M.EERI<sup>2</sup>,  
Christopher Motter<sup>3</sup>, and John Thornley, M.EERI<sup>4</sup>

### Abstract

The 2018 M7.1 Anchorage earthquake damaged over 120 schools in the Anchorage and Matanuska-Susitna (Mat-Su) School Districts. Many remained closed for a week or more for cleanup and repairs, primarily due to nonstructural damage. Major structural damage occurred in three of 132 school buildings across both districts, and a number of additional schools had minor to moderate damage. Most observed damage was to nonstructural components, including suspended ceilings, lighting, architectural finishes, building utility systems, and equipment. Middle and high schools were in session at the time of the earthquake. Despite ceiling damage and fallen ceiling tiles, books, and supplies (heavy furniture was anchored) and objects swinging from the ceiling, both districts reported very few injuries. Statements by the school districts and administrators, media reports, and available video indicate that most students dropped, covered, and held on as practiced in regular drills. The combination of life-safety structural performance (with a few exceptions) due in part to moderate shaking, as well as anchoring of heavy furnishings, and student preparedness and drills to practice protective action, appears to have protected students. Both districts' experiences provide evidence that school seismic safety programs are valuable, even if efforts to mitigate risks from older, vulnerable schools are in process and more work remains.

### Keywords

Nonstructural damage, structural damage, reconnaissance, suspended ceiling, masonry walls, seismic resilience, preparedness, protective action, strong motion, school earthquake safety

Date received: 21 May 2020; accepted: 21 November 2020

<sup>1</sup>GeoHazards International, Menlo Park, CA, USA

<sup>2</sup>University of Alaska Anchorage, Anchorage, AK, USA

<sup>3</sup>Washington State University, Pullman, WA, USA

<sup>4</sup>Golder Associates Inc., Anchorage, AK, USA

### Corresponding author:

Janise Rodgers, GeoHazards International, 687 Bay Road, Menlo Park, CA 94025, USA.

Email: [rodders@geohaz.org](mailto:rodders@geohaz.org)

1     **Structural Performance of Buildings during**  
2     **the November 30, 2018 M7.1 Anchorage,**  
3     **Alaska Earthquake**  
4

5     **Wael M. Hassan,<sup>a)</sup> M.EERI, Janise Rodgers,<sup>b)</sup> M.EERI, Christopher Motter,<sup>c)</sup>**  
6     **M.EERI and John Thornley,<sup>d)</sup> M.EERI**

7             Southcentral Alaska, the most populous region in Alaska, was violently shaken by a  
8     M<sub>w</sub> 7.1 earthquake on Nov 30, 2018 at 8:29 am Alaska Standard Time. This was the largest  
9     magnitude earthquake in the U.S. close to a population center in over 50 years. The earthquake  
10    was 46 kilometers deep, and the epicenter was 12 kilometers north of Anchorage and 19  
11    kilometers west of Eagle River. The event affected some 400,000 residents, causing  
12    widespread damage in highways, non-structural components, non-engineered and older  
13    buildings, and structures on poorly compacted fills. A few isolated serious injuries and partial  
14    collapses took place. Minor structural damage to code-conforming buildings was observed. A  
15    significant percentage of the structural damage was due to geotechnical failures. Building stock  
16    diversity allows use of the region as a large testbed to observe how building practices impacted  
17    earthquake damage levels. The prevailing PGA was 0.2-0.32g, causing shaking intensity at  
18    most sites of 50-60% of the design-basis earthquake acceleration. Thus, the seismic  
19    vulnerability of building stock in the region was not truly tested. Reinforced concrete buildings  
20    had minor structural damage, except in a few cases of concerning shear wall and transfer girder  
21    shear cracking. FRP retrofitted buildings performed satisfactorily. CMU masonry buildings  
22    experienced serious structural damage in many cases, including relatively newer buildings. The  
23    earthquake caused widespread structural damage in non-engineered buildings (primarily wood  
24    and CMU masonry) that exist widely in the region, especially in Eagle River. Of these, non-  
25    engineered single-family wood buildings had the heaviest structural damage. No structural  
26    damage could be observed in steel buildings. The aftershock sequence, which included seven  
27    M5+ and 50 M4+ events, exacerbated structural damage in all types of buildings.

---

<sup>a)</sup> University of Alaska, Anchorage, AK, 3211 Providence Dr., Anchorage, AK 99508

<sup>b)</sup> GeoHazards International, Menlo Park, CA

<sup>c)</sup> Washington State University, Pullman, WA

<sup>d)</sup> Golder Associates, Inc. Anchorage, AK